Doctoral Dissertation
Doctoral Program in Mechanical Engineering (38th Cycle)

Necking in ductile metals: development and assessment of efficient identification methods

Marta Beltramo

* * * * * *

Supervisors
Prof. L. Peroni, Supervisor
Prof. M. Scapin, Co-Supervisor

Coordinator
Prof. A. Vigliani

Politecnico di Torino
2026

I hereby declare that the contents and organization of this dissertation constitute my own original work and does not compromise in any way the rights of third parties, including those relating to the security of personal data.

Marta Beltramo

....

Marta Beltramo

Turin, July 3rd, 2026

Summary

The present Ph.D. thesis addresses the development of effective strategies for identifying hardening behavior of ductile metals by exploiting the post-necking phase of tensile tests. The availability of methods capable of calibrating elasto-plastic constitutive models appropriately and efficiently is of utmost importance for the reliability of Finite Element Analyses (FEA), increasingly employed in many engineering fields (e.g., metal-forming processes, dynamic impact events, energy-absorption systems, etc.). From a practical standpoint, elasto-plastic constitutive models are usually calibrated using experimental data and appropriate identification strategies within a phenomenological framework.

Among the wide variety of experimental techniques that can be employed, tensile tests on dog-bone specimens are still widely used for characterizing hardening of massive components. Indeed, these tests are both simple to execute and able to induce large plastic strains in ductile metals, thus broadening the calibration range of material laws. In addition, tensile tests can be readily adapted, through proper experimental setups, to study the effect of strain rate, temperature, and other environmental conditions. This makes such tests particularly attractive for both academic and industrial applications. Nevertheless, the largest strains are achieved during necking, because of a progressive strain localization. The non-uniform strain and stress fields, as well as the loss of stress uniaxiality, cause tensile test data to no longer be interpreted based on uniform deformation assumptions. This has motivated, over the past decades, the development of several analytical, experimental, and numerical approaches. Their final objective has been to exploit tensile tests fully, taking advantage of their well-known benefits, while enabling the reliable calibration of constitutive models for large-strain applications.

Based on the advances of previous research and supported by modern experimental and computational tools, further progress can be made towards methods that effectively combine efficiency and accuracy. This represents the main scope of the present thesis. Necking is regarded as an intrinsic feature of tensile loading that can be modeled and systematically used for material identification. The proposed approaches explicitly use the necking deformed configuration of the specimen as primary source of information. Specifically, FE simulations are used

to establish quantitative links between observable quantities, primarily the evolution of necking silhouettes, and the underlying material behavior. On this basis, inverse and shape-based identification strategies are developed to extract material information over an extended deformation range. Additional effects such as strain rate sensitivity, thermal coupling, and material anisotropy are properly addressed whenever they significantly influence necking behavior and material parameter identification. Comparison with well-established methods on some experimental case studies highlights the advantages that the proposed approach offers in terms of combining accuracy and efficiency. Furthermore, experimental investigation proved the overall practical applicability, potentiality, and flexibility of the proposed framework of analysis.

Acknowledgment

Part of this work has been carried out within the framework of the EUROfusion Consortium, funded by the European Union via the Euratom Research and Training Programme.

Contents

List of Tables

List of Figures

Chapter 1

Introduction

Currently, Finite Element (FE) simulations are widely employed in many engineering fields, from product and process design to structural integrity assessment. A noteworthy class of FE applications involves loading conditions in which metals undergo large plastic deformation. This includes metal-forming processes, dynamic impact events, energy-absorption systems, etc. The reliability of FE analyses (FEA) highly depends on the capability of selecting and calibrating appropriate constitutive models for representing material behavior. In metallic materials, a comprehensive description of the material irreversible response under complex stress states is provided by the plasticity theory, which underpins elasto-plastic constitutive models in FE formulations. Specifically, material hardening represents the core topic of this thesis, hence Section 1.1 is devoted to placing the hardening law within the broader framework of plasticity and, more generally, of continuum mechanics.

Elasto-plastic constitutive models are usually calibrated using experimental data and appropriate characterization strategies within an empirical framework. Various experimental techniques can be used: from standard mechanical tests, such as tensile and compression tests, to more complex configurations designed to induce multiaxial stress states, including bulge tests and specially tailored specimen geometries. Among them, tensile tests on dog-bone specimens are still commonly employed for identifying hardening of massive components. This is thanks to a series of uncontested advantages detailed in Section 1.1.

When testing specimens of ductile metals, necking usually occurs; Section 1.2 focuses on phenomenological strategies proposed in the literature for post-necking hardening identification, highlighting their underlying assumptions and typical fields of applicability.

1.1 Hardening law

In engineering applications, it is common to adopt the continuum mechanics framework to analyze and describe various physical phenomena. Physical bodies are considered as macroscopic systems without detailed knowledge of the complexity of their internal structures. They are conceived as continuous media whose properties are described through continuous fields in space, obtained by averaging the underlying atomic structure over a small representative volume. Continuum mechanics comprises fundamental equations to characterize kinematics, stresses and balance principles, that hold for any continuum body. Then, constitutive laws, specific for the material under investigation, are required to predict the observed physical behavior of real deformable bodies under specific conditions [1]. By implementing fundamental equations and constitutive laws and integrating them within numerical solution schemes, computational mechanics provides the numerical framework for the solution of continuum mechanics problems.

In metals, large deformations are enabled by irreversible rearrangements of atomic positions, which manifest at the macroscopic scale as plastic flow. The transition from elastic to plastic behavior, together with the subsequent evolution of plastic deformation, can be effectively described by elasto-plastic constitutive models. These models are based on the plasticity theory, which consists of three fundamental concepts: the yield criterion, which defines the onset and continuance of plastic flow; the flow rule, which dictates the direction of the plastic strain increments once yielding occurs; and the evolution equations for internal variables, including hardening relation for governing the evolution of the yield function [2]. Generally, the hardening behavior of the material is a function of the prior history of plastic deformation. The latter is usually described by the equivalent (or effective) plastic strain and represents the main example of internal variable.

Plasticity theory has been developed mainly with the aim of describing permanent deformations under multiaxial stress states: indeed, real-world components are seldom subjected to uniaxial stresses only. To simplify the mathematical description of such complex loading conditions, the concept of equivalent stress is introduced. This scalar quantity reduces any multiaxial stress or strain state to a single, representative value. More specifically, the choice is such that the equivalent stress coincides with the longitudinal stress that a dog-bone specimen experiences during a tensile test, as long as uniform deformation takes place. In this condition, also the equivalent plastic strain coincides with the longitudinal component, being the equivalent plastic strain rate defined as the work conjugate of the equivalent stress. The tensile test ascends to its role of foundational cornerstone for material characterization thanks to the ease of execution, the uniaxiality of the force, and the simplicity of the stress and strain states that are generated within the dog-bone specimen during uniform deformation. This allows the macroscopic measurements of force and elongation to be straightforwardly converted to longitudinal stresses and strains. Due to these aspects, it is also the main test, among all the possible mechanical ones, which can be coupled with non-standard environmental conditions (in terms of temperature, corrosion, etc.). This is of utmost importance considering that, due to the deformation mechanisms of metals, their mechanical response does not depend only on strain, but also on strain rate and temperature. Through adequate techniques, tensile tests can be performed at different strain rates, from quasi-static condition up to 10^3 s^{-1}, or even 10^4 s^{-1} with a proper specimen design. Hence, in addition to identifying material strain-hardening behavior, tensile tests also allow thermal effects, strain rate sensitivity, ductile damage insurgence, etc. to be investigated. These effects must be properly considered in applications where the material undergoes large deformations across a wide range of strain rates and temperatures.

Focusing on isotropic materials, a single test at a given environmental condition provides the experimental data necessary to calibrate the yield criterion and to define the hardening law in that condition. This is valid provided that the effect of triaxiality on material plastic flow can be neglected for the application of interest of the calibrated model. If this last assumption is not satisfied, the tensile test on a dog-bone specimen provides information for a single triaxiality value only (when the analysis is limited to uniform deformation), and additional tests need to be carried out for calibrating an adequate yield criterion. Another critical situation regards anisotropic materials; even in this case, tensile tests still play a central role in yielding and hardening determination. However, to account for the material directional behavior, complex yield functions are needed, which in turn require proper calibration via experimental tests performed on dog-bone specimens with different orientations of the loading axis with respect to the material crystallographic structure. Regarding equivalent variables, it is up to the researchers who calibrate the yield criterion to choose which orientation to adopt as reference one; the strength at other orientations is then expressed relatively to the reference one. Finally, a subsequent level of complexity is related to the flow rule, since probing it requires sophisticated multiaxial testing. Actually, for most metals, the normality rule is used: plastic strain increments are assumed to occur perpendicular to the yield surface. This flow rule is based on the postulate of maximum plastic dissipation, which was also derived from considerations of crystal plasticity by Bishop and Hill [3]. The normality rule is also known as associated (or associative) flow rule, in the sense of being associated with the yield criterion: indeed, normality mathematically derives from considering the yield surface itself as plastic potential. Conversely, when the plastic potential differs from the yield surface, the flow rule is called non-associated. This is well-suited to model soil and granular materials, but some researchers used it also for describing certain anisotropic behaviors of metals [4, 5]. The necessity of employing a non-associated flow rule depends not only on the material itself, but also on the application for which the calibrated model will be used and the level of detail required.

Within this context, the present thesis deals with the identification of the hardening law, focusing on materials and/or conditions for which the normality rule can be assumed. Regarding yielding, the Von Mises criterion is adopted for isotropic materials, while its anisotropic generalization, the Hill's 1948 criterion, is used for anisotropic ones. This means that yielding is assumed to be independent of both the pressure and of the specific stress state. While the first of these assumptions is widely acknowledged for metals (plastic flow is governed by deviatoric shear-driven dislocation motion rather than by the hydrostatic stress in these materials) the second may not be valid in general. Nevertheless, Von Mises and Hill's 1948 criteria have been chosen as they offer a good trade-off between physical relevance, identifiability from standard tests, and engineering applicability in FE simulations.

1.2 Tensile test for hardening identification

In the present thesis a phenomenological approach to the characterization problem has been chosen: the hardening behavior is identified by properly post-processing measurements acquired during experimental tensile tests. Complex tests [6] and/or geometries [7, 8] have been proposed in the literature, but they generally require dedicated fixtures and complicated measurement setups. This is why, for limiting the experimental cost and effort, uniaxial tensile tests on dog-bone specimens remain attractive.

With reference to the scheme of Figure 1.1, during a tensile test, the specimen undergoes an elongation Δx due to the displacements imposed on the specimen's heads (x_1 and x_2). Consequently, the specimen counteracts this deformation by generating forces (F_1 and F_2). In quasi-static tests the forces at the two sides are equal $F_1 = F_2 = F$ and depend on deformation and loading conditions. This is valid also in dynamic tests once equilibrium is established.

In the first phase of the test, the specimen gradually elongates while uniformly reducing its cross-section, and the load F progressively increases (configurations A and B of Figure 1.1). At a certain point, a maximum of force is achieved, i.e., when material hardening cannot compensate for the reduction of the cross-section. Soon after this condition, the deformation localizes in a limited region of the specimen, which assumes the typical neck shape depicted in configuration C of Figure 1.1. During the post-necking phase, the load required to continue deforming the specimen decreases. This is due to the localization itself and may not necessarily be linked to voids nucleation, growth, or coalescence. For instance, pure metals do not undergo ductile damage, but a decreasing load during necking still occurs. Hence, the post-necking phase is still representative of material hardening behavior. This is important considering that such phase can constitute a great part of the test for ductile metals. Therefore, many efforts have been devoted over the past decades to dealing with necking. The aim was to exploit the large strains achieved during this phase for identifying the material behavior over a broad strain range.

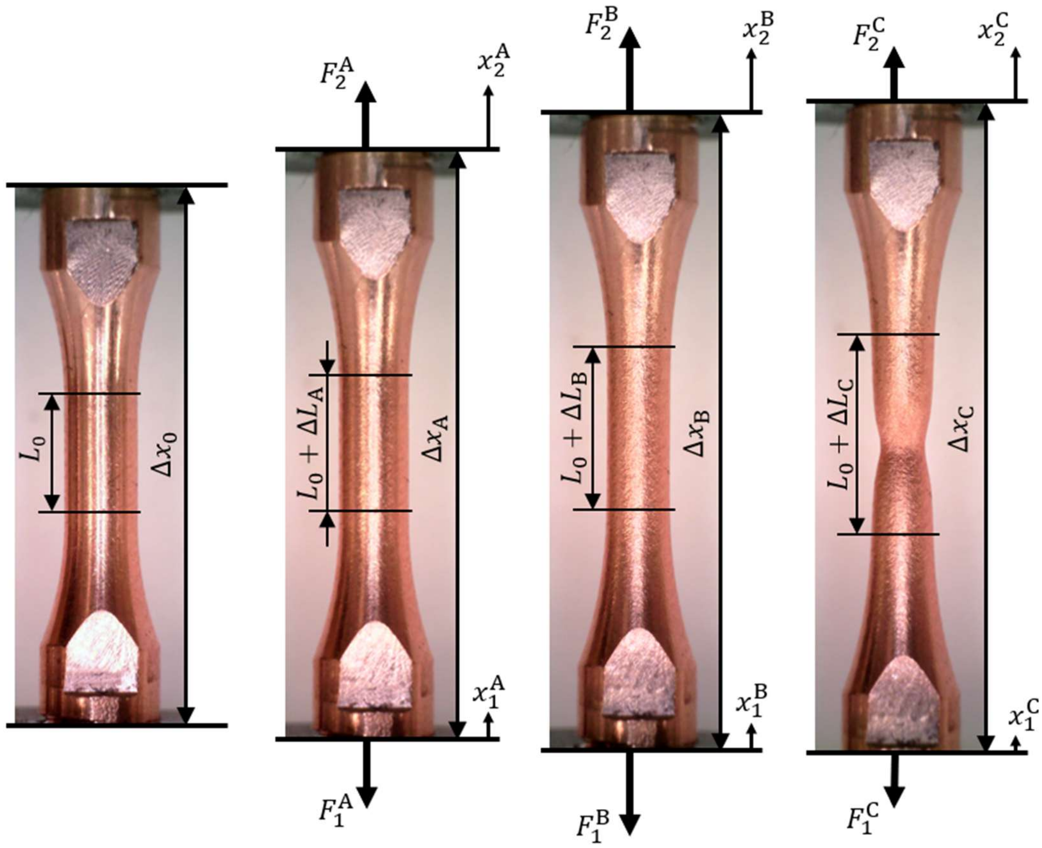

Figure 1.1 Deformation steps of a dog-bone specimen during a uniaxial tensile test.

The next subsections provide a literature background on the strain-hardening identification techniques that are based on tensile tests on dog-bone specimens. Starting from the traditional approach, which is limited to the pre-necking phase, the different strategies proposed so far for post-necking identification are described. Solutions for characterizing strain rate and temperature dependences of the hardening law for isotropic materials will be presented in Chapter 5.

1.2.1 Pre-necking data processing

For strain-hardening identification, macroscopic measurements of force and deformation need to be converted into equivalent stress σ_{eq} and plastic strain $\varepsilon_{eq,p}$ values in order to establish the relationship between them. When the gauge length deforms uniformly, the identification of the $\sigma_{eq} - \varepsilon_{eq,p}$ curve is easy and immediate.

As the stress state is uniaxial, yield criteria for isotropic materials conventionally consider the axial stress σ_a and plastic strain $\varepsilon_{a,p}$ as equivalent quantities:

$$\sigma_{eq} \equiv \sigma_a, \tag{1.1a}$$

$$\varepsilon_{eq,p} \equiv \varepsilon_{a,p}. \tag{1.1b}$$

Moreover, since elastic strains can be reasonably neglected with respect to plastic ones for the applications of interest, it can be assumed that:

$$\varepsilon_{a,p} \approx \varepsilon_a. \tag{1.2}$$

These quantities must be determined referring to the gauge length or to a portion of it. It is well-known, indeed, that evaluating the deformation from the displacement of the crosshead of the testing machine would overestimate the real values. This is due to the machine deformability, which can be higher than that of the specimen itself. Such measurements would require the identification and application of a correction factor to obtain reliable estimates of the deformation. Hence, traditionally the deformation of the specimen gauge length was directly measured by extensometers. More recently, virtual extensometers have become increasingly common. They exploit digital image analysis for tracking markers painted on the specimen surface for determining the elongation. When the initial gauge length L_0 has achieved a length L, the logarithmic axial strain (uniformly distributed within the region considered) can be computed as:

$$\varepsilon_a = \ln(L/L_0). \tag{1.3}$$

Regarding the axial stress in a generic configuration characterized by a cross-sectional area A, it can be determined as:

$$\sigma_a = F/A. \tag{1.4}$$

In a traditional approach, only axial measurements are conducted, hence the area A can be computed by considering that plastic deformation of metals is a constant volume transformation and that during the pre-necking phase the shape remains a right circular cylinder. In addition, elastic deformations are neglected, leading to the following formula:

$$A = A_0 L_0/L. \tag{1.5}$$

By plugging this last equation into Equation 1.3, the axial stress can be expressed as:

$$\sigma_a = \frac{F}{A_0}\frac{L}{L_0}. \tag{1.6}$$

More commonly, the concepts of engineering stress $s = F/A_0$ and strain $e = \Delta L/L_0$ are used, thus Equations 1.3 and 1.6 can be re-written as:

$$\varepsilon_a = \ln(1 + e) \tag{1.7a}$$

$$\sigma_a = s(1 + e). \tag{1.7b}$$

Axial strain and stress are usually denoted as true strain ε_t and true stress σ_t respectively.

Equations 1.3 and 1.6 (or equivalently 1.7) are sometimes grouped under the term length-based approach since they are all based on axial measurements. In contrast to this, an area-based approach has been introduced. As the denomination suggests, it employes areal rather than axial measurements. The axial stress can be directly estimated using Equation 1.4, while the axial deformation requires plugging Equation 1.5 into Equation 1.3, thus obtaining:

$$\varepsilon_a = \ln(A_0/A). \tag{1.8}$$

Areal measurements can be derived by digitally analyzing images recorded from a single view of the specimen in case of isotropic materials (or more views for anisotropic ones).

Figure 1.2 shows an example of $\sigma_a - \varepsilon_a$ curves, comparing the length-based approach applied to different bases L_0 for length measurements and the area-based approach applied to the minimum cross-section. The former are represented as solid lines and are denoted with letters from a to d, from the larger to the smaller L_0.The latter is represented as a dashed line and denoted with letter e. As long as deformation is uniform, both approaches provide the same results, also regardless of L_0.

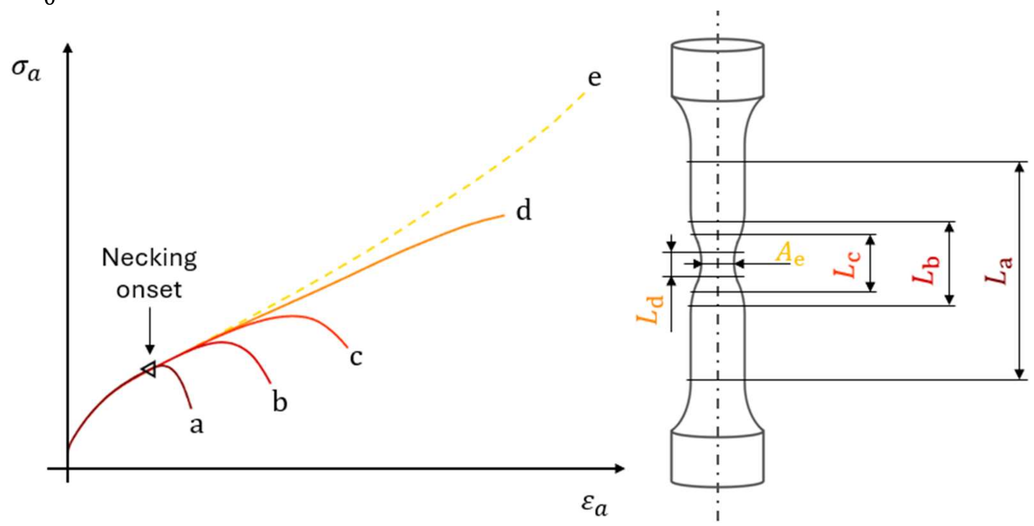

Figure 1.2 Comparison between length-based approach (solid lines with each color corresponding to a different L_0) and area-based approach (dashed line).

Once the specimen begins to neck, the different estimates start deviating from one another. This apparent non-uniqueness of the material behavior occurs because length measurements cannot catch the stress and strain gradients that characterize such localization phenomenon. Conversely, the area-based approach only averages over the cross-section and not along the axial direction. Hence, this is the approach that best represents the local material response in terms of axial strain and stress. As shown in Figure 1.2, length-based strategy provides results closer to this estimate when L_0 decreases. Nevertheless, for determining the $\sigma_{eq} - \varepsilon_{eq,p}$ curve other techniques are required in order to account for stress triaxiality; this theme is addressed in the next subsection.

1.2.2 Post-necking data analysis

Dog-bone specimens of ductile materials commonly undergo necking during uniaxial tensile tests. Although the cross-section in which the deformation will localize cannot be predicted (as this depends on material inhomogeneities, specimen roughness, inaccuracies in its metal working, etc.), it is possible to estimate the strain to necking. The observation that necking takes place approximately at the maximum force was first recorded by Considère at the end of the nineteenth century [9]. The mathematical expression for the necking onset, according to Considère's criterion, comes from the instability condition of the maximum load. This can be described as a null derivate of F with respect to an arbitrary quantity, such as the axial strain:

$$\frac{dF}{d\varepsilon_a} = 0. \tag{1.9}$$

By developing the relationship through Equation 8, it results that:

$$\frac{d(\sigma_a A)}{d\varepsilon_a} = 0;$$

$$\left(\frac{d\sigma_a}{d\varepsilon_a}\right) A + \sigma_a \left(\frac{dA}{d\varepsilon_a}\right) = 0;$$

$$\frac{d\sigma_a}{d\varepsilon_a}\frac{1}{\sigma_a} = -\frac{dA}{d\varepsilon_a}\frac{1}{A} = 1;$$

$$\frac{d\sigma_a}{d\varepsilon_a} = \sigma_a. \tag{1.10}$$

Since necking onset represents the limit condition for uniform deformation, Equation 1.10 can be also written as:

$$\frac{d\sigma_{eq}}{d\varepsilon_{eq,p}} = \sigma_{eq}. \tag{1.11}$$

Hence, according to this criterion, necking onset depends only on the material strain-hardening behavior. Actually, later studies proved that necking onset is also influenced by other variables, such as the specimen aspect-ratio [11-13], the strain rate sensitivity [14, 15], and the temperature [15]. In some of these works, necking onset was studied by means of the bifurcation theory, i.e., as a deviation from a uniformly deformed configuration, and it was shown that necking does not necessarily occur at the maximum force. More specifically, the specimen aspect-ratio and the strain rate sensitivity tend to delay the bifurcation with respect to the maximum load, while temperature dependence results in anticipating bifurcation.

Beyond the necking onset, the peculiar shape of the specimen causes the strain and stress to lose uniformity and the stress to become triaxial (as shown in Figure 1.3). These aspects become progressively more evident as necking develops. Figure 1.3 refers to a round dog-bone specimen made of isotropic and homogeneous material. Due to the axialsymmetry of the system, the axial, the radial, and the circumferential directions are the principal directions of both strain and stress. At each cross-section, the circumferential and radial components obviously coincide along the specimen axis and tend to diverge towards the surface. Hence, according to Von Mises yield criterion, the equivalent plastic strain and stress still coincide with the axial component only on the axis.

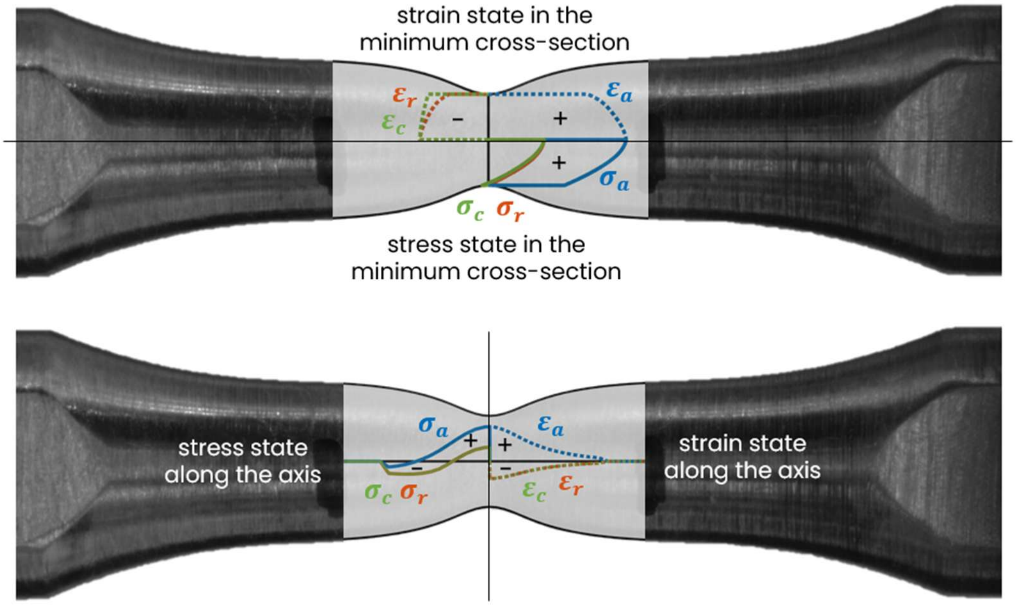

Figure 1.3 Stress and strain distributions at the neck (on the top) and along the longitudinal axis (on the bottom) of a cylindrical dog-bone specimen. [85]

Because of the strain gradients, Equations 3 and 5 (and all equations derived from them) are no longer valid, as well as Equation 1a because of the developed stress triaxiality. Due to the significative non-linearities of both the geometry and the material, no exact analytical solution for necking has been found yet. This significantly complicates the use of experimental measurements for material characterization during necking compared to uniform deformation.

For sake of simplicity, sometimes a hardening model is fitted to pre-necking experimental data and then extrapolated to post-necking strains. Over the last decades several phenomenological models have been developed and implemented with the aim of describing the various strain-hardening responses exhibited by different materials. They consist of closed-form expressions characterized by a limited number of parameters so that a compact and smooth representation of the material response is provided, while facilitating implementation in numerical solvers and law identification. The most widespread models implemented in many FE codes include Hollomon [16, 17], simplified Johnson-Cook [18], and Voce [19] hardening laws. The choice of the hardening model for fitting and extrapolating experimental data represents a critical issue and can lead to very different results [20-22]. It is never advisable to extrapolate a model to strain levels far exceeding the calibration range because the predictions would not be guaranteed [20-23]. Furthermore, there are materials and/or conditions that cause the specimens to neck immediately after necking; in those cases, being able to use post-necking data becomes essential for hardening identification. Even in other cases, the large strains achieved in this stage, together with all the advantages of tensile tests on dog-bone samples highlighted in Section 1.1, make it attractive to exploit necking for hardening identification.

Therefore, many efforts have been devoted since the last century to dealing with the non-uniformity and triaxiality that characterize necking. Proposed strategies can be grouped into two main categories: direct methods that use experimental data straightforwardly to estimate the hardening law (they include traditional correction formulas but also advanced metamodels), and hybrid experimental-numerical methods that identify the law by combining experimental measurements with a numerical framework in a way that inherently enforces physical consistency. They are presented in the following paragraphs, focusing on strain-hardening of isotropic metals. Literature review on thermo-visco-plastic characterization of isotropic materials and on strain-hardening of anisotropic materials (in case of cylindrical specimens) are reported in Chapters 5 and 7, respectively.

Direct methods

Direct identification methods include several analytical strategies that have been proposed in the past decades. Traditionally, they determine the strain-hardening law starting from experimental measurements in a neighborhood of the neck. Reference is made to the minimum cross-section because it is the easiest to track and it represents the position of maximum deformation, thus allowing the hardening law to be determined over a large strain range.

One of the earliest and most well-known theories for cylindrical specimens undergoing necking is the one proposed by Bridgman [24]. It assumed the axial strain distribution $\varepsilon_a(r)$ to not undergo significant gradients within the neck, i.e., for $r \in [0, R]$. The volume conservation, hence, implied that $\varepsilon_r(r) \equiv \varepsilon_c(r)$, leading to the following expression for the equivalent strain ε_{eq} at the minimum cross-section:

$$\varepsilon_{eq} = 2 \ln\left(\frac{R_0}{R}\right), \quad (1.12)$$

being R_0 the outer radius at the beginning of the test.

Under the assumption of isotropic strain-hardening, the stress system satisfying equilibrium, boundary conditions, and von Mises plasticity with the above strain state at the neck, was found. An approximate method was adopted which consisted of approximating the contour of the neck by its osculating circle and one of the surfaces of principal stress by a sphere. It resulted that the equivalent stress σ_{eq}, constant within the neck cross-section, could be estimated by applying a correction factor k_B to the average axial stress $\sigma_{a,avg}$ at that section. Indeed, σ_{eq} differs from $\sigma_{a,avg}$, more specifically, it is lower than $\sigma_{a,avg}$, due to the increasing triaxiality generated by the progressive localization. The average axial stress at the neck is also denoted as true stress σ_t and can be computed from Equation 1.4, that in case of circular cross-section assumes the following form:

$$\sigma_t = \frac{F}{\pi R^2}. \quad (1.13)$$

The multiplicative correction factor found by Bridgman was:

$$k_B = \frac{1}{\left(1+\frac{2\rho}{R}\right)\ln\left(1+\frac{R}{2\rho}\right)}, \tag{1.14}$$

with ρ the radius of curvature at the neck. This represents the radius of the circle fitting the necking silhouette; from a 3D point of view, it represents the radius of the circle whose revolution about the specimen longitudinal axis generates a torus fitting the neck geometry, as displayed in Figure 1.4.

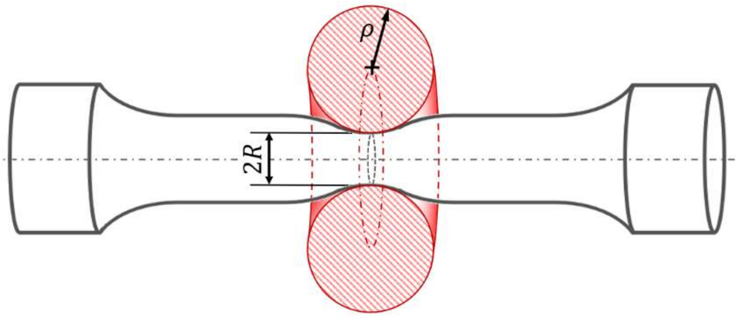

Figure 1.4 Schematic representation of torus that locally fits the neck.

Despite being widely used, Bridgman's theory was found to be inaccurate at large strains by many researchers [25, 26]. For instance, La Rosa et al. [25] showed that the stress error of Bridgman's correction could range from 3% up to more than 10%.

In scientific literature, several analytical stress corrections for smooth cylinders were inspired by Bridgman's theory, for instance, Davidenkov and Spiridonova [27], Siebel and Schwaigerer [28], and Malinin and Rżysko [29]. In Gromada et al. [30], a comprehensive review of these methods and their mathematical derivations is provided, together with novel proposals. According to the numerical analyses conducted in that work, various stress corrections showed an improvement over Bridgman. This was demonstrated across different hardening behaviors; however, ideal plastic materials are those for which the greatest inaccuracy can occur. Among the different correction formulas, the one that performed best was the following:

$$\sigma_{eq} = \frac{\sigma_t}{\xi}, \tag{1.15}$$

$$\text{being } \xi = 1 - \frac{5\Lambda}{7(1+5\Lambda)} - \frac{2(1-6\Lambda)}{7(1+5\Lambda)} + \frac{2}{7} + \frac{30\Lambda(8\Lambda-\delta-5\delta\Lambda)}{49\delta(1+5\Lambda)^2} + \frac{3(8\Lambda-\delta-5\delta\Lambda)}{7\delta(1+5\Lambda)}\left(\frac{2(1-6\Lambda)}{7(1+5\Lambda)} - \frac{2}{7} - \frac{30\Lambda(8\Lambda-\delta-5\delta\Lambda)}{49\delta(1+5\Lambda)^2}\right)\ln\left|1+\frac{7\delta(1+5\Lambda)}{3(8\Lambda-\delta-5\delta\Lambda)}\right|,$$

$$\Lambda = 1 - R_0/R,$$

$$\delta = R/\rho,$$

by Gromada et al. [30].

From the experimental point of view, Bridgman-like methods require measuring the minimum radius R and the necking curvature radius ρ. Usually, they are both obtained by digitally analyzing images. While the minimum radius is immediately determined, the curvature entails fitting the experimental silhouette with a predefined function [25, 31-33]. In some studies, R and ρ were, instead, estimated using 3D geometry information of the necking region [33, 34]. These works all shared the use of Digital Image Correlation (DIC), a non-contact optical technique that measures full-field displacements by tracking a random speckle pattern applied to the specimen surface. This technique was combined with fringe projection in Siegmann et al. [33] to reconstruct the 3D geometry, that was then fitted with a torus in the necking zone. A similar approach was adopted by Chen and Pan [34] but using a mirror-assisted multi-view DIC technique for 3D reconstruction. These strategies required complex and advanced experimental setups and are subjected to the inherent limitations of performing DIC measurements during necking. The speckle pattern may become damaged or may detach from the specimen surface under large strains. These effects can compromise the reliability of the measurements. Moreover, when it comes to fitting the 2D or 3D geometry to measure the curvature radius, the result highly depends on the region and function considered for fitting.

To overcome these issues, some researchers worked on identifying a relationship between ρ and R, so that just R needed to be measured. This approach was first suggested by Bridgman himself [24], and the relationship he found was exploited, for instance, in [35]. Also, Hill [36] proposed an empirical formula approximating the R/ρ ratio as a function of ε_t. An important contribution came from Le Roy et al. [37], who proposed to express R/ρ as a linear function of $\varepsilon_t - \varepsilon_n$ (with ε_n denoting the true strain at the necking onset). Recently, Lu et al. [38] proposed an improvement of that function by introducing an additional term, again a function of $\varepsilon_t - \varepsilon_n$. The use of $\varepsilon_t - \varepsilon_n$ was based on the consideration that necking development is governed only by the amount of post-necking plastic deformation.

Another approach to avoid evaluating the curvature at the neck consisted of replacing Bridgman's correction factor with a function that did not involve that variable. For instance, Majzoobi et al. [39] analytically derived a correction formula based on the radius of the neck and on the superficial axial strain. The method had the advantage of not requiring the curvature radius but did not show a substantial improvement in the results with respect to Bridgman's correction. Another study that is worth citing is the one by Mirone [40], in which a numerical analysis based on experimental data was conducted. This resulted in the identification of the ratios $\sigma_{a,avg}/\sigma_{eq,avg}$ and $\varepsilon_{r,avg}/\varepsilon_{r,avg}$ as material-independent functions of $\varepsilon_t - \varepsilon_n$. These functions are denoted as MLR. By introducing some hypotheses on strain and stress distributions, mathematical expressions of these fields in the minimum cross-section were also derived. This method not only avoided measuring the curvature radii but also showed better agreement with FE simulations than Bridgman's theory. MLR corrections were extended to high strain rates [41] and anisotropic behavior [42].

Overall, analytical strategies owed their success mainly to the limited computational and experimental effort, even if evaluating the radius of curvature, when needed, can be challenging. In addition, Tu et al. [23] recognized that the choice of the stress correction formula is somewhat arbitrary since the accuracy, for a certain material, of the various correction functions is still unclear.

Finally, it is important to note that previous methods for identifying the plastic flow curve determine local variables, σ_{eq}^* and $\varepsilon_{eq,p}^*$, by correcting global variables, σ_t and ε_t. Associating global with local variables is implicitly based on assuming that when a material point r^* of the minimum cross-section is characterized by $\sigma_{eq}(r^*) = \sigma_{eq}^*$, then it is also characterized by $\varepsilon_{eq,p}(r^*) = \varepsilon_{eq,p}^*$. To the best of the author's knowledge, this situation may not always be verified. Nevertheless, this limitation can be, at least partially, overcome when using numerical analysis for the identification of the correction factors and formulas. This is because, although global variables are still used, they result from accurate stress and strain distributions, instead of being based on simplified assumptions.

Recently, the increasing demand for efficient identification strategies and availability of large datasets has boosted the spread of machine learning (ML) algorithms. This term refers to tools that learn from large datasets for making predictions and decisions. In practice, they consist of a metamodel that is trained on already available datasets for establishing relationships between a set of inputs and the corresponding set of outputs. In the field of material characterization, several simulations or experiments can be collected into a structured dataset. Then ML models can be trained to learn the underlying relationships between constitutive parameters and selected quantities that can be measured experimentally. These quantities are usually the force-displacement curve [43-45] or the combination of load history with geometry and strain fields of a region of the sample [46]. Once trained, these algorithms efficiently predict material parameters directly from experimental data. This is why they have been classified as direct methods in this thesis.

A critical aspect of ML is the training phase, in terms of both computational cost and dataset adequacy [45]. In this sense, it seems promising to use FE simulations for generating the training datasets [43, 44, 46, 47]. They should include a sufficient variety of material hardening behaviors to guarantee that suitable material parameters can be found for real experiments [43]. However, the larger the datasets the higher the computational effort for building them and for training the metamodel. Furthermore, as observed in [48, 49], most ML algorithms are at present conceived as black boxes. This means that the operations they perform are difficult to understand and control. To overcome this issue, researchers are currently working to develop simple, reduced, and interpretable models [50, 51].

Hybrid experimental-numerical methods

To address the limitations of analytical approaches, hybrid experimental-numerical methods have been developed, and they are still widely employed, despite the recent advancements in ML algorithms. As the name suggests, they integrate experimental measurements with numerical models. Such models enable a physically consistent identification of the hardening law by embedding governing equations and constitutive laws. Moreover, the use of numerical models makes hybrid experimental-numerical methods highly versatile, in terms of loading condition and specimen geometry. Hence, the following paragraphs also refer to works that did not specifically deal with tensile tests on smooth cylindrical specimens, with the idea that such scenarios could also be addressed with similar approaches. Depending on how experimental data and numerical models are combined, hybrid methods can be distinguished into two main categories. The first uses governing equations and constitutive relations in a numerical simulation that is iteratively updated. Conversely, the second category directly employs those equations and laws in a variational formulation that uses measured kinematic fields.

The recursive updating of the numerical models belonging to the first category is based on the comparison of some measured quantities with the corresponding quantities predicted by the numerical model. To this aim, optimization algorithms are employed. The material hardening law is parametrized and a cost function is defined to quantify the deviation of the numerical model from the target function, which in turn represents the experimental measurements to be reproduced. Starting from a trial set of values, the unknown parameters are iteratively adjusted in order to minimize the cost function, i.e., in order to provide numerical results sufficiently close to the experimental target. Despite the availability of efficient algorithms, these methods are characterized by a non-negligible computational effort because of the need for optimization.

Regarding the numerical model, it should be considered that nonlinear FE codes have undergone considerable development and, hence, increasing spread during the past decades. Due to their accurate representation of necking heterogeneity and triaxiality, many researchers employed a FE model as numerical part of hybrid approaches for hardening identification. These approaches are also called FE-based inverse methods (iFEM) or FE model updating methods (FEMU). FEMU approaches can differ from one another for the optimization strategy adopted and for the target function chosen. The latter is strongly related to the experimental data available and/or intended for this use.

A common choice has been to use macroscopic quantities, like the force vs. displacement curve $F(\Delta L)$ beyond the maximum force [52-56]. Conversely, Shokeir et al. [57] preferred to use the force vs. diameter reduction curve $F(|\Delta R|)$ as target, to better account for material local behavior. Defaisse et al. [58], instead, combined the previous proposals by using $F(\Delta L)$ as target for the pre-necking phase and $F(|\Delta R|)$ for the post-necking domain. Some researchers still used the $F(\Delta L)$

curve (or equivalently the true curve derived with a length-based approach) as target of the optimization but provided *a posteriori* local validation of the identified model. For example, in the works by Zeng and Huo [59] and those by Scapin et al. [60, 61], this was done by comparing the numerical prediction of the specimen deformed shape with the one measured experimentally during necking or after fracture. Conversely, in Pham et al. [62] the validation was conducted on additional tests by comparing the surface strain evolution. Some research went further and directly used one or more necking shapes as additional target functions to the $F(\Delta L)$ curve. For instance, this was done by Peroni et al. [63], by Scapin et al. [64, 65], and more recently by Zhang et al. [66]. In addition, Peroni and Scapin [67] and Beltramo et al. [68] showed that in FEMU approaches having a necking shape as target it is possible, under certain conditions, to limit the information about the force to the maximum value only. Furthermore, in the studies by Majzoobi et al. [39, 69] and Almasi et al. [70], the experimental data required was further limited to displacements of few points on the specimen surface. However, omitting information about the force could cause non-uniqueness of the identified law. Finally, it is worth mentioning FEMU approaches in which the target consisted of full-field measurements (typically obtained via DIC) coupled with the force-history. This methodology has been mainly applied to metal sheets [71-73]. Indeed, cylindrical specimens would require more complex experimental setups since stereo-DIC is needed to avoid inaccuracies associated with loss of focus caused by out-of-plane deformations.

Full-field measurements bring the discussion to methods belonging to the second category of hybrid identification techniques. They directly use the equilibrium equation in combination with the full-field strain distributions measured experimentally with DIC. Different strategies were developed, including the one by Coppieters et al. [74, 75] and the stepwise modelling method by Marth et al. [76]. However, the most widespread approach is represented by the Virtual Field Method (VFM). This relies on the consideration that internal virtual work must balance external virtual work for any admissible virtual displacement field. In practice, VFMs consist of minimizing the difference between internal and external virtual work for selected virtual displacement fields. The actual stress field required for the internal work is expressed using the experimental strain field measured by DIC and a constitutive model with unknown parameters. Then, the global cost function results from evaluating the difference between external and internal work at different loading steps. Because of the nature of plastic constitutive equations, iterative algorithms are required for identifying the unknown material parameters that minimize the global cost function. Several examples of VFMs application to elasto-plastic behaviors can be found in the literature: for instance, Grédiac and Pierron [77], Kim et al. [78], Fu et al. [79], and Park et al. [80].

Figure 1.5 schematically illustrates the workflows of a VFM with respect to a FEMU approach (the experimental data used is not specified, since it depends on the selected target function). The main advantage of VFMs with respect to FEMU approaches is represented by not requiring recurrent FE simulations. However, since experimental strain fields are only available at the specimen surface, VFMs require assumptions on internal strain fields. Moreover, being based on DIC measurements, their application was generally limited to sheet metal specimens.

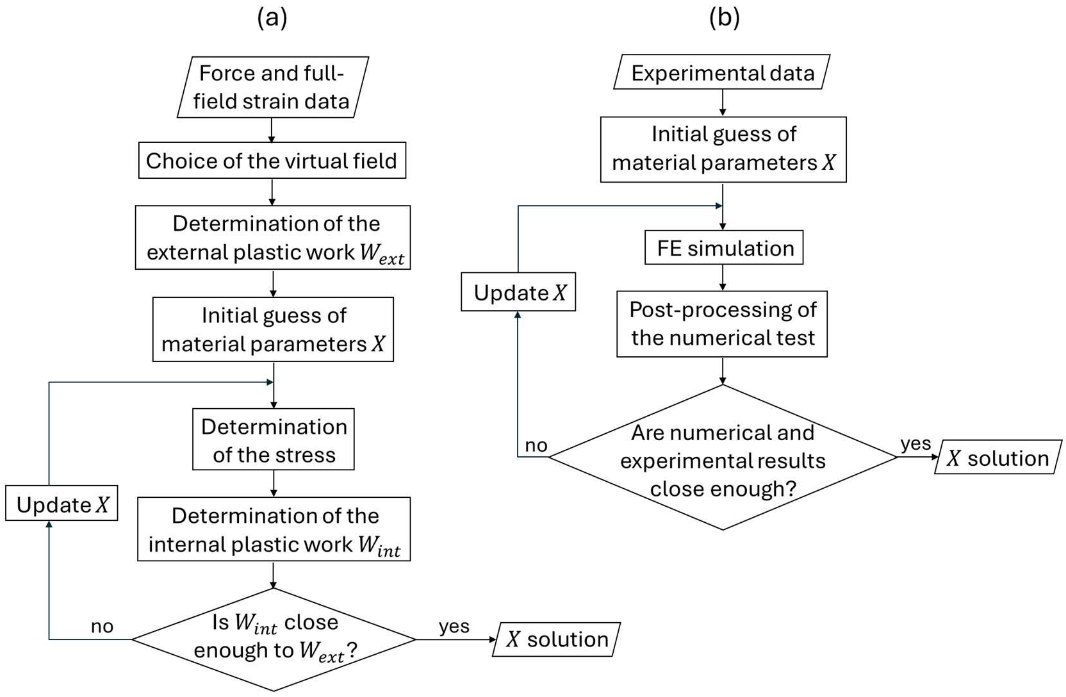

Figure 1.5 Flowcharts of VFM (a) and FEMU (b) approaches (adapted from [77]).

Overall, hybrid experimental-numerical approaches ensure that the reconstructed stress and strain fields, obtained from the identified parameters, satisfy equilibrium and represent realistic behaviors. However, these methods require assuming a pre-selected constitutive model, which can prevent an adequate hardening law from being identified. This limitation may be mitigated by separating the pre-necking and the post-necking regime: traditional equations can be used for the first regime, and hybrid experimental-numerical approaches for the second, as done by Pham et al. [81]. Further improvements can be obtained by combining classical hardening models with each other or by using a piecewise linear relationship for the hardening law [52, 58, 59, 75, 76, 79, 80, 82-84]. Nevertheless, more versatile hardening models lead to an increasing number of unknown parameters and, consequently, a higher computational effort for calibration. This occurs also when it is necessary to account for additional features, such as strain rate and thermal sensitivities, work-to-heat conversion, and anisotropy, as detailed in Chapters 5, 6, and 7, respectively.

1.3 Research motivation

The literature review presented in the previous section highlighted the role of deformed specimen geometry in post-necking identification. Indeed, it showed that many approaches considered the time evolution of the necking geometry, in a tiny surrounding of the neck or in a wider specimen region. This represented a key element in the interpretation of tensile test data beyond uniform deformation.

Advantages and disadvantages of applying existing strategies were mentioned. While direct methods like correction formulas are computationally efficient, they often lack accuracy and robustness (especially in determining the curvature radius at the neck). Conversely, hybrid methods like FEMU provide better accuracy, but entail a non-negligible computational cost due to iterative optimizations.

In addition, all methods based on full-field measurements would require, for cylindrical specimens, to perform stereo-DIC. Furthermore, the speckle necessary for DIC may degrade or detach under the large strain typical of the late post-necking phase, potentially compromising measurement reliability. A convenient alternative is offered by Digital Image Analysis (DIA) used for simply identifying the boundary between the specimen and the background. Rather than replacing the comprehensive data provided by DIC, DIA aims to simplify the experimental phase by focusing only on the specimen's outer shape. Hence, it is particularly attractive when experimental simplicity and post-processing speed are prioritized over full-field data.

Therefore, the present thesis proposes alternative post-necking identification approaches that exploit the deformed necking geometry through this silhouette-based approach. These alternative approaches have been published in [85-88]. They aim to overcome the limitations of traditional analytical methods without the computational cost of FEMU strategies. Robustness is improved by considering the entire necking region instead of the minimum cross-section only, while accuracy is ensured by FE simulations and by limited usage of section-averaged quantities. Specific strategies are adopted for integrating FE simulations into the identification method with the purpose of limiting the computational effort compared to FEMU techniques.

Going into more detail on the structure of the thesis, Chapter 2 addresses in detail the correlation between plastic flow behavior and necking silhouettes, providing the basis for the methodologies developed in the subsequent chapters. More specifically, a database-driven identification framework is presented for the characterization of isotropic material behavior at large strains. The principles of the method are introduced, and its application is first illustrated for relatively simple material responses, namely strain rate insensitive materials tested under quasi-static conditions in Chapter 3 Chapters 4, 5, and 6 extend the database-driven approach to account for additional physical effects and more complex loading conditions. Strain rate sensitivity affecting post-necking deformation within a single test is first considered in Chapter 4. For the sake of brevity, strain rate sensitive and strain rate insensitive materials will be denoted as rate sensitive and insensitive. Then, the analysis is extended to dynamic loading conditions in Chapter 5, where self-heating effects become relevant and can be implicitly or explicitly taken into account. Finally, the integration of the database approach with complementary identification strategies is discussed in Chapter 6 for the characterization of the conversion of plastic work into heat under non-isothermal conditions. Chapter 7 addresses the influence of material anisotropy on necking behavior and proposes a different shape-based identification procedure to account for it. In each chapter, experimental case studies are presented for showing the practical applicability, potentiality, and flexibility of the proposed framework. The tests were conducted in the DYNLab laboratory of the Mechanical and Aerospace Engineering Department of Politecnico di Torino. The experimental procedures and measurement techniques are described in direct connection with each application, allowing the identification process to be followed from experimental data acquisition to numerical modeling and parameter identification. Since the proposed methods of analysis do not explicitly model damage, the final stages of the tests were withdrawn from the analyses to limit its effect on the results. Nevertheless, the possible residual damage should not be conceived as a severe limitation of these specific methods: it would imply that the identified hardening laws intrinsically account for it as well, which could also be a reasonable engineering approach to the problem.

References

[1] Holzapfel, G. A. (2002). *Nonlinear solid mechanics: a continuum approach for engineering science*. John Wiley & Sons.

[2] Belytschko, T., Liu, W. K., Moran, B., & Elkhodary, K. (2014). *Nonlinear finite elements for continua and structures*. John Wiley & Sons.

[3] Bishop, J. F. W., & Hill, R. (1951). XLVI. A theory of the plastic distortion of a polycrystalline aggregate under combined stresses. *The London, Edinburgh, and Dublin Philosophical Magazine and Journal of Science*, *42*(327), 414-427.

[4] Stoughton, T. B. (2002). A non-associated flow rule for sheet metal forming. *International Journal of Plasticity*, *18*(5-6), 687-714.

[5] Zhang, Y., Duan, Y., Mu, Z., Fu, P., & Zhao, J. (2024). Non-associated flow rule constitutive modeling considering anisotropic hardening for the forming analysis of orthotropic sheet metal. *Experimental Mechanics*, *64*(3), 305-323.

[6] Rossi, M., Lattanzi, A., Barlat, F., & Kim, J. H. (2022). Inverse identification of large strain plasticity using the hydraulic bulge-test and full-field measurements. *International Journal of Solids and Structures*, *242*, 111532.

[7] Zhang, C., Lou, Y., Zhang, S., Clausmeyer, T., Tekkaya, A. E., Fu, L., ... & Zhang, Q. (2021). Large strain flow curve identification for sheet metals under complex stress states. *Mechanics of Materials*, *161*, 103997.

[8] Li, Y., Zhang, Y., & Li, S. (2021). Viscoplastic constitutive modeling of boron steel under large strain conditions and its application in hot semi-cutting. *Journal of Manufacturing Processes*, *66*, 532-548.

[9] Yu, R., Li, X., Yue, Z., Li, A., Zhao, Z., Wang, X., ... & Lu, T. J. (2022). Stress state sensitivity for plastic flow and ductile fracture of L907A low-alloy marine steel: From tension to shear. *Materials Science and Engineering: A*, *835*, 142689.

[10] Considère, A. (1885). Annales des ponts et chaussées. *Comm. Ann. Ponts Chaussees Paris*, *9*, 574-575.

[11] Hutchinson, J. W., & Miles, J. P. (1974). Bifurcation analysis of the onset of necking in an elastic/plastic cylinder under uniaxial tension. *Journal of the Mechanics and Physics of Solids*, *22*(1), 61-71.

[12] Audoly, B., & Hutchinson, J. W. (2016). Analysis of necking based on a one-dimensional model. *Journal of the Mechanics and Physics of Solids*, *97*, 68-91.

[13] Yan, Y., Li, M., Zhao, Z. L., & Feng, X. Q. (2022). An energy method for the bifurcation analysis of necking. *Extreme Mechanics Letters*, *55*, 101793.

[14] Audoly, B., & Hutchinson, J. W. (2019). One-dimensional modeling of necking in rate-dependent materials. *Journal of the Mechanics and Physics of Solids*, *123*, 149-171.

[15] Mirone, G., & Barbagallo, R. (2021). How sensitivity of metals to strain, strain rate and temperature affects necking onset and hardening in dynamic tests. *International Journal of Mechanical Sciences*, *195*, 106249.

[16] Ramberg, W., & Osgood, W. R. (1943). *Description of stress-strain curves by three parameters* (No. NACA-TN-902).

[17] Hollomon, J. H. (1945). Tensile deformation. *Aime Trans*, *12*(4), 1-22.

[18] Johnson, G. R. (1983). A constitutive model and data for metals subjected to large strains, high strain rates and high temperatures. In *Proceedings of the 7th International Symposium on Ballistics, Am. Def. Prep. Org.(ADPA), Netherlands, 1983* (pp. 541-547).

[19] Voce, E. (1955). A practical strain hardening function. *Metallurgia*, *51*, 219-226.

[20] Coppieters, S., Cooreman, S., Sol, H., Van Houtte, P., & Debruyne, D. (2011). Identification of the post-necking hardening behaviour of sheet metal by comparison of the internal and external work in the necking zone. *Journal of Materials Processing Technology*, *211*(3), 545-552.

[21] Gupta, M. K., & Singh, N. K. (2021). Post necking behaviour and hardening characterization of mild steel. *Solid State Phenomena*, *319*, 7-12.

[22] Zhu, L., Huang, X., & Liu, H. (2022). Study on constitutive model of 05Cr17Ni4Cu4Nb stainless steel based on quasi-static tensile test. *Journal of Mechanical Science and Technology*, *36*(6), 2871-2878.

[23] Tu, S., Ren, X., He, J., & Zhang, Z. (2020). Stress–strain curves of metallic materials and post-necking strain hardening characterization: A

review. *Fatigue & Fracture of Engineering Materials & Structures*, *43*(1), 3-19.

[24] Bridgman, P.W. (1952). Studies in large plastic flow and fracture. Metallurgy and metallurgical engineering series. *McGraw Hill, New York.*

[25] La Rosa, G., Risitano, A., & Mirone, G. (2003). Postnecking elastoplastic characterization: Degree of approximation in the Bridgman method and properties of the flow-stress/true-stress ratio. *Metallurgical and Materials Transactions A*, *34*(3), 615-624.

[26] Murata, M., Yoshida, Y., & Nishiwaki, T. (2018). Stress correction method for flow stress identification by tensile test using notched round bar. *Journal of Materials Processing Technology*, *251*, 65-72.

[27] Davidenkov, N. N., & Spiridonova, N. I. (1947). Mechanical methods of testing. Analysis of the state of stress in the neck of a tension specimen. In *Proc. ASTM, 46,* 1147-1158.

[28] Siebel, E., & Schwaigere, S. (1948). Mechanics of tensile test. *Arch Eisenhuttenwes*, *19*, 145-152.

[29] Malinin, N. N., & Rżysko, J., Mechanics of Materials (in Polish), *PWN*, *Warsaw*.

[30] Gromada, M., Mishuris, G., & Öchsner, A. (2011). *Correction formulae for the stress distribution in round tensile specimens at neck presence*. Springer Science & Business Media.

[31] Sancho, A., Cox, M. J., Cartwright, T., Davies, C. M., Hooper, P. A., & Dear, J. P. (2019). An experimental methodology to characterise post-necking behaviour and quantify ductile damage accumulation in isotropic materials. *International Journal of Solids and Structures*, *176*, 191-206.

[32] Lu, F., Mánik, T., Lægreid Andersen, I., & Holmedal, B. (2021). A Robust Image Processing Algorithm for Optical-Based Stress–Strain Curve Corrections after Necking. *Journal of Materials Engineering and Performance*, *30*(6), 4240-4253.

[33] Siegmann, P., Alén-Cordero, C., & Sánchez-Montero, R. (2019). Experimental approach for the determination of the Bridgman's necking parameters. *Measurement Science and Technology*, *30*(11), 114003.

[34] Chen, B., & Pan, B. (2022). Measuring true stress–strain curves of cylindrical bar samples with mirror-assisted multi-view digital image correlation. *Strain*, *58*(1), e12403.

[35] Cabezas, E. E., & Celentano, D. J. (2004). Experimental and numerical analysis of the tensile test using sheet specimens. *Finite Elements in Analysis and Design*, *40*(5-6), 555-575.

[36] Hill, R. (1998). *The mathematical theory of plasticity* (Vol. 11). Oxford university press.

[37] Le Roy, G., Embury, J. D., Edwards, G., & Ashby, M. F. (1981). A model of ductile fracture based on the nucleation and growth of voids. *Acta Metallurgica*, *29*(8), 1509-1522.

[38] Lu, F., Mánik, T., & Holmedal, B. (2021). Stress corrections after necking using a two-parameter equation for the radius of curvature. *Journal of Applied Mechanics*, *88*(6), 061006.

[39] Majzoobi, G. H., Fariba, F., Pipelzadeh, M. K., & Hardy, S. J. (2015). A new approach for the correction of stress–strain curves after necking in metals. *The Journal of Strain Analysis for Engineering Design*, *50*(2), 125-137.

[40] Mirone, G. (2004). A new model for the elastoplastic characterization and the stress–strain determination on the necking section of a tensile specimen. *International Journal of Solids and Structures*, *41*(13), 3545-3564.

[41] Mirone, G., Corallo, D., & Barbagallo, R. (2017). Experimental issues in tensile Hopkinson bar testing and a model of dynamic hardening. *International Journal of Impact Engineering*, *103*, 180-194.

[42] Mirone, G., & Corallo, D. (2013). Stress–strain and ductile fracture characterization of an X100 anisotropic steel: Experiments and modelling. *Engineering Fracture Mechanics*, *102*, 118-145.

[43] Koch, D., & Haufe, A. (2019). First Steps towards Machine-Learning supported Material Parameter Identification. In *12th European LS-DYNA Conference, DYNAmore GmbH, Koblenz*.

[44] Meißner, P., Watschke, H., Winter, J., & Vietor, T. (2020). Artificial neural networks-based material parameter identification for numerical simulations of additively manufactured parts by material extrusion. *Polymers*, *12*(12), 2949.

[45] Marques, A., Pereira, A., Ribeiro, B., & Prates, P. A. (2022). On the identification of material constitutive model parameters using machine learning algorithms. *Key Engineering Materials*, *926*, 2146-2153.

[46] Guo, Z., Bai, R., Lei, Z., Jiang, H., Liu, D., Zou, J., & Yan, C. (2021). CPINet: Parameter identification of path-dependent constitutive model with automatic denoising based on CNN-LSTM. *European Journal of Mechanics-A/Solids*, *90*, 104327.

[47] Meißner, P., Winter, J., & Vietor, T. (2022). Methodology for neural network-based material card calibration using LS-DYNA MAT_187_SAMP-1 considering failure with GISSMO. *Materials*, *15*(2), 643.

[48] Liu, Y., Zhao, T., Ju, W., & Shi, S. (2017). Materials discovery and design using machine learning. *Journal of Materiomics*, *3*(3), 159-177.

[49] Stoll, A., & Benner, P. (2021). Machine learning for material characterization with an application for predicting mechanical properties. *GAMM-Mitteilungen*, *44*(1), e202100003.

[50] Wagner, N., & Rondinelli, J. M. (2016). Theory-guided machine learning in materials science. *Frontiers in Materials*, *3*, 28.

[51] Karniadakis, G. E., Kevrekidis, I. G., Lu, L., Perdikaris, P., Wang, S., & Yang, L. (2021). Physics-informed machine learning. *Nature Reviews Physics*, *3*(6), 422-440.

[52] Dunand, M., & Mohr, D. (2010). Hybrid experimental–numerical analysis of basic ductile fracture experiments for sheet metals. *International journal of solids and structures*, *47*(9), 1130-1143.

[53] Scapin, M., Peroni, L., & Peroni, M. (2012). Parameters identification in strain-rate and thermal sensitive visco-plastic material model for an alumina dispersion strengthened copper. *International Journal of Impact Engineering*, *40*, 58-67.

[54] Zhao, K., Wang, L., Chang, Y., & Yan, J. (2016). Identification of post-necking stress–strain curve for sheet metals by inverse method. *Mechanics of Materials*, *92*, 107-118.

[55] Yao, Z., & Wang, W. (2022). Full-range strain-hardening behavior of structural steels: Experimental identification and numerical simulation. *Journal of Constructional Steel Research*, *194*, 107329.

[56] Zhang, H., Xu, C., Gao, T., Li, X., & Song, H. (2023). Identification of strain hardening behaviors in titanium alloys using tension tests and inverse finite element method. *Journal of Mechanical Science and Technology*, *37*(7), 3593-3599.

[57] Shokeir, Z., Besson, J., Belhadj, C., Petit, T., & Madi, Y. (2022). Edge tracing technique to study post-necking behavior and failure in Al alloys and anisotropic plasticity in line pipe steels. *Fatigue & Fracture of Engineering Materials & Structures*, *45*(9), 2427-2442.

[58] Defaisse, C., Mazière, M., Marcin, L., & Besson, J. (2018). Ductile fracture of an ultra-high strength steel under low to moderate stress triaxiality. *Engineering Fracture Mechanics*, *194*, 301-318.

[59] Zeng, X., & Huo, J. S. (2023). Rate-dependent constitutive model of high-strength reinforcing steel HTRB600E in tension. *Construction and Building Materials*, *363*, 129824.

[60] Scapin, M., Peroni, L., Fichera, C., & Cambriani, A. (2014). Tensile behavior of T91 steel over a wide range of temperatures and strain-rate up to 104 s− 1. *Journal of materials Engineering and Performance*, *23*(8), 3007-3017.

[61] Scapin, M., Peroni, L., Torregrosa, C., Perillo-Marcone, A., Calviani, M., Pereira, L. G., ... & Meyer, M. (2017). Experimental results and strength

model identification of pure iridium. *International Journal of Impact Engineering*, *106*, 191-201.

[62] Pham, Q. T., Nguyen-Thoi, T., Ha, J., & Kim, Y. S. (2021). Hybrid fitting-numerical method for determining strain-hardening behavior of sheet metals. *Mechanics of Materials*, *161*, 104031.

[63] Peroni, L., Scapin, M., & Fichera, C. (2015, June). An advanced identification procedure for material model parameters based on image analysis. In *Proceedings of 10th European LS-DYNA conference, Würzburg, Germany*.

[64] Scapin, M., Peroni, L., & Carra, F. (2016). Investigation and mechanical modelling of pure molybdenum at high strain-rate and temperature. *Journal of Dynamic Behavior of Materials*, *2*(4), 460-475.

[65] Scapin, M., Peroni, L., Torregrosa, C., Perillo-Marcone, A., & Calviani, M. (2019). Effect of strain-rate and temperature on mechanical response of pure tungsten. *Journal of Dynamic Behavior of Materials*, *5*(3), 296-308.

[66] Zhang, H., Gao, T., Xu, C., Wu, Q., Song, H., & Huang, G. (2025). Identification of hardening and fracture behaviors of titanium alloy by a hybrid digital image correlation and finite element method. *Optics & Laser Technology*, *181*, 111869.

[67] Peroni, L., & Scapin, M. (2018). Strength model evaluation based on experimental measurements of necking profile in ductile metals. In *EPJ Web of Conferences* (Vol. 183, p. 01015). EDP Sciences.

[68] Beltramo, M., Scapin, M., & Peroni, L. (2023). An advanced post-necking analysis methodology for elasto-plastic material models identification. *Materials & Design*, *230*, 111937.

[69] Majzoobi, G. H., Khosroshahi, S. F. Z., & Mohammadloo, H. B. (2010). Determination of materials parameters under dynamic loading: Part II: Optimization. *Computational Materials Science*, *49*(2), 201-208.

[70] Almasi, A. R. P., Fariba, F., & Rasoli, S. (2015). Modifying stress-strain curves using optimization and finite elements simulation methods. *Journal of Solid Mechanics*, *7*(1), 71-82.

[71] Kajberg, J., & Lindkvist, G. (2004). Characterisation of materials subjected to large strains by inverse modelling based on in-plane displacement fields. *International Journal of Solids and Structures*, *41*(13), 3439-3459.

[72] Gross, A. J., & Ravi-Chandar, K. (2015). On the extraction of elastic–plastic constitutive properties from three-dimensional deformation measurements. *Journal of Applied Mechanics*, *82*(7), 071013.

[73] Zhang, H., Coppieters, S., Jiménez-Peña, C., & Debruyne, D. (2019). Inverse identification of the post-necking work hardening behaviour of thick HSS through full-field strain measurements during diffuse necking. *Mechanics of Materials*, *129*, 361-374.

[74] Coppieters, S., Cooreman, S., Sol, H., Van Houtte, P., & Debruyne, D. (2011). Identification of the post-necking hardening behaviour of sheet metal by comparison of the internal and external work in the necking zone. *Journal of Materials Processing Technology*, *211*(3), 545-552.

[75] Coppieters, S., Sumita, S., Yanaga, D., Denys, K., Debruyne, D., & Kuwabara, T. (2016). Identification of post-necking strain hardening behavior of pure titanium sheet. In *Residual Stress, Thermomechanics & Infrared Imaging, Hybrid Techniques and Inverse Problems, Volume 9: Proceedings of the 2015 Annual Conference on Experimental and Applied Mechanics* (pp. 59-64). Cham: Springer International Publishing.

[76] Marth, S., Häggblad, H. Å., Oldenburg, M., & Östlund, R. (2016). Post necking characterisation for sheet metal materials using full field measurement. *Journal of Materials Processing Technology*, *238*, 315-324.

[77] Grédiac, M., & Pierron, F. (2006). Applying the virtual fields method to the identification of elasto-plastic constitutive parameters. *International Journal of Plasticity*, *22*(4), 602-627.

[78] Kim, J. H., Serpantié, A., Barlat, F., Pierron, F., & Lee, M. G. (2013). Characterization of the post-necking strain hardening behavior using the virtual fields method. *International Journal of Solids and Structures*, *50*(24), 3829-3842.

[79] Fu, J., Barlat, F., Kim, J. H., & Pierron, F. (2017). Application of the virtual fields method to the identification of the homogeneous anisotropic hardening parameters for advanced high strength steels. *International Journal of Plasticity*, *93*, 229-250.

[80] Park, J. S., Kim, J. M., Barlat, F., Lim, J. H., Pierron, F., & Kim, J. H. (2021). Characterization of dynamic hardening behavior at intermediate strain rates using the virtual fields method. *Mechanics of Materials*, *162*, 104101.

[81] Pham, Q. T., Nguyen-Thoi, T., Ha, J., & Kim, Y. S. (2021). Hybrid fitting-numerical method for determining strain-hardening behavior of sheet metals. *Mechanics of Materials*, *161*, 104031.

[82] Coppieters, S., & Kuwabara, T. (2014). Identification of post-necking hardening phenomena in ductile sheet metal. *Experimental mechanics*, *54*(8), 1355-1371.

[83] Dunand, M., & Mohr, D. (2011). On the predictive capabilities of the shear modified Gurson and the modified Mohr–Coulomb fracture models over a wide range of stress triaxialities and Lode angles. *Journal of the Mechanics and Physics of Solids*, *59*(7), 1374-1394.

[84] Wang, L., & Tong, W. (2015). Identification of post-necking strain hardening behavior of thin sheet metals from image-based surface strain data in uniaxial tension tests. *International journal of solids and structures*, *75*, 12-31.

[85] Beltramo, M., Scapin, M., & Peroni, L. (2024). An efficient shape-based procedure for strain hardening identification in the post-necking phase. *Mechanics of Materials*, *196*, 105066.
[86] Scapin, M., & Beltramo, M. (2024). A Methodology for Post-Necking Analysis in Isotropic Metals. *Metals*, *14*(5), 593.
[87] Beltramo, M., Peroni, L., & Scapin, M. (2025). A data-driven procedure for the analysis of high strain rate tensile tests via visible and infrared image processing. *International Journal of Impact Engineering*, *199*, 105232.
[88] Beltramo, M., Scapin, M., & Peroni, L. (2025). Analysis of the work-to-heat conversion beyond the necking onset in non-isothermal tensile tests. *International Journal of Impact Engineering*, 105503.

Chapter 2

Plastic flow behavior and specimen necking shape

This chapter first investigates, and then exploits for post-necking characterization, the strong correlation linking the plastic constitutive law of the material to the deformed geometries of a cylindrical tensile specimen. Even though this is implicitly exploited in existing strategies based on the necking profile of isotropic materials [1-9], detailed justification and efficient exploitation of such correlation are missing.

The objective of Section 2.1 is to provide foundations supporting the use of specimen necking shapes for identifying the post-necking plastic flow curve. Then, Section 2.2 highlights the role of the strain at the necking onset and the consequent similarities that allow different materials to be effectively compared during the post-necking phase. Finally, a database-driven approach is proposed in Section 2.3 as a natural framework for exploiting the shape-law correlation systematically. More specifically, a library storing relevant results of FE analyses is used to establish such correlation. The considerations presented in this chapter have been partially published in [10-12].

2.1 Shape-law correlation

To investigate the correlation between plastic flow curves and necking shapes, attention is first restricted to testing conditions and/or materials for which the equivalent plastic strain $\varepsilon_{eq,p}$ is the only variable governing plasticity. In such cases, the equivalent stress σ_{eq} experienced by each material point is uniquely determined by the current local value of equivalent plastic strain. Since during a monotonic tensile test each material point undergoes increasing deformations, the equivalent stress evolves too, according to the strain-hardening rate $d\sigma_{eq}/d\varepsilon_{eq,p}$ of the material tested. Thus, even though material points may differ one from another in terms of $\varepsilon_{eq,p}(t)$ and $\sigma_{eq}(t)$, which is typical of necking, they all evolve (until reached by the unloading boundary) along the same curve in the $\sigma_{eq} - \varepsilon_{eq,p}$ plane, namely, the material's strain-hardening law. This is qualitatively shown in Figure 2.1, where different material points on the specimen surface are denoted with capital letters. In the configuration analyzed, A and B are in the plastic domain, while C, D, and E have already undergone unloading. It should be noted that this analysis focuses on material points, rather than cross-sections, because previous considerations are true for local variables for definition, but not necessarily for variables averaged over the cross-sections.

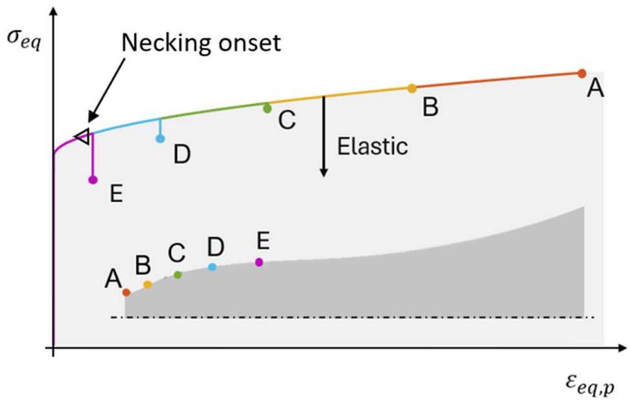

Figure 2.1 Deformation paths followed during a tensile test by different material points on the specimen surface for strain-dependent materials (adapted from [12]).

By looking at the problem from a Eulerian perspective, it can be observed that at any necked configuration different points exhibit different equivalent plastic strains and, consequently, different equivalent stresses, all lying on the material's strain-hardening law (if the points are within the plastic domain). This indicates that, when $\varepsilon_{eq,p}$ is the only variable governing plasticity, the strain-hardening rate $d\sigma_{eq}/d\varepsilon_{eq,p}$ determines not only the temporal evolution of equivalent stress at a given material point, but also the spatial equivalent stress distribution.

More specifically, as during necking all material points exhibit equivalent plastic strain values of at least $\varepsilon_{eq,p,n}$, it is the post-necking strain-hardening rate which relates the equivalent plastic strain and equivalent stress distributions. In this sense, and by focusing on the specimen's outer surface, the necking shape encodes information about the post-necking strain-hardening behavior of the material $\sigma_{eq}^{N}(\varepsilon_{eq,p})$. This is valid for isotropic materials, since for anisotropic ones, the yield function may also play a role. The remainder of this thesis, except for Chapter 7, refers to isotropic materials.

Since necking shapes of specimens made of isotropic materials are axisymmetric, they are completely defined by their 2D necking silhouette (or profile). Hence, returning to the previous discussion, it is possible to state that information about $\sigma_{eq}^{N}(\varepsilon_{eq,p})$ are encoded in the necking profile. Even regions of the specimen that are elastically unloaded retain information about such law. This is because the geometry of such regions has remained unchanged since the arrival of the unloading boundary, thereby preserving the strain-hardening information at the maximum equivalent plastic strain previously attained. Therefore, the entire necking profile, and not only the plastically loaded region, represents the post-necking hardening behavior of the material.

A qualitative representation is depicted in Figure 2.2. Each vertical thick line on the specimen indicates points on the outer surface characterized by the same equivalent plastic strain; the associated state on the hardening law is highlighted with a marker.

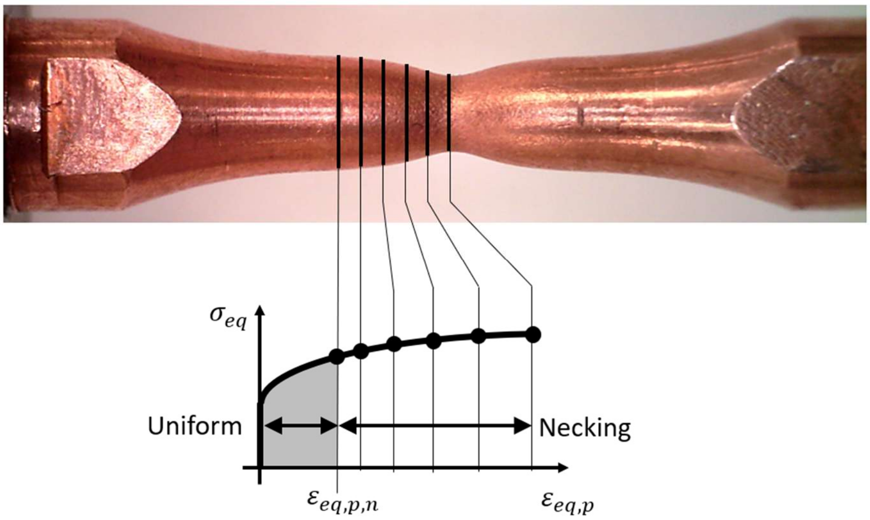

Figure 2.2 Scheme of the correlation between necking shape and strain-hardening law for an isotropic material (adapted from [8]).

Each infinitesimal portion of the profile encodes the hardening rate information at a different equivalent plastic strain, the maximum achieved in that infinitesimal portion at the configuration considered. In this sense, the profile altogether reflects both stress and strain histories after the necking onset. Consequently, when specimens are characterized by identical profiles at a given configuration, this indicates that they must share the same necking strain (as explained in Section 2.2) and the same post-necking histories, which in turn implies that the post-necking hardening laws must be identical. Actually, it should be noted that two identical necking profiles could also be obtained from material laws scaled in equivalent stress one with respect to the other, i.e. $\sigma_{eq,1}(\varepsilon_{eq,p}) = k_\sigma \sigma_{eq,2}(\varepsilon_{eq,p})$. This can be explained considering that, when elastic and inertial contributions are negligible, the necking strain and the shape are governed by relative equivalent stress variations. Above considerations prove the uniqueness of the shape-law correlation for monotonic uniaxial tests and strain-dependent behaviors; more specifically, the correlation between the neck geometry $R(x)$ and the functional form $\hat{\sigma}_{eq}^{N}(\varepsilon_{eq,p})$ of the post-necking strain-hardening law.

This results also means that, once the material (and so the $\hat{\sigma}_{eq}^{N}(\varepsilon_{eq,p})$ law) is fixed, a prescribed axial elongation uniquely corresponds to a specific specimen silhouette. In particular, the fact that the specimen reaches a specific geometry in the vicinity of the minimum cross-section means that the force is also uniquely determined. The existence of a unique correlation between the force-elongation curve (or better, the $s(e)$ engineering curve) and the hardening law is already acknowledged in the literature and is supported by the successful application of identification methods based on fitting the engineering response. The considerations of the previous paragraphs go one step further: not only the evolution of the region surrounding the neck is uniquely related to the constitutive law, but also the entire necking shape.

It is now worth illustrating better how strain-hardening affects the necking shape. During the post-necking regime, as the minimum cross-sectional area decreases, the local equivalent stress increases significantly for materials with high strain-hardening rates. This allows the sections surrounding the neck to continue deforming, resulting in a "long-wave" neck. In contrast, materials with low strain-hardening rates, approaching perfectly plastic behavior, cannot redistribute stress as effectively, and deformation concentrates at the minimum cross-section, leading to a more localized neck.

This is shown in Figure 2.3, by displaying a series of hardening laws (subfigure a) and the corresponding necking shapes (subfigure b). The results were obtained using a FE code for simulating tensile tests on geometrically identical cylindrical bars characterized by these different strain-hardening behaviors. Further details on FE modeling will be provided in Section 2.3. Hardening laws were defined so that necking occurred immediately at yielding, hence it holds $\sigma_{eq}^{N}(\varepsilon_{eq,p}) \equiv \sigma_{eq}(\varepsilon_{eq,p}), \forall \varepsilon_{eq,p}$. This aimed to focus only on the post-necking domain; the effect of a uniform deformation stage before the necking onset will be discussed in Section 2.2. For meaningful comparison, the shapes shown in Figure 2.3b were all selected in correspondence of the same maximum strain achieved on the specimen surface; in this case, without loss of generality, a value of 0.8 was chosen.

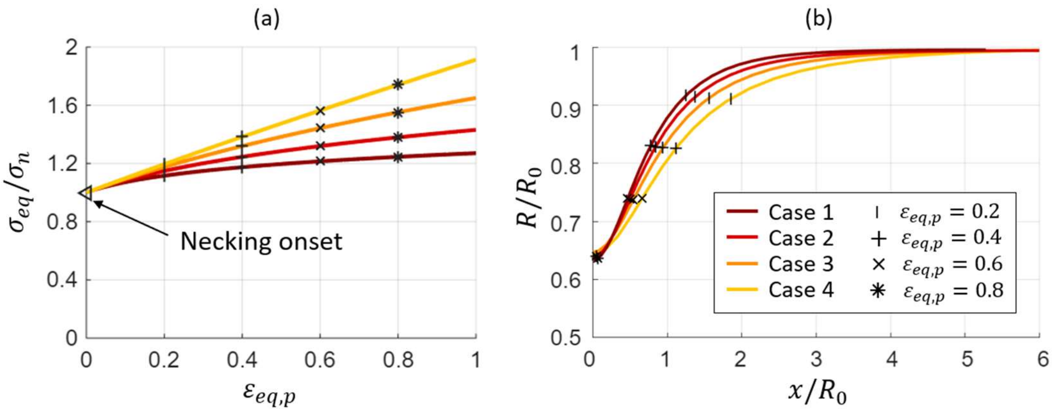

Figure 2.3 Correlation between hardening law (a) and corresponding necking shapes at the same max $\varepsilon_{eq,p} = 0.8$ (b). Markers in (b) indicate material points experiencing given states of (a) (adapted from [10]).

This plot shows that, even though all profiles share the same range R/R_0, the shapes themselves differ because of the different post-necking behavior. As anticipated, the higher the hardening rate, the less localized the deformation. Furthermore, in Figure 2.3b material points experiencing predefined equivalent plastic strain levels are indicated with markers on the different profiles. The fact that the same markers are almost horizontally aligned across the different shapes underlines the correlation between $\varepsilon_{eq,p}$ and R/R_0 in addition to the correlation between ε_c and R/R_0 which directly comes from the definition $\varepsilon_c = \ln(R/R_0)$.

Above results are twofold: they state which hardening rate leads to which necking shape, but also how necking shape can be interpreted to get information about the hardening rate. This further supports the correlation between necking profiles and post-necking strain-hardening laws.

The uniqueness of the relationship between $R(x)$ and $\hat{\sigma}_{eq}^N(\varepsilon_{eq,p})$ (and also $\hat{s}^N(e)$ for the sake of completeness) has been proved for strain-dependent scenarios. More precisely, the uniqueness holds whenever the strain-hardening rate inferred by moving forward in time coincides with that inferred by moving toward more highly deformed regions of the profile (see Figure 2.1). This happens when all material points evolve along the same curve in the $\sigma_{eq} - \varepsilon_{eq,p}$ plane before elastic unloading occurs. Such situation arises not only when the equivalent plastic strain is the sole governing variable, but also when additional variables q that influence the material strain-hardening rate are constant or uniquely related to $\varepsilon_{eq,p}$ under the testing conditions considered. Indeed, in these scenarios, when a point is characterized by $\varepsilon_{eq,p}^*$, the corresponding q^* and σ_{eq}^* are the same experienced by other points when they exhibited the same $\varepsilon_{eq,p}^*$. Hence, all material points evolve along the same path in the $\sigma_{eq} - \varepsilon_{eq,p} - q$ space, and therefore also along the same path in the projected $\sigma_{eq} - \varepsilon_{eq,p}$ plane. Such path no longer represents the strain-hardening law of the material but inherently includes the effects of q.

To conclude, whenever plasticity is influenced by variables that remain constant during necking, or that vary in a manner uniquely linked to equivalent plastic strain, the necking profile $R(x)$ (or equivalently the normalized engineering response $\hat{s}^N(e)$) can be uniquely associated with the material normalized post-necking path $\hat{\sigma}_{eq}^N(\varepsilon_{eq,p})$, which may intrinsically account for the effects of additional variables. This is the case of temperature in rate insensitive materials, as explained in Section 3.2.

Nevertheless, plastic behavior may also depend on additional variables $\tilde{q}$, whose variation with the equivalent plastic strain varies from one material point to another. In these cases, when a point is characterized by $\varepsilon_{eq,p}^*$, the corresponding $\tilde{q}^*$ and σ_{eq}^* differ from those experienced by other points at the same $\varepsilon_{eq,p}^*$. Hence, the deformation path is no longer the same for all material points: each of them follows a different evolution, as qualitatively shown in Figure 2.4.

As a result, the uniqueness of the correlation between $\hat{\sigma}_{eq}^N(\varepsilon_{eq,p})$, $R(x)$, and $\hat{s}^N(e)$ is no longer valid. In these cases, the information on the strain-hardening rate inferred from a single necking profile appears to contradict that obtained from the

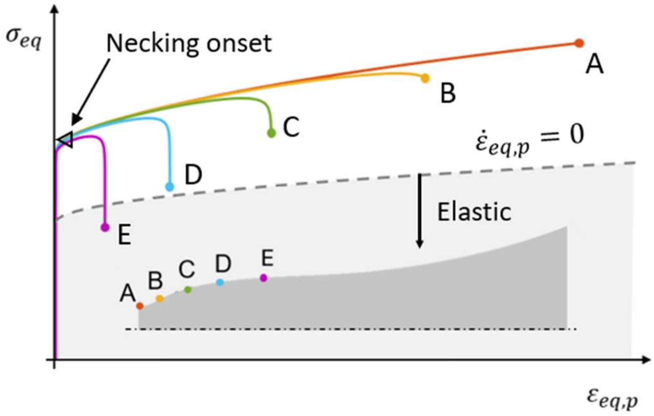

Figure 2.4 Deformation paths followed during a tensile test by different material points on the specimen surface for strain rate sensitive materials (adapted from [12]).

temporal evolution of the test. This apparent inconsistency arises because, when moving along the profile from point B to a point A characterized by a higher equivalent plastic strain, the equivalent stress at point A differs from the equivalent stress that point B exhibits at the time it reaches the same equivalent plastic strain. The origin of this discrepancy lies in the difference in variables $\tilde{q}$ between the two points and times considered. It follows that the material law cannot be reconstructed from a single deformed configuration, nor from the engineering curve alone. For instance, this is the case of rate sensitive material, as discussed in Section 5.1.

Nevertheless, instantaneous necking profiles, within the plastically loaded region, still provide a good approximation of the "spatial" strain-hardening rate, i.e., of how equivalent stress and equivalent plastic strain vary along the profile at that time instant. In other words, the outer shape correlates well to the normalized $\hat{\sigma}_{eq} - \varepsilon_{eq,p}$ curve representing the instantaneous state of superficial material points. Moreover, it is also correlated to the equivalent plastic strain rate distribution $\dot{\varepsilon}_{eq,p}(x)$ at that moment on the specimen surface, provided that monotonic tensile tests are considered. Actually, due to the differential nature of equivalent plastic strain rate, this distribution $\dot{\varepsilon}_{eq,p}(x)$ can be assumed to depend only on how equivalent plastic strain distribution evolves in an infinitesimal neighborhood of the time considered. It results that the absolute scale of $\dot{\varepsilon}_{eq,p}(x)$ depends on the speed applied to the specimen ends, while the normalized distribution $\hat{\dot{\varepsilon}}_{eq,p}(x)$ can be assumed to depend solely on the equivalent plastic strain distribution.

Hence, if the necking profiles of different materials coincide, the materials can be considered instantaneously analogous. This is valid in a normalized post-necking perspective and regardless of the material sensitivity to internal variables q or $\tilde{q}$. Such analogy implies that the superficial equivalent plastic strain and strain rate distributions, as well as the superficial equivalent stress distribution can be considered approximately the same once the stress scale and speed coefficient have been removed.

Above considerations suggest that a sequence of normalized necking shapes can be used to identify loci of points in the $\sigma_{eq} - \varepsilon_{eq,p}$ plane. Each necking shape actually provides plastic information about the range of equivalent plastic strains I_ε experienced at that instant by superficial material points, provided that $\dot{\varepsilon}_{eq,p} > 0$. This last condition determines the range $I_\varepsilon = [\varepsilon_{eq,p}^{min}, \varepsilon_{eq,p}^{max}]$ associated with the given shape. As deformation proceeds, subsequent shapes provide information over ranges I_ε that progressively shift to higher values: $\varepsilon_{eq,pl}^{max}$ increases because of continuous localization, while $\varepsilon_{eq,pl}^{min}$ increases due to progressive unloading. This is schematically depicted in Figure 2.5.

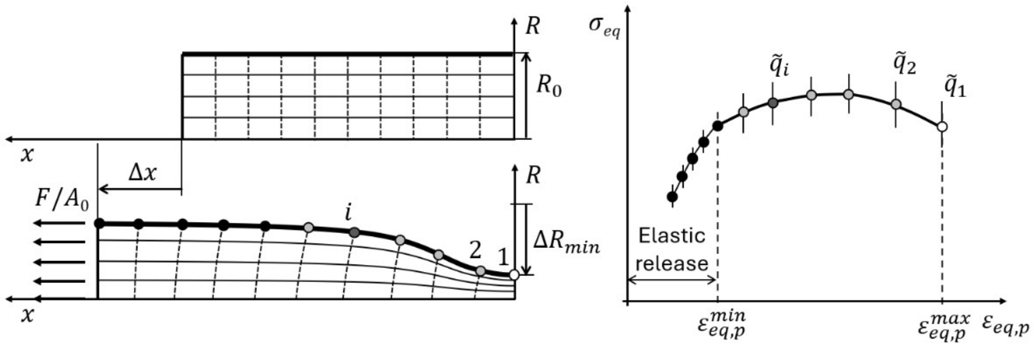

Figure 2.5 Correlation between necking shape and instantaneous states of superficial material points (adapted from [12]).

Analyzing different necking configurations, hence, results in a set of curves representing the projection of the plastic flow surface in the $\sigma_{eq} - \varepsilon_{eq,p}$ plane on a broad strain domain. The plastic flow surface in the $\sigma_{eq} - \varepsilon_{eq,p} - \tilde{q}$ space can be reconstructed by associating to each material point the local and instantaneous values of $\tilde{q}$, either measured experimentally or evaluated through post-processing analyses. Furthermore, by tracking individual material points, it would also be possible to estimate their distinct deformation paths.

Previous considerations also apply to materials in which all points follow the same $\sigma_{eq}(\varepsilon_{eq,p})$. In this case, analyzing multiple configurations is not necessary, as a much stronger correlation already holds, but it improves stability by introducing redundancy.

2.2 Pre- and post-necking uncoupling

As extensively discussed in Chapter 1, the onset of necking marks a fundamental transition in the deformation mode of the specimen. Prior to necking, the specimen gauge length is characterized by uniform fields of strain, stress and possibly other variables affecting the material response. These fields can remain constant or evolve uniformly, depending on the material and test conditions. From a Lagrangian viewpoint, this means that distinct material points exhibit a synchronous evolution of internal variables. In pre-necking regime, the specimen gauge length maintains the geometry of a right cylinder, whose size derives from the reduction in cross-sectional area caused by the prescribed axial elongation. In this sense, the pre-necking constitutive law dictates the evolution of the uniformly distributed stress field (and hence the force) but does not influence the specimen shape, since its size mainly results from plastic incompressibility. In this sense, materials characterized by different hardening laws exhibit the same geometry evolution before necking onset. In other words, during this uniform stage, the geometry alone carries no information about the specific hardening behavior. Then, beyond necking onset, the specimen develops spatial gradients of stress, strain, and possibly additional internal variables. The constitutive law dictates not only the force but also the neck shape itself and its evolution. Actually, as all material points within the gauge length experience equivalent plastic strains at least equal to that associated with incipient necking, the subsequent geometric evolution is governed by the post-necking constitutive behavior. This is also supported by some works that recognized $\varepsilon_{eq,p} - \varepsilon_{eq,p,n}$ as necking governing variable [13-15].

Starting from this consideration, it can be proved that the shape-law correlation introduced in Section 2.1 referring to the absolute necking shape $R(x)$, remains valid also in relative terms, i.e., independently of the specimen size. Considering the circumferential strain, which is directly and accurately inferable from the necking profile $R(x)$, it results that:

$$\varepsilon_c - \varepsilon_{c,n} = \ln\left(\frac{R}{R_0}\right) - \ln\left(\frac{R_n}{R_0}\right) = \ln\left(\frac{R}{R_n}\right) \stackrel{\text{def}}{=} \ln \hat{R}. \tag{2.1}$$

This relationship indicates that the relevant measure for necking description is represented by the radial coordinate normalized by its value at the necking onset R_n. Axial coordinates must be normalized by R_n too, since axial elongation and radial contraction are coupled (primarily through plastic incompressibility). It follows that it is the normalized shape $\hat{R}(\hat{x})$ which carries information about the normalized post-necking hardening rate. R_n can be further expressed as:

$$R_n = R_0 e^{\varepsilon_{c,n}} = R_0 e^{-\varepsilon_{eq,n}/2}, \tag{2.2}$$

by considering volume conservation and the fact that the necking onset is at the boundary of uniform deformation. This expression of the normalization factor highlights that the proposed approach uncouples the post-necking deformation from the initial size of the specimen and the pre-necking deformation.

The need to remove the influence of the initial size could also be explained by considering two tensile specimens made of the same material but characterized by different initial diameters. Regardless of the initial dimensions, their deformed configurations must convey the same information regarding the strain-hardening rate (provided that the specimens are sufficiently long to avoid boundary effects). Conversely, uncoupling from the pre-necking phase could not be expected at first glance, but it is possible as uniform deformation preserves the shape of right cylinder and simply causes a different absolute size at the necking onset. This suggests that materials sharing the same post-necking hardening behavior but not the uniform response are equivalent in terms of normalized necking profile. Above considerations are valid not only for scenarios where the $\sigma_{eq}(\varepsilon_{eq,p})$ curve fully describes the material behavior, but also for more complex behaviors introduced at the end of Section 2.1.

Focuses on the simplest cases, the correlation described in Section 2.1 also includes the engineering response. Hence, materials sharing $\sigma_{eq}^{N}(\varepsilon_{eq,p})$ should provide not only analogous necking profiles, but also analogous post-necking engineering responses. At first glance, this may seem unverified, but due to an improper viewpoint. Uncoupling pre- and post-necking behaviors enables a more appropriate comparison between engineering responses.

As during necking the engineering strain of a length-based approach highly depends on the reference length itself [16], another definition of engineering strain is preferred. It is based on the radial contraction at the minimum cross-section, according to the following expression:

$$c \stackrel{\text{def}}{=} \frac{|\Delta R|_{min}}{R_0} = \frac{R_0 - R_{min}}{R_0} = 1 - \frac{R_{min}}{R_0}. \tag{2.3}$$

This represents the radial engineering strain, as well as the circumferential engineering strain for definition.

For removing the effect of uniform deformation from the engineering response $s(c)$, it can be useful to consider the radial engineering strain at the necking onset:

$$c_n = 1 - \frac{R_n}{R_0}. \tag{2.4}$$

Plugging this relationship into Equation 2.3, it results:

$$c = 1 - \frac{R_{min}}{R_n}\frac{R_n}{R_0} = 1 - \frac{R_{min}}{R_n}(1 - c_n). \tag{2.5}$$

Then, a post-necking radial engineering strain $\hat{c}$ can be defined:

$$\hat{c} \stackrel{\text{def}}{=} 1 - \frac{R_{min}}{R_n} = 1 - \hat{R}_{min}, \tag{2.6}$$

which is consistent with the normalization applied to the necking silhouette.
The relationship between c and $\hat{c}$ is, thus, derived from Equation 2.5:

$$\hat{c} = 1 - \frac{1-c}{1-c_n} = \frac{c-c_n}{1-c_n} \tag{2.7}$$

It should be noted that also the engineering stress s is affected by uniform deformation. The correction must ensure that modified engineering stresses $\hat{s}$ coincide for materials sharing $\sigma_{eq}^{N}(\varepsilon_{eq,p})$. Consider the following algebraic manipulation:

$$s = \frac{F}{A_0} = \frac{\sigma_{a,avg}A}{A_n}\frac{A_n}{A_0} = \sigma_{a,avg}\left(\frac{R_{min}}{R_n}\right)^2\left(\frac{R_n}{R_0}\right)^2 = \sigma_{a,avg}(1-\hat{c})^2\left(\frac{R_n}{R_0}\right)^2. \tag{2.8}$$

Specimens of materials sharing $\sigma_{eq}^{N}(\varepsilon_{eq,p})$ are characterized by the same normalized shape when their $\hat{c}$ coincide, hence they also develop the same $\sigma_{a,avg}$. Thus, the definition that ensures obtaining the same $\hat{s}$ is:

$$\hat{s} \stackrel{\text{def}}{=} s\left(\frac{R_0}{R_n}\right)^2 = \frac{s}{(1-c_n)^2}. \tag{2.9}$$

The conversion of $s(c)$ into $\hat{s}(\hat{c})$ can be proved to depend on the amount of uniform deformation. Indeed, by plugging Equation 2.2 into Equation 2.4 and then into 2.7, it results:

$$\hat{c} = 1 - (1-c)e^{\frac{\varepsilon_{eq,n}}{2}}; \tag{2.10}$$

while by substituting Equation 2.2 into 2.9, leads to:

$$\hat{s} = s e^{\varepsilon_{eq,n}}. \tag{2.11}$$

The resulting engineering curve will be denoted as $\hat{s}^N(\hat{c})$ in the post-necking phase.

Above mathematical derivations are of utmost importance for meaningful comparison between post-necking of different materials. For comparing deformed shapes, it is sufficient to scale them down of the corresponding R_n. Regarding engineering response, it is necessary to apply Equations 2.7 and 2.9 (or equivalently, 2.10 and 2.11).

Alternatively, instead of modifying all shapes and engineering responses, a material can be taken as reference, and all others are corrected to be comparable to it. Hereinafter, variables related to the reference material have no peculiar subscripts, whereas those related to a generic i-th material have i subscripts.

Regarding deformed shapes, those of the i-th material $R_i(x_i)$ need to be scaled down of $R_{n,i}$ and then up of R_n to be comparable to $R(x)$. A scaling coefficient $1/k_g$ can, thus, be defined as:

$$1/k_g \overset{\text{def}}{=} R_n/R_{n,i} \tag{2.12}$$

By expressing the radii at the necking onset as $R_n = R_0 e^{-\varepsilon_{eq,n}/2}$, it results:

$$k_g = \frac{R_{0,i}}{R_0} e^{\frac{\varepsilon_{eq,n}-\varepsilon_{eq,n,i}}{2}}. \tag{2.13}$$

Regarding the radial engineering strain, Equation 2.7 applied to the i-th material, gives:

$$\hat{c}_i = 1 - \frac{1-c_i}{1-c_{n,i}}. \tag{2.14}$$

For obtaining a radial engineering strain c_i' comparable to c of the reference material, the following expression of c must first be considered:

$$c = 1 - (1-\hat{c})(1-c_n). \tag{2.15}$$

Then, replacing $\hat{c}$ of Equation 2.14 with $\hat{c}_i$ of Equation 2.15, leads to the following radial engineering strain c_i' for the i-th material:

$$c_i' = 1 - (1-c_i)\frac{1-c_n}{1-c_{n,i}}. \tag{2.16}$$

Regarding the engineering stress, a similar line of thinking is applied. For the i-th material, Equation 2.9 gives:

$$\hat{s}_i = \frac{s_i}{(1-c_{n,i})^2}. \tag{2.17}$$

Then, for the reference material it holds:

$$s = \hat{s}(1-c_n)^2. \tag{2.18}$$

So, by plugging $\hat{s}_i$ of Equation 2.17 into $\hat{s}$ of Equation 2.18, the engineering stress s_i' for making the i-th material comparable to the reference one is obtained:

$$s_i' = s_i\left(\frac{1-c_n}{1-c_{n,i}}\right)^2. \tag{2.19}$$

It can be useful to express how both c_i' and s_i' are related to k_g. To this aim, let's replace $1-c_n = R_n/R_0$ and $1-c_{n,i} = R_{n,i}/R_{0,i}$ in Equations 2.16 and 2.19:

$$c_i' = 1 - (1-c_i)\frac{R_n/R_0}{R_{n,i}/R_{0,i}} = 1 - \frac{1}{k_g}(1-c_i)\frac{R_{0,i}}{R_0}; \tag{2.20}$$

$$s_i' = s_i \left(\frac{R_n/R_0}{R_{n,i}/R_{0,i}}\right)^2 = \frac{s_i}{k_g^2}\left(\frac{R_{0,i}}{R_0}\right)^2. \tag{2.21}$$

Now, it is possible to move on to an example of these analogies for materials sharing the post-necking hardening law, but not the uniform deformation phase.

Consider conducting a tensile test on a cylindrical bar (of initial radius R_0) made of a material characterized by the hardening law 1, plotted as solid light curve in Figure 2.6a. The marker '◁' in that graph indicates the necking onset according to Considère condition. The macroscopic tensile response of the material is shown as solid light curve again, in Figure 2.6b in terms of engineering stress plotted against the radial engineering strain. Moreover, the specimen shape at a given time is the one plotted as solid light curve in Figure 2.6c.

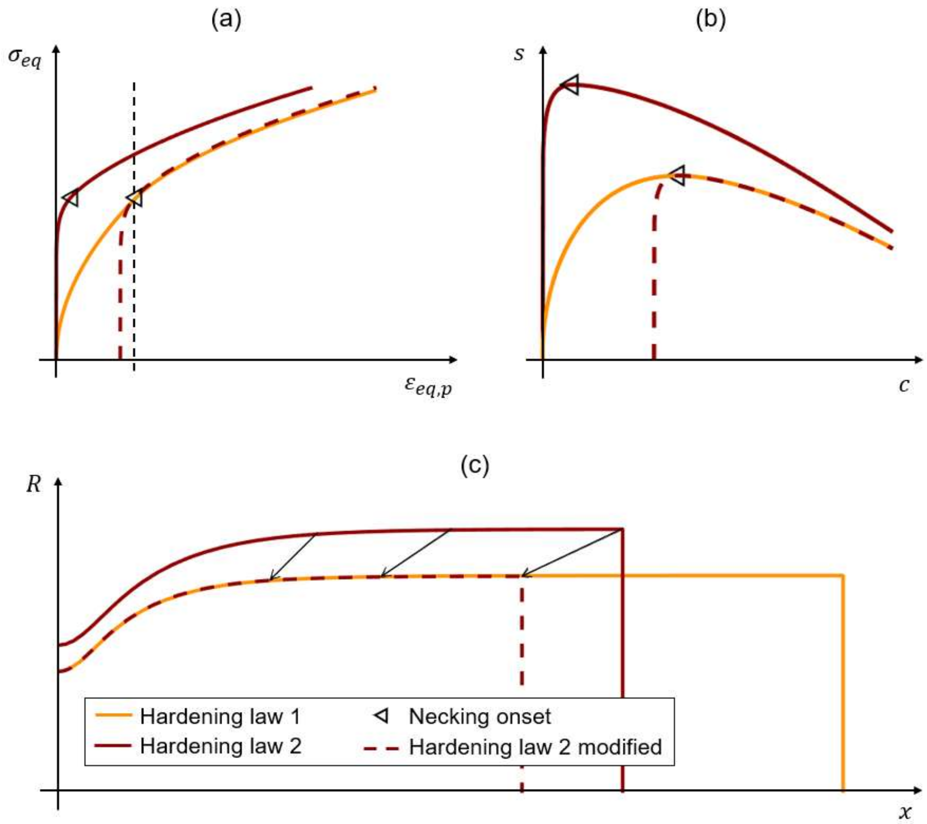

Figure 2.6 Similarities between materials characterized by the same post-necking hardening law, in terms of hardening law itself (a), radial engineering response (b), and necking silhouettes (c). [10]

Consider now another material characterized by a hardening law 2, with the same post-necking as law 1, but smaller ε_n. This is shown as solid dark line in Figure 2.6a. By horizontally translating law 2 to align necking onsets, the dashed dark line is obtained. It can be immediately noted that the post-necking part overlaps with that of law 1. If a cylindrical specimen (of initial radius R_0) made of the material with law 2 undergoes a tensile test, the macroscopic response will be the one plotted as dark solid line in Figure 2.6b. As expected, the maximum load $F_{2,max}$ is reached at a smaller engineering strain compared to case 1. The maximum load $F_{2,max}$ is also higher than $F_{1,max}$. This is consistent with the fact that at the necking onset the two laws are characterized by the same equivalent stress but different equivalent plastic strains $\varepsilon_{n,p}$ (see Figure 2.6a). Being necking onset at the boundary of uniform deformation, this means that the same axial stress acts on different cross-section areas, hence resulting in different forces for the two cases. Nevertheless, as anticipated, it is possible to properly modify the engineering responses to level off the different $\varepsilon_{n,p}$.

In this example, instead of modifying both engineering responses into $\hat{s}(\hat{c})$, it was chosen to act only on case 2 for obtaining a response comparable to case 1 (Equations 2.20, 2.21). This leads to the dashed dark curve of Figure 2.6b for case 2, which indeed overlaps with case 1 in the post-necking domain. Regarding the specimen necking shape, it is possible to find a configuration of test 2 (solid dark line in Figure 2.6c) that, once properly scaled to compensate for the different $\varepsilon_{n,p}$ (dashed dark line in Figure 2.6c), coincides with the necking shape considered for test 1.

These analogies can be readily proved through numerical investigations, but some experimental evidence of the correlation between $\hat{R}(\hat{x})$ and $\sigma_{eq}^{N}(\varepsilon_{eq,p})$ was already presented in [10] and is recalled hereinafter. Annealed and non-annealed pure copper specimens were tested. The pre-necking hardening law was identified with the length-based approach, while for the post-necking identification two FEMU methods were compared, one having the engineering curve as target and the other a single necking shape. Both methods are affected by experimental and modeling uncertainties; hence, it cannot be stated that one performs better than the other. However, the fact that their solutions were in good agreement supports the conclusion that both methods consistently captured the underlying material behavior. This is because, for these materials and testing conditions, the hardening law is uniquely correlated to both the engineering curve and the necking shape. In Figure 2.7a the laws were horizontally translated to align their $\varepsilon_{n,p}$. This highlights

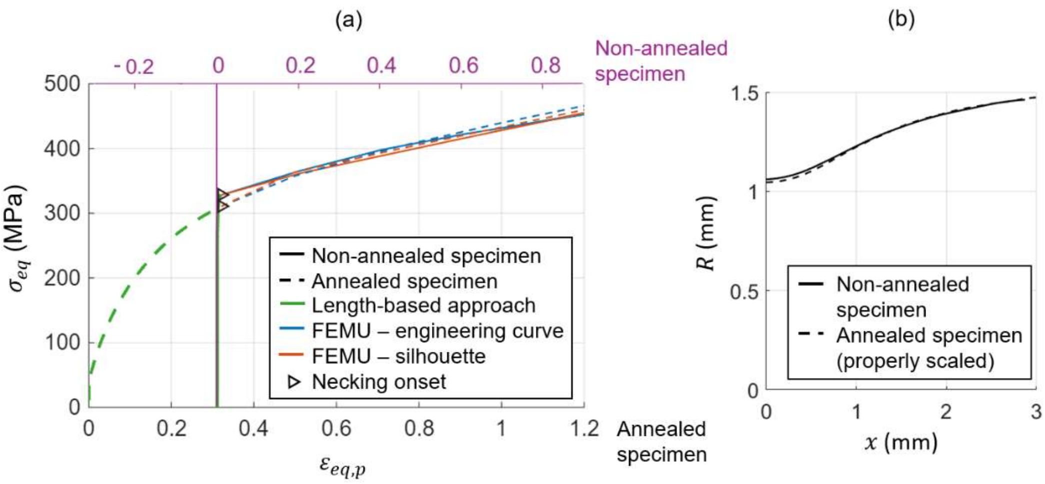

Figure 2.7 Experimental evidence of correlation between post-necking hardening law (a) and necking shape (b) for specimens of annealed and non-annealed pure copper. In (a) plastic flow curves obtained with the length-based approach during pre-necking and FEMU approaches during post-necking (adapted from [8]).

that the identified laws for annealed and non-annealed copper were very close to each other in the post-necking regime. From a physical point of view, this peculiar behavior may be explained considering that the two specimens differed only for annealing. This heat treatment only reduced the dislocation density, thus restoring the capability of the material to plastically deform at lower stresses. Figure 2.7b shows that deformed shapes of these materials sharing the same post-necking behavior coincide when properly scaled.

This experimental result further corroborates the existence of a correlation between the post-necking behavior and the normalized necking profile, rather than the absolute profile.

2.3 Database-driven approach

The shape-law correlation established in Section 2.2 forms the basis for the efficient approach presented in this section for the post-necking characterization of the hardening behavior of isotropic cylindrical specimens.

The correlation could, in principle, be exploited to develop an analytical approach conceived as an extension of Bridgman's theory [17] but formulated over the entire necking profile rather than restricted to the vicinity of the minimum cross-section. However, such formulation would inevitably require simplifying assumptions that would compromise the accuracy of the results.

Alternatively, higher levels of accuracy can be achieved when the correlation is exploited within a numerical framework, for instance through FE simulations. This strategy has already been proposed in the literature in the form of FEMU approaches, in which the objective function is defined in terms of the specimen's necking geometry [1-9]. The increasing demand for efficient identification procedures has, however, exposed several limitations of standard FEMU strategies. Their computational cost is intrinsically high, since the information generated during each optimization is discarded once the procedure is completed; consequently, similar simulations must be repeatedly performed when moving from one material characterization to another.

In this context, a database-driven approach provides a natural framework for exploiting the shape-law correlation systematically. More specifically, a library storing relevant results of FE analyses is used to establish such correlation. The simulations outputs considered relevant for this purpose are summarized in the tabular representation of Figure 2.8.

They consist of some macroscopic responses, and several necking shapes, each with the corresponding superficial distributions of local variables (i.e., fields obtained from elements on the outer surface). The equivalent stress is considered only for a portion of the surface that has not undergone unloading yet in the configuration considered. Actually, this portion is determined as the one characterized by an equivalent plastic strain rate higher than a predefined threshold, namely 10% of the nominal strain rate. Even though FE simulation outputs appear as continuous functions in Figure 2.8, they are actually discretized in space and time depending on the simulation mesh and settings.

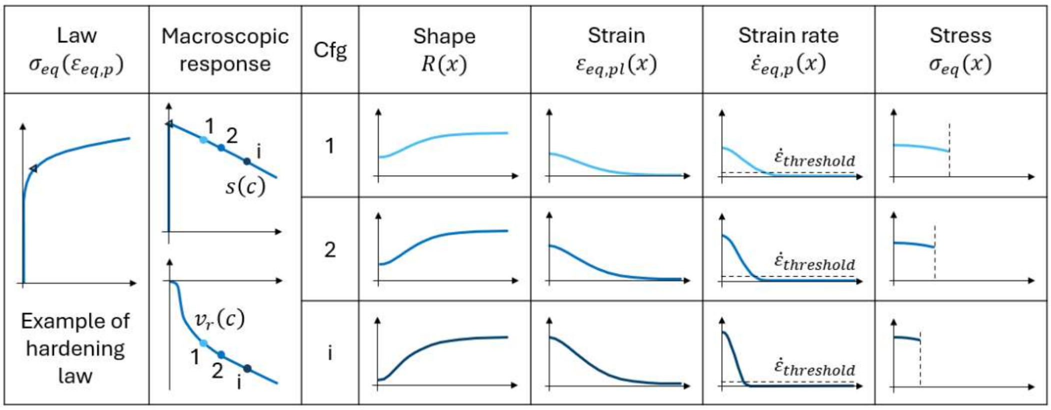

Figure 2.8 Schematic representation of data stored in the database for each FE simulation ("cfg" stands for "configuration"). [12]

To understand the specific macroscopic responses and local variables saved to the database, observations made in Sections 2.1 and 2.2 must be considered. In particular, the fact that when normalized necking profiles $\hat{R}(\hat{x})$ of different materials coincide, the corresponding superficial distributions $\varepsilon_{eq,p}(\hat{x}) - \varepsilon_{eq,p,n}$, $\hat{\dot{\varepsilon}}_{eq,p}(\hat{x})$, and $\hat{\sigma}_{eq}(\hat{x})$ can be considered approximately the same. The hat notation indicates that this consideration is valid once the different necking onset, stress scale and speed coefficient have been removed. Thus, equivalent plastic strain and strain rate and equivalent stress distributions are those of interest, but then macroscopic responses are needed for normalizing them. To compensate for the stress scale, engineering stress s is stored as a function of radial engineering strain c. Similarly, to account for the speed scale, the radial speed $v_r = dR/dt$ evaluated at the neck is stored as a function of radial engineering strain c.

For material characterization purposes, this database can be queried with a "brute-force search", thus avoiding the need for repeated simulations typical of FEMU approaches. This database-driven approach has been used in different studies [10-12, 18]. Detailed procedures for identifying the material constitutive law will be provided in Chapters 3, 4, and 5. Instead, the following paragraphs focus on the construction of the database through FE simulations.

Monotonic tensile tests on cylindrical specimens made of isotropic Von Mises materials were simulated with the commercial FE code Ansys LS-DYNA. A 2D axisymmetric model of the sample was considered, exploiting material isotropy and the axisymmetric geometry and loading conditions. An axisymmetric shell formulation with a single integration point was adopted to limit the computational cost associated with the construction of the database. For the same reason, remeshing techniques to control element distortion at large deformations were not employed. Instead, a carefully designed mesh was adopted, with appropriate element sizes and shapes. The mesh is characterized by smaller elements in the region where necking is expected to develop, and progressively larger elements moving away from this region, as shown in Figure 2.9. The initial element aspect-ratios were chosen such that element shapes tend to regularize during necking. Similar mesh strategies have been commonly used since the work of Tvergaard and Needleman [19]. Although this technique limits excessive distortion, it cannot fully prevent it; therefore, simulation results were stored in the database only up to configurations where element distortion remained acceptable. Finally, elements of the central section of the specimen were assigned a slight reduction in mechanical strength to trigger necking at that location. It was verified that this numerical expedient did not affect the overall results. Alternatively, an equivalent effect could be obtained by introducing a small geometric imperfection instead of locally reducing the material strength [19-21].

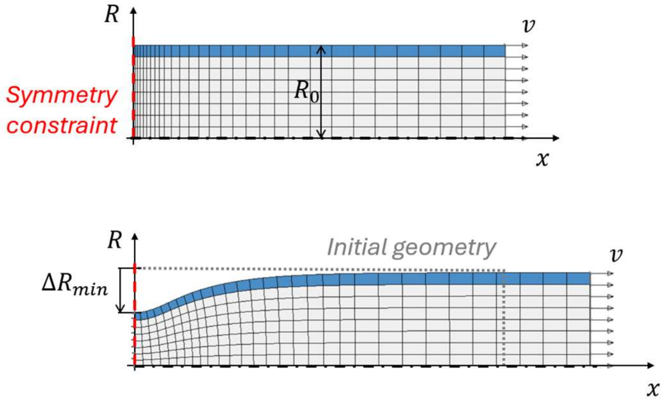

Figure 2.9 FE model used for building the database; elements on the outer surface, from which local quantities are extracted, are highlighted in blue. [12]

Regarding the specimen geometry, a cylindrical slender bar ($L_0/D_0 = 4$), rather than a dog-bone specimen, was used, as observable from Figure 2.9. This limited boundaries effect on the neck deformed shape and, hence, aimed to improve the generality of the method. As a result, the database could be applied to dog-bone specimens with different aspect-ratios L_0/D_0 provided that the gauge length is sufficiently long to allow necking to develop undisturbed from the fillets. A detailed analysis of this aspect will be presented in Section 3.3. The diameter of the slender bar was arbitrarily set to 3 mm since, as discussed in Section 2.2, the shape-law correlation is independent of the absolute size of the specimen.

The specimen was modeled only for half of its length by applying a symmetry constraint at the central section (highlighted with a dashed red line in Figure 2.9). Conversely, a prescribed speed v was imposed at the specimen end for generating the tensile load. Since an explicit solver was used, it was verified that the prescribed motion, consisting of a smoothly varying curve, did not introduce inertial effects. In practice, the highest speed that did not generate inertial effects was chosen. Its specific value had no influence on the results because rate insensitive materials were used.

This choice was motivated by the fact that, as explained in Section 2.1, a $\sigma_{eq}(\varepsilon_{eq,p})$ curve could represent the material response either instantaneously or, in some cases, even completely, despite the material dependence on additional internal variables beyond the equivalent plastic strain. Consequently, when building the database, it was not necessary to account for all internal variables that can possibly govern plastic deformation. Instead, it was sufficient to explore different dependencies on the equivalent plastic strain. Moreover, the observation that scaled laws lead to analogous results allowed the size of the database to be further reduced. Accordingly, the FE models used to build the database differed from one another only in the normalized $\hat{\sigma}_{eq}(\varepsilon_{eq,p})$ laws given as input.

For ensuring a sufficient variety of material responses, linear, power-law, and saturating constitutive models were adopted and implemented through specific LS-DYNA material models. Non-monotonically increasing laws were also included, as they are essential to capture softening phenomena, such as those induced by thermal effects. For each model, the corresponding parameters varied across simulations to populate the database. The parameterization was carried out carefully, taking into account that scaled constitutive laws would be redundant. For instance, considering the family of power-law hardening curves $\sigma_{eq} = K\varepsilon_{eq,pl}^{N}$, the different responses were obtained simply by varying the hardening exponent N. This was enough to obtain all relevant shapes of the post-necking flow curve. For what the strength coefficient K is concerned, its specific value is not meaningful, provided that the ratio K/E, being E the Young's modulus, lies in the typical range for metals.

Other material properties of the FE model used to build the database have a secondary effect on the post-necking behavior when compared to the hardening law. This is the case of material density, which did not influence the results since inertial effects were carefully avoided; it was therefore assigned a representative value for metals. Regarding elastic properties, such as Young's modulus and Poisson's ratio, they were fixed at predefined values too. This choice is justified by the fact that elastic deformations are two to three orders of magnitude smaller than the plastic deformations reached during the post-necking phase.

To sum up, all simulations shared the same FE model in terms of geometry, boundary conditions, mesh and base material properties, while the plastic constitutive law varied across the database. Some choices adopted in building the database inherently limit its applicability in certain situations. For instance, since inertial effects were avoided, the present database cannot be directly applied to tests where inertia plays a significant role, because it cannot distinguish between plasticity and inertial contributions. Regarding specimen geometry, generality was pursued by using a cylindrical bar; therefore, cases in which the specimen aspect-ratio is too small to prevent the influence of the fillets cannot be addressed. Finally, all materials included in the database are isotropic and follow a von Mises yield criterion; hence, the same assumptions must hold for the materials to which the present database is applied. Nevertheless, these limitations do not necessarily imply that the database-driven approach cannot be extended to other geometries or yield models, possibly including anisotropic ones. In principle, the approach is relatively simple, being a "brute-force search" algorithm. Hence, extending the approach to other cases would be possible by constructing an adequate database, but the main challenge would lie in reasoning as in Sections 2.1 and 2.2. That line of thinking is fundamental for understanding whether and how the size of the database can be reduced without losing the capability to represent a wide range of material behaviors.

Apart from the scenarios mentioned above, the resulting database proved flexible enough to represent a wide range of plastic behaviors. This will be shown in Chapter 3, 4, and 5 with its successful application to different strain-hardening behaviors, as well as strain rate and temperature sensitivities. It should, indeed, be noted that only the post-necking portion of the FE models is intended to represent the post-necking behavior of the analyzed material. Therefore, although specific material models were employed for building the database, the post-necking response would be representative also of materials whose pre-necking behavior is not consistent with the selected constitutive formulation. Moreover, when needed the database could be enriched with additional material laws without increasing the complexity of the proposed methodology.

References

[1] Majzoobi, G. H., Khosroshahi, S. F. Z., & Mohammadloo, H. B. (2010). Determination of materials parameters under dynamic loading: Part II: Optimization. *Computational Materials Science*, *49*(2), 201-208.

[2] Majzoobi, G. H., Fariba, F., Pipelzadeh, M. K., & Hardy, S. J. (2015). A new approach for the correction of stress–strain curves after necking in metals. *The Journal of Strain Analysis for Engineering Design*, *50*(2), 125-137.

[3] Almasi, A. R. P., Fariba, F., & Rasoli, S. (2015). Modifying stress-strain curves using optimization and finite elements simulation methods. *Journal of Solid Mechanics*, *7*(1), 71-82.

[4] Peroni, L., Scapin, M., & Fichera, C. (2015, June). An advanced identification procedure for material model parameters based on image analysis. In *10th European LS-DYNA Conference in Würzburg (Germany)*.

[5] Scapin, M., Peroni, L., & Carra, F. (2016). Investigation and mechanical modelling of pure molybdenum at high strain-rate and temperature. *Journal of Dynamic Behavior of Materials*, *2*(4), 460-475.

[6] Peroni, L., & Scapin, M. (2018). Strength model evaluation based on experimental measurements of necking profile in ductile metals. In *EPJ Web of Conferences* (Vol. 183, p. 01015). EDP Sciences.

[7] Scapin, M., Peroni, L., Torregrosa, C., Perillo-Marcone, A., & Calviani, M. (2019). Effect of strain-rate and temperature on mechanical response of pure tungsten. *Journal of Dynamic Behavior of Materials*, *5*(3), 296-308.

[8] Beltramo, M., Scapin, M., & Peroni, L. (2023). An advanced post-necking analysis methodology for elasto-plastic material models identification. *Materials & Design*, *230*, 111937.

[9] Zhang, H., Gao, T., Xu, C., Wu, Q., Song, H., & Huang, G. (2025). Identification of hardening and fracture behaviors of titanium alloy by a hybrid digital image correlation and finite element method. *Optics & Laser Technology*, *181*, 111869.

[10] Beltramo, M., Scapin, M., & Peroni, L. (2024). An efficient shape-based procedure for strain-hardening identification in the post-necking phase. *Mechanics of Materials*, *196*, 105066.

[11] Scapin, M., & Beltramo, M. (2024). A Methodology for Post-Necking Analysis in Isotropic Metals. *Metals*, *14*(5), 593.

[12] Beltramo, M., Peroni, L., & Scapin, M. (2025). A data-driven procedure for the analysis of high strain rate tensile tests via visible and infrared image processing. *International Journal of Impact Engineering*, *199*, 105232.

[13] Le Roy, G., Embury, J. D., Edwards, G., & Ashby, M. F. (1981). A model of ductile fracture based on the nucleation and growth of voids. *Acta Metallurgica*, *29*(8), 1509-1522.

[14] Lu, F., Mánik, T., & Holmedal, B. (2021). Stress corrections after necking using a two-parameter equation for the radius of curvature. *Journal of Applied Mechanics*, *88*(6), 061006.

[15] Mirone, G. (2004). A new model for the elastoplastic characterization and the stress–strain determination on the necking section of a tensile specimen. *International Journal of Solids and Structures*, *41*(13), 3545-3564.

[16] Rösler, J., Harders, H., & Bäker, M. (2007). *Mechanical behaviour of engineering materials: metals, ceramics, polymers, and composites*. Springer Science & Business Media.

[17] Bridgman, P.W. (1952). Studies in large plastic flow and fracture. Metallurgy and metallurgical engineering series. *McGraw Hill, New York.*

[18] Beltramo, M., Scapin, M., & Peroni, L. (2025). Analysis of the work-to-heat conversion beyond the necking onset in non-isothermal tensile tests. *International Journal of Impact Engineering*, 105503.

[19] Tvergaard, V., & Needleman, A. (1984). Analysis of the cup-cone fracture in a round tensile bar. *Acta metallurgica*, *32*(1), 157-169.

[20] Zhang, Z. L., Hauge, M., Ødegård, J., & Thaulow, C. (1999). Determining material true stress–strain curve from tensile specimens with rectangular cross-section. *International Journal of Solids and Structures*, *36*(23), 3497-3516.

[21] Roy, B. K., Korkolis, Y. P., Arai, Y., Araki, W., Iijima, T., & Kouyama, J. (2022). Plastic deformation of AA6061-T6 at elevated temperatures:

Experiments and modeling. *International Journal of Mechanical Sciences*, *216*, 106943.

Chapter 3

Strain rate insensitive materials

This chapter presents a post-necking characterization method that relies on the database-driven approach of Section 2.3 for exploiting the shape-law correlation of materials and/or conditions where the $\sigma_{eq}(\varepsilon_{eq,p})$ curve fully describes the material response. As stated in Section 2.1, this category includes cases with strain dependence only, but also cases in which other relevant variables remain constant during testing or are univocally linked to the equivalent plastic strain.

In such cases, as deeply discussed in Section 2.1, a single highly deformed necking configuration is representative of the entire post-necking response in the $\sigma_{eq} - \varepsilon_{eq,p}$ plane. More specifically, the normalized necking shape is linked just to the normalized post-necking hardening law. This means that the geometrical shape allows the normalized post-necking hardening law $\hat{\sigma}_{eq}^{N}(\varepsilon_{eq,p})$ to be identified, whereas information on the force is needed for determining the absolute stress values. In brief, the proposed method consists of a "brute-force search" within a precomputed library of FE analysis of the numerical shape which best matches the experimental one, regardless of the absolute size. The post-necking hardening law that led to the best numerical shape is known and is then properly adjusted to reconstruct the post-necking hardening law of the material under investigation.

The analyses developed in this chapter have been partially published in [1]. In Section 3.1 the identification procedure is first explained. Then, its capability of dealing with thermal sensitivity is investigated in Section 3.2. Sections 3.3 and 3.4 numerically evaluate how different sources of error can affect the results. Finally, the experimental application is illustrated with different case studies in Section 3.5.

3.1 Identification procedure

This section focuses on the procedure for characterizing the post-necking domain in the testing scenarios introduced above. As anticipated, the experimental data required is the force history (or part of it) and one highly deformed necking silhouette. The identification procedure is composed of two main steps: searching the database for the best-matching numerical shape and modifying the corresponding law to obtain the experimental one.

1) The algorithm searches the FE library for the best-matching numerical silhouette, i.e., the profile that most closely fits the experimental one when adopting a proper viewpoint. This requires removing the effect of absolute specimen size, which manifests as different radii at the necking onset, as explained in Section 2.2. However, determining such quantities may introduce unavoidable uncertainties, since necking onset can be difficult to identify precisely. Hence, the experimental silhouette is taken as reference, and all silhouettes in the database are optimally scaled to minimize the difference with the experimental profile itself.
   Being (x_{db}, R_{db}) the data couples representing a generic silhouette stored in the database, the optimized scaling coefficient k_g leads to a modified silhouette (x'_{db}, R'_{db}), with $R'_{db} = R_{db}/k_g$ and $x'_{db} = x_{db}/k_g$. The experimental profile (x_{exp}, R_{exp}) is, then, interpolated on x'_{db} and the distance δ between the resulting radii and R'_{db} is evaluated as Euclidean norm. Actually, the axial portion considered for computing δ is limited to the specimen gauge length (or even less). Otherwise, the fact that the database specimens are cylindrical bars, while experimental ones have a dog-bone geometry would affect the results.
   This procedure is repeated for each profile stored in the database and the one characterized by the smallest distance is selected. The corresponding scaling coefficient accounts for the different radii at the necking onset. Figure 3.1 qualitatively shows the experimental shape with a solid dark line and the selected numerical shape with a lighter color both before and after scaling (solid and dashed lines respectively).

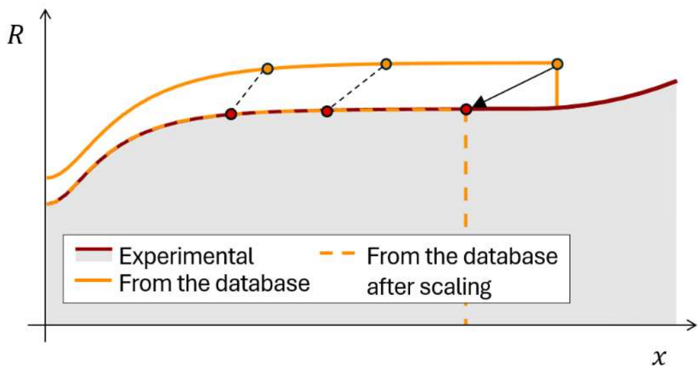

Figure 3.1 Scaling of the numerical profile to be comparable with the experimental one. [2]

2) Thanks to the shape-law correlation, once a numerical shape close enough to the experimental one has been found, then the post-necking law of the real material is well-represented by the post-necking law that led to the selected

numerical shape. This is valid in terms of normalized post-necking hardening law, i.e., $\hat{\sigma}^N_{eq,exp}(\varepsilon_{eq,p} - \varepsilon_{eq,n,exp}) \equiv \hat{\sigma}^N_{eq,db}(\varepsilon_{eq,p} - \varepsilon_{eq,n,db})$.

For obtaining $\sigma^N_{eq,exp}(\varepsilon_{eq,p})$, it is necessary to compensate for the different necking onset and stress scale, as described hereinafter in sub-steps I and II respectively.

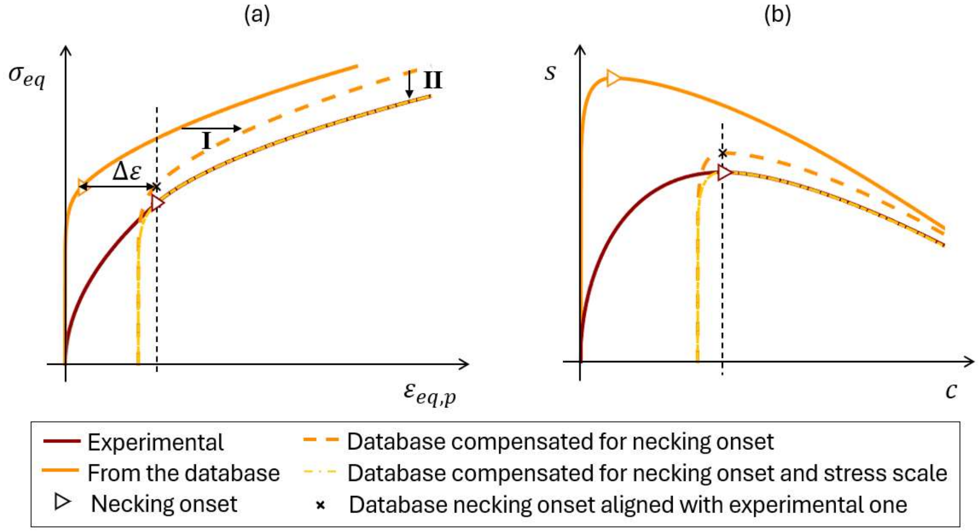

Figure 3.2 Operations performed on the numerical hardening law (a) and the radial engineering curve (b) to identify the unknown post-necking hardening law of the investigated material. [2]

I) Due to the above-mentioned difficulty in identifying the necking onset precisely, the law shift $\Delta\varepsilon = \varepsilon_{eq,n,exp} - \varepsilon_{eq,n,db}$ can be obtained by considering the scaling coefficient k_g determined in Step 1. Indeed, Section 2.2 establishes the following relationship:

$$k_g = \frac{R_{0,db}}{R_{0,exp}} e^{\frac{\varepsilon_{eq,n,exp} - \varepsilon_{eq,n,db}}{2}}, \tag{3.1}$$

from which it results that:

$$\varepsilon_{eq,n,exp} - \varepsilon_{eq,n,db} = 2\ln\left(k_g \frac{R_{0,exp}}{R_{0,db}}\right). \tag{3.2}$$

Hence, by knowing the difference in the initial size of the specimens and having determined k_g in Step 1, the hardening law from the database can be properly shifted. Referring to Figure 3.2a, the solid light-colored line is the law identified from the database, while the dashed line represents its horizontal translation.

II) For determining the stress scale, the experimental forces are compared with the numerical ones of the selected simulation. For meaningful comparison the radial engineering curve of the simulation $s_{db}(c_{db})$ is modified accordingly to the expressions (derived in Section 2.2):

$$c'_{db} = 1 - (1 - c_{db})\frac{1 - c_{n,exp}}{1 - c_{n,db}}, \tag{3.3}$$

$$s'_{db} = s_{db}\left(\frac{1-c_{n,exp}}{1-c_{n,db}}\right)^2, \tag{3.4}$$

being $c_{n,exp}$ and $c_{n,db}$ the radial engineering strains at the necking onset for the experiment and the selected simulation respectively. As done in sub-step I, it is possible to exploit the scaling coefficient k_g by using the following relationships (derived again in Section 2.2):

$$c'_{db} = 1 - \frac{1}{k_g}(1 - c_{db})\frac{R_{0,db}}{R_{0,exp}}, \tag{3.5}$$

$$s'_{db} = \frac{s_{db}}{k_g^2}\left(\frac{R_{0,db}}{R_{0,exp}}\right)^2. \tag{3.6}$$

The modified engineering stresses s'_{db} are now directly comparable to the experimental ones s_{exp}. This allows the stress coefficient k_σ to be determined as average of the ratio s_{exp}/s'_{db} over a certain surrounding of the configuration considered. The hardening law of the database, already shifted, can be scaled in stress for k_σ, thus reconstructing the post-necking law of the material under investigation.

Operations on the radial engineering curve are qualitatively shown in Figure 3.2b. The solid light-colored line represents $s_{db}(c_{db})$, while the dashed light-colored line represents $s'_{db}(c'_{db})$, i.e., the curve modified to account for the different necking onset. The latter is the one directly comparable to the experimental response $s_{exp}(c_{exp})$, represented with a solid dark line. Finally, the stress scale k_σ is applied to $s'_{db}(c'_{db})$ and the shifted hardening law, leading to the dash-dot lines of Figure 3.2a and b respectively.

It is important to underline that the experimental curve displayed in Figure 3.2a is unknown *a priori* and represents the result of the procedure.

The post-necking hardening law obtained with the above process should then be properly joined with the pre-necking law determined through analytical formulas. Transition between the two laws can be set in correspondence of the maximum load, neglecting the delay of the bifurcation with respect to instability [3]. Figure 3.3 schematizes the entire procedure in a flowchart.

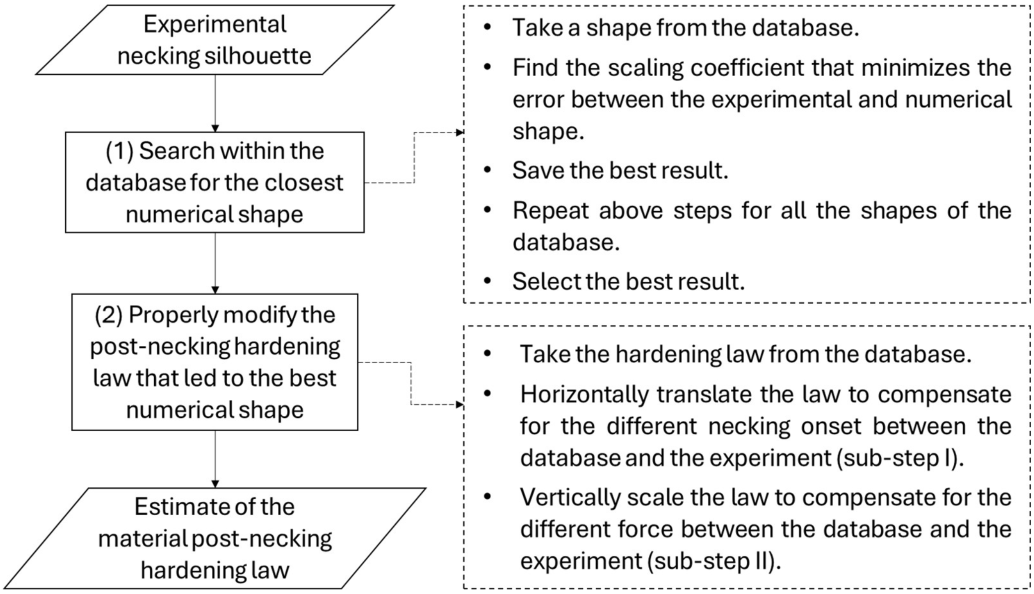

Figure 3.3 Workflow of the identification process for strain rate insensitive materials. [2]

3.2 Thermal sensitivity

The identification procedure described above can be applied to the entire family of plastic behaviors analyzed in the present chapter. This includes cases in which plasticity is governed by the equivalent plastic strain and by additional internal variables q that either remain constant during testing or are uniquely associated with the equivalent plastic strain. An example of these variables is represented by temperature in isothermal and adiabatic tests.

Isothermal conditions are satisfied in quasi-static tests as the low strain rates allow heat generated by plastic deformation to dissipate, and thus temperature remains constant during testing. When tested at non-standard temperatures, materials exhibit strain-hardening rates that may differ from standard conditions. More specifically, due to thermally activated mechanisms of deformation, higher temperatures generally reduce the strain-hardening rate. Since the equivalent plastic strain is the only variable affecting plasticity that changes during testing, then a single necking profile still reflects the material's response under the given conditions and the identification procedure explained in Section 3.1 can be applied.

Adiabatic conditions occur, instead, at strain rates sufficiently high to prevent dissipation of the heat generated by plastic work. In these cases, heat remains within the material, leading to an increase in temperature, which in turn affects the material response, generally through thermal softening. Demonstrating that, under these conditions, a single necking configuration is enough for identifying the material response in the $\sigma_{eq} - \varepsilon_{eq,p}$ plane, requires proving that all material points follow the same path. Consider the thermo-mechanical law governing self-heating under adiabatic conditions for a monotonic loading history, the infinitesimal temperature increment is given by:

$$dT = \frac{\beta}{\rho c_p}\sigma_{eq}\left(\varepsilon_{eq,p},T\right)d\varepsilon_{eq,p}, \tag{3.7}$$

being β the work-to-heat coefficient, also known as Taylor-Quinney coefficient, ρ the density and c_p the specific heat. In this phase, for the sake of simplicity, these coefficients are considered constant.

Writing Equation 3.7 in the following form:

$$\frac{dT}{d\varepsilon_{eq,p}} = \frac{\beta}{\rho c_p}\sigma_{eq}\left(\varepsilon_{eq,p},T\right) \tag{3.8}$$

makes it evident that it is an ordinary differential equation (ODE). Assuming that the temperature at zero strain, i.e. at the beginning of the test, is known, the above expression defines an initial value problem, or Cauchy problem. According to the global existence and uniqueness theorem for Cauchy problems, if the plastic flow law is continuous, locally Lipschitz continuous in T, uniformly in $\varepsilon_{eq,p}$, and sublinear (i.e., it has at most linear growth in T), then the solution exists and it is unique. For the physical mechanisms governing plastic deformation in metals (see, for example, MTS-type models [4]), the plastic flow law satisfies these conditions (in particular, it is Lipschitz continuous because it is continuously differentiable). Therefore, the relationship between equivalent plastic strain and temperature is unique. Material points that at different times experience the same equivalent plastic strain are also characterized by the same temperature and, consequently, by the same equivalent stress. Hence, all material points evolve along the same path in the $\sigma_{eq} - \varepsilon_{eq,p} - T$ space, and therefore also along the same path in the projected $\sigma_{eq} - \varepsilon_{eq,p}$ plane. As a result, even in this case, necking geometry reflects the $\sigma_{eq} - \varepsilon_{eq,p}$ path followed by material points. This path can, thus, be identified as described in Section 3.1 and if thermal softening is significant, the resulting curve may become non-monotonically increasing, leading to more pronounced necking than in a perfectly plastic material.

Figure 3.4 considers the two extreme conditions of isothermy and adiabaticity. On subfigure (a) the different paths are qualitatively shown, highlighting the progressive thermal softening occurring in the adiabatic case. In strain rate

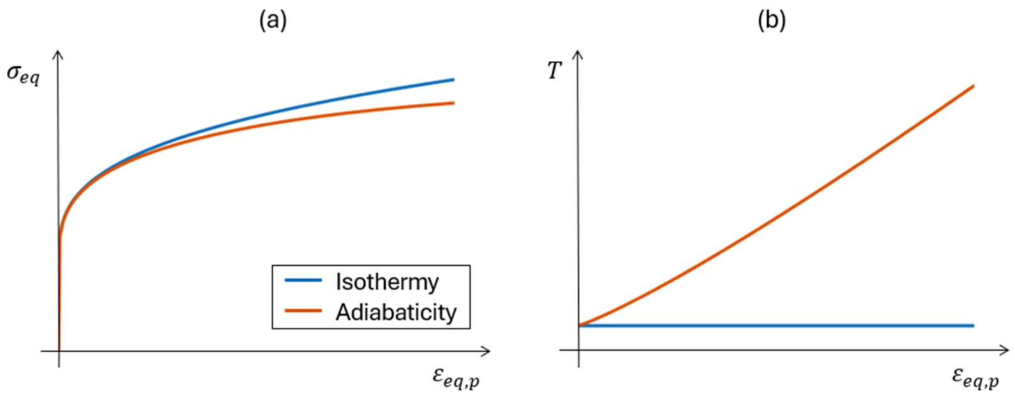

Figure 3.4 Stress-strain (a) and temperature-strain (b) paths for tests under adiabatic or isothermal conditions on a strain rate insensitive material.

insensitive materials, every material point, before being reached by the unloading boundary, follows the same deformation path of the profile center. Thus, the plastic work executed on every material point, until a given equivalent plastic strain (if achieved), coincides. Under the assumption of constant ${}^{\beta}/_{\rho c_p}$ within the test, it results that every point follows also the same temperature vs. equivalent plastic strain paths shown in red in subfigure (b). This is valid even if ${}^{\beta}/_{\rho c_p}$ varies in a way univocally related to equivalent plastic strain. These considerations provide an intuitive explanation of the unique relationship between equivalent plastic strain and temperature in strain rate insensitive materials.

Nevertheless, it is worth noting that, due to such correlation, the identified deformation path intrinsically accounts for thermal effects and distinguishing the contributions of temperature and equivalent plastic strain in a single adiabatic test may be unfeasible if information about isothermal conditions is not available. Nevertheless, this does not represent a limitation of the present approach but a problem that would affect any identification method in these conditions. Hence, the issue of separating different physical contributions affecting plasticity (equivalent plastic strain and temperature in this case) is not addressed in the present chapter which, instead, aims to assess the capability of the proposed identification strategy to determine a law able of reproducing the observed behavior.

3.3 Applying a database of cylinders to dog-bone specimens

The database used for identification was built by simulating tensile tests on cylindrical bars, with the aim of ensuring applicability to experimental specimens characterized by different aspect-ratios. In this section, a numerical study is presented, to investigate the effect of dog-bone geometry on identification. To this aim, tensile tests on dog-bone samples characterized by different aspect-ratios and made of materials with different strain-hardening rates were simulated with Ansys LS-DYNA.

Regarding specimen geometry, reference was made to the sketch shown in Figure 3.5a and five different values of the gauge length L_0 were considered for

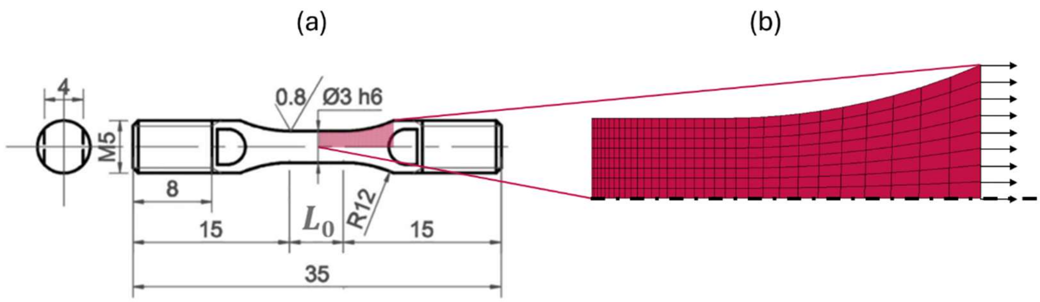

Figure 3.5 Sketch of a cylindrical dog-bone specimen (a) and corresponding FE model (b) (adapted from [1]).

varying the slenderness from a ratio L_0/D_0 of 1 up to a ratio of 7. Specimens were actually modelled up to the end of the fillets, as shown in Figure 3.5b and no strength or dimensional perturbation was necessary to trigger necking in the central cross-section. All other features of the FE model (e.g., boundary conditions, mesh strategy, etc.) were the same described in Section 2.3.

Regarding material hardening, five different behaviors were considered. They were all defined to guarantee necking immediately at yielding so that only post-necking influenced the result of the analysis. The laws are denoted with capital letters and are plotted as black lines in Figure 3.6, each normalized for the stress at the necking onset σ_n.

For each law, five tensile tests were simulated that differed from one another for the ratio L_0/D_0. Each simulation was treated as an experimental test and the post-necking identification procedure described in Section 3.1 was applied.

The gray regions of Figure 3.6 offer a graphical representation of the highest errors made by the proposed identification procedure when applied to the different materials. It can be noted that lower hardening rates are associated with smaller uncertainties. This can be attributed to more localized deformation, which makes the identification less sensitive to the fillets.

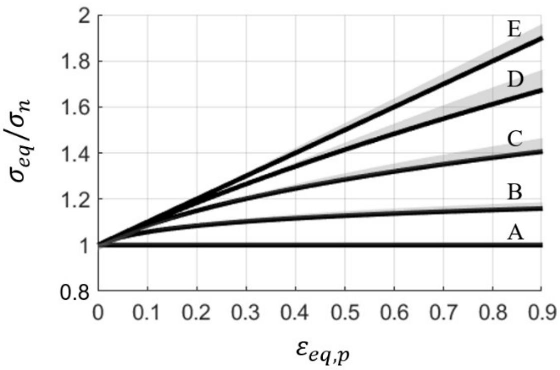

Figure 3.6 Effect of applying a database of cylinders to dog-bone specimens: the gray region represents the highest error made when identifying the corresponding reference law in black. [1]

The error between identified and reference equivalent stress ($\tilde{\sigma}_{eq}$ and σ_{eq} respectively) was quantified, over the strain range shown in Figure 3.6, by computing the Normalized Root-Mean-Square Errors (NRMSE). More specifically, the expression adopted was the following:

$$\mathrm{NRMSE} = \frac{\sqrt{\frac{1}{N}\sum_{i=1}^{N}\left(\tilde{\sigma}_{eq,i}-\sigma_{eq,i}\right)^2}}{\frac{1}{N}\sum_{i=1}^{N}\sigma_{eq,i}} \tag{3.9}$$

Table 3.1 collects this error for all 25 tests analyzed. As expected, the slenderer the specimen, the lower the error on the identified law. Indeed, the boundary effect introduced by dog-bone geometry becomes negligible with specimen slender enough.

Table 3.1 Error of the identified law with respect to the reference one, evaluated as NRMSE (Equation 3.9). [1]

	A	B	C	D	E
$L_0/D_0 = 1$	< 1 %	1.6 %	2.5 %	3.3 %	2.4 %
$L_0/D_0 = 1.5$	< 1 %	1.1 %	1.8 %	2.1 %	1.8 %
$L_0/D_0 = 2$	< 1 %	< 1 %	1.4 %	1.7 %	1.0 %
$L_0/D_0 = 3$	< 1 %	< 1%	< 1 %	1.1 %	< 1 %
$L_0/D_0 = 7$	< 1%	< 1%	< 1 %	< 1%	< 1 %

Even though the acceptable error depends on the engineering application, the results overall demonstrate that a database of cylinders can be effectively used for tests on dog-bone specimens.

3.4 Effect of experimental uncertainties in measuring necking silhouette

Both the specimen deformed shape and the radial engineering strain are essential for the proposed identification strategy. Since they highly depend on the capability of measuring the necking profile, this section presents a numerical investigation into the approach robustness against noisy experimental measurements.

To this aim, noisy profiles were generated by perturbing a reference silhouette selected from the database; in this way other sources of error were not introduced. The perturbation consisted of a uniformly distributed random noise with zero mean and amplitude η. More precisely, four noisy profiles were considered by varying the amplitude η from 10 μm up to 100 μm. An example of reference and noisy profile is depicted in Figure 3.7, but the noisy silhouette could be a random one within the gray region. The identification procedure described in Section 3.1 was applied to each noisy profile, as if they came from experimental measurements. The error made by the identification strategy was computed as NRMSE, according to Equation 3.9 and is reported in the table of Figure 3.7 for the different levels of noise. Considering again that the threshold for error acceptability varies from one engineering application to another, the proposed method appears sufficiently robust. Indeed, the non-physical high-frequency perturbations are automatically filtered when searching the FE library for the best-matching profile. The only exception is represented by the case of 100 μm of noise amplitude, which however corresponds to a very noisy profile (the one shown in Figure 3.7). Such large measurement errors are in practice difficult to obtain if reasonable care is taken during image acquisition.

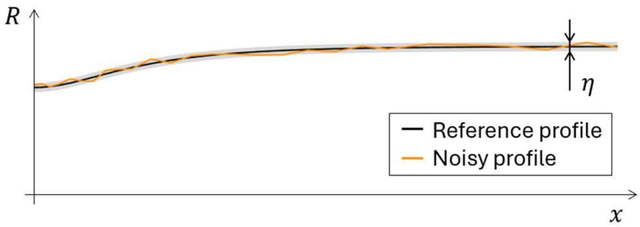

	NRMSE
$\eta = 10\ \mu m$	< 1%
$\eta = 20\ \mu m$	1.4 %
$\eta = 50\ \mu m$	3.7 %
$\eta = 100\ \mu m$	6.7 %

Figure 3.7 Effect of uncertainties in the input profile: graphical example of a noisy profile (a random one within the gray region) and table collecting NRMSEs of the identified laws for different levels of noise. [1]

3.5 Experimental case studies

After demonstrating the method's robustness with respect to different sources of error, the proposed strategy was applied to experimental case studies for highlighting its adaptability to different hardening behaviors.

As anticipated, the family of plastic behaviors analyzed in the present chapter includes cases in which plasticity is governed by the equivalent plastic strain and by additional internal variables q that either remain constant during testing or are uniquely associated with the equivalent plastic strain. Both isothermal and adiabatic tests formally fall within this category, provided that materials can be considered strain rate insensitive over the range of strain rates experienced during the tests. As will be discussed in Chapter 4, strain rate sensitivity alters the loading path followed by material points, hence the problem would no longer belong to the simplified framework considered here. The assumption of rate insensitive material is reasonable for isothermal tests on FCC metals, since their rate sensitivity within a single test is negligible at low strain rates. Conversely, at the high strain rates at which adiabaticity is typically satisfied, even strain rate sensitivity of an FCC metal becomes evident within a single test. Hence, practically, isothermal tests are the main application field for the proposed identification strategy.

Since isothermal tests at non-standard temperatures complicate the experimental setup but not the characterization, which is the focus of this thesis, the experimental case studies presented in this section are limited to room-temperature quasi-static tests. The materials under investigations were pure copper (simply called Cu), aluminum alloy Al6082-T6, and martensitic stainless steel 17-4PH H900. Since the proposed method relies on material isotropy, specimen axial-symmetry was verified with post-mortem analyses. The experimental setup and data analysis are described, followed by results and discussion. For comparison, identification was also carried out using Bridgman's correction and FEMU methods.

3.5.1 Experimental setup and image analysis

Tensile tests were conducted with a standard electromechanical testing machine, Zwick-Z100, at a speed of 0.05 mm/s. Considering that the specimens had a gauge length of 5 mm, this results in a nominal strain rate of 10^{-2} s^{-1}. Specimens were characterized by threaded ends and a gauge diameter of 3 mm, according to the sketch of Figure 3.5a. This is not a standard geometry for quasi-static tests that allows investigating the practical applicability of the proposed identification strategy in a case of limited sample slenderness.

A 100 kN load cell was used for acquiring the force at 10 Hz, while a PixeLINK PL-B777 equipped with a Tokina Macro 100 F2.8 D camera lens was employed for acquiring images at 1 Hz. Load data and images were properly synchronized since a time mismatch could lead to significant errors in the identification.

The imaging setup provided a resolution of 7 µm/px, which the analysis of Section 3.4 suggests being adequate for applying the proposed identification strategy. Since the aim of image acquisition is extracting the specimen silhouette, the camera was focused on the plane on which the profile lied. The fact that this plane reasonably remains fixed during testing means that the measurements did not suffer from loss of focus.

For determining the specimen outer contour, recorded images were post-processed in the programming environment MATLAB. For this purpose, several edge detection algorithms were developed in past research [5-7]. In this thesis, an image segmentation technique based on k-means clustering [8] was used for separating the area of interest from the background. This was done via the MATLAB built-in function “imsegkmeans”. Then, specimen edges were detected; an example of segmented images is shown in Figure 3.8.

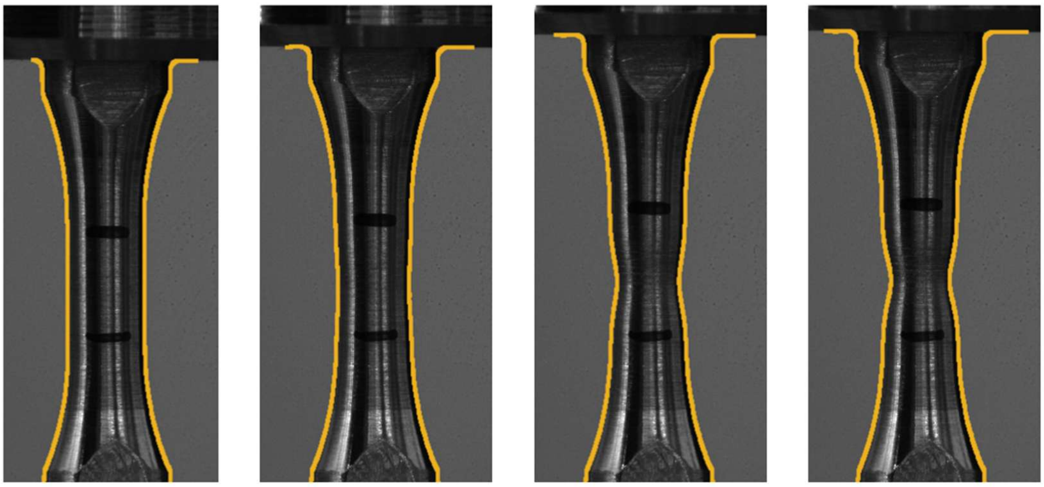

Figure 3.8 Sequence of images, cropped for graphical reasons (test on Al6082-T6), with highlighted the silhouette detection result.

Exploiting the ideal symmetry of the specimen during testing, the silhouettes on the two sides of the longitudinal axis were used to determine the diameter, and hence the radius, as a function of the axial coordinate. Theoretically, this must be done by measuring the distance of the edges along a direction normal to the longitudinal axis of the specimen. This is straightforward if the longitudinal axis is aligned with one of the image axes, otherwise the tilt angle needs to be determined.

With reference to Figure 3.8, denote the two edges as $X_1(Y)$ and $X_2(Y)$. A first estimate of the axis $X_{axis}^{tmp}(Y)$ can be found as linear fit of the average of $X_1(Y)$ and $X_2(Y)$. This raw estimate can be improved to $X_{axis}(Y)$ by minimizing the difference between $\|X_1 - X_{axis}\|_2$ and $\|X_2 - X_{axis}\|_2$ (being $\|X_i - X_{axis}\|_2$ the distance between X_i and X_{axis} along the direction normal to X_{axis}). This means finding the axis that ensures the maximum symmetry between the two edges. Considering $X_{axis}^{tmp}(Y)$ instead of $X_{axis}(Y)$ introduces an error of $\cos\theta$, which can be considered acceptable if the longitudinal axis is only slightly tilted with respect to the image axis (y-axis with reference to Figure 3.8).

In the present analysis, despite the small tilt angles, the rigorous approach was applied with the aim of limiting as much as possible the uncertainties in specimen silhouette determination.

Once the radius as a function of the axial coordinate was obtained, measurements were further averaged for minimizing the noise. Before the necking onset, the silhouettes were used to determine an average radius over the entire gauge length. Conversely, each silhouette during necking was used to determine an average semi-profile, by taking advantage of the theoretical symmetry at the two sides of the neck. The position of the symmetry axis was identified by minimizing the difference between the radii of corresponding points on the two sides of the axis itself.

3.5.2 Data analysis

This section explains how acquired and post-processed data was used to determine the strain-hardening law of the materials under investigation.

The area-based approach presented in Section 1.2.1 was used for pre-necking identification. The equations used (i.e., Equations 1.4 and 1.8) are rewritten here explicitly for the case of round cross-sections:

$$\sigma_t = \frac{F}{\pi R_{avg}^2}, \quad \varepsilon_t = 2\ln\left(\frac{R_0}{R_{avg}}\right). \tag{3.10}$$

R_{avg} stands for the current radius of the specimen determined by averaging over the gauge length, as anticipated. Before the necking onset, true strain and true stress are known to coincide with equivalent variables σ_{eq} and ε_{eq}. Hence, the plastic flow curve during uniform deformation can be straightforwardly identified.

Conversely, for comparative purposes, post-necking behavior was determined by applying different strategies. As none of them explicitly account for ductile damage, preliminary tests were conducted to guarantee that the present data analysis was limited to a stage of the tests in which void nucleation and coalescence did not significantly affect the mechanical strength [9]. The post-necking identification strategies applied were Bridgman's correction formula [10], the proposed database-driven approach and two FEMU methods. All methodologies exploited the specimen silhouettes obtained through DIA, as detailed hereinafter.

- For applying Bridgman's correction, i.e., Equations 1.12 and 1.14, it was necessary to evaluate the radius and the curvature at the neck at different configurations. To limit the noise, especially in evaluating the curvature, a polynomial function was fitted to each average necking semi-profile (as done in [11, 12] for example). In this way, the unknown radius and curvature at the neck were approximated with those of the fitting polynomial.
- Regarding the proposed database-driven strategy, the procedure described in Section 3.1 was implemented in MATLAB. For applying it, the time history of the radius at the neck $R_{min}(t)$ needed to be considered, as well as one highly deformed necking configuration. The former was obtained from the measured semi-profiles, by applying a moving average filter to reduce the level of noise. The latter was actually represented by an average necking semi-profile $R(x)$, the one to be compared with numerical semi-profiles stored in the FE library. At the time these analyses were carried out, the database included only power-law hardening behaviors. Nevertheless, the satisfactory results shown in Section 3.5.2 indicate that, for the materials considered, such a limited database proved to be acceptable.
- For the two FEMU methods, the required optimization was implemented on the commercial program Ansys LS-OPT. In particular, a metamodel-based optimization was adopted and a sequential strategy with domain reduction was chosen. Regarding the FE model, it was analogous to the one presented in Section 3.3. Strain-hardening was defined as a piecewise linear law (implemented as *MAT_024 in Ansys LS-DYNA), in which the pre-necking phase was analytically computed, while the post-necking phase needed to be identified via optimization. For meaningful comparison with the proposed database-driven approach, the post-necking law was defined as the post-necking part of a power-law hardening model, properly parametrized. By enforcing continuity at the Considère condition for necking onset, it resulted that only one parameter, i.e., the hardening exponent, was needed.
  One of the two FEMU approaches used the radial post-necking engineering curve as target of the optimization. To this aim, the time evolution of the radius at the neck $R_{min}(t)$ was required and was determined as explained in the previous point. The other FEMU approach employed a single average semi-profile (the same used by the proposed method) as target. More details on the implementation of this target can be found in [13].

3.5.3 Results and discussion

The resulting plastic flow curves $\sigma_{eq} - \varepsilon_{eq,p}$ of the three materials analyzed are presented in Figures 3.9-3.11, subfigure (a). When necking did not occur immediately at yielding, i.e., for Al6082-T6 and 17-4PH, Equations 3.10 were used for analytically determining the pre-necking hardening laws, plotted as black solid lines. If the same expressions were applied to the minimum cross-section (see Equations 1.12 and 1.13) beyond the necking onset, the so-called area-based true curves would be obtained. They are shown as black dashed lines which, as expected, soon deviate from all other estimates of the post-necking behavior, since the neglected triaxiality introduces a non-negligible error.

Among the post-necking estimates resulting from the different identification procedures, the laws identified by FEMU approaches can be considered as the most reliable ones, since they are not based on simplifying assumptions that, instead, characterize the database-driven method and Bridgman's correction. Plots displayed in subfigures (b) and (c) of Figures 3.9-3.11 prove the capability of FEMU to replicate experimental results in terms of engineering response and deformation respectively. The first is shown with black dot markers, while the second with black dotted lines. The latter is actually shown via the four semi-profiles that were averaged altogether to obtain the average semi-profile used as

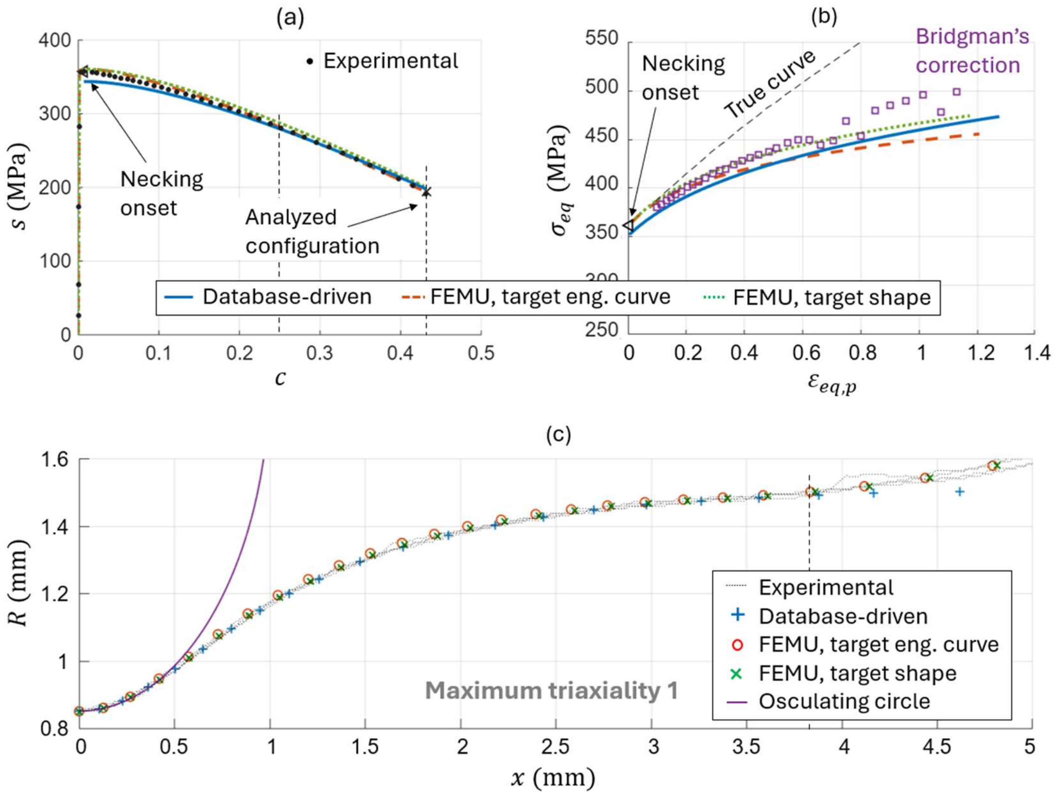

Figure 3.9 Results for Cu: comparison of experimental data and numerical predictions done by different identification strategies, in terms of radial engineering curve (a), area-based true curve and hardening law (b) and specimen profile (c) in comparison with. [1]

target for one of the two FEMU strategies, as well as for the database-driven method and Bridgman's theory. A vertical dashed line indicates the region considered for averaging, highlighting that, within such portion, it is reasonable to consider a unique semi-profile given the small discrepancy between the four. Regarding FE predictions, as observable from subfigures (b) of Figures 3.9-3.11, the FEMU method having the engineering curve as target describes this experimental macroscopic response better than the other method. *Viceversa*, as shown in subfigures (c), the method having the necking semi-profile as target better describes experimental deformation. When analyzing deformed silhouettes, it is useful to compare the markers associated with the two FEMU methods (red circles and green crosses). Since they represent the positions of nodes and the two FE models use the same mesh, their overlap indicates that the identified laws are in good agreement with each other.

Overall, the two FEMU strategies provided very similar results, especially for Al6082-T6 and 17-4PH. The slightly higher difference noticed for Cu can, however, be attributed to the use of a power-law hardening model which may not be the most suitable for representing Cu post-necking behavior. In any case, the hardening laws identified by the two FEMU approaches do not perfectly coincide. Nevertheless, it is not possible to state that one strategy performs better than the other, as discussed in [13] and in Section 2.2. Hence, both laws (red dashed line and green dotted line) are considered for evaluating if the database-driven method,

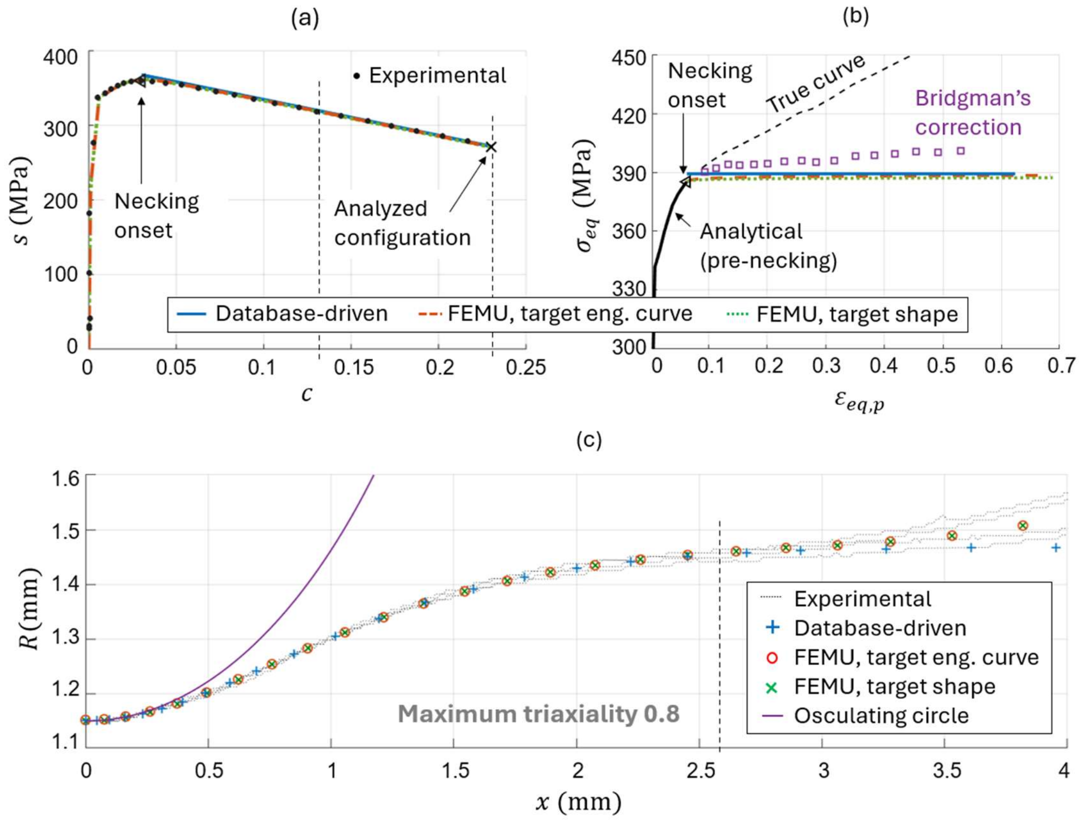

Figure 3.10 Results for Al6082-T6: comparison of experimental data and numerical predictions done by different identification strategies, in terms of radial engineering curve (a), area-based true curve and hardening law (b) and specimen profile (c) in comparison with. [1]

which is far less computationally expensive than FEMU methods, is able to give comparable results.

In subfigures (c) of Figures 3.9-3.11 blue plus markers display the best semi-profiles found in the database, once properly scaled, as explained in Section 3.1, step 1. The vertical dashed line indicates that, when searching the FE library, the specimen shoulders were excluded from the average experimental semi-profile considered as reference. This was done to limit the effects of applying a database built from cylindrical bars on dog-bone specimens. The engineering curves corresponding to the database silhouettes are shown as blue solid lines on subfigures (b), once modified for being comparable with the experimental one in terms of necking onset and stress scale. The vertical dashed lines indicate the region of the curve used to determine the stress coefficient, as explained in Section 3.1, step 2)II. The macroscopic response reconstructed by the database-driven approach is in good agreement with the experimental one, especially for Al6082-T6 and 17-4PH. Conversely, Cu is characterized by a larger discrepancy. This could be attributed to the above-mentioned limitation of having assumed power-law hardening. Finally, the hardening laws identified with the database-driven methodology are plotted in subfigures (a) as blue solid lines. They could then be properly joined with the pre-necking law to guarantee continuity and ensure the monotonically decreasing hardening rate typical of metals. Overall, the discrepancy of the proposed method with respect to FEMU strategies, was found to be 2.5% for

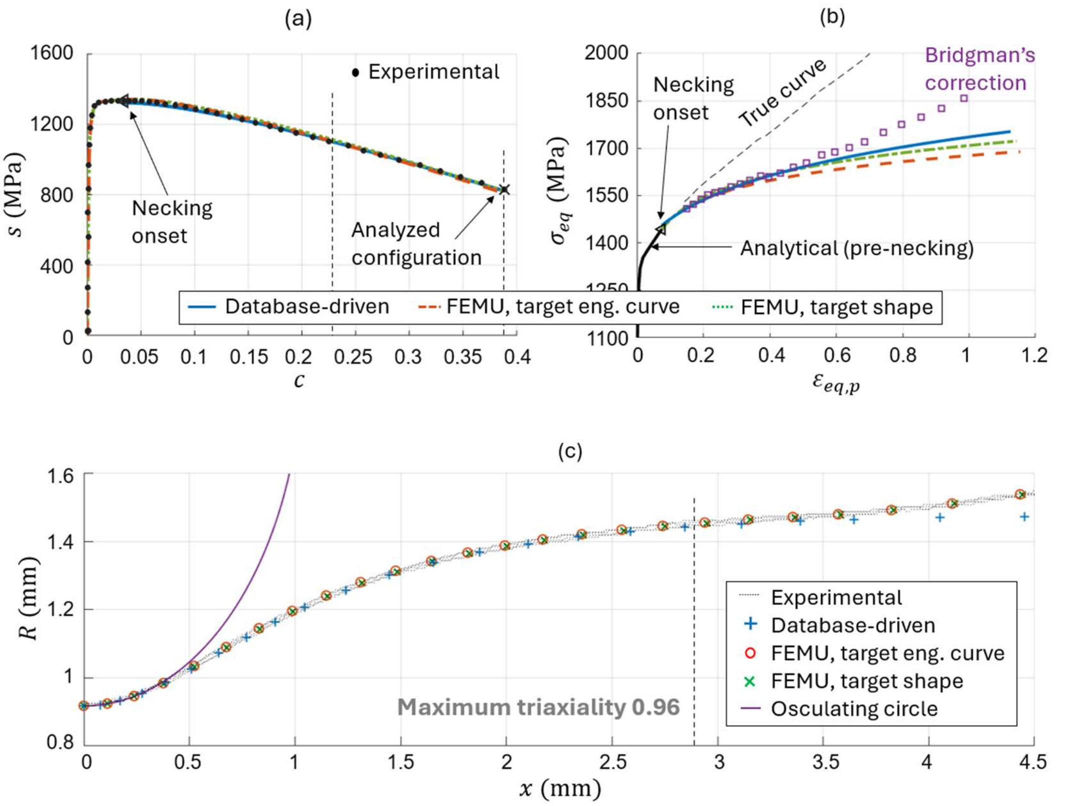

Figure 3.11 Results for 17-4PH: comparison of experimental data and numerical predictions done by different identification strategies, in terms of radial engineering curve (a), area-based true curve and hardening law (b) and specimen profile (c) in comparison with. [1]

Cu, 1% for Al6082-T6, and 2% for 17-4PH (evaluated as NRMSEs on equivalent stress, according to Equation 3.9). These results are consistent with the trend observed in the numerical analysis of Section 3.3, namely that better results are obtained for lower hardening rates.

For comparison purposes, Bridgman's theory was applied too, and the resulting hardening laws are shown on subfigures (a) as purple square markers. This method is as fast as the proposed database-driven approach but relies on simplifying hypotheses about stress and strain fields. The result obtained for Al6082-T6 confirms that Bridgman's correction fails to provide reliable results for materials with low hardening rates [14, 15]. Conversely, the results of Cu and 17-4PH highlight that the correction is good at relatively low post-necking strains, while it introduces an increasing error at larger strains. Moreover, there are some outliers in Bridgman's equivalent stress estimate for Cu. They may be explained by the fact that Bridgman's theory is based on a local evaluation of the silhouette. In the present analysis, the experimental average semi-profiles were fitted with polynomials that then allowed the circles osculating the neck to be determined. The polynomial fitting region was limited to the vertical dashed lines in subfigures (c), and the resulting osculating circles are represented by purple solid lines for the configurations analyzed. Finally, it is well known that the technique used to determine these circles affects the resulting hardening law. In this sense, the database-driven approach takes advantage of not being limited to a local analysis of the necking center.

Before moving on to the final remarks, it is worth explaining why the hardening laws are plotted up to different strains: each law was limited to the maximum equivalent plastic strain $\varepsilon_{eq,p}^{max}$ that can be determined by the respective method. For instance, FEMU approaches also account for internal deformation, hence $\varepsilon_{eq,p}^{max}$ represented the value reached at the center of the specimen. Conversely, the database-driven approach can only determine the equivalent plastic strain at the outer surface of the minimum cross-section, while Bridgman's theory can estimate the average value over the minimum cross-section.

Overall, the results presented here demonstrate that the proposed method aligns well with computationally expensive techniques that do not rely on simplifying geometric hypotheses. At the same time, a comparison with Bridgman's correction, which offers similar computational speed, highlights the benefits of avoiding specific stress and strain field assumptions and of analyzing a broader portion of the profile (rather than focusing solely on the necking center). These considerations are valid for quite different behaviors like those analyzed. Satisfying results were obtained for conventional behaviors (17-4PH) as well as for more peculiar ones (Cu and Al6082-T6). More specifically, Cu reached instability soon after yielding, while Al6082-T6 showed an abrupt change in hardening behavior at the onset of necking, with a sharp reduction in the hardening rate. These two cases clearly illustrate that simply extrapolating the pre-necking hardening law can lead to significant errors in the identified equivalent curve.

Furthermore, it is worth noting that saturating behaviors, such as that observed in the aluminum alloy, can be captured even when using a database constructed from a power-law hardening model. This is possible because only the post-necking part of the power-law model is used to describe the corresponding phase of the analyzed material. Consequently, a hardening exponent approaching zero yields a behavior very similar to that of a saturating law.

Finally, since the characterization process consists of a straightforward search within a precomputed database, the proposed method is much more efficient than FEMU techniques: it requires only a few seconds to determine the plastic flow curve.

3.6 Concluding remarks

This chapter focused on materials and/or conditions where the $\sigma_{eq}(\varepsilon_{eq,p})$ curve fully describes the material response. The objective was to demonstrate that the post-necking phase of this response can be effectively determined using a database of necking profiles. The identification method focuses on a single experimental silhouette and operates by searching the FE database for the hardening law that produced a numerical profile which closely matches the experimental one.

First, numerical analyses were conducted to ensure that acceptable errors are introduced when applying a database built from cylindrical specimens to dog-bone geometries. Then, method's robustness against uncertainties in silhouette measurement was also verified. This result can be explained by the fact that the proposed approach actually interpolates the experimental profile by using curves that represent physically feasible necking shapes. Finally, experimental case studies on materials characterized by different behaviors (in terms of strength, ductility, and hardening rate) were presented. These experiments demonstrated the practical applicability of the proposed method, which maintains a computational effort comparable to analytical strategies, but significantly improves accuracy, approaching that of FEMU methods. Although it was shown that a database built with a power-law hardening model could describe saturating behaviors too, for the analysis conducted in the remainder of this thesis the database was enriched with other constitutive models as explained in Section 2.3.

References

[1] Beltramo, M., Scapin, M., & Peroni, L. (2024). An efficient shape-based procedure for strain-hardening identification in the post-necking phase. *Mechanics of Materials*, *196*, 105066.

[2] Scapin, M., & Beltramo, M. (2024). A Methodology for Post-Necking Analysis in Isotropic Metals. *Metals*, *14*(5), 593.

[3] Hutchinson, J. W., & Miles, J. P. (1974). Bifurcation analysis of the onset of necking in an elastic/plastic cylinder under uniaxial tension. *Journal of the Mechanics and Physics of Solids*, *22*(1), 61-71.

[4] Follansbee, P. S. (2014). *Fundamentals of strength*. Wiley NJ, 10, 9781118808412.

[5] Yu, J. H., McWilliams, B. A., & Kaste, R. P. (2016). Digital image correlation analysis and numerical simulation of aluminum alloys under quasi-static tension after necking using the Bridgman's correction method. *Experimental Techniques*, *40*(5), 1359-1367.

[6] Sancho, A., Cox, M. J., Cartwright, T., Davies, C. M., Hooper, P. A., & Dear, J. P. (2019). An experimental methodology to characterise post-necking behaviour and quantify ductile damage accumulation in isotropic materials. *International Journal of Solids and Structures*, *176*, 191-206.

[7] Lu, F., Mánik, T., Lægreid Andersen, I., & Holmedal, B. (2021). A Robust Image Processing Algorithm for Optical-Based Stress–Strain Curve Corrections after Necking. *Journal of Materials Engineering and Performance*, *30*(6), 4240-4253.

[8] Arthur, D., & Vassilvitskii, S. (2007, January). k-means++: The advantages of careful seeding. In *Proceedings of the SODA '07: Proceedings of the Eighteenth Annual ACM-SIAM Symposium on Discrete Algorithms*, New Orleans, LA, USA, 7–9 January 2007; Volume 7, pp. 1027–1035.

[9] Tvergaard, V., & Needleman, A. (1984). Analysis of the cup-cone fracture in a round tensile bar. *Acta metallurgica*, *32*(1), 157-169.

[10] Bridgman, P.W. (1952). Studies in large plastic flow and fracture. Metallurgy and metallurgical engineering series. *McGraw Hill, New York.*

[11] La Rosa, G., Risitano, A., & Mirone, G. (2003). Postnecking elastoplastic characterization: Degree of approximation in the Bridgman method and properties of the flow-stress/true-stress ratio. *Metallurgical and Materials Transactions A*, 34, 615-624.

[12] Dunnett, T., Balint, D., MacGillivray, H., Church, P., & Gould, P. (2012). Scale effects in necking. In *EPJ Web of Conferences* (Vol. 26, p. 01008). EDP Sciences.

[13] Beltramo, M., Scapin, M., & Peroni, L. (2023). An advanced post-necking analysis methodology for elasto-plastic material models identification. *Materials & Design*, *230*, 111937.

[14] Gromada, M., Mishuris, G., & Öchsner, A. (2011). Correction formulae for the stress distribution in round tensile specimens at neck presence. *Springer Science & Business Media.*

[15] Tu, S., Ren, X., He, J., & Zhang, Z. (2020). Stress–strain curves of metallic materials and post-necking strain-hardening characterization: A

review. *Fatigue & Fracture of Engineering Materials & Structures*, *43*(1), 3-19.

Chapter 4

Strain rate sensitive materials

In this chapter, the focus shifts to material behaviors for which the $\sigma_{eq}(\varepsilon_{eq,p})$ paths followed by material points during necking do not overlap. As stated in Section 2.1, these behaviors are due to internal variables $\tilde{q}$ that affect plasticity but whose variation with the equivalent plastic strain is not unique for all material points.

When a unique path does not exist, a single necking profile is no longer sufficient to identify the post-necking behavior. If the database-driven method were applied as presented in Chapter 3, it would still be possible to identify a $\sigma_{eq}(\varepsilon_{eq,p})$ curve associated with the observed necking shape. However, the dependence on additional variables $\tilde{q}$ causes the strain-hardening rate inferred from a single necking profile to differ from that obtained from the temporal evolution of the test. Hence, the engineering curve associated with that $\sigma_{eq}(\varepsilon_{eq,p})$ law would not approximate the experimental one. This shows that the methodology proposed in Chapter 3 cannot be directly applied since it cannot account for this type of variables $\tilde{q}$. More generally, no identification method that neglects them can reproduce the observed behavior.

Nevertheless, even in these situations, the necking profiles contain information about material behavior; more specifically, about the superficial distributions of equivalent plastic strain, equivalent plastic strain rate, and equivalent stress, as discussed in Section 2.1. When the normalized necking profiles of two materials coincide, one material can be used to instantaneously approximate the other in terms of such distributions. In the remainder of this chapter, "instantaneous approximation" will always refer to such superficial distributions. If the normalized necking profile of the tested material (which is sensitive to variables $\tilde{q}$) coincides with that of a material insensitive to $\tilde{q}$, then the first material can be instantaneously approximated by the second. As a result, the material behavior throughout the test may be approximated as a sequence of different materials insensitive to $\tilde{q}$. This idea can be implemented through the database-driven approach presented in Section 2.3. Briefly, a brute-force search within a precomputed database of FE analysis can be used for associating each necking profile measured experimentally with a $\sigma_{eq}(\varepsilon_{eq,p})$ curve. All the $\sigma_{eq}(\varepsilon_{eq,p})$ curves correspond to the states of superficial material points at different times of the test and represent the projections of curves located in the $\sigma_{eq} - \varepsilon_{eq,p} - \tilde{q}$ space. The method can also be attractive for materials insensitive to these variables since in such cases it provides a set of overlapping curves, thereby adding redundancy to the approach of Chapter 3.

This chapter focuses on the most common variable $\tilde{q}$, namely equivalent plastic strain rate $\dot{\varepsilon}_{eq,p}$. Indeed, due to the deformation mechanisms of metals, their mechanical response does not only depend on strain and temperature, but also on strain rate. Its heterogeneity during necking is caused by the kinematics of the localization itself and may affect the tensile response of a material sufficiently rate sensitive, as detailed in Section 4.1. To isolate the effect of this variable, isothermal testing conditions are considered. This scenario is nevertheless representative of real situations, as it corresponds, for instance, to BCC metals, whose strain rate sensitivity remains significant even at quasi-static strain rates. The identification procedure is detailed in Section 4.2, while Section 4.3 presents two experimental case studies: one involving a strain rate insensitive material and one involving a strain rate sensitive material. The analyses and considerations presented in this chapter have been published partially in [1] and partially in [2].

4.1 Strain rate sensitivity in tensile tests

This section examines the strain rate evolution during tensile testing and the influence of strain rate sensitivity on the material response.

During the pre-necking phase, strain rate in the gauge length can be computed as:

$$\dot{\varepsilon}_{eq} = \frac{1}{L}\frac{dL}{dt} = \frac{v(t)}{L}, \tag{4.1}$$

where v is the speed imposed on the specimen gauge length. As the specimen elongates, the speed applied to the gauge length cannot be precisely controlled, and strain rate cannot be maintained constant. However, it remains uniformly distributed in the gauge length allowing different material points to follow the same evolution in the $\varepsilon_{eq,p} - \dot{\varepsilon}_{eq,p}$ plane. Thus, a unique $\sigma_{eq}(\varepsilon_{eq,p})$ curve, that implicitly accounts for strain rate hardening, represents material behavior during uniform deformation.

In contrast, during necking the central cross-section deforms faster than the surrounding regions and its equivalent plastic strain rate continuously increases, reaching values up to ten times the nominal strain rate of the test [3]. Other material points, after an initial acceleration, undergo deceleration and eventually stop deforming plastically as they return to the elastic domain. This is schematically illustrated in Figure 4.1 through materials points denoted by capital letters from A to E, moving farther from the profile center.

Considering the specimen surface, when a generic material point (e.g., B, C, D

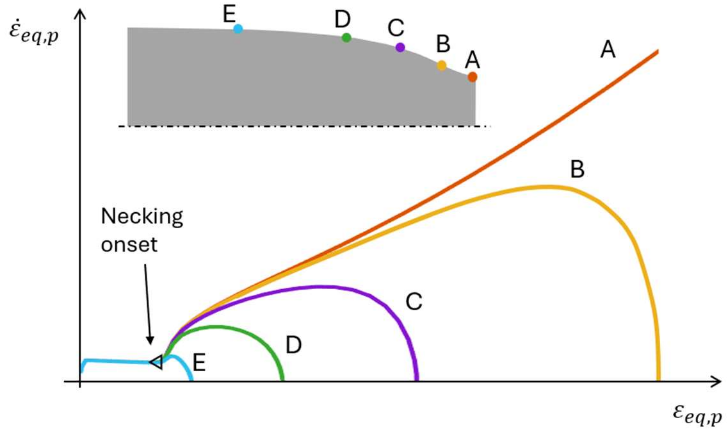

Figure 4.1 Strain rate – strain paths followed during a tensile test by different material points on the specimen surface.

or E) reaches the same equivalent plastic strain previously achieved by the central point (A), it will be characterized by a lower equivalent plastic strain rate than that experienced earlier by the central point. It is, hence, evident that equivalent plastic strain rate is not uniquely associated with equivalent plastic strain. While this heterogeneity has no effect on strain rate insensitive materials, it may affect the response of strain rate sensitive ones.

It is well-known that, under isothermal conditions and in the thermally activated regime, increasing strain rate reduces the possibility for dislocation motion to be activated, causing the material to experience higher stresses at the same strain. During necking, the central point of the silhouette is always characterized by the highest equivalent plastic strain rate, hence when other points achieve the same equivalent plastic strain previously experienced by that central point, they do so at lower stresses. This can be seen on the $\sigma_{eq} - \varepsilon_{eq,p}$ plane as a progressive deviation of the deformation paths followed by different material points with respect to that of the profile center (see Figure 2.4).

Above considerations demonstrate that strain rate sensitive materials belong to the behaviors analyzed in the present chapter for which a unique path on the $\sigma_{eq} - \varepsilon_{eq,p}$ plane cannot be identified. Traditional direct methods would deal with it by following the time evolution at the minimum cross-section (and by averaging over it) via Equation 1.12 for the equivalent plastic strain, Equation 4.1 for the equivalent strain rate and correction formulas for the equivalent stress. Instead, the database-driven approach considers multiple necking configurations, thus providing information about material hardening at different combinations of strain and strain rate. Thanks to the correlation highlighted in Section 2.1, it can determine the equivalent stress experienced by superficial material points at any given configuration, even if the flow curve is unknown yet; Section 4.2 explains in detail how this is implemented.

4.2 Identification procedure

This section focuses on the procedure for characterizing the post-necking domain in the testing scenarios introduced above. As explained in Section 2.1, the outer shape is correlated to the normalized $\hat{\sigma}_{eq} - \varepsilon_{eq,p}$ curve representing the instantaneous state of superficial material points, as well as to the normalized equivalent plastic strain rate distribution $\hat{\dot{\varepsilon}}_{eq,p}(x)$ at that moment on the specimen surface. Hence, the procedure entails, at each time instant t_i, searching the FE database for a necking profile that very closely matches the experimental one in relative shape and over a wide axial region. When the adequate numerical profile is found, its superficial post-necking normalized distributions $\varepsilon_{eq,p}(\hat{x}) - \varepsilon_{eq,p,n}$, $\hat{\dot{\varepsilon}}_{eq,p}(\hat{x})$, $\hat{\sigma}_{eq}(\hat{x})$ well approximate those of the experimental silhouette. This is valid regardless of whether the numerical material model is strain rate sensitive or not; thus, no additional material behavior needs to be included in the database. Finally, estimating the experimental distributions $\varepsilon_{eq,p,exp}(x)$, $\dot{\varepsilon}_{eq,p,exp}(x)$, $\sigma_{eq,exp}(x)$ starting from the numerical ones, i.e., $\varepsilon_{eq,p,db}(x)$, $\dot{\varepsilon}_{eq,p,db}(x)$, $\sigma_{eq,db}(x)$, requires accounting for uniform deformation, test speed and stress scale. Hence, the experimental data required are the engineering curve (or part of it), the speed of radial contraction at the minimum cross-section and multiple necking silhouettes. A detailed explanation of the operations to be carried out at each time of interest is provided hereinafter.

1) The algorithm searches the database for the numerical shape that best matches the experimental one over a wide axial region of the specimen gauge length. The search identifies a database profile (x_{db}, R_{db}) and a scaling coefficient k_g that allow the data couples $(x_{db}/k_g, R_{db}/k_g)$ to overlap with the experimental ones (x_{exp}, R_{exp}). For further details, refer to Section 3.1, since the present operation coincides with Step 1 of that section too. From this perspective, the present strategy can, hence, be conceived as an extension of the method of Chapter 3 to more complex responses.
2) As discussed in Section 2.2, when the numerical and experimental silhouettes are characterized by the same normalized shape, the distributions of post-necking equivalent plastic strain coincide: $\varepsilon_{eq,p,db}(\hat{x}) - \varepsilon_{eq,p,n,db} \equiv \varepsilon_{eq,p,exp}(\hat{x}) - \varepsilon_{eq,p,n,exp}$. Thus, it results that the experimental distribution can be determined as:

$$\varepsilon_{eq,p,exp}(\hat{x}) = \varepsilon_{eq,p,db}(\hat{x}) - \varepsilon_{eq,p,n,db} + \varepsilon_{eq,p,n,exp}. \tag{4.2}$$

By plugging Equation 3.2 into 4.2, it also results that:

$$\varepsilon_{eq,p,exp}(\hat{x}) = \varepsilon_{eq,p,db}(\hat{x}) + 2\ln\left(k_g \frac{R_{0,exp}}{R_{0,db}}\right) \tag{4.3}$$

Since k_g was optimized in the previous step, this latter expression can be useful for determining $\varepsilon_{eq,p,exp}(\hat{x})$ without introducing uncertainties related to identification of the necking onsets.

In practice, the data couples $(x_{db}, \varepsilon_{eq,p,db})$ are modified to $\left(x_{db}/k_g\,, \varepsilon_{eq,p,db} + 2\ln\left(k_g \frac{R_{0,exp}}{R_{0,db}}\right)\right)$, as shown in Figure 4.2, to estimate the experimental $(x_{exp}, \varepsilon_{eq,p,exp})$.

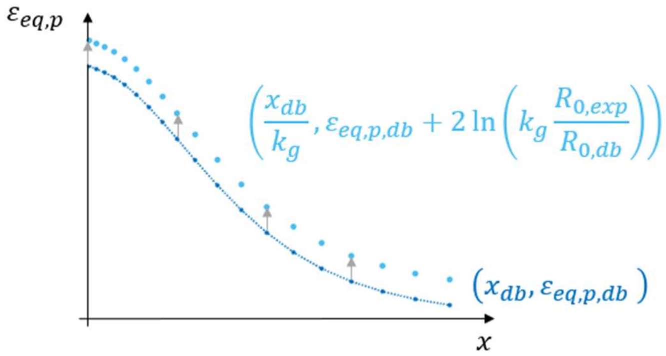

Figure 4.2 Operation performed on the equivalent plastic strain distribution of the database to estimate the experimental one. [2]

3) The database also allows estimating the actual equivalent plastic strain rate. It holds that $\hat{\dot{\varepsilon}}_{eq,p,exp}(\hat{x}) \equiv \hat{\dot{\varepsilon}}_{eq,p,db}(\hat{x})$, where the normalization accounts for both the different specimen sizes at the necking onset and the different speeds at the configuration considered. The latter is actually the speed of radial contraction v_r at the minimum cross-section, computed as time derivative of $R_{min}(t)$. This is consistent with the entire approach that primarily focuses on radial measurements rather than axial ones. Hence, once the geometric coefficient k_g and the instantaneous speeds $v_{r,db}$ and $v_{r,exp}$ are known, $\dot{\varepsilon}_{eq,p,exp}(\hat{x})$ can be determined as:

$$\dot{\varepsilon}_{eq,p,exp}(\hat{x}) = \dot{\varepsilon}_{eq,p,db}(\hat{x}) k_g \frac{v_{r,exp}}{v_{r,db}}. \tag{4.4}$$

Practically, by adjusting the pairs $(x_{db}, \dot{\varepsilon}_{eq,p,db})$ to $(x_{db}/k_g, \dot{\varepsilon}_{eq,p,db} k_g v_{r,exp}/v_{r,db})$, the experimental pairs $(x_{exp}, \dot{\varepsilon}_{eq,p,exp})$ are found, as shown in Figure 4.3.

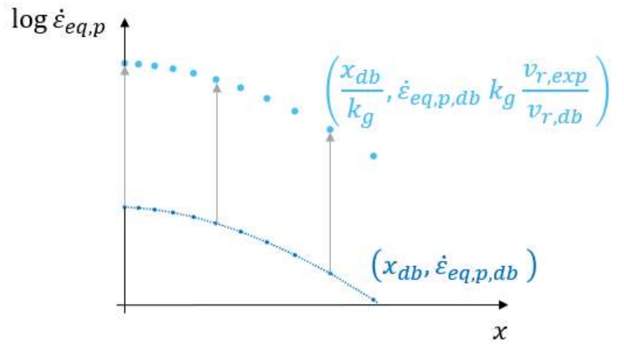

Figure 4.4 Operation performed on the equivalent plastic strain rate distribution of the database to estimate the experimental one. [2]

4) Finally, the experimental distribution of equivalent stress can be estimated from the numerical one by considering the same correction adopted in Section 3.1, Step 2)II. Briefly, a stress coefficient k_σ is determined by proper comparison of the numerical and experimental engineering quantities at the configuration considered. Then, the pairs $(x_{db}, \sigma_{eq,db})$ are modified into $\left(\frac{x_{db}}{k_g}, \sigma_{eq,db} \frac{k_\sigma}{{k_g}^2}\left(\frac{R_{0,db}}{R_{0,exp}}\right)^2\right)$, leading to an estimate of $(x_{exp}, \sigma_{eq,exp})$ as shown in Figure 4.4.

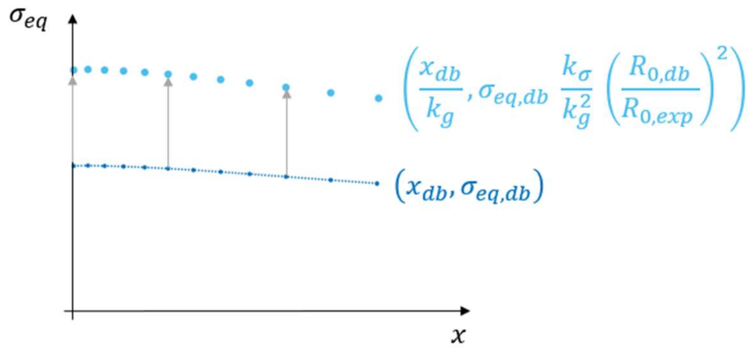

Figure 4.3 Operation performed on the equivalent stress distribution of the database to estimate the experimental one. [2]

To sum up, the output of this procedure is represented by a locus of points in the $\varepsilon_{eq,p} - \dot{\varepsilon}_{eq,p} - \sigma_{eq}$ space, whose projection in the $\sigma_{eq} - \varepsilon_{eq,p}$ plane is expected to be an increasing curve. This is because, at a given configuration, material points characterized by higher equivalent plastic strains are also characterized by higher equivalent plastic strain rates and both equivalent plastic strain and strain rate cause material hardening. The portion of the locus $(\varepsilon_{eq,p}, \dot{\varepsilon}_{eq,p}, \sigma_{eq})$ satisfying the condition $\dot{\varepsilon}_{eq,pl} > 0$ reflects the visco-plastic behavior of the material. This condition, thus, determines the range of equivalent plastic strain $I_\varepsilon = [\varepsilon_{eq,pl}^{min}, \varepsilon_{eq,pl}^{max}]$ over which the shape provides information on material visco-plastic behavior. A subsequent profile would provide information over a range of equivalent plastic strains shifted to higher values. Applying Steps 1 to 4 to multiple necking silhouettes allows the generation of a 3D point cloud and ensures consistent results over a broader strain and strain rate domain. The projection of the 3D point cloud on the $\sigma_{eq} - \varepsilon_{eq,p}$ plane provides qualitative insights on strain rate sensitivity. If the projection is well approximated by a unique curve, then the material can be considered rate insensitive under the tested conditions. Otherwise, this may suggest material dependence on strain rate within the test. The advantage of the proposed method is the capability of efficiently detecting the possible presence of these effects without the need to assume any *a priori* dependence, as would be required with a FEMU approach instead.

Finally, a visco-plastic law for FE simulations can be derived by applying proper data fitting techniques to the 3D point cloud. The entire process is schematically depicted in Figure 4.5.

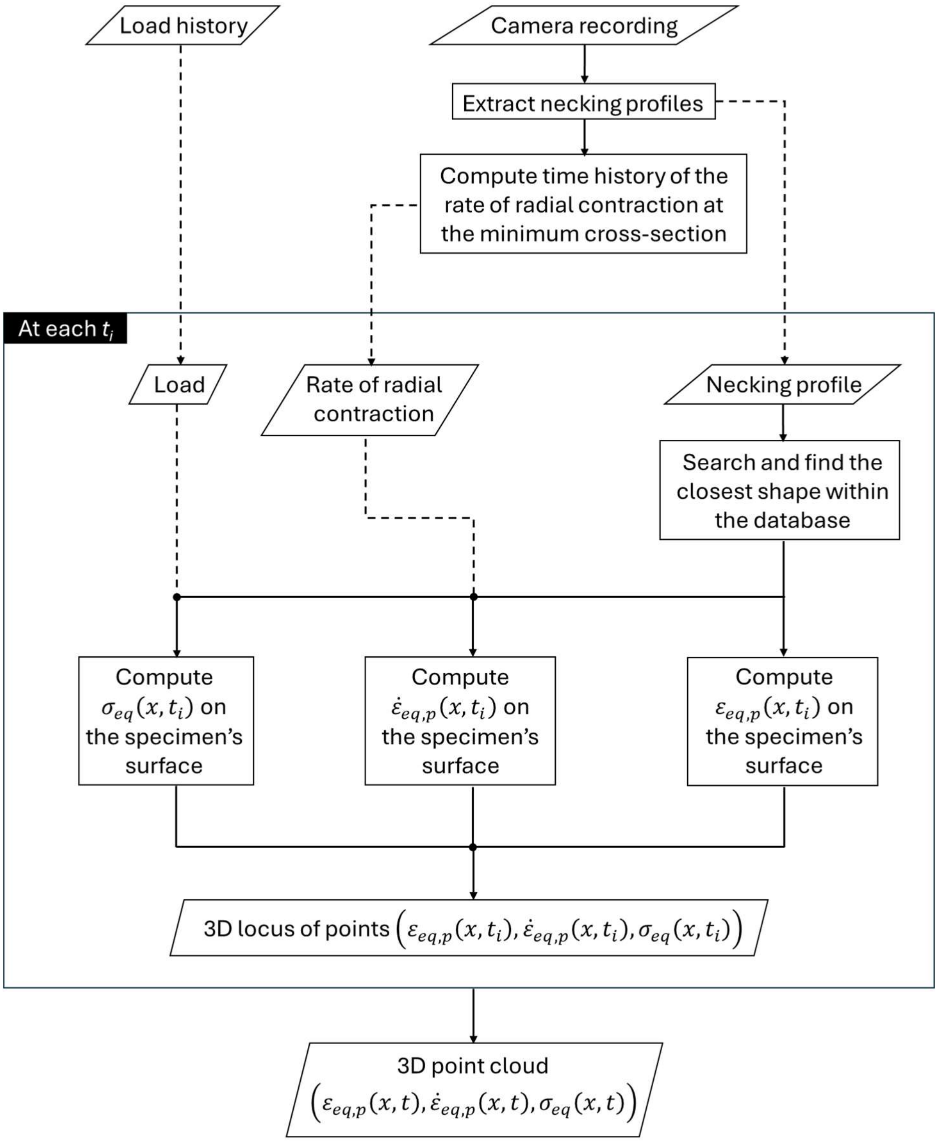

Figure 4.5 Workflow of the identification process for strain rate sensitive materials (adapted from [4]).

4.3 Experimental case studies

After explaining the identification procedure, this section presents the application of the proposed method to two quasi-static tensile tests. The aim is to highlight how the proposed approach can deal with two extreme conditions, i.e., negligible and considerable strain rate sensitivity, under isothermal conditions.

The first case study regards pure copper since it is a well-known and widely studied material [5-7], which exhibits low strain rate sensitivity. Thus, it can be reasonably considered strain rate insensitive within a quasi-static test. The second study is represented by pure molybdenum as it is instead known to be highly sensitive to strain rate [8, 9]. In this case, the strain rate variation and non-uniformity that characterizes necking causes the material response to be affected by the strain rate even within a single test.

In Section 4.3.1 the experimental setup, that the two tests shared, is described. It was very similar to the one described in Section 3.5.1, except for the imaging apparatus, as the present tests offered the opportunity to further refine it. Data analysis is then explained in Section 4.3.2, while the results are reported separately for the two case studies in Sections 4.3.3 and 4.3.4. For comparison, identification was also carried out using analytical corrections and a FEMU strategy. Finally, since all adopted methods rely on the assumption of material isotropy, this hypothesis was verified through post-mortem analyses.

4.3.1 Experimental setup

A standard electromechanical testing machine, Zwick-Z100, was employed for testing the specimens at nominally 10^{-3} s^{-1}. The specimen geometry was the same as in Section 3.5, characterized by a 3 mm gauge diameter and a 5 mm gauge length. A 100 kN load cell acquired the load at 10 Hz, while a high-resolution camera (Opto Engineering ITA81-GM-20C) monitored the specimen deformation at 0.5 Hz. The two acquisitions were properly synchronized.

The main difference with respect to the experimental setup described in Section 3.5.1 is represented by some improvements in the imaging apparatus. Indeed, accurately measuring the profile is essential in all procedures that highly rely on the specimen silhouette. Special care was taken not only regarding resolution but also regarding image distortion and perspective errors. Since these issues typically affect entocentric lenses, which are also the most common ones, telecentric optics were employed in these tests. They are characterized by a constant magnification factor independently of the object's location, thus eliminating perspective effects.

Object-space telecentric lenses are designed to collect only rays parallel to the main opto-mechanical axis, however these rays can still reach the detector from different angles. This introduces some inaccuracies, for instance, by making the system highly sensitive to vignetting, i.e., to the reduction in image brightness at the periphery compared to the center of the image. Ideally, for blurred images, the centroid height of the blur does not change with the object location, but since the system is not image-space telecentric vignetting causes the blur spots to become asymmetric and their centroid to shift from true location. This is why bi-telecentric lenses are preferred. Since they are telecentric in both object and image space, principal rays enter and exit the lenses parallelly to the opt-mechanical axis, thus ensuring the height of the blurred image to be independent of axial object shifts or image plane shifts.

Moreover, since the proposed method does not need to track markers on the specimen surface, images were acquired in backlight so to improve image contrast and accurate edge detection. Backlight configurations represented another reason for employing bi-telecentric lenses. Indeed, in backlighting, all rays that reach the detector are considered as part of the background, but with entocentric optics some rays can actually come from object reflections. This could happen due to the ambient light and the specimen geometry, causing imprecise image segmentation (since some portions of the object would appear as belonging to the background). Telecentric optics significantly limit this issue as reflected rays that can reach the detector are restricted to those parallel to the main axis. To further optimize telecentric effect in backlight configuration, a collimated illuminator was used.

Specifically, for the present tests the optical bench Opto Engineering TCBENCH036, which featured a bi-telecentric lens and a collimated illuminator, was used for installing the camera. As shown in Figure 4.6, this equipment required accurate positioning of the specimen between the camera and the light source.

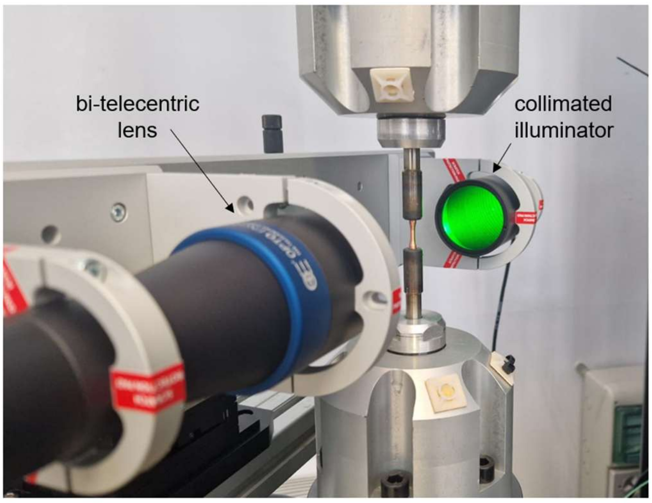

Figure 4.6 Experimental setup with the telecentric optical bench. [1]

As deeply explained above, this imaging setup allowed high contrast images to be obtained with minimum distortion errors and perspective effects. This is the key experimental advancement with respect to the setup adopted in Section 3.5. The improved contrast can be seen from the frames presented in Figure 4.7. Thanks to such higher signal-to-noise ratio, DIA, especially image segmentation, was facilitated. The extracted silhouettes shown in Figure 4.7 were, then, post-processed for obtaining an average semi-profile for each time considered. This was done in the programming environment MATLAB by implementing the same procedure already described in Section 3.5.1.

4.3.2 Data analysis

Data acquired during experiments was analyzed to determine material hardening behavior as described in the present section.

Regarding the pre-necking phase, analytical expressions with an area-based approach were used (see Equations 3.10). This was also the only feasible approach since the traditional length-based one could not be applied since backlight illumination would prevent tracking markers on the specimen surface.

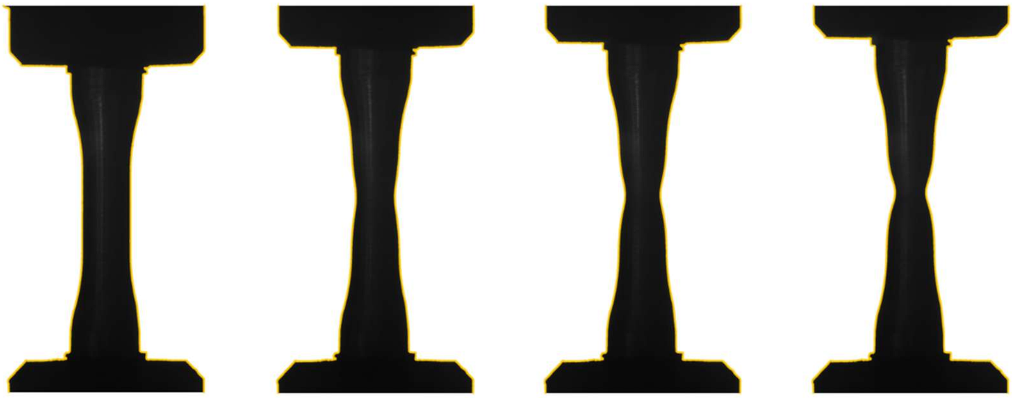

Figure 4.7 Sequence of images acquired with telecentric optics in backlighting, with highlighted the silhouette detection result. [1]

Theoretically, for rate sensitive materials, it would also be necessary to determine the true strain rate history $\dot{\varepsilon}_t(t)$ by computing the time derivative of the true strain. However, due to the well-known logarithmic dependence of flow stress on strain rate in the thermally activated regime, strain rate effects can be considered negligible during pre-necking of a single test. Hence, this phase of the test can be associated with a single equivalent plastic strain rate value.

For the post-necking phase, different approaches were applied: analytical corrections, the proposed database-driven approach, and a FEMU strategy, as detailed in the bullet list. Actually, the tests were not analyzed in their entirety: only the portion sufficiently far from the onset of a significant reduction in mechanical strength was considered to limit the effects of void nucleation and coalescence [10].

- Regarding analytical corrections, Bridgman's [11] and Gromada's [12] formulas were considered. The first was chosen for still being widely used, the second for providing an improvement with respect to the first, while still using local curvature measures. They used Equations 1.14 and 1.15 respectively for estimating the equivalent stress, while they both used Equation 1.12 for the equivalent strain. In both cases, the curvature at the neck was estimated as the curvature of a fourth order polynomial that fits the silhouette region satisfying the condition $2\ln(R_0/R) > \varepsilon_{eq,n}$. This was done to exclude the specimen shoulder from the fitting.
- For the proposed method, several experimental necking configurations were considered, and the procedure described in Section 4.2 was applied (once implemented in MATLAB). At the time these analyses were conducted, the proposed method relied on a database built according to the explanation of Section 2.3. In particular, it contained 1250 sets of parameters able to describe the plastic flow curve $\sigma_{eq} - \varepsilon_{eq,p}$ of metallic materials. When searching the database for the best-matching numerical profile, only the region of the experimental semi-profile satisfying the condition $2\ln(R_0/R) > \varepsilon_{eq,n}$ was considered. This was again done to exclude the specimen shoulder from the analysis.
- For the FEMU approach, a metamodel-based optimization was implemented on Ansys LS-OPT as detailed in Section 3.5.1. The target function was represented by the force at given increments of radial contraction. Regarding FE simulation, the same modeling choices described in Section 3.3 and depicted in Figure 3.5 were adopted. Briefly, a 2D axisymmetric model of half specimen (up to the end of the fillets) with a prescribed motion applied to one end (and a symmetry constraint on the other) was used and the mesh was specifically designed for limiting element distortion during necking. For what the material law is concerned, it was properly parametrized, depending on the model adopted. Further details are provided in the following sections as different models were used in the two case studies.

4.3.3 Results for a rate insensitive material

This section refers to the test conducted on pure copper, which was already known to neck immediately at yielding from Section 3.5. Experimental results are collected in Figure 4.8. Subfigure (a) shows the radial engineering response as a black solid line, whereas some necking silhouettes (indicated in subfigure (a) with black crosses) are displayed in subfigure (b) as black circular markers. Both the engineering curve and the necking shapes clearly show that necking occurred at yielding. Thus, proper strategies were required from the very beginning to identify the hardening law.

Similarly to what was done in Section 3.5, the FEMU approach was first applied, since it can be considered the most reliable strategy. However, differently from Section 3.5, the hardening law was modelled as a piecewise linear function (implemented as *MAT_024 in Ansys LS-DYNA) to ensure a better description of material plastic behavior. The optimization variables were, hence, represented by the slopes of the different intervals. The results of the FE model in terms of engineering curve and necking profiles are displayed in Figure 4.8a and b, as blue dashed lines. They show that the experiment is predicted very well, thus validating the identified hardening law shown in Figure 4.8c (as a blue dashed line).

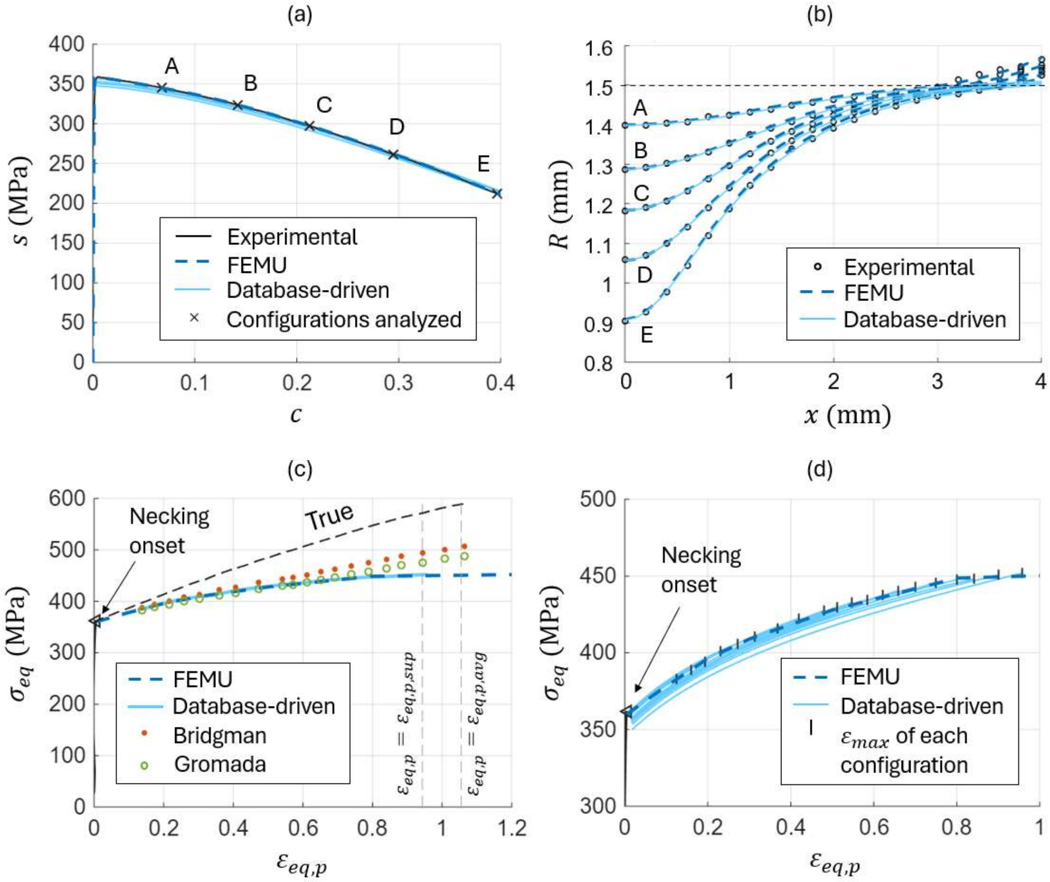

Figure 4.8 Experimental results of Cu, in terms of radial engineering curve (a) and necking shapes (b) predicted by the hardening law (c) identified with different strategies; (d) is a zoomed-in view of (c) for a closer comparison of FEMU and database-driven approach. [1]

Figure 4.8c also allows comparing this reference law with other identification approaches, i.e., Bridgman and Gromada analytical corrections, and the proposed database-driven approach. The area-based true curve is presented too (black dashed line), to highlight the effect of triaxiality. It can be noticed that Bridgman and Gromada theories, plotted as red and green markers respectively, provided a good estimate up to values of 50 % and 80 % of equivalent plastic strain respectively, but fail to estimate the hardening behavior at larger strains. Conversely, the proposed method (solid light blue curve) agrees very well with the reference law.

Actually, as explained in Section 4.2, the proposed method identified a locus of points in the space $\varepsilon_{eq,p} - \dot{\varepsilon}_{eq,p} - \sigma_{eq}$ for each necking configuration considered. In Figure 4.8b, the numerical semi-profile that allowed these loci to be identified are shown in light blue. They match very well with the experimental average semi-profiles within the region considered, i.e., below the horizontal black dashed line. This line, indeed, indicates the experimental portion considered for searching the database. In Figure 4.8a, the modified engineering curves corresponding to the selected numerical shapes are shown in light blue. The fact that they are all close to the experimental one indicates that pure copper can be considered strain rate insensitive during the tested conditions. Although this is already known in the present case, it suggests that the proposed method can, in general, reveal strain rate sensitivity. This is further highlighted in Figure 4.8d by the limited discrepancy of the loci projections in the $\sigma_{eq} - \varepsilon_{eq,p}$ plane (light blue curves). The maximum percentage difference is, indeed, 2.4 % in terms of stress. In subfigure (d) each locus is shown over the strain range I_{ε} for which it provides information about plastic behavior, i.e., the portion satisfying the condition $\dot{\varepsilon}_{eq,p} > 0$. Practically, a threshold equivalent plastic strain rate was defined (10 % of the nominal strain rate) and only the part above it was considered. For determining a unique curve representative of the material behavior, different techniques could be used; however, the chosen method would not significantly affect the result. In the present analysis, the final output was obtained by joining the points at $\varepsilon_{eq,p}^{max}$ of the different configurations, indicated with black vertical markers in subfigure (d). The resulting law is the light blue one of subfigure (c). As in Section 3.5.3, in this subfigure the hardening laws identified with different strategies are plotted up to different equivalent plastic strains: analytical corrections up to the average equivalent plastic strain at the last configuration considered and the database-driven approach up to the maximum superficial equivalent plastic strain.

To conclude, the advantages of the proposed method compared to analytical corrections are the same as the method presented in Chapter 3: a higher accuracy at large strains and a more robust procedure. From a certain perspective, the approach proposed in this chapter can be conceived as an evolution of Bridgman-like methods. For each necking shape, Bridgman-like corrections focus on the necking center and determine a single point of the hardening law. However, each silhouette is representative of a region of the plastic flow curve (and not only of a point), and the proposed method can extract this information.

With respect to the method presented in Chapter 3, the one proposed here, when applied to rate insensitive materials, improves stability and robustness by means of redundancy, since multiple necking configurations are considered. This comes at the cost of a slightly higher computational effort, but still lower than that of FEMU strategy.

4.3.4 Results for a rate sensitive material

This section refers to the test conducted on pure molybdenum, but the purpose is not simply to illustrate the application of the proposed method to a strain rate sensitive material. On one hand, it aims to show the consequence of neglecting strain rate dependence. On the other hand, it intends to highlight the capability of the database to adapt to strain rate sensitive behaviors by comparison with a constitutive law identified through the FEMU approach. Analytical solutions are not reported here, as they may be affected by larger errors, as shown in the previous section, and are generally less robust since they rely only on average quantities evaluated at the minimum cross-section.

Experimental results are shown in Figure 4.9a in terms of some necking semi-profiles (black circular markers) and in Figure 4.9b in terms of engineering response (black line). First, the results of the FEMU strategy are presented since they are then used for critically analyzing the results of the proposed method. Since the material is known to be highly sensitive to strain rate [8, 9], a material model accounting for strain rate sensitivity was adopted. More specifically, the Johnson-Cook hardening model was chosen (implemented as *MAT_015 in Ansys LS-DYNA). Under quasi-static conditions, the flow stress equation can be expressed as:

$$\sigma_{eq} = \left(A + B\varepsilon_{eq,p}^{n}\right)\left(1 + C\ln\frac{\dot{\varepsilon}_{eq,p}}{\dot{\varepsilon}_0}\right), \tag{4.5}$$

where A, B, n, and C were the optimization variables.

Even though Johnson-Cook model is not generally appropriate for BCC metals, it could be successfully used in this analysis, since only a local approximation of strain rate dependence was needed. This is proved by the FE results displayed in Figure 4.9a and b as blue dashed lines, which show a very good prediction of both deformation and engineering response.

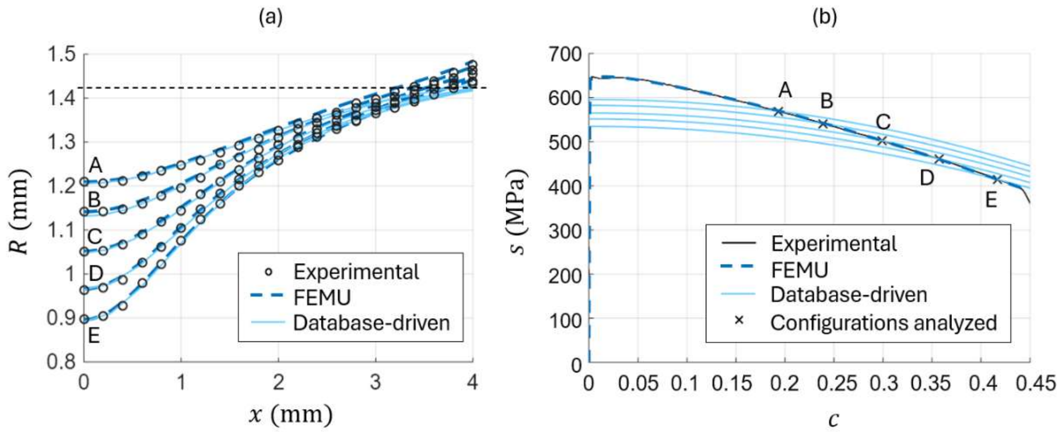

Figure 4.9 Experimental results of Mo, in terms of necking profiles (a) and radial engineering curve (b), in comparison with the prediction obtained from different identification strategies. [1]

Regarding the database-driven approach, the best-matching numerical shapes found in the database are displayed in Figure 4.9a as light blue curves. Again, they were identified by considering only the experimental region below the black dashed line. The good agreement observable from this subfigure supports the fact that strain rate insensitive material models are able to represent a rate sensitive behavior instantaneously. Nevertheless, the FE simulation that provided the closest numerical profile changes from one configuration to another. None of the corresponding radial engineering curves, shown in the subfigure (b), can approximate well the experimental response. This is because the radial engineering curve refers to the history of the minimum cross-section, which is affected by the increasing strain rate and this effect cannot be captured with a unique strain frate insensitive hardening law.

The curves $\sigma_{eq}(\varepsilon_{eq,p})$ of the database found for the necking shapes plotted in Figure 4.9a are shown in Figure 4.10 as light blue lines. Each of them is defined over the strain range I_ε satisfying the condition $\dot{\varepsilon}_{eq,p} > \dot{e}/10$, being $\dot{e}$ the nominal strain rate. The area-based true curve is displayed too (as dashed line) for the sake of comparison and since it is representative of the pre-necking behavior. As explained in Section 4.2, the database $\sigma_{eq}(\varepsilon_{eq,p})$ curves represent the equivalent stress-strain states experienced by superficial material points at different instants during necking and do not overlap for a strain rate sensitive material.

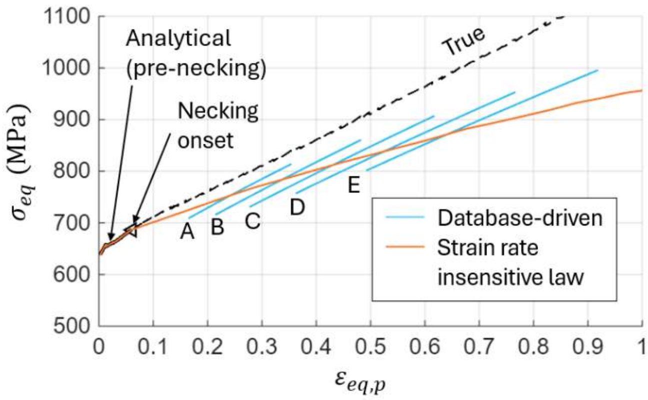

Figure 4.10 Loci of points identified by the database-driven approach and a fitting hardening law if strain rate sensitivity was neglected (adapted from [2])

If this discrepancy was mistakenly attributed to measurement errors and a single $\sigma_{eq}(\varepsilon_{eq,p})$ curve was sought, the average curve could be considered a possible choice. Such curve is displayed in Figure 4.10 as orange solid line and was used as hardening law of a strain rate insensitive material in a FE simulation of the tensile test under analysis. The model accurately predicted the experimental force (as shown Figure 4.11a) but did not match the experimental silhouettes (as depicted in Figure 4.11b). This result could be expected as strain rate sensitivity was neglected, although it was known to affect the material response.

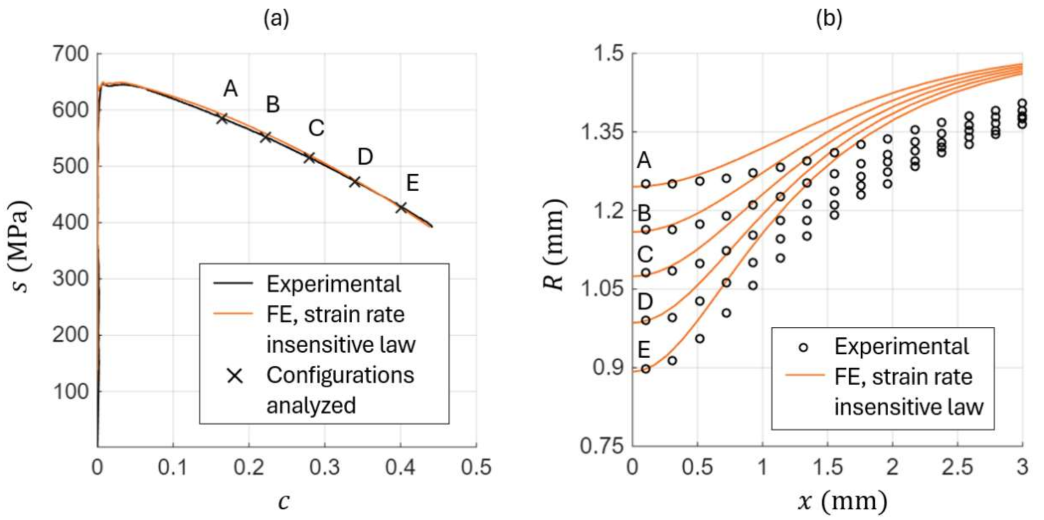

Figure 4.11 Comparison of experimental and numerical results, in terms of radial engineering curve (a) and necking profiles (b), if strain rate sensitivity was neglected (adapted from [2]).

The discrepancy between the database $\sigma_{eq}(\varepsilon_{eq,p})$ curves shown in Figure 4.10 is inherent to the material behavior and should not be removed. Instead, it must be properly considered by associating the strain rate distribution to the loci of points in the $\sigma_{eq} - \varepsilon_{eq,p}$ plane, hence reconstructing loci of points in the $\varepsilon_{eq,pl} - \dot{\varepsilon}_{eq,pl} - \sigma_{eq}$ space. To this end, it is possible to exploit the capability of the proposed method to estimate the strain rate distribution on the specimen surface. This was explained in Step 3 of Section 4.2, and the results are shown in Figure 4.12 for the different configurations analyzed.

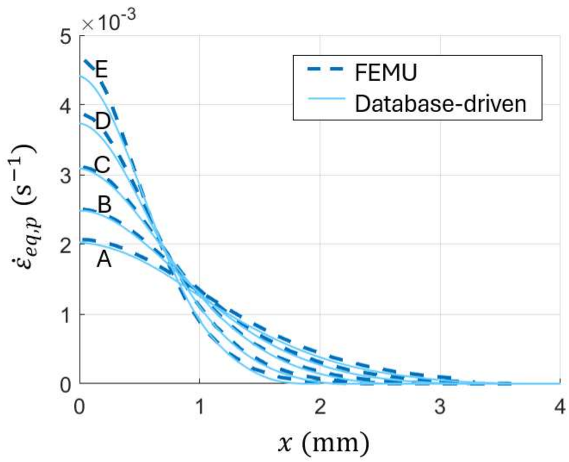

Figure 4.12 Equivalent plastic strain rate distribution at the same configurations of previous figures: comparison between the prediction of the FEMU-identified law and of the database-driven approach. [1]

This figure, in addition to highlighting the non-uniformity of the strain rate experienced during necking, also proves that the database-driven approach estimates the superficial distribution very well. Such conclusion derives from observing that the database distributions are in very good agreement with those obtained from the reference law identified at the beginning of the present section.

This finding is of utmost importance: it practically proves that the normalized equivalent plastic strain rate distribution only depends on the necking silhouette; otherwise, the database-driven approach would not have been able to provide such good results. This also means that the proposed approach allows the strain rate distribution to be estimated with very limited experimental effort and *a priori* of material characterization. Indeed, direct experimental evaluation of the strain rate distribution would require tracking markers painted on the specimen surface, estimating their strain with DIC and then computing the time derivative, which could also be very noisy. A simplification could consist of considering only the silhouette, determining the average strain at the minimum cross-section through Equation 1.12, and then computing its time derivative. However, this would only provide average strain rate information over a single cross-section, while the proposed method provides local strain rate values of several superficial points. Through FEMU techniques, instead, equivalent plastic strain rate fields would be fully determined, on the surface and inside the specimen, but only once the material had been identified.

The above results show that the database-driven method allows material strain rate sensitivity to be detected and a series of points on the hardening surface $\sigma_{eq}(\varepsilon_{eq,pl}, \dot{\varepsilon}_{eq,pl})$ to be determined. In a practical application, the material behavior is intended to be identified directly by the database-driven method, without previously applying a FEMU strategy, in order to reduce the computational cost. The reliability of the law identified using the proposed method can be readily verified by using it as input of a FE simulation of the tensile test and by comparing the predicted and experimental responses.

This was applied to the present experiment. First, a function $f(\varepsilon_{eq,pl}, \dot{\varepsilon}_{eq,pl})$ was fitted to the 3D point cloud obtained by associating equivalent plastic strain rates to the loci of Figure 4.10 (and to many other loci). Actually, the point cloud also included pre-necking data. This was obtained by applying the area-based approach for true strain and stress, while the true strain rate was considered constant and equal to nominal strain rate of the test. The $f(\varepsilon_{eq,pl}, \dot{\varepsilon}_{eq,pl})$ function was then used as material hardening law input into the FE simulation of the test. Figure 4.13 compares the results (green dashed lines) with experimental results (black lines and markers), demonstrating that the identified model was able to accurately predict both the deformation and the engineering response, as shown in subfigures (a) and (c) respectively. In subfigure (b), instead, some equivalent plastic strain rate distributions obtained from the FE simulation are compared with those estimated by the database-driven approach, further confirming the reliability of this estimate.

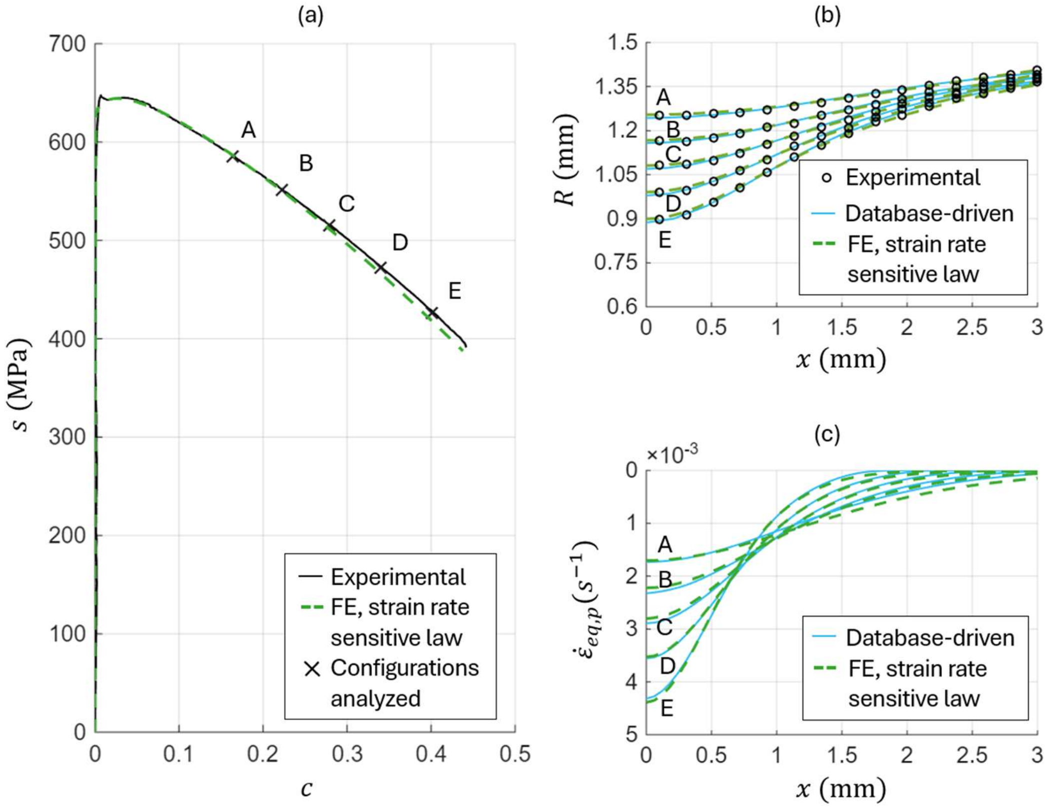

Figure 4.13 Comparison of experimental and numerical results, in terms of radial engineering curve (a), necking profiles (b), and equivalent plastic strain rate distributions (c), if strain rate sensitivity is accounted for with the database-driven approach (adapted from [2]).

4.4 Concluding remarks

This chapter analyzed material and/or conditions for which a unique $\sigma_{eq}(\varepsilon_{eq,p})$ path cannot fully describe the post-necking behavior. In particular, the investigation focused on strain rate sensitive materials, first showing that they belong to this class of behaviors and then demonstrating how the database-driven method can be used for post-necking characterization. More specifically, although strain rate variation and heterogeneity can affect material response during a single test, the observed behavior can be instantaneously approximated by the rate insensitive material model of the database that predicted the closest necking silhouette. Appropriate techniques and considerations, hence, allow the equivalent plastic strain, strain rate and equivalent stress distributions on the specimen's outer surface to be estimated. From the experimental point of view only force history and silhouette evolution are needed. With the purpose of improving accuracy and repeatability in silhouette detection, this chapter proposed to modify the imaging apparatus to frame the specimen in backlight with bi-telecentric lenses and a collimated illuminator.

The capability to estimate the superficial equivalent plastic strain rate field during the necking and without the need for speckle painting or extremely high-frame-rate imaging is an important advancement of the proposed approach. Even more significant, however, is the possibility of estimating the corresponding distribution of equivalent stress. The output of the proposed method is represented by a point cloud in the space $\varepsilon_{eq,p} - \dot{\varepsilon}_{eq,p} - \sigma_{eq}$ that reflects the material's visco-plastic behavior, without any assumption about material behavior, apart from isotropic Von Mises plasticity.

The potential of the approach was illustrated through the successful experimental application to pure molybdenum, a material known to be highly sensitive to strain rate. The method developed in this context still remains applicable to the special case of negligible strain rate sensitivity, as proved by its application to the experimental case study of pure copper. In this sense, compared to the method described in Chapter 3, considering multiple silhouettes slightly increases the computational cost, but significantly improves stability and robustness.

References

[1] Scapin, M., & Beltramo, M. (2024). A Methodology for Post-Necking Analysis in Isotropic Metals. *Metals*, *14*(5), 593.

[2] Beltramo, M., Peroni, L., & Scapin, M. (2025). A data-driven procedure for the analysis of high strain rate tensile tests via visible and infrared image processing. *International Journal of Impact Engineering*, *199*, 105232.

[3] Zhang, L., Gour, G., Petrinic, N., & Pellegrino, A. (2020). Rate dependent behaviour and dynamic strain localisation of three novel impact resilient titanium alloys: Experiments and modelling. *Materials Science and Engineering: A*, *771*, 138552.

[4] Beltramo, M., Scapin, M., & Peroni, L. (2025). Analysis of the work-to-heat conversion beyond the necking onset in non-isothermal tensile tests. *International Journal of Impact Engineering*, 105503.

[5] Scapin, M., Peroni, L., & Fichera, C. (2014). Investigation of dynamic behaviour of copper at high temperature. *Materials at High Temperatures*, *31*(2), 131-140.

[6] Follansbee, P. S. (2014). *Fundamentals of strength*. Wiley NJ, 10, 9781118808412.

[7] Sancho, A., Cox, M. J., Cartwright, T., Davies, C. M., Hooper, P. A., & Dear, J. P. (2019). An experimental methodology to characterise post-necking behaviour and quantify ductile damage accumulation in isotropic materials. *International Journal of Solids and Structures*, *176*, 191-206.

[8] Scapin, M., Peroni, L., & Carra, F. (2016). Investigation and mechanical modelling of pure molybdenum at high strain-rate and temperature. *Journal of Dynamic Behavior of Materials*, *2*(4), 460-475.

[9] Chen, S., Li, W. B., Wang, X. M., Yao, W. J., Song, J. P., Jiang, X. C., & Yan, B. Y. (2021). Comparative study of the dynamic deformation of pure

molybdenum at high strain rates and high temperatures. *Materials*, *14*(17), 4847.

[10] Tvergaard, V., & Needleman, A. (1984). Analysis of the cup-cone fracture in a round tensile bar. *Acta metallurgica*, *32*(1), 157-169.

[11] Bridgman, P.W. (1952). Studies in large plastic flow and fracture. Metallurgy and metallurgical engineering series. *McGraw Hill, New York*.

[12] Gromada, M., Mishuris, G., & Öchsner, A. (2011). Correction formulae for the stress distribution in round tensile specimens at neck presence. *Springer Science & Business Media.*

Chapter 5

Strain rate - temperature interaction

The methods presented in Chapters 3 and 4 allow the material behavior to be identified under quasi-static conditions, even in the presence of significant strain rate sensitivity. In that form, the approach is already applicable to experimental campaigns of quasi-static tensile tests performed at different controlled temperatures. The procedure would simply consist of applying the method to each test and constructing the corresponding material response surface $\sigma_{eq} = f_T(\varepsilon_{eq,p}, \dot{\varepsilon}_{eq,p})$, which varies with temperature. If desired, each response surface, or the whole set of surfaces altogether, can then be fitted with an appropriate constitutive model. This approach is useful, for example, to characterize material behavior at different working temperatures.

For many applications, however, it is also necessary to evaluate the material response at higher strain rates. In the context of such tensile campaigns, the issue of self-heating during testing arises. The deformation process may be sufficiently fast to prevent thermal equilibrium with the environment, causing the material temperature to increase. The resulting stress experienced by material points would, thus, be the result of both strain rate and temperature dependencies. Moreover, both variables would be characterized by heterogeneous fields during necking. The present chapter addresses material post-necking characterization under such complex conditions.

Section 3.2 showed that, in case of adiabatic self-heating and negligible strain rate sensitivity, material thermal dependence does not increase the complexity of post-necking characterization, because temperature is uniquely related to deformation. Chapter 4, conversely, demonstrated how strain rate complicates the identification of the material behavior during necking, even under isothermal testing conditions. Hence, if adiabatic self-heating occurs and the material is sufficiently sensitive to strain rate (in addition to strain and temperature), the same issue described in Chapter 4 arises, namely the non-uniqueness of the deformation paths in the $\sigma_{eq} - \varepsilon_{eq,p}$ plane. A similar situation occurs under testing conditions that are neither isothermal nor adiabatic.

In any situation in which a single $\sigma_{eq}(\varepsilon_{eq,p})$ law cannot describe the tensile response, the methodology described in Chapter 4 remains applicable. The method is, indeed, based on the idea that a normalized necking profile provides information on the instantaneous state of the material, independently of the variables influencing plastic behavior. These variables are determined by the physics of plastic deformation mechanisms and mainly include strain, strain rate, and temperature. Back-projecting the loci of points representing necking configurations onto the $\varepsilon_{eq,p} - \dot{\varepsilon}_{eq,p} - T - \sigma_{eq}$ space reflects the thermo-visco-plastic behavior (for the part characterized by $\dot{\varepsilon}_{eq,p} > 0$). However, to do so temperature distributions are needed.

In the present chapter, the first section is devoted to introducing self-heating and how consequent temperature rises can be theoretically evaluated. Section 5.2 deals, instead, with measuring this temperature rise through infrared imaging. Before moving on to the proposed identification strategy (Section 5.4), an overview of the literature regarding material thermo-visco-plastic characterization is provided. This allows understanding the context in which the proposed method is located. Finally, Section 5.5 reports an experimental case study for proving the method's capability of characterizing a material over broad ranges of strain and strain rate, also accounting for self-heating, regardless of whether adiabatic conditions are satisfied. This topic has been objective of the publication [1].

5.1 Self-heating and consequent temperature rise

During irreversible deformation of metals, part of the plastic work is used to generate defects, while the remainder (typically the majority) is released as heat. When deformation occurs sufficiently fast, the material experiences rising temperatures because the heat produced by plastic deformation cannot be fully transferred to the external environment. This thermal increase can influence the material's mechanical behavior, a phenomenon commonly known as thermal softening.

In coupled thermo-mechanical problems of solids, the thermal field T and the mechanical field are linked through the heat conduction equation [2]:

$$\dot{T} = \frac{\beta}{\rho c_p}\dot{W}_p + \alpha \nabla^2 T - \frac{k}{\rho c_p}\frac{E}{1-2\nu}T_0 \mathrm{tr}(\dot{\boldsymbol{\varepsilon}}_e), \tag{5.1}$$

being α the thermal diffusivity, $\dot{W}_p$ the rate of plastic work, k the coefficient of thermal expansion, E the Young's modulus, ν the Poisson's ratio, T_0 the initial temperature, and $\dot{\boldsymbol{\varepsilon}}_e$ the elastic strain rate tensor. The term on the left side represents the variation in internal energy, which typically depends on irreversible plastic deformation (first term on the right side [3, 4]), as well as on heat conduction (second term on the right side) and reversible thermoelasticity (third term on the right side). This last term is generally considered negligible when large plastic deformation takes place, resulting in the simplified equation:

$$\dot{T} = \frac{\beta}{\rho c_p}\dot{W}_p + \alpha \nabla^2 T. \tag{5.2}$$

Furthermore, when the strain rate is high enough to assume adiabatic conditions, Equation 5.2 can be simplified even further by taking advantage of the fact that no heat conduction occurs [2, 5-13]. In these cases, it results:

$$\dot{T} = \frac{\beta}{\rho c_p}\dot{W}_p. \tag{5.3}$$

The strain rate level at which adiabatic conditions are verified specifically depends on material properties. A dimensionless parameter that is commonly used for characterizing transient conduction and, thus, assessing adiabaticity is the Fourier number Fo. This is defined as:

$$Fo = \frac{\alpha t}{L^2}, \tag{5.4}$$

where t is the test duration, and L the characteristic length through which conduction occurs. 10^{-2} is the commonly accepted threshold below which the process can be considered essentially adiabatic [14].

Equation 5.3 shows that, under adiabatic conditions, temperature results just from the integral of the deformation path. This highlights that temperature represents a special variable, meaning that it cannot be *a priori* defined as either a q variable or a $\tilde{q}$ variable, according to the notation introduced in Section 2.1. Indeed, it may behave like one type or the other depending on whether additional variables (e.g., strain rate sensitivity) alter the deformation paths of material points.

When Equation 5.2 holds because of non-negligible heat conduction, different material points follow different paths even in the absence of strain rate sensitivity. When a material point reaches a given strain, its temperature is generally different from that experienced by another point when it reached the same strain. This difference is caused by different heat conduction contributions, i.e., to different temperature distributions in the surroundings of the two points. As a result, deformation paths on the $\sigma_{eq} - \varepsilon_{eq,p}$ plane deviate from one another. This is another example in which, due to a certain phenomenon, temperature behaves as a $\tilde{q}$ variable.

As anticipated, the method proposed in this chapter requires knowing self-heating temperature rise on the specimen outer surface. This information cannot be determined directly from the database established as explained in Section 2.3. Indeed, as evident from above equations, temperature represents an integral quantity that depends on previous deformation path and on thermal conduction from the surroundings of the point analyzed. No curve in the precomputed database may be able to represent the entire temporal evolution of the test in the presence of strain rate sensitivity and/or thermal conduction. Even though the database could be in principle enriched with further simulations, this would come at the cost of a much larger database, so this solution was not pursued. Furthermore, although temperature rises could in principle be computed by solving Equations 5.2 and 5.3, there are some issues in applying them. In presence of thermal conduction, using Equation 5.2 requires knowing the thermal field within the specimen, which cannot be reconstructed without simplifying assumptions. Conversely, under adiabatic conditions, the following equation could be applied:

$$T = T_0 + \frac{\beta}{\rho c_p} \int_0^{\varepsilon} \sigma_{eq}\left(\varepsilon_{eq,pl}\right) d\varepsilon_{eq,p}, \tag{5.5}$$

by using the initial temperature, and assuming the Taylor-Quinney coefficient, the density, and the specific heat. However, the plastic work (i.e., the integral of Equation 5.5) can be computed easily only for rate insensitive materials. In these cases, the $\sigma_{eq}\left(\varepsilon_{eq,pl}\right)$ path is common to all material points and can be identified immediately using the database-driven approach. For rate sensitive materials, instead, the paths of the different material points are not reconstructed straightforwardly, since this would require tracking the evolution of material points in a Lagrangian perspective. Thus, the final choice for the method proposed in this chapter was to measure temperature experimentally, rather than computing it.

5.2 Infrared imaging

The present section focuses on temperature measurements through devices based on infrared radiation. The aim is twofold: highlighting their effectiveness in investigating material behavior and underlining some important aspects for reliable thermal measurements.

Infrared detectors have been widely used for temperature measurement in high strain rate experiments because of their short response time and high acquisition rate [2, 5-8]. Recently, however, there has been an increasing use of infrared imaging, which enables full-field measurements.

Assuming uniform and adiabatic deformation, full-field thermal information is employed to improve measurement consistency by calculating the average temperature across a specific sample area [9-11]. For example, Vazquez-Fernandez et al. [9] used infrared imaging to qualitatively evaluate whether the adiabatic assumption was valid. As a matter of fact, during uniform deformation, adiabaticity is expected to produce a uniform temperature distribution within the gauge section; if this does not occur, the assumption of adiabaticity is probably incorrect.

As demonstrated in a comparative study by Goviazin et al. [15], the main drawback of high-speed cameras with respect to infrared detectors during dynamic loading is their lower sampling frequency. In this sense, this technology still has significant room for improvement, as also thoroughly discussed by Soares et al. [16]. Nevertheless, infrared imaging remains highly effective for full-field analysis of non-uniform temperature distributions resulting from complex stress states and/or non-adiabatic conditions. This application field includes studies on Lüders band propagation [17-20], Portevin-Le Chatelier effect [21,22] and post-necking deformation [13,16,23-25].

Since the latter case is the focus of the present thesis, infrared imaging was chosen to monitor temperature distribution. Acquisition rates of infrared cameras, however, are lower than those of modern optical cameras, which partially limited the possibilities of simultaneous optical and infrared imaging.

An important setting parameter in infrared cameras is integration time, which needs to be suitable for monitoring the temporal evolution of the event. For fast thermal processes, a shorter integration time is better for measuring instantaneous temperatures; otherwise, the recorded values reflect the mean temperatures over the integration window. This effect is especially relevant when recording an object that is both heating up and moving (like in tensile testing), as its motion also leads to spatial averaging. This phenomenon is analogous to motion blur in photography and can be limited by reducing the integration time. Nevertheless, the integration time must be long enough for sufficient infrared radiation to be captured by camera's sensor. In this sense, the amount of radiation emitted by the specimen (which is partially determined by its temperature) affects the sensitivity of the camera. Although short integration windows are suitable for high-temperature measurements (where much radiation is emitted), their use at near-room-temperature experiments may prevent measuring temperatures reliably. In cases where temperature changes significantly during testing, selecting the integration time required balancing the need to accurately measure low temperatures and to follow high-speed deformation.

Another important aspect of infrared imaging is the conversion of radiometric measurements into temperature. This requires accounting for the emissivity of the target surface which mainly depends on the material, but that may also be affected by temperature and observation angle [26]. A typical dependence of metal emissivity on the observation angle is displayed in Figure 5.1. It remains nearly

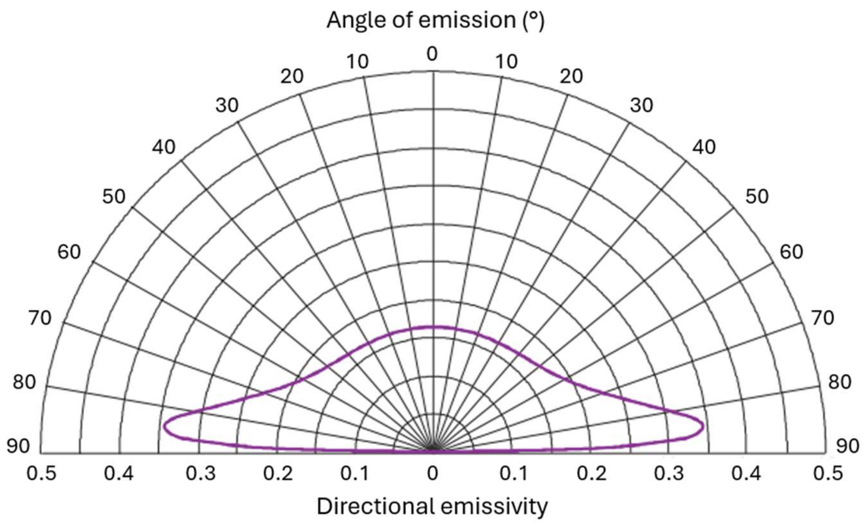

Figure 5.1 Emissivity dependence on viewing angles for metals (adapted from [26]).

constant up to about 50°, then it increases rapidly and reaches a maximum beyond 80°, before dropping to zero at 90°.

Sometimes the emissivity is increased and uniformized by coating the target surface, e.g. as done by Salehi and Kingstedt [27]. Nevertheless, during necking material undergoes large plastic deformations, which may cause the coating to not remain perfectly adherent to the material surface throughout the test, thus leading to unreliable measurements. It was, hence, preferred to convert measured radiometric temperatures to actual ones by performing a calibration with the same configuration and setting used during testing (as already done in some works [9, 24, 25]). The last aspect is important since the resulting calibration curve is specific to material, experimental setup, and camera setting. This approach allows the thermal and angular dependencies of emissivity to be accounted implicitly, provided that the two effects are uncoupled.

Finally, a variation of the material emissivity may also be caused by changes in surface roughness during plastic deformation; nevertheless, some studies showed this effect to be relatively small in metals [2, 24, 28].

5.3 Literature background

Before going into details of the proposed method for thermo-visco-plastic characterization, this section summarizes empirical approaches proposed in the literature. They usually entail conducting experimental tests under different conditions, in terms of temperature and strain rates.

Considering tensile tests, the analytical formulas summarized in Section 1.2.1 can be used to directly convert the engineering response during uniform deformation into the pre-necking hardening law. This law is generally assumed to be isothermal and associated with a constant strain rate. Data obtained from different loading conditions can then be fitted with a selected material model. It can be an empirical material model, such as Johnson-Cook [29], or a physically based material model, such as Zerilli-Armstrong [30] or the Mechanical Threshold Stress model [31]. A common calibration approach consists of dividing the process into subsequent steps, each aimed at identifying a single term of the model (as illustrated, for instance, in Song and Sanborn [32]). Alternative fitting strategies were also proposed; regarding Johnson-Cook hardening model, several calibration procedures were thoroughly reviewed by Gambirasio and Rizzi [33].

In some cases, tensile tests on ductile metals are characterized by limited uniform deformation, as necking occurs soon after yielding. Nevertheless, useful information about material behavior can still be obtained from post-necking data. This was already discussed for strain-hardening laws, but the problem complexity increases here, as it is necessary to account for the non-uniformity of strain rate and, in cases of self-heating, of temperature too. In these cases of strain rate-temperature interaction distinguishing hardening from self-heating becomes challenging. Moreover, in such scenarios, thermal dependence should not be inferred from quasi-static tests performed at different temperatures because the underlying physical mechanisms differ. Adiabatic heating mainly affects the ability of dislocations to overcome obstacles, whereas high working temperatures can also influence microstructural structure, such as grain size, texture, or dislocation density.

Another difficulty arises when attempting to combine post-necking information from different tests for identifying material behavior over broad ranges of strain, strain rate and temperature.

Among the analytical approaches proposed in the literature, it is worth citing the work of Vilamosa et al. [34]. Tests at different temperatures and strain rates were conducted. For each test, Bridgman's theory was employed to reconstruct the stress-strain path of the minimum cross-section. Then, each path was associated with the corresponding evolution of the local strain rate and temperature. According to an area-based approach, the average strain rate at the neck was evaluated as:

$$\dot{\varepsilon}_{eq} = -\frac{2}{r}\frac{dr}{dt}. \tag{5.6}$$

For adiabatic tests, the temperature history was also required, and it was estimated from the conversion of plastic work into heat. Finally, data from all tests was combined and parameters of a constitutive model were optimized.

Actually, for this kind of characterization, hybrid experimental-numerical methods are more commonly adopted than analytical approaches. Despite their higher computational effort, they have the advantage of not relying on strong assumptions and of considering the entire specimen rather than only the minimum section. Hereinafter, only works that employ FEMU approaches are mentioned, due to the difficulties in applying DIC, and hence VFMs, to cylindrical geometries.

A widely used identification strategy consists of optimizing material parameters by simultaneously considering different loading conditions. Since this can be computationally expensive, techniques are adopted to reduce the number of optimization variables. For instance, a good fitting of the quasi-static test can be forced, so that only the parameters describing temperature and/or strain rate dependencies still need to be identified with other tests. This was done, for instance, by Sasso et al [35] and Sedighi et al. [36]. However, the resulting set of parameters may not optimally predict the material behavior in case of simultaneous variation of strain, strain rate and temperature. A better prediction would be obtained if strain-hardening parameters were optimized together with strain rate and temperature coefficients. This was demonstrated with compression tests by Milani et al. [37]. In this regard, identification strategies that differed from one another for optimization variables were compared by Scapin et al. [38]. They proved that the influence of parameters changes depending on the range of variation of strain rate and temperature occurring during the experiments. This observation, despite originally being related to compression tests, could be extended to tensile tests too and leads to the conclusion that a universally optimal optimization strategy does not exist. It depends on the application of interest, more specifically on the variation range of the variables of interest.

Previous approaches, despite being able to provide an acceptable description of the overall behavior, may not accurately predict single loading conditions. Hence, an effective alternative is to optimize each loading condition separately, allowing the chosen hardening law to approximate material behavior locally within specific ranges of strain rate and temperature. This provides a better description of each test, as presented by Zinovev et al. [39]. However, the issue of non-uniqueness of the identified model arises. Such issue can be addressed by using both force and deformed geometry measurements as objective of the optimization process. For example, in Scapin et al. [40] the necking shape was used as additional target function. Once the material models for the different loading conditions have been identified, several states (in terms of strain, strain rate, temperature, and stress) experienced during the tests can be reconstructed. All resulting data can be used to re-fit a single global constitutive model. A similar approach was applied by Yao et al. [41], even though it used a damage evolution model for describing necking.

Overall, the main drawbacks of these approaches, independently of the specific optimization strategy, are the need to assume the material model *a priori* and the high computational cost required by multi-objectives optimizations involving many optimization variables. The procedure described in the next section aims to overcome these issues through the database-driven approach.

5.4 Identification procedure

When self-heating causes coupling of thermal and strain rate effects, the database-driven post-necking identification procedure to be applied to the test basically corresponds to that presented in Section 4.2.

Several necking silhouettes are considered and, for each of them, a locus of points in the $\sigma_{eq} - \varepsilon_{eq,p}$ plane is identified by searching for the closest profile in the database. When only strain and strain rate dependences are relevant, this locus is generally expected to be a monotonically increasing curve. When temperature dependence is introduced, however, thermal softening may lead to a necking profile associated with a non-monotonically increasing curve. Since this locus represents the states exhibited by the material in a given configuration, this simply means that the point corresponding to the maximum strain (at the necking center) is associated with a lower stress than other points. This may occur despite the higher strain rate, due to the particularly high temperature that can be reached in that region.

The loci obtained from multiple necking configurations must, then, be mapped onto the hypersurface $\sigma_{eq}\left(\varepsilon_{eq,p}, \dot{\varepsilon}_{eq,p}, T\right)$. To this aim, the surface distributions of strain rate and temperature at each configuration must also be known. While the strain rate distributions can be obtained from the database itself due to the kinematics of the phenomenon, temperature distributions are assumed to be measured through an infrared camera, as anticipated in Section 5.1.

The resulting point cloud in the $\varepsilon_{eq,p} - \dot{\varepsilon}_{eq,p} - T - \sigma_{eq}$ space, hence, collects the states experienced by material points during the post-necking phase of the test analyzed. Then, various monotonic tensile tests can be considered, each one conducted under a different loading condition. This allows enriching the 4D point cloud $(\varepsilon_{eq,p}, \dot{\varepsilon}_{eq,p}, \sigma_{eq}, T)$ with additional states so that a broader strain rate and temperature domain is explored. The portion of the point cloud characterized by $\dot{\varepsilon}_{eq,p} > 0$ reflects the thermo-visco-plastic behavior of the material, regardless of the variables influencing it and of the testing conditions (isothermal, adiabatic, or with conduction). Figure 5.2 summarizes this identification process with a schematic representation.

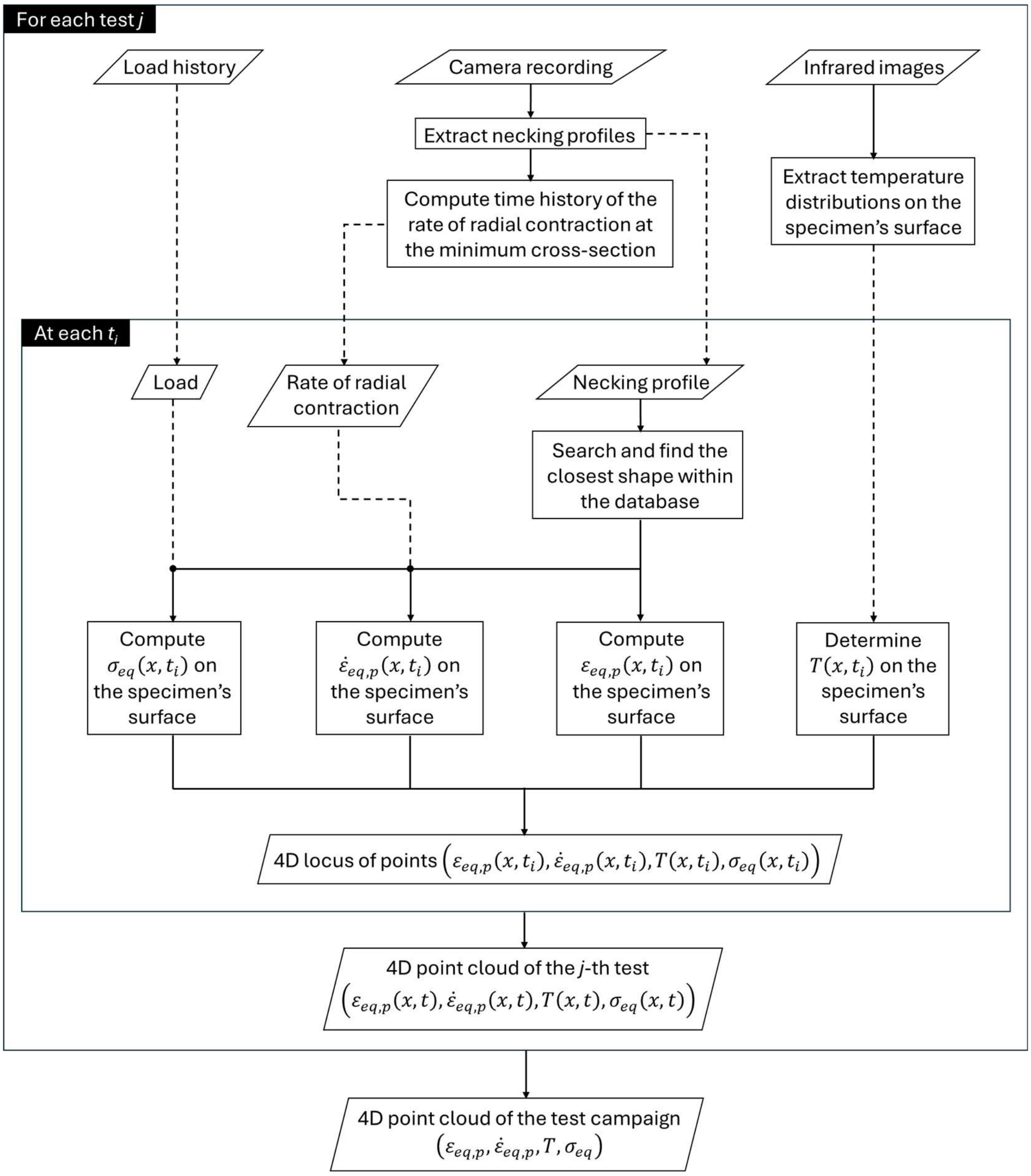

Figure 5.2 Workflow of the identification process for thermo-visco-plastic characterization (adapted from [42]).

Finally, data fitting techniques can be applied to the 4D point cloud for deriving a material model $\sigma_{eq} = f\left(\varepsilon_{eq,p}, \dot{\varepsilon}_{eq,p}, T\right)$ for FE simulations. In this phase, distinguishing the contribution of thermal softening from strain and strain rate hardening becomes challenging. Furthermore, thermal effects from self-heating should be separated from those associated with externally imposed temperatures, because of the different underlying physical mechanisms. Such difficulties are common to all identification methods and lie beyond the scope of the present chapter, which instead focuses on evaluating the proposed strategy's ability to reproduce the observed material behavior.

If temperature distributions were not available, data fitting techniques would be applied to a 3D point cloud in the space $\varepsilon_{eq,p} - \dot{\varepsilon}_{eq,p} - \sigma_{eq}$ by implicitly considering thermal effects. In this case, the point cloud of each test would be fitted with a different model $\sigma_{eq} = f_j\left(\varepsilon_{eq,p}, \dot{\varepsilon}_{eq,p}\right)$ and none of them could be generalized to other applications. Each model would be valid only if the temperature exhibited at a given strain and strain rate coincides with that experienced, at the same strain and strain rate, during the test used for calibration. This does not generally occur; hence, the previous approach that explicitly accounts for thermal effects is preferable. Indeed, it can deal with applications where different temperatures are encountered at the same strain and strain rates (compared to calibration tests). Although this entails extrapolating the model, the results would still be more reliable compared to the other approach.

5.5 Experimental case study

In this section the proposed method is applied to a campaign of tensile tests performed at different speeds. The main purpose is proving that it can deal with self-heating, whether under adiabatic conditions or not. Hence, the material under investigation was 17-4PH (H900), a martensitic stainless steel, moderately sensitive to strain rate and prone to exhibit significant self-heating because of its low thermal conductivity.

In Section 5.5.1 the experimental setups adopted for the different strain rates are described. Data acquisition still resembles that of experimental case studies presented in Section 3.5.1 and 4.3.1, except for the introduction of an infrared camera to monitor the temperature field. Section 5.5.2 is, thus, entirely devoted to thermal data acquisition and infrared images post-processing. Finally, Section 5.5.3 reports the analyses of acquired data and the results, together with a critical discussion. As in all previous tests, data analysis regarded only the portion sufficiently far from a significant reduction in mechanical strength to limit the effects of void nucleation and coalescence [43]. Finally, post-mortem investigations were conducted to verify the assumption of material isotropy underlying the proposed methodology.

5.5.1 Experimental setup

The tests were conducted at room temperature and at four different nominal strain rates: 10^{-2}, 1, 10, 10^3 s^{-1}. The two intermediate speeds were chosen based on the behavior exhibited in dynamic tests. The details of all experimental tests are summarized in Table 5.1.

A servo-hydraulic testing machine, Dartec-HA100, was used for all tests, except for the highest strain rate test (10^3 s^{-1}), which was conducted with a Split Hopkinson Tension Bar (SHTB) apparatus in direct configuration. A detailed description of the setup developed at DYNLab can be found in [40], here only a very brief explanation is provided. A specimen is mounted between an input and an output bar by means of the threaded ends. A tensile stress wave in the input bar is generated by pneumatically accelerating a striker which hits an anvil connected to one end of the bar itself. When the wave reaches the specimen, a part is reflected into the input bar while the remainder is transmitted into the output bar. By measuring the strain on the output bar, the stress on the bar and, thus, the force acting on the specimen can be determined by considering one-dimensional wave propagation in elastic bars and that dynamic equilibrium has been reached.

Table 5.1 Details of experimental tests (adapted from [1]).

Test type	Nominal strain rate (1/s)	Equipment	Optical camera	Infrared camera
1	10^{-2}	Dartec HA100	Opto Engineering ITA81-GM-20C 2856×2848 px×px 11 μm/px 1 fps	-
2	1	Dartec HA100	Photron Mini AX50 1024×1024 px×px 24 μm/px 500 fps	FLIRX6900sc SLS 640×512 px×px 45 μm/px 500 fps
3	10	Dartec HA100	Photron Mini AX50 1024×1024 px×px 24 μm/px 5,000 fps	FLIRX6900sc SLS 640×88 px×px 45 μm/px 5,000 fps
4	10^3	SHTB	Photron SA 5 640×208 px×px 37 μm/px 50,000 fps Photron Nova S6 256×128 px×px 15 μm/px 100,000 fps	FLIRX6900sc SLS 640×16 px×px 45 μm/px 16,040 fps

Regarding specimen geometry, the same adopted throughout this thesis was chosen: cylindrical dog-bone with threaded heads, 5 mm gauge length and 3 mm gauge diameter. This was specifically designed for SHTB tests [40] but was also used for all other tests, despite not being the standard, to guarantee consistency across all loading conditions.

Tests were recorded with both different optical cameras depending on the test speed. In quasi-static tests, the high-resolution camera Opto Engineering ITA81-GM-20C was used, while in intermediate-speed tests, the high-resolution high-speed camera Photron Mini AX50 was employed. The latter captured the full specimen shape at 500 and 5,000 fps for tests at nominal strain rates of 1 and 10 s^{-1}, respectively. In SHTB tests, two high-resolution high-speed cameras were used, a Photron FASTCAM SA 5 and a Photron FASTCAM Nova S6. The first recorded the entire specimen shape at a maximum frame rate of 50,000 fps. The second was used, instead, to reach higher frame rates for monitoring the minimum radius. By cropping the image to frame a smaller region around neck, this camera was able to achieve an acquisition rate of 100,000 fps. The two cameras were placed at small angles, one with respect to the other. Apart from quasi-static tests in which bi-telecentric optics and illumination were used (as previously done in Section 4.3), entocentric lenses were employed. In these cases, preliminary analyses with a checkerboard pattern were conducted to verify that the imaging setup minimized distortion and perspective effects. Finally, in all tests, backlight illumination was used to obtain high-contrast images. Figure 5.3 displays a sequence of images acquired by the Photron FASTCAM SA 5 during a SHTB test. The final frames highlight the cup-and-cone fracture, resulting from microcracks nucleation and growth within the specimen [43]) and significant heat release (with temperatures exceeding 350°C on the specimen surface).

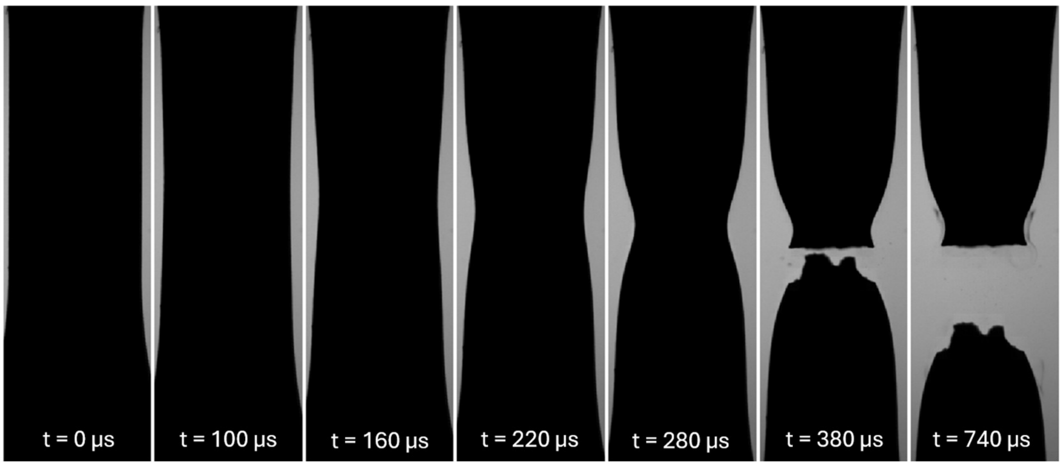

Figure 5.3 Sequence of recorded images during a test on the SHTB. [1]

All images acquired by optical cameras were post-processed in MATLAB as explained in Section 3.5.1 for extracting the specimen silhouette and then determining a single average semi-profile by exploiting the symmetry of the deformed sample.

Additionally, an infrared high-speed camera (FLIRX6900sc SLS) was employed to monitor temperature changes due to self-heating. All infrared images were post-processed in MATLAB to obtain the temperature distribution along the axial direction, as described in the following section.

Optical and infrared cameras were arranged orthogonally to each other as schematically shown in Figure 5.4. It was checked that the light source used for backlight acquisition of the optical camera did not affect thermal measurements. Moreover, the fact that optical and infrared cameras recorded different sides of the specimen was not considered as an issue, since this would be automatically included in the assumption of axialsymmetry at the basis of the entire procedure.

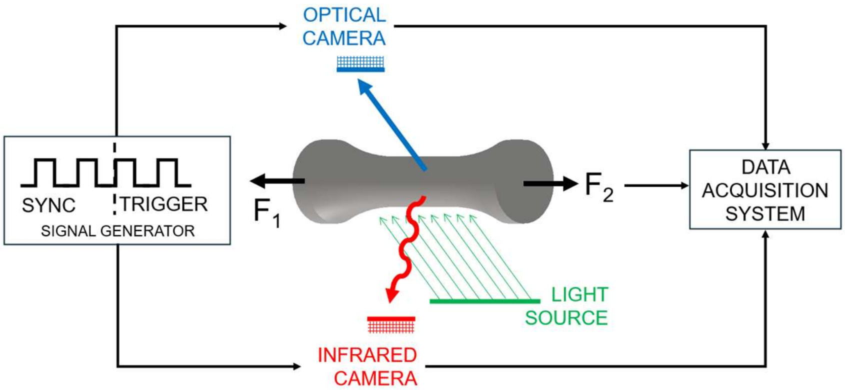

Figure 5.4 Schematic representation of experimental setup and data acquisition. [42]

Finally, acquisition of visible and infrared images should be synchronous and simultaneous ideally. This was feasible during the tests at low-medium strain rates, but not at high strain rates, as reported in Table 5.1 and better explained hereinafter. In any case, the same signal was used for triggering both systems so that they shared the same time reference.

5.5.2 Thermal data acquisition and analysis

This section provides details on the thermal measurements performed in the present test campaign and their post-processing.

Regarding acquisition rates, synchronous visible and infrared acquisition was possible in low-medium strain rates tests, as reported in Table 5.1; acquisition rates of 500 and 5,000 fps were used for tests at 1 and 10 s^{-1} respectively. Figure 5.5 shows some configurations during a test at nominally 10 s^{-1} by graphically coupling infrared and optical images.

At the highest strain rates, very high frame rates were needed. For ensuring an adequate spatial resolution, an acquisition rate of 50,000 fps was used the optical

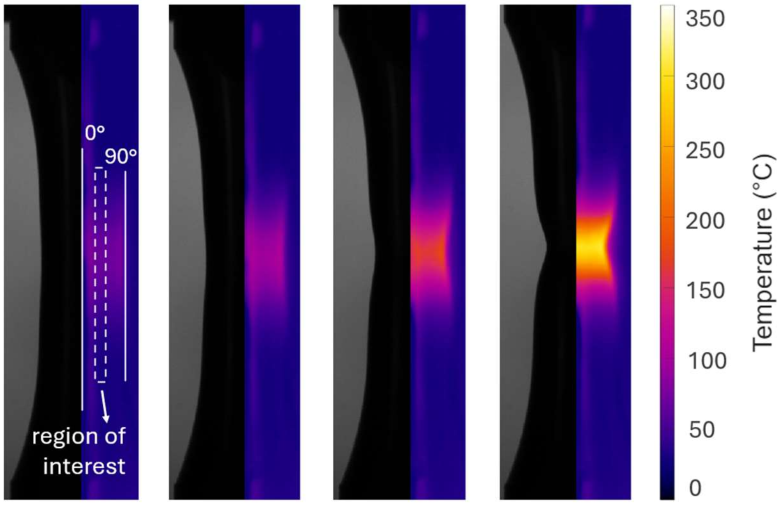

Figure 5.5 Optical and infrared images acquired during a 10 s^{-1} test, with indicated in the first image the region of interest for the analyses and the boundary viewing angles of the infrared camera. [42]

camera monitoring the whole shape. Conversely, the infrared camera could reach only 16,040 fps (with an image size of 16 x 640 pixels). Thus, instead of reducing the optical camera's rate to obtain synchronous and simultaneous acquisitions, each camera used a different frame rate. As a result, fewer infrared frames were grabbed, and at different times with respect to optical frames. Nevertheless, a shared time reference was maintained since the same signal was used for triggering them.

A critical point of infrared imaging was the choice of the integration time, as explained in Section 5.2. Indeed, the specimens, which were initially at room temperature, achieved temperatures above 300 °C during necking in some tests under investigation. The selected integration time (50 μs for all tests) was, therefore, a trade-off between accuracy at low temperature and capability of following high-speed deformation. Actually, this integration time was relatively long for high strain rate tests so that it was chosen to temporally locate infrared images at the center of the integration window.

Finally, for converting the measured radiometric temperatures to actual ones, a single calibration curve was used for all tests. This was possible by ensuring that all tests shared the same features of the calibration in terms of camera settings, distance from the sample and viewing angle. In practice, calibration was carried out by heating the specimen with an induction system and then by monitoring its cooling using both the infrared camera and K-type thermocouples spot-welded to the samples' surface. Since the emissivity depends on the viewing angle (see Section 5.2) and the target surface was cylindrical, the region indicated with a white dashed rectangle in the first frame of Figure 5.5 was used for evaluating radiometric temperatures. This was chosen to avoid the effects of both reflection and high observation angles. The resulting calibration curve (specific to material, experimental setup, and camera setting) is shown in Figure 5.6. For measuring temperature during the tests, the same region was considered, assuming that the corresponding observation angles, although affected by necking, remain within the nearly constant region of emissivity.

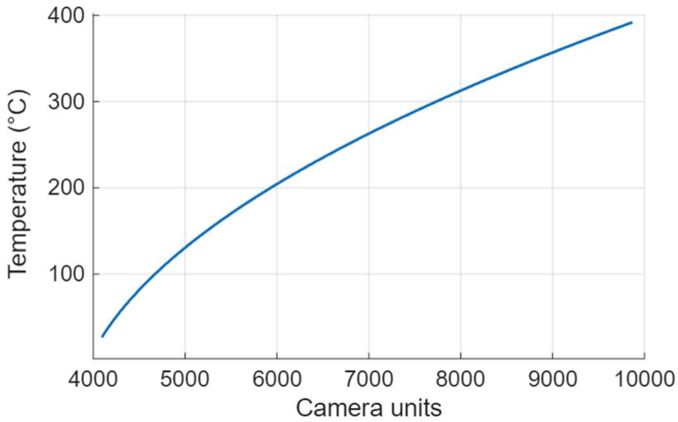

Figure 5.6 Calibration curve determined for the specific material, experimental setup, and camera settings. [42]

The selected region of each infrared image was post-processed to determine the thermal field on the specimen's surface, specifically its variation in the axial direction. Full-field imaging improves redundancy by allowing distributions obtained from different sets of pixels aligned with the axis to be averaged. Indeed, thanks to the axialsymmetry of isotropic materials considered, all pixels aligned along the axial direction yield theoretically the same temperature distribution.

Image post-processing is illustrated in Figure 5.7. With reference to Figure 5.7a, the columns in region A and B were extracted, thus leading to the temperature distributions plotted with dotted lines in Figure 5.7b. It can be noted that the regions at lower temperatures, located farther from the neck center, were characterized by higher data scatters. Nevertheless, this would not affect material thermo-visco-

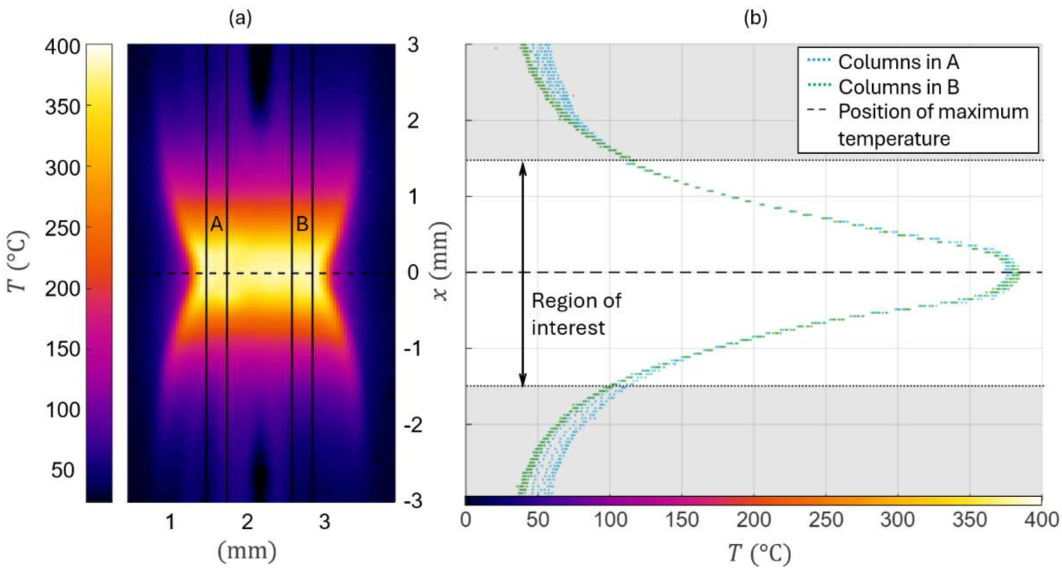

Figure 5.7 Example of infrared images post-processing: in (a) an infrared image from a 10 s^{-1} test, highlighting the regions used for determining the thermal field along the axial direction; in (b) the temperature distributions from region A, B (adapted from [1]).

plastic characterization. Indeed, the database-driven approach showed that these high-scatter parts did not belong to the plastic domain and, thus, the procedure described in Section 5.4 automatically excluded them from subsequent analyses.

Since the proposed method focuses on a semi-profile, only one-half of the mean temperature distribution was considered, specifically the one corresponding to the specimen side moving more slowly (to limit motion blur effects). At low-medium strain rates, the center of the profile can be estimated by either overlapping the silhouettes from the visible and infrared frames or by identifying the position of the maximum temperature. The two methods were found to provide very similar results. Therefore, in high strain rate tests, where infrared images were so cropped that it was not possible to determine the silhouettes, the profile center was determined as the point at the maximum temperature.

Some of the resulting mean temperature semi-profiles are shown in Figure 5.8 for tests at different nominal strain rates. To facilitate comparison across tests, the selected configurations shared approximately the same equivalent plastic strain at the profile center (according to the database-driven estimate). These values are written close to the corresponding configuration. As could be expected, the temperatures experienced by the material during a 1 s^{-1} test were lower than the corresponding ones in a 10 s^{-1} test. It is reasonable to attribute this evidence mainly to heat conduction. However, it cannot be excluded a contribution from the positive strain rate sensitivity which causes lower plastic work to be executed on material points at lower speeds. This observation is only partially confirmed by a test at 10^3 s^{-1}. Less deformed configurations exhibited higher temperatures compared to the analogous configurations of other tests, whereas the maximum temperature achieved at the last configuration was lower. Furthermore, the thermal field at this last configuration was less localized than the corresponding one for a test at 10 s^{-1}, while it would be expected that adiabatic conditions enhanced localization at higher strain rates. This might also be an artefact due to a relatively high integration time

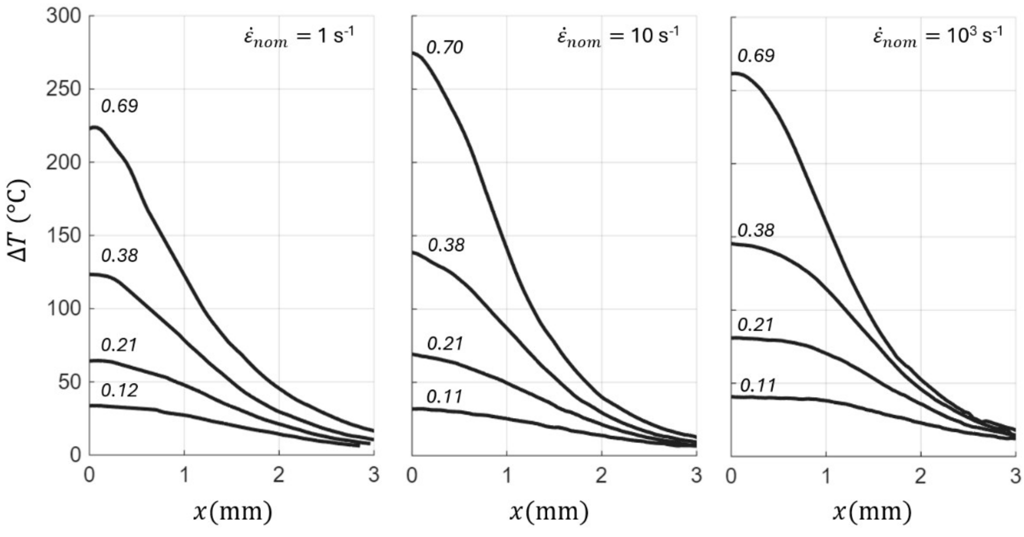

Figure 5.8 Temperature distributions recorded during tests at different strain rates; next to each configuration the database estimate of $\varepsilon_{eq,p}$ at the profile center is written (adapted from [42]).

with respect to the motion of the specimen, which causes resulting thermal fields to be averaged more significantly both in time and space. Reducing the integration time would improve this aspect but would worsen the camera sensitivity to infrared radiation at near-room temperatures.

5.5.3 Data analysis and results

In this section data analysis is explained along with the presentation and discussion of intermediate and final results.

Uniform deformation was analyzed using an area-based approach (Equations 3.10). Theoretically, each point $(\varepsilon_{eq,p}, \sigma_{eq})$ should also be associated with the correct $\dot{\varepsilon}_{eq,p}$ and T even during uniform deformation [44]. This is because, as uniform deformation proceeds, the specimen elongation changes the strain rate, while self-heating can generate temperature rises (if thermoelasticity is neglected). Nevertheless, in the present experimental campaign necking began soon after yielding. On one hand, this led to negligible strain rate and temperature variations during pre-necking so that nominal strain rate and room temperature were considered for the pre-necking deformation. On the other hand, a post-necking identification strategy was essential for characterizing material behavior.

The proposed database-driven strategy explained in Section 5.4 was implemented in MATLAB and applied to the present tests. Only one test per condition was analyzed and presented here due to the low dispersion of macroscopic results. For each condition, the test closest to the average of all tests performed under that same condition was chosen. For each selected test, several necking deformed configurations were considered and the corresponding set of 3D loci of points in the space $\varepsilon_{eq,p} - \dot{\varepsilon}_{eq,p} - \sigma_{eq}$ was identified. The results are displayed in Figure 5.9 as projections on the two planes $\dot{\varepsilon}_{eq,pl} - \varepsilon_{eq,p}$ and $\sigma_{eq} - \varepsilon_{eq,p}$ (gray scale lines). Actually, only the portions within the plastic domain are shown; they were found by considering only the part of each locus satisfying the condition $\dot{\varepsilon}_{eq,p} > \dot{e}/10$. At each configuration, the state exhibited by the point at the profile center corresponds to the one at the maximum strain and is denoted with a light blue marker.

Area-based true curves were plotted too, as dashed lines, in $\sigma_{eq} - \varepsilon_{eq,p}$ planes. These lines are thicker in the pre-necking phase to indicate that they correspond to the hardening laws, while they are thinner after necking onset where they no longer represent material hardening. The comparison of pre-necking phase between different loading conditions shows the moderate strain rate sensitivity of 17-4PH.

Then, by focusing on the paths followed by material points at the profile center (light blue dots), it can be observed that they are non-monotonic for intermediate-high strain rate tests. This underlines that considerable thermal softening was taking place prevailing over strain rate hardening. This is typical of stainless steels, whose low thermal conductivity makes them prone to exhibit noticeable self-heating.

The $\sigma_{eq}(\varepsilon_{eq,p})$ path followed by the profile center is not representative of all material points, as suggested by the discrepancy of light blue dots and gray lines of Figure 5.9, $\sigma_{eq} - \varepsilon_{eq,p}$ planes. The degree of overlap among the lines qualitatively

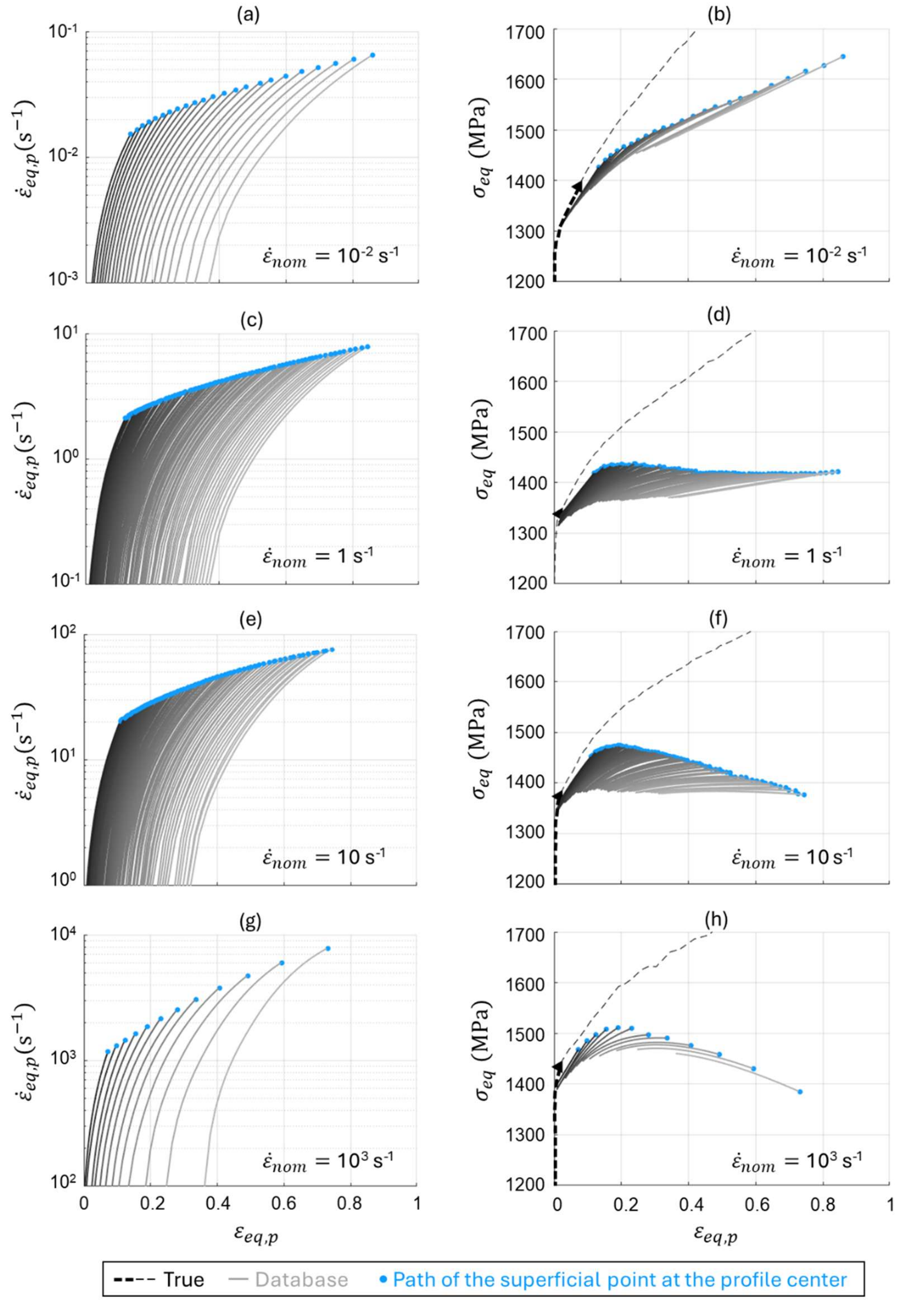

Figure 5.9 Material response (in the $\varepsilon_{eq,p} - \dot{\varepsilon}_{eq,p} - \sigma_{eq}$ space) during different tensile tests (one per condition), according to the database predictions; light blue dots refer to the profile center. [1]

indicates the effects of strain rate and thermal conduction within each test: the greater the divergence, the higher these effects.

Given the low thermal conductivity of 17-4PH, tests at 10^3 s^{-1} reasonably satisfied adiabatic conditions. This suggests that the divergence observed between loci of points in the $\sigma_{eq} - \varepsilon_{eq,p}$ plane is due to strain rate sensitivity combined with the strain rate heterogeneity that characterizes necking. Adiabaticity was verified referring to the Fourier number Fo, as anticipated in Section 5.1. By considering a characteristic length of conduction equal to half the initial gauge, $Fo_L \approx 2 \cdot 10^{-4}$ was obtained, which is two orders of magnitude lower than the adiabaticity threshold of 10^{-2} [14].

Tests at 10 s^{-1} resulted, instead, to lie at the boundary of adiabaticity, being $Fo_L \approx 1 \cdot 10^{-2}$. Furthermore, since heat conduction occurs both in the axial and in the radial direction, it is interesting to compute the Fourier number considering also the initial gauge radius as characteristic length. It resulted that $Fo_R \approx 4 \cdot 10^{-2}$, suggesting that the process is not fully adiabatic. Hence, for the test at 10 s^{-1}, the divergence between loci of points in the $\sigma_{eq} - \varepsilon_{eq,p}$ plane may be due to both strain rate sensitivity and thermal conduction. This statement holds even more so for the 1 s^{-1} test, for which $Fo_L \approx 1 \cdot 10^{-1}$.

Regardless of whether adiabatic conditions are verified or not, each 3D loci of points in the $\varepsilon_{eq,p} - \dot{\varepsilon}_{eq,p} - \sigma_{eq}$ space is representative of material response under given loading conditions. As anticipated, this data was enriched with experimental measurements of the superficial thermal field, thus obtaining for each loading condition a 4D point cloud in the $\varepsilon_{eq,p} - \dot{\varepsilon}_{eq,p} - T - \sigma_{eq}$ space.

The final step consisted of fitting the material response with a model that could then be easily implemented in FE simulations for the application of interest. More specifically, the chosen strategy consisted of fitting a unique material model to the different loading conditions altogether. An empirical model was chosen since it aligned more closely with the overall approach. More specifically, the following equation was employed:

$$\sigma_{eq} = f_1(\varepsilon_{eq,p})\, f_2(\log(\dot{\varepsilon}_{eq,p}))\, f_3(T). \tag{5.7}$$

To enhance adaptability a tabular definition was adopted, thus avoiding predefined influences of strain, strain rate and temperature. The strain-dependent term $f_1(\varepsilon_{eq,p})$ was directly obtained from the quasi-static test, since strain rate sensitivity was proved to be negligible in such condition (see Figure 5.9). Regarding the coefficients $f_2(\log(\dot{\varepsilon}_{eq,p}))$ and $f_3(T)$, simple linear functions were found to already provide satisfactory results. Since both coefficients must be set to 1 at standard conditions (room temperature and quasi-static strain rates), it resulted that two parameters were to be optimized for fitting the 4D point cloud. To this purpose, the error was computed according to the following expression:

$$error = \frac{1}{\sqrt{N}} \sum_{i=1}^{N} \frac{\sigma_{eq,i} - f_1(\varepsilon_{eq,p,i})\, f_2(\log(\dot{\varepsilon}_{eq,p,i}))\, f_3(T_i)}{\sigma_{eq,i}}. \tag{5.8}$$

A minimum of 2% was obtained with the coefficients displayed in Figure 5.10, alongside the cold curve $f_1(\varepsilon_{eq,p})$.

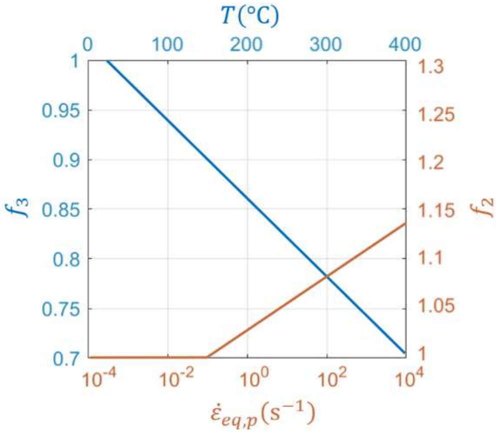

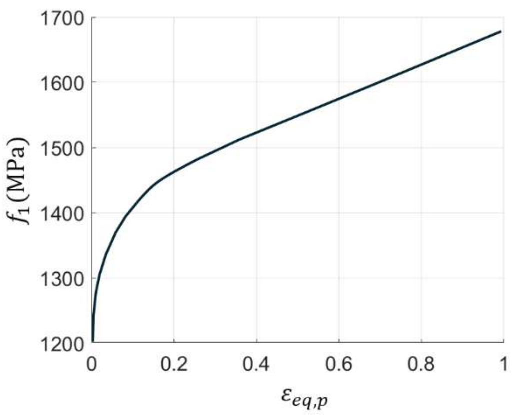

Figure 5.10 Functions of the model $\sigma_{eq} = f_1\left(\varepsilon_{eq,p}\right)f_2(\dot{\varepsilon}_{eq,p})f_3(T)$ representing material behavior according to the fitting of the 4D point cloud provided by the database-driven approach. [1]

It is important to remark that the material model was identified from dynamic tests conducted at initial room temperature. Temperature is, however, known to affect material behavior in two different ways: by facilitating dislocation motion (in the thermally activated regime) and by changing material structure (e.g., in terms of grain size, texture, etc.) [45]. Since the present model only accounts for the first contribution, its application is limited to self-heating scenarios. For dealing with applications characterized by different initial temperatures, further experiments for model calibration would be needed.

The accuracy of the identified material model was evaluated via FE simulations performed in Ansys LS-DYNA and subsequent comparison with experimental responses. The same FE model described in Section 3.3 was used, but it implemented the constitutive model obtained above (using material type *MAT_224). Accounting for self-heating during plastic deformation requires defining thermal properties, such as specific heat and thermal conductivity, as well as the work-to-heat conversion coefficient. This may introduce additional uncertainty. To limit this issue and focus mainly on assessing the capability of the identified model to reproduce the observed behavior, only isothermal and nearly adiabatic conditions were considered in this chapter. This included all test conditions except for the test performed at a nominal strain rate of 1 s^{-1} which would require a fully coupled thermo-mechanical analysis to properly account for heat conduction. All other tests could be, instead, simulated through structural-only analyses. For adiabatic simulations, a Taylor-Quinney coefficient of 0.95 was used, according to preliminary estimation that assumed the density and specific heat to be 7800 kg/m^3 and 460 J/(kg·K), respectively.

The results of the FE simulations are shown in Figure 5.11 in comparison with experimental data in terms of radial engineering curves, geometric profiles, and temperature evolution.

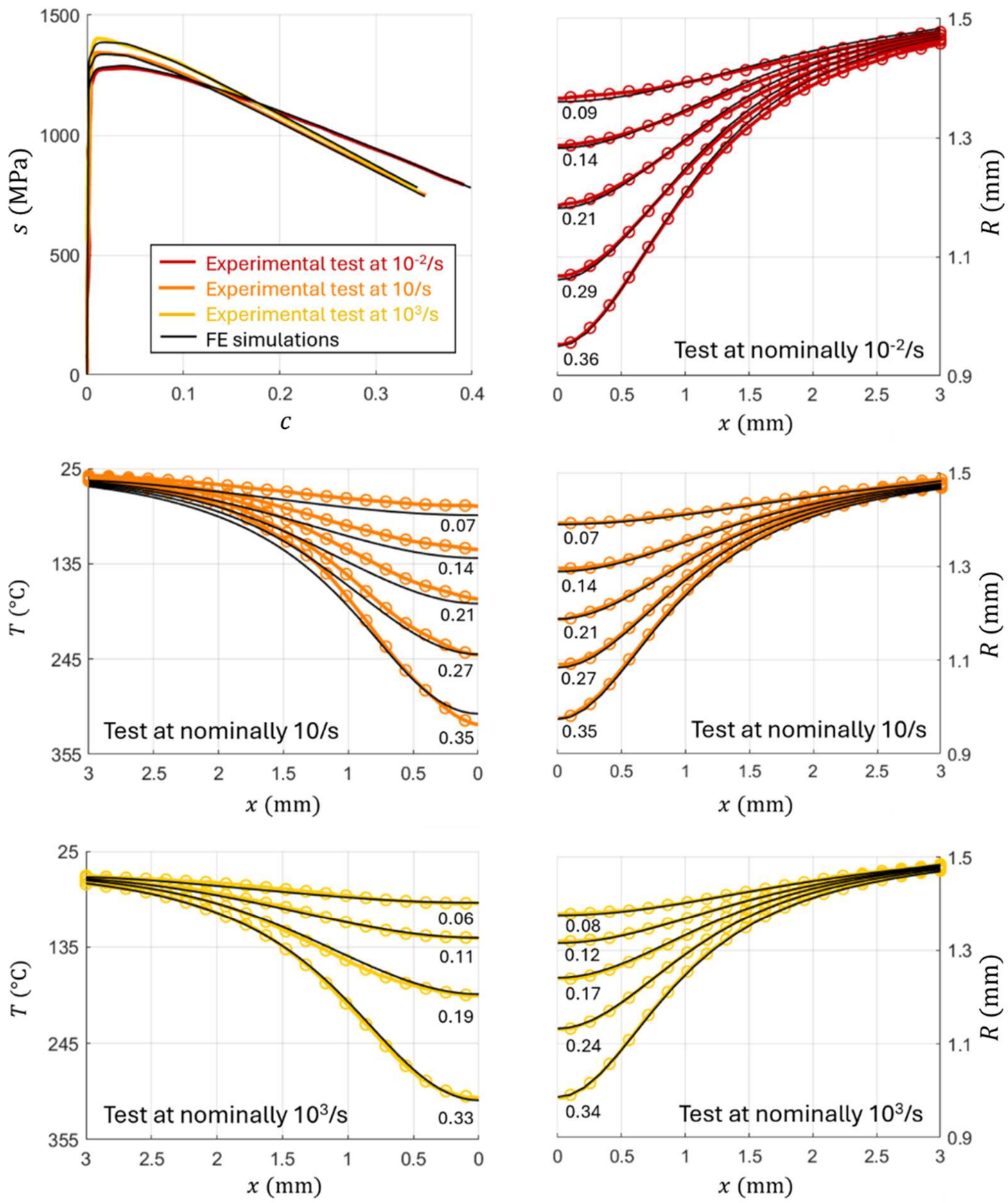

Figure 5.11 Comparison between experimental and numerical results, predicted with the identified model, in terms of engineering radial curve, necking profiles and temperature profiles (for dynamic tests); next to each geometric and thermal profile, the corresponding value of c is written. [1]

A very good agreement is observed for all tests, proving the potentiality of the method. Slightly larger discrepancies can be found in the temperature distributions for the test at nominally 10 s^{-1}. This can be attributed to the fact that this test condition is only nearly adiabatic, so that heat conduction may still affect the temperature field without compromising force and deformation predictions.

5.6 Concluding remarks

This chapter addressed the strain rate-temperature interaction that characterizes testing conditions in which self-heating occurs. It was shown that the database-driven methodology developed in Chapter 4 can be directly applied to such conditions. Indeed, the approach relies on the idea that, even if not all relevant variables are explicitly included in the database, the latter can still provide a good approximation of the instantaneous stress distribution on the specimen surface based solely on the deformed geometry, independently of the physical variables that generated it. Then, if the objective is to identify the plastic flow surface, such stress distribution can be associated with the distributions of the physical variables affecting plastic response. For instance, the strain and strain rate distributions can be estimated through the database, while other variables that cannot be inferred from it can be measured experimentally, such as temperature via infrared imaging.

During dynamic tests, the proposed approach provides, for each necking configuration, the quadruplets $(\varepsilon_{eq,p}, \dot{\varepsilon}_{eq,p}, T, \sigma_{eq})$ experienced by superficial material points. By simply applying it to multiple configurations of different tests, the plastic flow hypersurface can be progressively enriched. The capability of identifying material response as a point cloud represents a significant advantage of the proposed approach for thermo-visco-plastic characterization. It does not require any hypotheses on whether tests are adiabatic or not and on material behavior, in addition to isotropic Von Mises plasticity.

A tensile campaign on martensitic stainless steel 17-4 PH was used as experimental case study for the proposed method. The identified point cloud was fitted with a tabularly defined material model for strain, strain rate and temperature dependencies. The resulting model was able to successfully predict experimental results for tests under isothermal and nearly adiabatic conditions. This was shown to be valid also in terms of superficial thermal fields, despite the preliminary assumption of constant Taylor-Quinney coefficient. The next chapter focuses on further exploiting thermal measurements combined with the database-driven approach to gain insight into the work-to-heat conversion during non-isothermal tests, whether adiabatic conditions are verified or not.

References

[1] Beltramo, M., Peroni, L., & Scapin, M. (2025). A data-driven procedure for the analysis of high strain rate tensile tests via visible and infrared image processing. *International Journal of Impact Engineering*, *199*, 105232.

[2] Mason, J. J., Rosakis, A. J., & Ravichandran, G. (1994). On the strain and strain rate dependence of the fraction of plastic work converted to heat: an experimental study using high speed infrared detectors and the Kolsky bar. *Mechanics of Materials*, *17*(2-3), 135-145.

[3] Taylor, G. I., & Quinney, H. (1934). The latent energy remaining in a metal after cold working. *Proceedings of the Royal Society of London. Series A, Containing Papers of a Mathematical and Physical Character*, *143*(849), 307-326.

[4] Bever, M. B., Holt, D. L., & Titchener, A. L. (1973). The stored energy of cold work. *Progress in materials science*, *17*, 5-177.

[5] Hodowany, J., Ravichandran, G., Rosakis, A. J., & Rosakis, P. (2000). Partition of plastic work into heat and stored energy in metals. *Experimental mechanics*, *40*(2), 113-123.

[6] Macdougall, D. (2000). Determination of the plastic work converted to heat using radiometry. *Experimental mechanics*, *40*(3), 298-306.

[7] Rittel, D., Zhang, L. H., & Osovski, S. (2017). The dependence of the Taylor–Quinney coefficient on the dynamic loading mode. *Journal of the Mechanics and Physics of Solids*, *107*, 96-114.

[8] Zhang, T., Guo, Z. R., Yuan, F. P., & Zhang, H. S. (2018). Investigation on the plastic work-heat conversion coefficient of 7075-T651 aluminum alloy during an impact process based on infrared temperature measurement technology. *Acta Mechanica Sinica*, *34*(2), 327-333.

[9] Vazquez-Fernandez, N. I., Soares, G. C., Smith, J. L., Seidt, J. D., Isakov, M., Gilat, A., ... & Hokka, M. (2019). Adiabatic heating of austenitic stainless steels at different strain rates. *Journal of Dynamic Behavior of Materials*, *5*(3), 221-229.

[10] Soares, G. C., & Hokka, M. (2021). The Taylor–Quinney coefficients and strain-hardening of commercially pure titanium, iron, copper, and tin in high rate compression. *International Journal of Impact Engineering*, *156*, 103940.

[11] Kingstedt, O., Lew, A., Pratt, M., Salehi, S. D., & Rao, S. (2024). Investigation of thermomechanical coupling in inconel 718 at homologous temperatures of 0.2 and 0.5. *Metallurgical and materials transactions A*, *55*(9), 3591-3600.

[12] Lew, A., Loeffler, C., Varga, J., Jones, A., Salehi, S. D., & Kingstedt, O. T. (2025). A comparison of techniques to measure the conversion of plastic work to heat in 304L stainless steel under adiabatic conditions. *International Journal of Impact Engineering*, *198*, 105220.

[13] Smith, J. L., Seidt, J. D., Fietek, C. J., & Gilat, A. (2025). Taylor-Quinney coefficient determination from simultaneous strain and temperature measurements of uniform and localized deformation in tensile tests. *Journal of the Mechanics and Physics of Solids*, *199*, 106099.

[14] Zehnder, A. T., Babinsky, E., & Palmer, T. (1998). Hybrid method for determining the fraction of plastic work converted to heat. *Experimental mechanics*, *38*(4), 295-302.

[15] Goviazin, G. G., Shirizly, A., & Rittel, D. (2023). A comparative study of the performance of IR detectors vs. high-speed cameras under dynamic loading conditions. *Experimental Mechanics*, *63*(1), 115-124.

[16] Soares, G. C., Vázquez-Fernández, N. I., & Hokka, M. (2022). Simultaneous full-field strain and temperature measurements in high strain rate testing. In *Advances in Experimental Impact Mechanics* (pp. 255-285). Elsevier.

[17] Chrysochoos, A., & Louche, H. (2000). An infrared image processing to analyse the calorific effects accompanying strain localisation. *International journal of engineering science*, *38*(16), 1759-1788.

[18] Louche, H., & Chrysochoos, A. (2001). Thermal and dissipative effects accompanying Lüders band propagation. *Materials Science and Engineering: A*, *307*(1-2), 15-22.

[19] Schlosser, P., Louche, H., Favier, D., & Orgéas, L. (2007). Image processing to estimate the heat sources related to phase transformations during tensile tests of NiTi tubes. *Strain*, *43*(3), 260-271.

[20] Dumoulin, S., Louche, H., Hopperstad, O. S., & Børvik, T. (2010). Heat sources, energy storage and dissipation in high-strength steels: Experiments and modelling. *European Journal of Mechanics-A/Solids*, *29*(3), 461-474.

[21] Louche, H., Vacher, P., & Arrieux, R. (2005). Thermal observations associated with the Portevin–Le Châtelier effect in an Al–Mg alloy. *Materials Science and Engineering: A*, *404*(1-2), 188-196.

[22] Ait-Amokhtar, H., Fressengeas, C., & Boudrahem, S. (2008). The dynamics of Portevin–Le Chatelier bands in an Al–Mg alloy from infrared thermography. *Materials Science and Engineering: A*, *488*(1-2), 540-546.

[23] Gilat, A., Kuokkala, V. T., Seidt, J. D., & Smith, J. L. (2017). Full-field measurement of strain and temperature in quasi-static and dynamic tensile tests on stainless steel 316L. *Procedia Engineering*, *207*, 1994-1999.

[24] Seidt, J. D., Kuokkala, V. T., Smith, J. L., & Gilat, A. (2017). Synchronous full-field strain and temperature measurement in tensile tests at low, intermediate and high strain rates. *Experimental Mechanics*, *57*(2), 219-229.

[25] Smith, J. L., Seidt, J. D., & Gilat, A. (2018, October). Full-Field Determination of the Taylor-Quinney coefficient in tension tests of Ti-6Al-4V at strain rates up to 7000 s-1. In *Advancement of Optical Methods & Digital Image Correlation in Experimental Mechanics, Volume 3: Proceedings of the 2018 Annual Conference on Experimental and Applied Mechanics* (pp. 133-139). Cham: Springer International Publishing.

[26] Kauder, L. (2005). *Spacecraft thermal control coatings references* (No. NASA/TP-2005-212792).

[27] Salehi, S. D., & Kingstedt, O. (2023). Critical assessment and demonstration of high-emissivity coatings for improved infrared signal quality for Taylor–Quinney coefficient experimentation. *International Journal of Impact Engineering*, *178*, 104593.

[28] Rittel, D., Bhattacharyya, A., Poon, B., Zhao, J., & Ravichandran, G. (2007). Thermomechanical characterization of pure polycrystalline tantalum. *Materials Science and Engineering: A*, *447*(1-2), 65-70.

[29] Johnson, G. R. (1983). A constitutive model and data for metals subjected to large strains, high strain rates and high temperatures. In *Proceedings of the 7th International Symposium on Ballistics, The Hague, Netherlands, 1983*.

[30] Zerilli, F. J., & Armstrong, R. W. (1987). Dislocation-mechanics-based constitutive relations for material dynamics calculations. *Journal of applied physics*, *61*(5), 1816-1825.

[31] Follansbee, P. S. (2014). *Fundamentals of strength*. Wiley NJ, 10, 9781118808412.

[32] Song, B., & Sanborn, B. (2019). A modified Johnson–Cook model for dynamic response of metals with an explicit strain-and strain-rate-dependent adiabatic thermosoftening effect. *Journal of Dynamic Behavior of Materials*, *5*(3), 212-220.

[33] Gambirasio, L., & Rizzi, E. (2014). On the calibration strategies of the Johnson–Cook strength model: Discussion and applications to experimental data. *Materials Science and Engineering: A*, *610*, 370-413.

[34] Vilamosa, V., Clausen, A. H., Børvik, T., Holmedal, B., & Hopperstad, O. S. (2016). A physically-based constitutive model applied to AA6082 aluminium alloy at large strains, high strain rates and elevated temperatures. *Materials & Design*, *103*, 391-405.

[35] Sasso, M., Newaz, G., & Amodio, D. (2008). Material characterization at high strain rate by Hopkinson bar tests and finite element optimization. *Materials Science and Engineering: A*, *487*(1-2), 289-300.

[36] Sedighi, M., Khandaei, M., & Shokrollahi, H. (2010). An approach in parametric identification of high strain rate constitutive model using Hopkinson pressure bar test results. *Materials Science and Engineering: A*, *527*(15), 3521-3528.

[37] Milani, A. S., Dabboussi, W., Nemes, J. A., & Abeyaratne, R. C. (2009). An improved multi-objective identification of Johnson–Cook material parameters. *International journal of impact engineering*, *36*(2), 294-302.

[38] Scapin, M., Peroni, L., & Peroni, M. (2012). Parameters identification in strain-rate and thermal sensitive visco-plastic material model for an alumina dispersion strengthened copper. *International Journal of Impact Engineering*, *40*, 58-67.

[39] Zinovev, A., Delannay, L., & Terentyev, D. (2021). Plastic deformation of ITER specification tungsten: Temperature and strain rate dependent constitutive law deduced by inverse finite element analysis. *International Journal of Refractory Metals and Hard Materials*, *96*, 105481.

[40] Scapin, M., Peroni, L., & Carra, F. (2016). Investigation and mechanical modelling of pure molybdenum at high strain-rate and temperature. *Journal of Dynamic Behavior of Materials*, *2*(4), 460-475.

[41] Yao, D., Guan, Y., Li, M., Zhang, Y., & Duan, Y. (2023). Inverse identification method for determining stress–strain curves of sheet metals at high temperatures. *Engineering Fracture Mechanics*, *284*, 109246.

[42] Beltramo, M., Scapin, M., & Peroni, L. (2025). Analysis of the work-to-heat conversion beyond the necking onset in non-isothermal tensile tests. *International Journal of Impact Engineering*, 105503.

[43] Tvergaard, V., & Needleman, A. (1984). Analysis of the cup-cone fracture in a round tensile bar. *Acta metallurgica*, *32*(1), 157-169.

[44] Huh, H., Ahn, K., Lim, J. H., Kim, H. W., & Park, L. J. (2014). Evaluation of dynamic hardening models for BCC, FCC, and HCP metals at a wide range of strain rates. *Journal of Materials Processing Technology*, *214*(7), 1326-1340.

[45] Peroni, L., Scapin, M., & Song, B. (2024). Dynamic behavior of metals and alloys designed for high-temperature applications. In *Dynamic Behavior of Materials* (pp. 339-372). Elsevier.

Chapter 6

Work-to-heat conversion in non-isothermal tests

Accounting for the conversion of plastic work into heat is important in both material characterization and engineering applications involving large plastic deformation under dynamic conditions. It is well-known that material temperature rises if the deformation process is sufficiently fast, and this temperature increase may in turn affect the mechanical response of the material. Accurate prediction of temperature fields and consequent mechanical response depends not only on a reliable constitutive model, as highlighted in Chapter 5, but also on the knowledge of the fraction of plastic work converted into heat. In thermo-mechanics, this fraction is referred to as Taylor-Quinney Coefficient β (TQC), named after the researchers who first investigated this issue experimentally [1]. This coefficient and the heat conduction equation governing coupled thermo-mechanical problems in solids have been already introduced in Section 5.1. The present chapter investigates how the database-driven approach can be used to characterize effectively this phenomenon during the post-necking phase of non-isothermal tensile tests.

First, combining the database-driven approach with tracking of superficial material points allows the plastic work done on each point to be estimated. Then, by comparing it with the thermal history of those points the work-to-heat conversion coefficient can be identified via Equation 5.3, provided that adiabaticity holds. Conversely, under non-adiabatic conditions, the database-driven approach can still be used for thermo-visco-plastic identification (as explained in Chapter 5), but then some iterations are needed to characterize the work-to-heat conversion. This is because of thermal heat conduction, which is difficult to be directly accounted for.

Figure 6.1 provides a concise yet complete overview of both methods, highlighting that, in any case, for applying the database-driven approach, it is necessary to monitor the test with optical and infrared cameras and to acquire the applied load. Then, which of the two strategies should be adopted depends on whether adiabatic conditions are verified or not: one approach is characterized by higher versatility, while the other by higher efficiency when applicable.

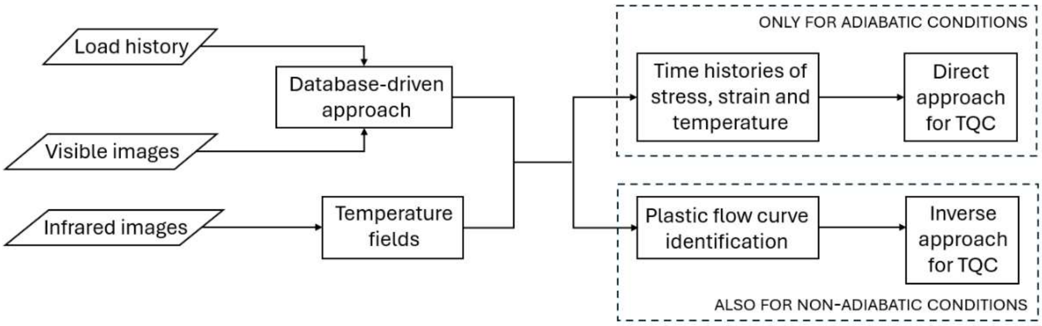

Figure 6.1 Workflow of the proposed methods for investigating the work-to-heat conversion (adapted from [2]).

Before going into the details of the two approaches, in Section 6.2 and 6.3 respectively, an overview of past research on the coupling between plastic deformation and heat generation is provided in Section 6.1. This aims to show how this phenomenon was investigated in the past and which advantages can be obtained with these newly proposed methods. Finally, the practical application of the proposed methods is illustrated with the experimental case study of Chapter 5. The work presented in this chapter has been published in [2].

6.1 Literature background

A comprehensive review of the work-to-heat conversion was recently presented by Nassar [3]. The present section focuses on studies that proposed particularly relevant approaches or reported significant results in relation to the methods introduced in this chapter.

Over the past decades, both physical and phenomenological approaches have been used. The first were based on the mechanisms underlying the energy storage in metals, hence they include models founded on the residual stress theory or on the dislocation theory, as done by Aravas et al. [4] and Zehnder respectively [5] in the early nineties. More recently, thermodynamically consistent frameworks for stored energy were developed, for instance by Rosakis et al. [6] and Lieou and Bronkhorst [7]. Meanwhile, more insights into the physics of stored energy were provided by advanced numerical methods, like crystal plasticity [8], dislocation dynamics [9], and molecular dynamics [10]. These studies highlighted the complexity of the phenomenon, which cannot be described with simple physically based models. Conversely, phenomenological approaches for investigating work-to-heat conversion lack direct physical interpretation but offer a relatively easier way of analysis. They are able to provide experimentally informed TQC, which is particularly attractive for industrial applications. The following paragraphs focus on phenomenological approaches for establishing the context of the novel strategies proposed in this chapter which belong to this category too, since they rely on the database-driven approach.

Under adiabatic conditions, empirical methods usually entailed applying the heat equation to experimental data. The equation was already presented in Chapter 5, but is recalled here for the sake of readability:

$$\dot{T} = \frac{\beta}{\rho c_p}\dot{W}_p. \tag{6.1}$$

Once the physical quantities ρ and c_p had been measured or assumed, the TQC β can be determined by considering the time derivatives of both the temperature and the plastic work of material points. This is why past research usually referred to this variable as β_{diff}. Being based on derivatives, this quantity is prone to noise and can be unstable. Hence, an engineering evaluation of the TQC, denoted as β_{int} was sometimes preferred, especially in combination with experimental analyses. Specifically, this quantity was defined as:

$$\beta_{int} = \frac{\rho c_p \Delta T}{W_p}, \tag{6.2}$$

being W_p and ΔT the total plastic work and temperature rise until a given time of the test. This quantity was used in many works, such as Kapoor and Nemat-Nasser [11], Rittel et al. [12], Zhang et al. [13], Kingstedt et al. [14], and Lew et al. [15]. However, as first pointed out by Rittel [16], β_{int} cannot reflect the work-to-heat evolution during deformation, so that β_{diff} is more adequate for material constitutive description.

For applying Equations 6.1 or 6.2, plastic work was estimated based on experimental measurements of strains and stresses. Since adiabatic conditions generally resulted from high strain rate tests carried out with Hopkinson bar apparatuses, strains and stresses were determined with the theory one-dimensional wave propagation if specimen deformation was uniform [12-15, 17-20]. Regarding temperature measurements in these high strain rate tests, infrared detectors were commonly employed thanks to their short response time and high acquisition rates [12, 13, 17-19], as already mentioned in Section 5.2. Nevertheless, for dealing with heterogeneous thermal fields, which may also occur under adiabatic conditions in case of localized deformation, infrared imaging was used. In the field of work-to-heat conversion, these measurements were often integrated with DIC technique, as deeply discussed in the review by Soares et al. [21]. In such cases, spatial synchronization was needed for adopting the Lagrangian viewpoint required by Equations 6.1 or 6.2. For instance, Smith et al. [22] performed a projective transformation on the coordinates of the infrared image pixels to map the measured temperatures to the coordinate space of the DIC image.

Infrared imaging was also commonly adopted in case of non-adiabatic self-heating conditions and, as for adiabatic conditions, it was usually combined with DIC measurements. Regarding spatial synchronization, it is worth citing the motion compensation technique applied by Pottier et al. [23] and the algorithm to map the deformation field to the thermal one employed by Nowak and Maj [24]. Conversely, Dæhli et al. [25] chose to avoid such complex approaches by limiting the analysis to the maximum temperature achieved within a predefined subdomain. This was possible since the study regarded notched sheet specimens, for which the maximum temperature is known to be reached in the central region of the sample. However, using this thermal data for investigating the TQC in non-adiabatic test requires accounting for all heat transfer phenomena, mainly conduction and convection. Knysh and Korkolis [26], for instance, adopted a Eulerian viewpoint by focusing on a single point, fixed in space, and applying Equation 5.1 (in its Eulerian formulation). This was enabled by considering only the pre-necking phase of tensile tests conducted on specimen slender enough to be subjected to uniaxial stress state. Generally, however, this simplification was not feasible and FEMU approaches were used instead. Nevertheless, in low strain rate tests a different simplification is possible: plastic and thermal responses could be uncoupled thanks to the limited temperature increments. First, an optimization identified the plastic flow curve using the engineering response as target function, then another optimization determined the TQC by comparing temperatures [23, 25]. The main drawback is the typical one of FEMU methods: they are computationally expensive, especially when a lot of parameters need to be identified.

Regarding the experimental tests used for investigating the work-to-heat conversion, tensile tests have been widely used, given their ease of execution and the possibility of exploring different strain rates and/or temperatures. Much research focused on the pre-necking phase [12, 15, 27], however post-necking data can provide further insights into the TQC, especially at large deformation. Indeed, if temperature rises are of utmost importance during localization, then this phase can also be exploited to gain information about work-to-heat conversion. This was done, for instance, by Smith et al. [22], who estimated the TQC at different locations along the length of flat specimens by combining full-filed strain and temperature measurements. Nevertheless, this study was limited to adiabatic scenarios. The methods proposed in the next section developed further the idea of exploiting post-necking deformation to investigate the TQC. By adopting the database-driven approach, the experimental effort is reduced since only the specimen silhouette is required. This makes the method suitable for cases where DIC measurements are not available (e.g., on cylindrical specimens). Furthermore, a method adequate also for non-adiabatic test conditions is proposed.

6.2 Direct approach

This section presents a method for determining the TQC during necking under adiabatic conditions by directly applying the heat equation; this is why it will be referred to as “Direct approach”. As other direct strategies proposed in the literature, it entails measuring the temperature history of material points, as well as their equivalent plastic strain and equivalent stress histories (needed for computing the plastic work). While temperature is obtained by post-processing infrared images, as commonly done, equivalent plastic strain and equivalent stress are derived by adopting the database-driven approach explained in Section 4.2. Nevertheless, both infrared camera and the database-driven approach offer a Eulerian viewpoint of the deformation process.

On one hand, the Eulerian formulation of the heat equation could in principle be used for investigating the TQC. However, even in the simplest case of adiabaticity and negligible thermoelasticity, the velocity field and temperature gradient would be needed, but there could be difficulties and uncertainties in computing them. On the other hand, the Lagrangian expression of Equation 6.1 could be used, provided that superficial material points are tracked during deformation. Tracking allows equivalent plastic strain, equivalent stress and temperature to be converted from a Eulerian to a Lagrangian perspective.

Overall, the second strategy is preferred. The equivalent plastic strain and equivalent stress histories of different material points are used to compute the plastic work associated with each material point by integrating its path in the $\sigma_{eq} - \varepsilon_{eq,p}$ plane. Then, comparing them with temperature rises via Equations 6.1 or 6.2 provides the evolution of β_{diff} and β_{int} during necking. Finally, for each material point, it is possible to plot the identified TQC as a function of the equivalent plastic strain, strain rate and/or temperature experienced by that point. This highlights TQC's dependencies on such variables, even within a single test. In this sense, direct methods are advantageous since they provide insights into these dependencies without relying on any *a priori* assumptions. This is important since past research proved that the work-to-heat conversion can depend on strain [15, 16, 18, 20, 25, 27, 28] and the strain rate [15, 16, 18, 27, 29].

Furthermore, applying the proposed method to several material points enhances stability and reliability of the results. However, when images are acquired in backlight to facilitate edge detection, only the profile center is tracked straightforwardly during necking. Thus, a technique for tracking also other material points during necking, even with a backlight imaging setup, was developed. Section 6.2.1 is devoted to explaining this method, while Section 6.2.2. presents a numerical benchmark to test this novel direct TQC identification strategy.

6.2.1 Tracking strategy

In this section, a novel strategy for tracking superficial points during necking is proposed. Unlike traditional techniques that track markers painted on the specimen itself and recorded by a camera, this proposal simply relies on the silhouette evolution.

The theoretical foundations of the present approach lie in the 1D necking model developed by Audoly and Hutchinson [30, 31] for axisymmetric bars. It consists of an analytical framework that describes necking by adopting a Lagrangian viewpoint. The key outcome exploited here is the material independence of the relationship between material points' coordinates in the undeformed configuration and the corresponding coordinates in a given deformed configuration. Audoly and Hutchinson shown it to be valid for both strain rate insensitive [30] and sensitive materials [31]. More specifically, deformed and undeformed coordinates were proved to be related to each other through the silhouette itself but regardless of the material that led to that specific silhouette. This means that, once material points in the undeformed configuration have been selected, it is possible to determine their position in each deformed configuration of interest, by simply knowing the corresponding silhouette. Hence, by considering the same undeformed coordinates and subsequent silhouettes, material points can be tracked. Focusing on superficial material points of initial coordinates (x_0, R_0), this means identifying their coordinates (x, R) on the specimen outer surface at subsequent times.

The mathematical expressions of the 1D model are reported at the beginning of Appendix A but are not directly employed here. The precomputed FE database established in Section 2.3 already contains the correlation between undeformed and deformed coordinates of material points. Hence, when a numerical shape is found to match well with the experimental one, the experimental undeformed-deformed correlation coincides with the numerical one. Then, the numerical correlation can be interpolated on the initial coordinates of interest, and their deformed position is determined.

Nevertheless, the numerical shapes of the database and the experimental one are compared in normalized terms due to the pre- and post-necking uncoupling discussed in Section 2.2. This must be taken into account when attributing the numerical undeformed-deformed correlation to the corresponding experimental configuration. As done in Section 4.2 for different variables, it is necessary to post-process properly the undeformed-deformed correlation to compensate for the different necking onset that may characterize the experimental and numerical configurations. To this aim, it is required to identify which material points of the numerical model best represent experimental ones.

Referring to Figure 6.2a, consider that the numerical profile shown as orange solid line is the one that best matches the outer shaper of the deformed specimen (gray region), after proper scaling (dashed orange line). Numerical material points that, after scaling, overlap with experimental ones are those that best represent experimental points. In Figure 6.2a they are plotted as orange vertical markers overlapping black dots. For instance, points $\left(x_{exp,i}, R_{exp,i}\right)$ and $\left(x_{db,i}, R_{db,i}\right)$ represent analogous point: $x_{db,i} = x_{exp,i}k_g$ and $R_{db,i} = R_{exp,i}k_g$. It is evident that, despite being coincident in the deformed configuration, these analogous points differ in the undeformed configuration. Thus, the corresponding undeformed-deformed correlations are apparently different between the experiment and the simulation. Nevertheless, the 1D model by Audoly and Hutchinson can be used to identify the relationship between initial coordinates of experimental and numerical points that appear analogous in the deformed configuration. Specifically, if $R_{0,db} =$

$R_{0,exp}$ it resulted that $x_{0,db,i} = k_g^3 x_{0,exp,i}$. This proves that accounting for the different necking onsets actually allows the two undeformed-deformed correlations to become analogous one to another. Complete analytical derivations are reported in Appendix A.

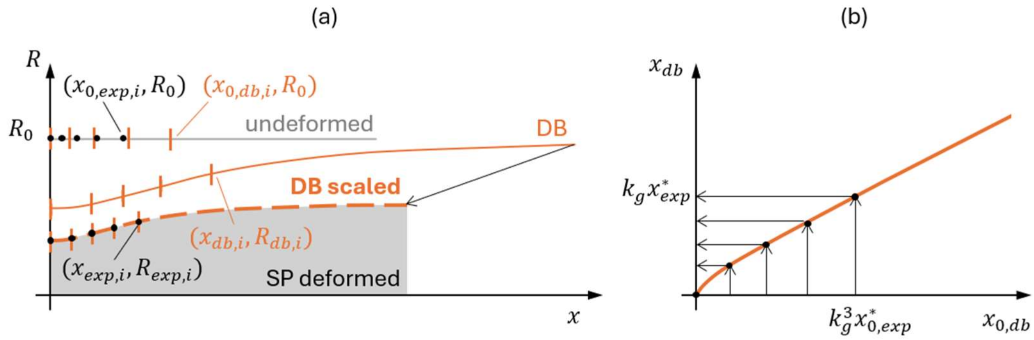

Figure 6.2 Tracking material points during necking: the numerical shape that best matches the experimental one (a) establishes the undeformed-deformed axial position correlation (b), that is interpolated to estimate the deformed position of experimental material points (adapted from [2]).

Coming to the practical aspects of the tracking procedure, a set of points characterized by initial coordinates $x^*_{0,exp}$ is selected on the specimen's outer surface. For each experimental necking silhouette, the best-matching shape of the FE database is identified together with the scaling coefficient k_g, as explained in Section 3.1. Then, numerical material points analogous to the selected experimental ones are those characterized by initial coordinates $x^*_{0,db} = k_g^3 x^*_{0,exp}$. Since the FE simulation provides the relationship between $x_{0,db}$ and x_{db} at the given configuration, this can be interpolated at $x^*_{0,db}$ as shown in Figure 6.2b. This allows the deformed position x^*_{db}, coincident with x^*_{exp}, to be determined. By applying this process to subsequent necking silhouettes, i.e., at subsequent times during necking, superficial material points are tracked throughout the deformation. The potential concern related to applying this tracking technique to dog-bone specimens, despite being the theoretical framework developed for slender bars, is addressed with numerical investigations in the following section.

6.2.2 Numerical examples

Two ad-hoc numerical benchmarks are presented in this section, with the aim of showing the accuracy of the proposed tracking technique and of the direct method for TQC identification during necking of cylindrical dog-bone specimens. The two benchmarks differ from one another for the TQC, which was considered constant in one case and dependent on equivalent plastic strain in the other (indicated in the remainder as strain-dependent TQC for the sake of conciseness). This was motivated by the fact that past research highlighted the possible dependence of work-to-heat conversion on various factors, among which plastic strain.

Ansys LS-DYNA was used for simulating monotonic tensile tests on dog-bone cylindrical specimens characterized by the same geometry used throughout this thesis, namely a 5 mm gauge length and 3 mm gauge diameter. The FE model shared the same features as that described in Section 3.3 and depicted in Figure 3.5. Regarding the material, Armco Iron was considered since its considerable strain rate and thermal sensitivity make it a relevant case study. Specifically, the Johnson-Cook model was used, as reported hereinafter and according to Johnson and Cook's work [32]:

$$\sigma_{eq} = \left(175 + 380\varepsilon_{eq,p}^{0.32}\right)\left(1 + 0.06\ln\dot{\varepsilon}_{eq,p}\right)\left(1 - \left(\frac{T-298}{1811-298}\right)^{0.55}\right). \text{(MPa)} \tag{6.3}$$

This model was actually implemented as a tabular one with strain rate and thermal uncoupling that also allowed for introducing a variable TQC (*MAT_224). Then, to be consistent with Johnson and Cook's work [32], the density and heat capacity were assumed to be constant and equal to 7890 kg/m^3 and 452 J/(kg·K) respectively. A structural-only simulation was run since adiabatic conditions were considered, in agreement with the hypothesis of the direct approach.

The numerical simulations were then considered as if they were real experiments: several necking configurations were chosen and the tracking technique explained in Section 6.2.1 was applied. By choosing to track material points that coincided with FE nodes it was possible to evaluate directly the prediction of the proposed strategy.

Figure 6.3 shows some necking silhouettes for the case of variable TQC, providing a comparison between node positions x_{ij} known from the simulation and their predictions $\tilde{x}_{ij}$ from tracking. This plot proves that a good agreement was obtained but points farther from the neck are affected by a larger discrepancy. This can be attributed to geometrical differences between the dog-bone specimen of the case study and the slender bars of the database.

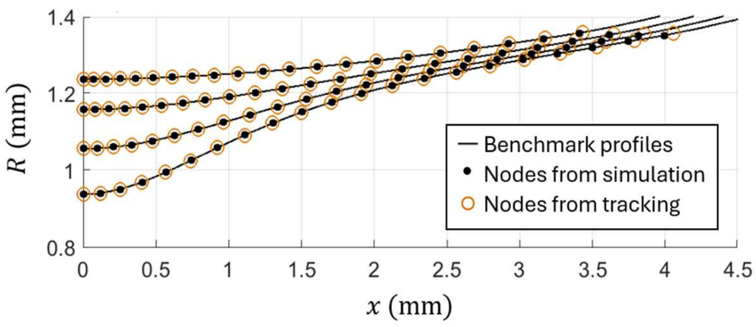

$x_{0,max}$ (mm)	Error (%)
2.50	0.29
2.30	0.24
2.1	0.21
1.9	0.19
1.7	0.19
1.6	0.19

Figure 6.3 Comparison between the nodes' position estimated by tracking and the actual one in the numerical benchmark of strain-dependent TQC; the table collects the average errors (Equation 6.9) obtained by varying the axial portion considered $x_0 \leq x_{0,max}$ (in a Lagrangian perspective) [2].

In addition, Figure 6.3 presents a table with a quantitative analysis of the tracking error. This was evaluated as relative difference between the reference value x_{ij} and the estimated one $\tilde{x}_{ij}$, then averaged over the different N_n nodes in the gauge length and over the different N_{cfg} configurations. For the sake of clarity, the expression is explicitly written hereinafter:

$$error = \frac{1}{N_{cfg}} \sum_{i=1}^{N_{cfg}} \left[\frac{1}{N_n} \sum_{j=1}^{N_n} \left(\frac{x_{ij} - \tilde{x}_{ij}}{x_{ij}} \right) \right]. \tag{6.4}$$

The table reports how this error varies when considering smaller portions of the initial gauge length. In practice, the error was evaluated considering only the nodes up to a maximum distance $x_{0,max}$ from the profile center and $x_{0,max}$ is progressively reduced. The resulting trend is reasonable considering the geometrical effects mentioned above.

The same analysis was carried out for the case of constant TQC and similar results were obtained. Overall, a maximum tracking error of about 0.3% (corresponding to having considered the whole gauge length) was obtained for both cases of constant and variable TQC. This can be considered as a relatively low error, thus demonstrating the accuracy of the developed tracking strategy.

After having successfully tracked material points, the next step required for TQC identification consisted of converting the superficial distributions $\varepsilon_{eq,p}(x)$ and $\sigma_{eq}(x)$ from Eulerian fields estimated with the database-driven approach (see Section 4.2) to Lagrangian fields. The accuracy of the estimated fields can be evaluated by comparing them with the actual fields computed by the FE simulation. Specifically, the error was computed for each material point as relative difference between the predicted and the actual values. Figure 6.4 graphically illustrates it for the case of variable TQC, but similar results were obtained for the constant TQC. In particular, error maps along the specimen silhouette and at different configurations (the same of Figure 6.3) are shown; for the sake of readability, each silhouette was normalized by its radius at the neck. A Lagrangian viewpoint was adopted by using the initial axial coordinate of material points as abscissa. Although this representation is in principle affected by tracking accuracy too, in practice it mainly reflects the accuracy of estimating equivalent plastic strain and equivalent stress fields. This is because tracking errors proved to be relatively low.

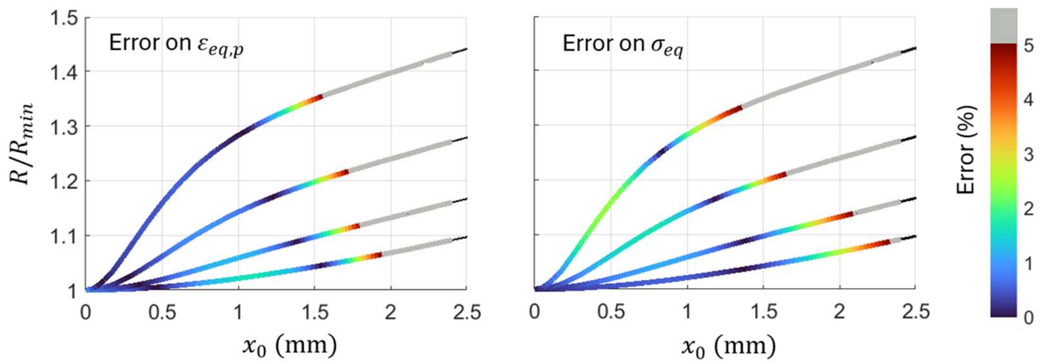

Figure 6.4 Error maps of the Lagrangian equivalent plastic strain and equivalent stress fields estimated with the database approach for the benchmark test with variable TQC. [2]

Overall, equivalent plastic strain and equivalent stress fields were found to be predicted quite well over a relatively wide portion. The larger discrepancies observable farther from the neck can be, again, ascribed to the geometrical difference between the case study and the database. Nevertheless, the resulting effect on the TQC identification is limited by the fact that progressive unloading causes the regions farther from the neck (or at least part of them) to not contribute to the plastic work.

Before moving on to TQC identification, it should be highlighted that the assumption of adiabaticity was not necessary for the above analyses. Indeed, both the tracking strategy and the database-driven approach are valid regardless of whether adiabatic conditions are met or not.

Conversely, adiabaticity becomes essential when directly comparing, for each material point of interest, the temperature rise and the plastic work for determining the TQC. For numerical benchmarks, temperatures were determined by interpolating the thermal field resulting from the FE simulation onto the points considered, while plastic work was computed as the integral of the $\sigma_{eq}(\varepsilon_{eq,p})$ path followed by the same material points. Then, Equation 6.2 was used to estimate β_{int} for different points and at different configurations, thus obtaining a point cloud.

This is shown in Figure 6.5a with orange dots for both cases of constant TQC (case I) and strain-dependent TQC (case II). For comparison reasons, Figure 6.5a also shows in black solid lines the β_{int} that would be expected for these numerical benchmarks. Indeed, β_{diff} was known because it represented the input for the FE simulations, and β_{int} could then computed as integral average of β_{diff}, according to the following expression:

$$\beta_{int}(\varepsilon_{eq,p}) = \frac{1}{\varepsilon_{eq,p}} \int_0^{\varepsilon_{eq,p}} \beta_{diff}(\tilde{\varepsilon}_{eq,p})\ d\tilde{\varepsilon}_{eq,p}, \tag{6.5}$$

in case of strain dependence. As expected, for the case of constant TQC, the integral and differential definitions coincide. Figure 6.5a shows that, for both cases I and II, theoretical expectations were captured well by the proposed direct approach.

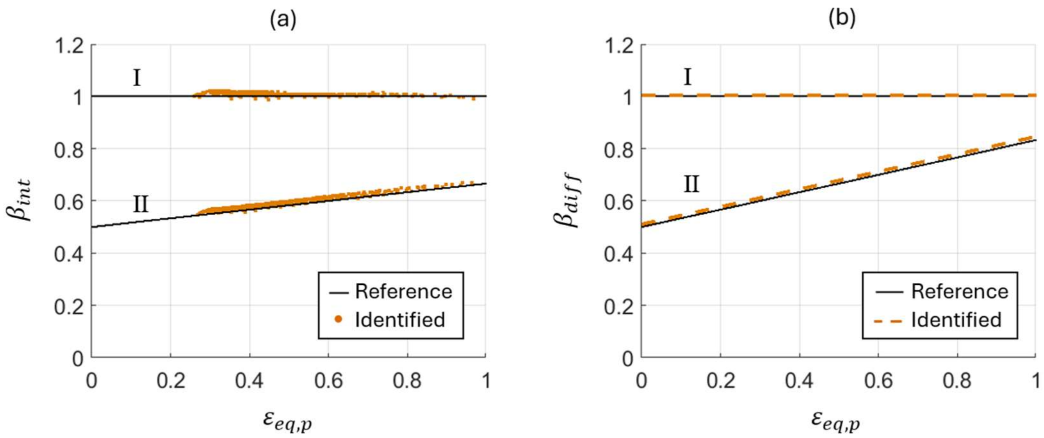

Figure 6.5 Result of the direct method applied to adiabatic tests with constant TQC (I) and strain-dependent TQC (II), in terms of $\beta_{int}(\varepsilon_{eq,p})$ (a) and $\beta_{diff}(\varepsilon_{eq,p})$ (b), in comparison with the reference laws. [2]

As discussed in Section 6.1, material behavior is better represented by β_{diff} rather than β_{int}. This could be determined through Equation 6.3, even though time differentiation may lead to noisy results. One possibility to limit this effect consists of fitting both the plastic work history and the temperature rise history with predefined functions to facilitate time differentiation. This was done, for instance, by Smith et al. [22]. In contrast, an alternative approach was adopted in the present analysis: each point cloud representing β_{int} was directly fitted with an analytical function, and the inverse formula of 6.5 was applied to derive β_{diff}.

To determine such inverse formulation, $B(\tilde{\varepsilon}_{eq,p})$ is first defined as the indefinite integral of β_{diff}:

$$B(\tilde{\varepsilon}_{eq,p}) \overset{\text{def}}{=} \int \beta_{diff}(\tilde{\varepsilon}_{eq,p})\, d\tilde{\varepsilon}_{eq,p}. \tag{6.6}$$

Then, by plugging this equation into Equation 6.5, it results that:

$$\beta_{int} = \frac{1}{\varepsilon_{eq,p}}\Big(B(\varepsilon_{eq,p}) - B(0)\Big), \tag{6.7}$$

and thus:

$$B(\varepsilon_{eq,p}) = \beta_{int}\varepsilon_{eq,p} + B(0). \tag{6.8}$$

Considering that Equation 6.6 can also be written as:

$$\beta_{diff} = \frac{dB}{d\varepsilon_{eq,p}}, \tag{6.9}$$

and plugging Equation 6.8 into 6.9, it is finally obtained that:

$$\beta_{diff}(\varepsilon_{eq,p}) = \frac{d\beta_{int}}{d\varepsilon_{eq,p}}\varepsilon_{eq,p} + \beta_{int}. \tag{6.10}$$

Hence, Equation 6.10 allows $\beta_{diff}(\varepsilon_{eq,p})$ to be analytically derived from a mathematical expression of $\beta_{int}(\varepsilon_{eq,p})$. The results are plotted in Figure 6.5b as dashed orange lines, in comparison with the reference TQC (black solid lines) inputted into the FE simulations. Again, the results were in good agreement for both cases I and II. This demonstrates the capability of the proposed direct method to estimate β_{int} and β_{diff} in both cases of constant and strain-dependent TQC. Furthermore, considering a wide axial region of the specimen enhanced reliability of the results with respect to considering only the profile center.

6.3 Inverse approach

This section addresses TQC identification during post-necking of tests conducted under non-adiabatic conditions. In such cases, using a direct approach to account for heat loss phenomena other than plastic dissipation would be challenging. For example, considering the heat conduction contribution in the heat equation (see Equation 5.1) would require estimating the Laplacian of the thermal field. Since internal temperature distribution influences this quantity but cannot be measured experimentally, assumptions on it would be necessary. However, introducing hypotheses may affect the reliability of the identification. Therefore, an inverse method, based on thermo-mechanical FE simulations, is proposed hereinafter to better deal with complex heat transfer phenomena.

A first drawback is related to the fact that inverse methods can account for strain, strain rate, and/or temperature dependencies of the parameters governing heat losses only through *a priori* selection of the variables expected to be relevant.

Moreover, inverse approaches are generally characterized by a high computational cost. This is even more valid in this field due to the strong coupling between mechanical and thermal responses. Indeed, the first is affected by temperature rises, which may be generated by heat loss phenomena that in turn partially depend on the mechanical response itself. This means that simultaneous identification of mechanical behavior and heat conversion is needed. Even though separate identification is possible when limited temperature rises occur, as underlined in Section 6.1, the computational cost would not decrease significantly. Moreover, this last strategy would not be applicable to scenarios in which significant temperature rises occur along with non-negligible heat conduction.

The proposed inverse method overcomes some of the above limitations by adopting the plastic flow identification strategy presented in Section 5.4. Indeed, such strategy is capable of estimating the mechanical response independently of the heat conversion and without assumptions about it. This is possible because the database-driven approach can estimate the current distributions $\varepsilon_{eq,p}(x)$, $\dot{\varepsilon}_{eq,p}(x)$, $\sigma_{eq}(x)$, without knowing the temperature experienced by material points. Then, the temperature distribution is obtained separately from infrared camera acquisition. Once thermo-visco-plastic behavior is identified by fitting altogether the 4D point clouds $(\varepsilon_{eq,p}, \dot{\varepsilon}_{eq,p}, T, \sigma_{eq})$ representing material responses during different tests, the only remaining aspect to be determined is the heat conversion. Hence, the overall computational cost is significantly reduced with respect to traditional FEMU approaches. The main drawback that is still present is related to the need to define in advance the variables affecting heat loss phenomena.

Being the proposed inverse method in an early stage of development, it was essential to focus on relatively simple cases. Thus, in the next sections, radiant and convective losses are neglected, while conduction is considered but under the hypothesis of constant thermal conductivity. Regarding the work-to-heat conversion, which actually represents the focus of the analysis, the case of a strain-dependent TQC is analyzed. Based on these simplifying assumptions an iterative procedure for TQC identification was developed, as explained in Section 6.3.1. The application of the method to numerical benchmarks is then presented in Section 6.3.2.

6.3.1 Iterative procedure

Under the hypothesis mentioned above, this section presents a tentative iterative procedure for identifying the work-to-heat conversion and its possible dependence on equivalent plastic strain. The proposed strategy can be conceived as a FEMU method with well-guided iterations that allow convergence to be achieved in a few steps, as proved in Section 6.3.2.

The target function is represented by the experimental temperature distribution $T_{exp}(x)$ on the outer surface of the specimen and at a highly deformed configuration, while the optimization variable is represented by a strain-dependent TQC, $\beta_{diff}(\varepsilon_{eq,p})$. In other words, the strategy consists of iteratively updating $\beta_{diff}(\varepsilon_{eq,p})$ until the numerical temperature distribution $T_{FE}(x)$ on the outer surface of the specimen is close enough to the experimental one $T_{exp}(x)$. It is worth highlighting that a single highly deformed configuration is sufficient to identify the TQC thanks to the heterogeneous equivalent plastic strain distribution typical of necking. From this perspective, the idea is similar to the one illustrated in Chapter 3, where the hardening law was obtained using a single highly deformed configuration. That approach was valid only for strain-dependent hardening laws, similarly also the present one is valid provided that a function of the type $\beta_{diff}(\varepsilon_{eq,p})$ can represent adequately the work-to-heat conversion.

In practice, the proposed method requires running a first thermal-structural FE simulation of the test under investigation, using as input a trial $\beta_{diff}^{(0)}(\varepsilon_{eq,p})$. The temperature of the elements on the outer surface is, then, extracted at a highly deformed configuration to obtain $T_{FE}(x)$. The comparison with the experimental thermal distribution $T_{exp}(x)$ is then attributed to an incorrect TQC. Hence, a correction factor is computed, according to the following definition $k_\beta(x) \stackrel{\text{def}}{=} \Delta T_{exp}/\Delta T_{FE}$, where ΔT are the temperature rises with respect to room temperature. This can be converted into a strain-dependent correction factor, denoted as $k_\beta(\varepsilon_{eq,p})$, by exploiting the discrete distribution $\varepsilon_{eq,p}(x)$ from the FE simulation (after having verified that the necking profile predicted numerically well approximated the experimental one). Finally, the updated TQC $\beta_{diff}^{(1)}(\varepsilon_{eq,p}) = k_\beta \beta_{diff}^{(0)}$ is input into a subsequent simulation. The above procedure is repeated until

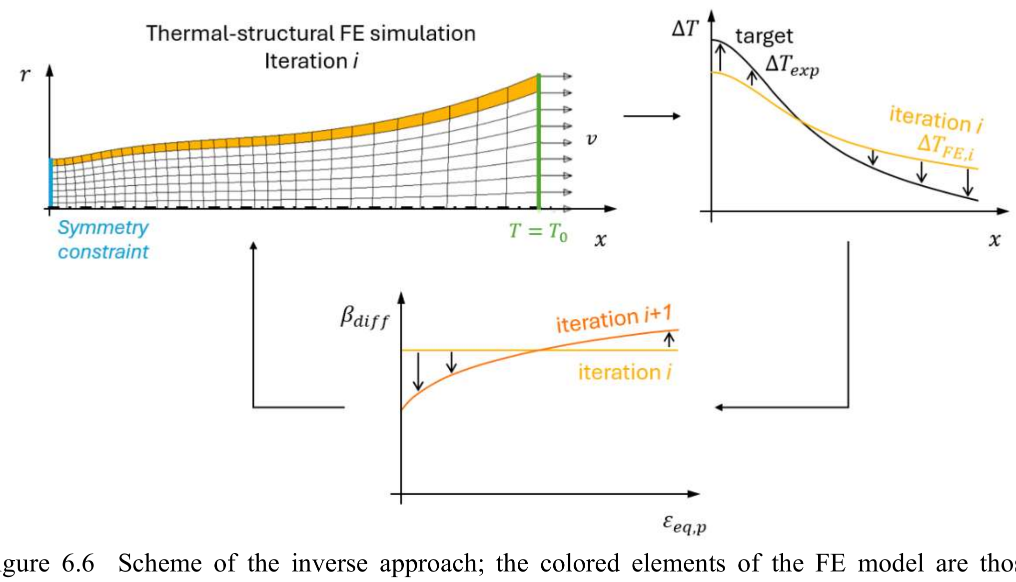

Figure 6.6 Scheme of the inverse approach; the colored elements of the FE model are those considered for extracting $\Delta T_{FE,i}(x)$. [2]

the distance $\|\Delta T_{exp} - \Delta T_{FE}\|_2$ is below a certain threshold (which depends on the specific application). A schematic representation of the process is depicted in Figure 6.6.

Even if the present strategy must be conceived as a preliminary proposal, some simplifying hypotheses are reasonable and commonly accepted (i.e., negligible radiation), whereas others are less restrictive than one could expect. This last case regards the choice of strain-dependent TQC, which apparently limits the applicability to cases where equivalent plastic strain is the only governing variable. Actually, during the test under investigation, there may be variables which evolve similarly to equivalent plastic strain; in this case, no method would be able to distinguish the effect of equivalent plastic strain from that of other variables. This means that a strain-dependent model for TQC can catch its variation without expecting equivalent plastic strain to be the only governing variable. Adequacy of a function of the type $\beta_{diff}(\varepsilon_{eq,p})$ in representing the work-to-heat conversion during a specific test can be assessed easily, provided that other hypotheses are verified. This can be done by comparing numerical and experimental results on different configurations, not used in the identification. If good results are obtained, then a strain-dependent model is appropriate; otherwise, this indicates that some variables are missing. This may be the case of a strain rate dependence of the TQC. Since during necking equivalent plastic strain rate variation differs significantly from that of equivalent plastic strain (see Section 4.1), a $\beta_{diff}(\varepsilon_{eq,p})$ function cannot account for it.

Finally, it is worth highlighting that the incapability of the method to distinguish which variables are physically affecting the work-to-heat conversion, is a limitation of the specific loading condition considered. Nevertheless, the purpose of this study is to exploit as much tensile data as possible for studying material behavior, and the resulting TQC would still represent a good starting point if further investigations are needed.

6.3.2 Numerical examples

This section aims to show the capability of the developed iterative procedure to rapidly converge on the expected result. To pursue this objective, numerical benchmarks were simulated in Ansys LS-DYNA via coupled thermal-mechanical FE analyses that satisfied the hypotheses discussed above. The structural analysis was solved with the explicit algorithm, while the thermal problem was solved with the implicit one.

The same thermo-visco-plastic material model of Armco Iron of Section 6.2.2 was used, as well as the same strain-dependent TQC. In addition, heat conduction, with a constant conductivity of 76.1 W/(m·K) was introduced. Actually, two simulations were run, differing one from the other for the test speed, to prove the versatility of the method in dealing with non-isothermal testing conditions, regardless of whether adiabaticity is verified or not. As stated in Section 5.1, the strain rate at which heat conduction becomes significant depends on material's thermal diffusivity. In the present analysis, nominal strain rates of 1 s^{-1} and 10^2 s^{-1} were suitable to represent scenarios with significant and negligible thermal conduction respectively.

These numerical simulations were considered as if they were experimental tests. For each one, a highly deformed configuration was chosen, and the corresponding temperature distribution was considered as target of the iterative procedure. The optimization variable was represented by the TQC, while both thermal conduction and plastic behavior were supposed to be known and/or correctly identified. In this way, it was possible to focus the attention only on the iterative strategy.

Algorithm effectiveness can be inferred, for both analyzed cases, from the results summarized in Figure 6.7. A quantitative assessment is provided by the tables, which collect the errors on the temperature predictions at all iterations. Specifically, for each iteration, the error accounted for several configurations, despite only one was used for updating $\beta_{diff}(\varepsilon_{eq,p})$ from one simulation to the next.

It.	Error on T (%)
1	62
2	10
3	3.3
4	1.8
5	1.1
6	0.6
7	0.4
8	0.1

It.	Error on T (%)
1	59
2	13
3	3.4
4	2.7
5	1.8
6	0.5

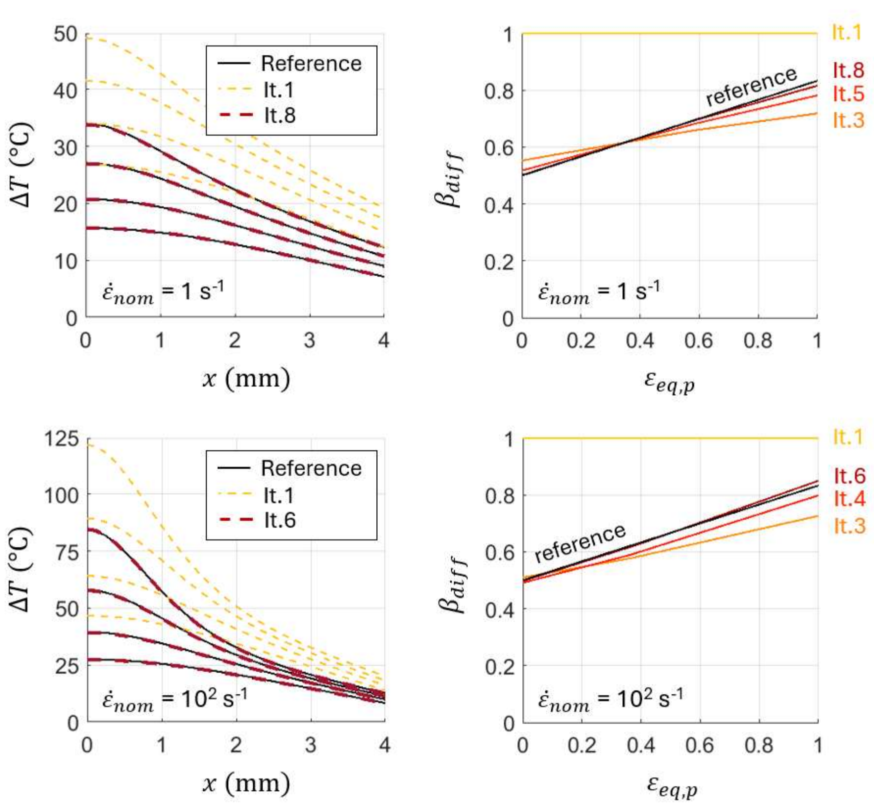

Figure 6.7 Result of the inverse approach applied to two benchmarks with variable TQC, one under non-adiabatic conditions (top part of the figure) and one under adiabatic conditions (bottom part of the figure); tables report the error on temperature computed via Equation 6.11 (adapted from [2]).

The errors were calculated according to the following expression:

$$error = \sqrt{\frac{1}{N}\sum_{i=1}^{N}\left(\frac{\Delta T_i - \Delta \tilde{T}_i}{\Delta T_i}\right)^2}, \tag{6.11}$$

being ΔT the temperature increment (with respect to the room temperature) obtained from the benchmark simulation, $\Delta \tilde{T}$ the temperature increment predicted by the simulation of the current iteration, and N the number of nodes multiplied for the number of configurations considered.

Moreover, Figure 6.7 also provides a graphical representation of the results. The plots on the left compare the reference temperature distributions at different configurations (black solid lines) with the corresponding temperature distributions predicted by the first (light and thin dashed line) and by the last simulation (dark and thick dashed line). This comparison highlights that the final simulation well predicted the reference thermal distribution, as indicated by the table of errors. Furthermore, the comparison of temperature distributions of the two benchmarks underlines the effect of heat conduction in limiting temperature localization.

It should be noted again that, although only the most highly deformed configuration was given as optimization target, previous configurations were predicted accurately too. This was possible because a wide axial portion of the specimen was considered, so that information about the work-to-heat conversion at different equivalent plastic strains was automatically provided.

As expected from previous considerations, the plots on the right of Figure 6.7, which display TQC trials from some iterations, show that they progressively approach the reference $\beta_{diff}(\varepsilon_{eq,p})$ given as input into the benchmark simulation (black solid line).

Overall, the accuracy of the results obtained in both scenarios of relevant and negligible heat conduction supports the general applicability of the proposed method and motivates its application to an experimental case study.

6.4 Experimental case study

In this section some experiments are analyzed to evaluate the practical applicability of the methods proposed in Section 6.2 and 6.3 for investigating the work-to-heat conversion during necking.

The tests are actually those presented in Section 5.4. Briefly, the material studied was 17-4PH (H900), which was tested at room temperature and at various strain rates. Details about experimental setup, thermal data post-processing, and plastic flow identification can be found in Section 5.4. Here, attention is focused on non-isothermal tests, i.e. those at 1, 10, and 10^3 s^{-1} of nominal strain rate. They represented suitable case studies for two main reasons: necking occurred at relatively low strains, and significant self-heating occurred even under conditions where thermal conduction could not be neglected. Thus, for still gaining information about the work-to-heat conversion, both the proposed techniques were applied.

For what the direct method for TQC identification is concerned, the starting point was represented by the Eulerian fields of temperature, equivalent plastic strain and equivalent stress at different times. The first were obtained by infrared imaging (see Section 5.5.2), while the second and the third by the proposed database-driven strategy (see Section 5.5.3). Then, the tracking strategy developed in Section 6.2.1 and implemented in MATLAB was applied to some selected material points. This allowed the deformation paths on the $\sigma_{eq} - \varepsilon_{eq,p}$ plane to be identified for those material points. An example is provided in Figure 6.8a for the 10 s^{-1} test. Only a few material points were considered for the sake of readability. They were denoted

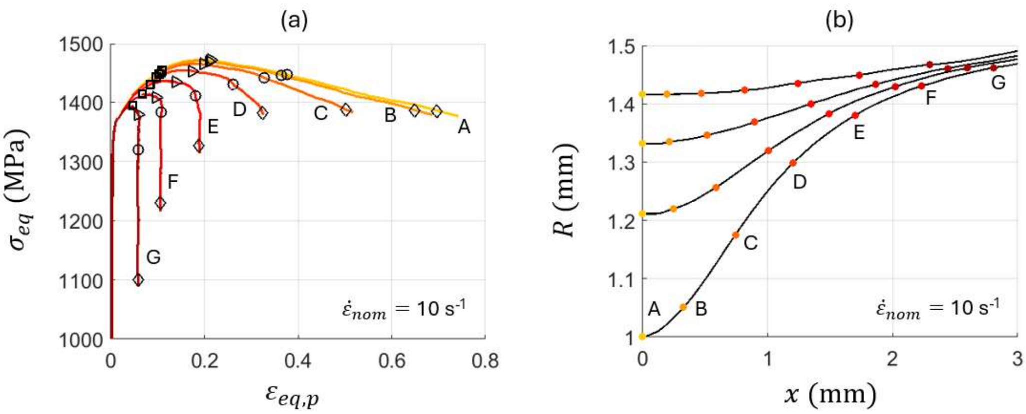

Figure 6.8 Deformation paths of various material points (a) and their position on the specimen's surface (b) at different configurations for a test at nominally 10 s^{-1}. [2]

with capital letters from A to G and were plotted as solid lines characterized by different colors. For reference, the positions of these points on the necking silhouette at different moments are shown in subplot (b) with the same color used in subplot (a). It is evident that the various paths progressively detach and deviate from that of the profile center. This is the typical result for cases where strain rate heterogeneity caused by necking affects material response within a single test, as highlighted in Section 2.1.

Moreover, it may be interesting to indicate in Figure 6.8a the states experienced by different material points at the same time. These states are marked with a different symbol for each configuration: first square, then triangle, circle, and finally diamond. Each curve that would be obtained by connecting identical symbols represents the locus of points identified by the database-driven approach at the given configuration.

The deformation paths were used to evaluate how the total plastic work executed on each material point varied during each test. Then, constant material density and specific heat were considered, equal to 7800 kg/m^3 and 460 J/(kg·K) respectively. Finally, the direct approach required applying Equation 6.2 to identify a set of integral TQCs for each test. Each set could be analyzed as function of any desired variable. In particular, the equivalent plastic strain was chosen to obtain results comparable with the inverse approach, which in the current form can deal only with strain-dependent TQC. Each resulting point cloud of integral TQCs was fitted with a mathematical law $\beta_{int}(\varepsilon_{eq,p})$, which was then inputted in Equation 6.10 for estimating $\beta_{diff}(\varepsilon_{eq,p})$. Figure 6.9 presents these functions as dashed lines, using different colors for different loading conditions; integral TQCs are displayed in subplot (a), whereas differential TQCs in subplot (b). Each line is shown over the entire post-necking range analyzed, underlining that considering necking in TQC identification allows it to be identified up to large strains.

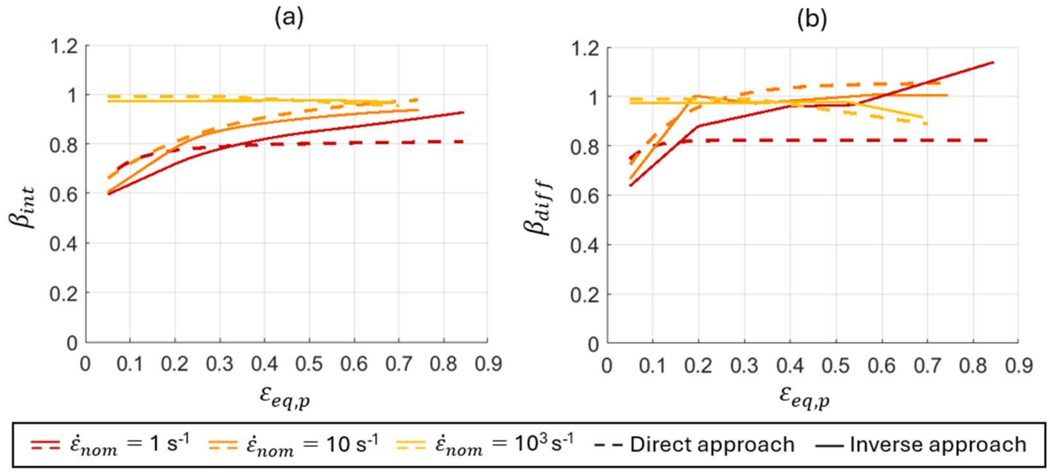

Figure 6.9 Integral (a) and differential (b) TQC estimated by both the direct and the inverse approach for three different nominal strain rates. [2]

Nevertheless, it should be noted that, having ignored thermal dependencies of density and specific heat, these possible variations are implicitly accounted in the identified TQCs. Furthermore, in case adiabaticity is not satisfied, the resulting TQC implicitly includes the effect of heat conduction and thus loses its meaning of work-to-heat conversion coefficient.

To deal better with non-adiabatic conditions, the proposed inverse approach was adopted. In this case, the starting point was represented by the thermo-visco-plastic model representing material response under self-heating conditions and the evolution of the thermal field on the specimen's outer surface. The first was identified in Section 5.5.3 by employing the database-driven approach and was input into the coupled thermal-mechanical simulations required by the inverse approach. Conversely, the second was obtained from infrared imaging (see Section 5.5.2) and was used partially as target of the iterative procedure. According to the procedure explained in Section 6.3.1, only one highly deformed configuration per test was actually used as target and a strain-dependent TQC was identified. Moreover, thermal conductivity was considered constant to 10 W/(m·K)), a value optimized for the test configuration. Density and specific heat were assumed to remain constant, as done in the direct approach.

The identified $\beta_{diff}(\varepsilon_{eq,p})$ and the corresponding $\beta_{int}(\varepsilon_{eq,p})$, computed via Equation 6.5, are displayed in Figure 6.9 as solid lines, colored on the basis of the corresponding loading condition.

Comparing these results with those of the direct approach, it can be noted that similar results were obtained for the high strain rate test. Indeed, this testing condition satisfied adiabaticity requirements, as already proved in Section 5.5.3 by analyzing the Fourier number (specifically, a value of $2 \cdot 10^{-4}$ was obtained). Regarding the 10 s^{-1} test, the direct and inverse method provided slightly different results that could be attributed to small deviations from adiabatic conditions. This consideration is also supported by the Fourier number estimate (found to be 10^{-2}, at the boundary of adiabaticity). Finally, the 1 s^{-1} test was characterized by a larger difference between the results of the two methods: due to non-negligible heat conduction (Fourier number of 10^{-1}), the direct method underestimated significantly the conversion of plastic work into heat.

Another aspect that is worth discussing is related to the dependence of the TQC on equivalent plastic strain. To pursue this objective, attention should focus on $\beta_{diff}(\varepsilon_{eq,p})$ results of the inverse approach as the direct one cannot deal with non-adiabatic conditions properly. Starting from the lowest strain rate, an increasing trend of $\beta_{diff}(\varepsilon_{eq,p})$ was found, as depicted in Figure 6.9b. This agrees with findings from previous research on steels and other metals too, for example with the work by Smith et al. on a titanium alloy [28], the one by Dæhli et al. on DP steels and aluminum alloys [25], and the one by Lew et al. [15] on austenitic stainless steel. The result for the intermediate strain rate, shown in Figure 6.9b, is characterized by a similar trend, even though $\beta_{diff}(\varepsilon_{eq,p})$ saturates above 20% of equivalent plastic strain. The deviation from a constant value at relatively low strains may explain why in Section 5.5.3 a constant TQC did not provide accurate results (see Figure 5.11). Finally, $\beta_{diff}(\varepsilon_{eq,p})$ obtained for the highest strain rate was found to remain nearly constant or even to slightly decrease at large strains. This could be attributed to the difficulty of measuring local temperature in experiments at such extreme conditions. This is mainly related to an integration time not short enough with respect to the characteristic time of mechanical deformation. The consequent temperature averaging can be further worsened by the fact that the neck (so the hottest point) changes its Eulerian position during the test. This is mainly due to a loading system that causes one end of the specimen to move faster than the other. Although improvements would be possible by decreasing the integration time, this would come at the cost of a lower sensitivity near room temperature.

Furthermore, comparison of the TQCs for the different tests suggests the presence of strain rate dependence too. Even if this effect was already acknowledged in literature for certain metals, the present results are not enough to prove it for 17-4PH. Further investigations are needed, in which strain rate effects must also be considered within single tests because of necking.

In addition, the TQCs identified here may implicitly account for other possible variables affecting thermal fields, including thermal sensitivity of specific heat, thermal conductivity and TQC itself. This feature is typical of empirical approaches, and attention must be paid to giving physical meaning to the results.

After having presented and discussed the identified differential TQCs, it must be verified that the thermal fields they numerically predict are in good agreement

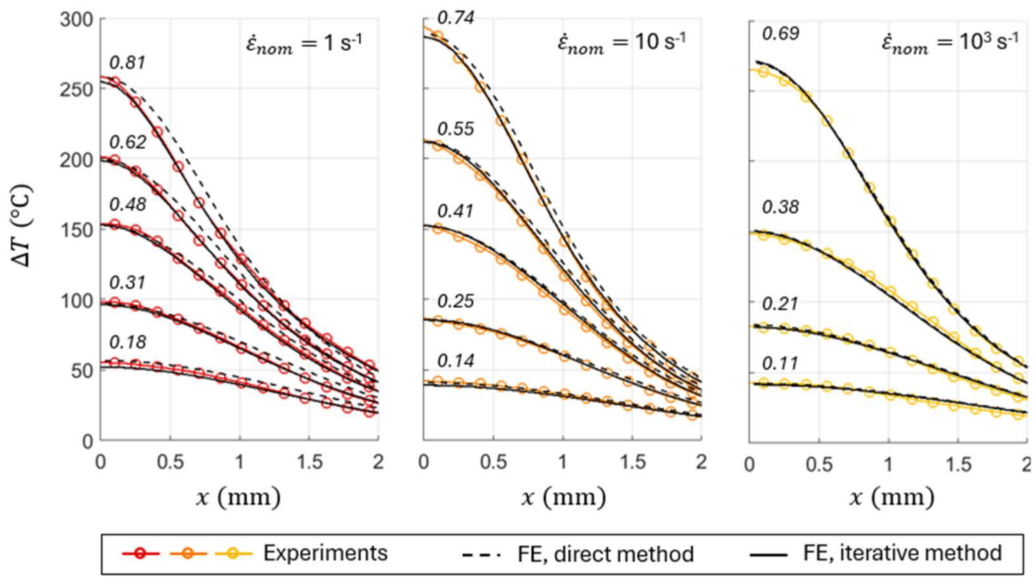

Figure 6.10 Experimental temperature distributions compared with numerical predictions; next to each configuration the database estimate of $\varepsilon_{eq,p}$ at the profile center is written. [2]

with experimental ones. For the inverse approach the fields were readily provided by the final iteration, whereas for the direct approach adiabatic FE simulations with the identified TQCs were run. In this last case, adiabaticity was needed since the TQCs already implicitly included heat conduction. Figure 6.10 compares, for each test, some temperature distributions: the experimental ones are shown as colored lines with circle markers, those associated with the direct approach as black dashed lines, and those corresponding to the inverse approach as black solid lines.

It can be observed that the inverse approach enabled accurate predictions for all tests considered, also for configurations different from the target one. As anticipated in Section 6.3.1, this does not necessarily mean that equivalent plastic strain is the only governing variable but indicates that the TQC variation during the tests analyzed can be modeled effectively as a function of $\varepsilon_{eq,p}$. Regarding the direct method, very good results can be seen at the highest strain rate, but discrepancies appeared in the other two testing conditions, especially in the lowest strain rate one. This could be attributed to heat conduction and its possibility of being modelled effectively via strain-dependent TQC. At 10 s^{-1}, this approach was found to be adequate since conductive losses were relatively low, but when such losses were relevant, as for the 1 s^{-1} test, the above approach failed to represent heat losses phenomena altogether. Thus, the inverse approach was found to be essential for considering thermal conduction properly and separating its contribution from that of the work-to-heat conversion.

Finally, it is worth proving that the identified models, combined with the thermo-visco-plastic model of Section 5.5.3, well reflect the overall thermal-mechanical behavior exhibited by 17-4PH in the tests analyzed. This is illustrated in Figure 6.11 by comparing numerical predictions and experimental results in terms of necking profiles and engineering response.

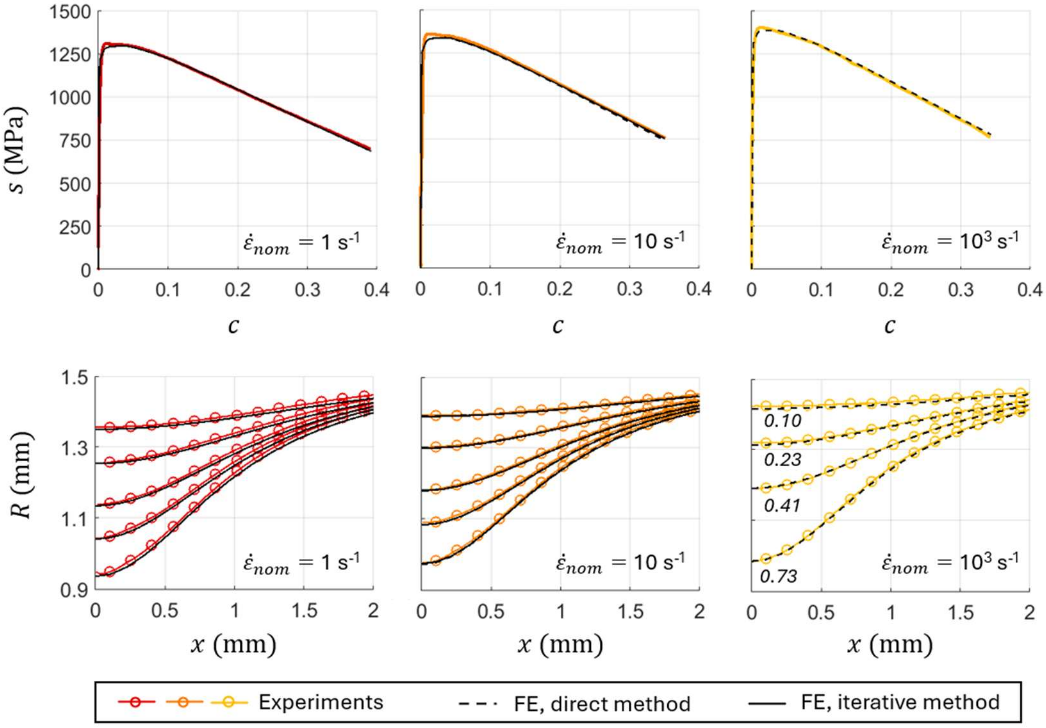

Figure 6.11 Comparison of experimental and numerical results in terms of necking profiles and radial engineering curve; the maximum superficial $\varepsilon_{eq,p}$ at each configuration is the same of Figure 6.10 for $\dot{\varepsilon}_{nom}$ of 1 s^{-1} and 10 s^{-1}, while for $\dot{\varepsilon}_{nom}$ of 10^3 s^{-1} is written on the plot. [2]

Actually, numerical predictions were obtained using the TQC identified by the direct and/or the inverse approach depending on the specific test. In particular, reference was made to the direct strategy, when applicable, for its lower computational cost. This was the case of the highest strain rate. Conversely, the inverse approach was adopted when non-negligible heat conduction occurred, as this strategy was found to outperform the direct one under such conditions. This was the case of the lowest strain rate. For the intermediate strain rate test, which was not fully adiabatic, both approaches were applied and proved to be analogous in terms of structural response.

6.5 Concluding remarks

The present chapter investigated the possible use of the database-driven approach to gain information about the work-to-heat conversion up to large strains, by exploiting the post-necking phase of tensile tests.

Specifically, a direct approach and an inverse one were proposed. The first directly employs the heat equation for adiabatic conditions, so it is very efficient but lacks generality. Conversely, the second requires an iterative process, thus it is less efficient but able to deal with heat losses other than plastic dissipation. The novelty of these proposals, published in [2], lies in the use of the database-driven approach. On one hand, this limits the applicability to cylindrical specimens made of isotropic Von Mises materials if the database is established according to Section 2.3. On the other hand, the database-driven approach facilitates TQC identification from experimental and analysis perspectives.

Indeed, direct methods generally entail measuring the strain field with DIC technique; however, these measurements can be challenging on cylindrical specimen. The database-driven approach, instead, provides strain fields by simply relying on the silhouette of the specimen. Moreover, it also allows tracking material points (essential for applying the Lagrangian formulation of the heat equation), even if backlighting has been used to improve silhouette detection.

Regarding the inverse method, the database-driven approach can be exploited to limit the computational time of FEMU strategies that require simultaneous identification of structural behavior and heat losses. As a matter of fact, and as proved in Chapter 5, the database-driven strategy can identify the thermo-visco-plastic flow without knowing how the measured temperature has been affected by heat losses. Thus, the inverse approach proposed here only needs to focus on this second aspect.

The overall feasibility and accuracy of both methods was demonstrated first through ad-hoc numerical benchmarks and then through an experimental case study. The direct method proved to be successful in identifying the TQC up to large strains, when the hypothesis of adiabaticity was verified, thus validating the proposed tracking strategy. The inverse approach, instead, provided very promising results regardless of whether adiabatic conditions were satisfied or not. Since such good results were obtained despite an approximate modeling of heat losses (e.g., only heat conduction with constant thermal conductivity in addition to plastic dissipation), the method appears worthy of future attention for further improvements. Finally, future efforts may also concern the experimental side; specifically, limiting motion blur in infrared acquisitions during high strain rate tests.

References

[1] Taylor, G. I., & Quinney, H. (1934). The latent energy remaining in a metal after cold working. *Proceedings of the Royal Society of London. Series A, Containing Papers of a Mathematical and Physical Character, 143*(849), 307-326.

[2] Beltramo, M., Scapin, M., & Peroni, L. (2025). Analysis of the work-to-heat conversion beyond the necking onset in non-isothermal tensile tests. *International Journal of Impact Engineering*, 105503.

[3] Nassar, O. (2025). On the conversion of plastic work into heat in metals. *Proceedings of the Royal Society A: Mathematical, Physical and Engineering Sciences, 481*(2308).

[4] Aravas, N., Kim, K. S., & Leckie, F. A. (1990). On the calculations of the stored energy of cold work.

[5] Zehnder, A. T. (1991). A model for the heating due to plastic work. *Mechanics Research Communications*, *18*(1), 23-28.

[6] Rosakis, P., Rosakis, A. J., Ravichandran, G., & Hodowany, J. (2000). A thermodynamic internal variable model for the partition of plastic work into heat and stored energy in metals. *Journal of the Mechanics and Physics of Solids*, *48*(3), 581-607.

[7] Lieou, C. K., & Bronkhorst, C. A. (2021). Thermomechanical conversion in metals: dislocation plasticity model evaluation of the Taylor-Quinney coefficient. *Acta Materialia*, *202*, 170-180.

[8] Kingstedt, O. T., & Lloyd, J. T. (2019). On the conversion of plastic work to heat in Mg alloy AZ31B for dislocation slip and twinning deformation. *Mechanics of Materials*, *134*, 176-184.

[9] Benzerga, A. A., Bréchet, Y., Needleman, A., & Van der Giessen, E. (2005). The stored energy of cold work: Predictions from discrete dislocation plasticity. *Acta Materialia*, *53*(18), 4765-4779.

[10] Kositski, R., & Mordehai, D. (2021). Employing molecular dynamics to shed light on the microstructural origins of the Taylor-Quinney coefficient. *Acta Materialia*, *205*, 116511.

[11] Kapoor, R., & Nemat-Nasser, S. (1998). Determination of temperature rise during high strain rate deformation. *Mechanics of materials*, *27*(1), 1-12.

[12] Rittel, D., Zhang, L. H., & Osovski, S. (2017). The dependence of the Taylor–Quinney coefficient on the dynamic loading mode. *Journal of the Mechanics and Physics of Solids*, *107*, 96-114.

[13] Zhang, T., Guo, Z. R., Yuan, F. P., & Zhang, H. S. (2018). Investigation on the plastic work-heat conversion coefficient of 7075-T651 aluminum alloy during an impact process based on infrared temperature measurement technology. *Acta Mechanica Sinica*, *34*(2), 327-333.

[14] Kingstedt, O., Lew, A., Pratt, M., Salehi, S. D., & Rao, S. (2024). Investigation of thermomechanical coupling in inconel 718 at homologous temperatures of 0.2 and 0.5. *Metallurgical and materials transactions A*, *55*(9), 3591-3600.

[15] Lew, A., Loeffler, C., Varga, J., Jones, A., Salehi, S. D., & Kingstedt, O. T. (2025). A comparison of techniques to measure the conversion of plastic work to heat in 304L stainless steel under adiabatic conditions. *International Journal of Impact Engineering*, *198*, 105220.

[16] Rittel, D. (1999). On the conversion of plastic work to heat during high strain rate deformation of glassy polymers. *Mechanics of Materials*, *31*(2), 131-139.

[17] Mason, J. J., Rosakis, A. J., & Ravichandran, G. (1994). On the strain and strain rate dependence of the fraction of plastic work converted to heat: an experimental study using high speed infrared detectors and the Kolsky bar. *Mechanics of Materials*, *17*(2-3), 135-145.

[18] Hodowany, J., Ravichandran, G., Rosakis, A. J., & Rosakis, P. (2000). Partition of plastic work into heat and stored energy in metals. *Experimental mechanics*, *40*(2), 113-123.

[19] Macdougall, D. (2000). Determination of the plastic work converted to heat using radiometry. *Experimental mechanics*, *40*(3), 298-306.

[20] Soares, G. C., & Hokka, M. (2021). The Taylor–Quinney coefficients and strain-hardening of commercially pure titanium, iron, copper, and tin in high rate compression. *International Journal of Impact Engineering*, *156*, 103940.

[21] Soares, G. C., Vázquez-Fernández, N. I., & Hokka, M. (2022). Simultaneous full-field strain and temperature measurements in high strain rate testing. In *Advances in Experimental Impact Mechanics* (pp. 255-285). Elsevier.

[22] Smith, J. L., Seidt, J. D., Fietek, C. J., & Gilat, A. (2025). Taylor-Quinney coefficient determination from simultaneous strain and temperature measurements of uniform and localized deformation in tensile tests. *Journal of the Mechanics and Physics of Solids*, *199*, 106099.

[23] Pottier, T., Toussaint, F., Louche, H., & Vacher, P. (2013). Inelastic heat fraction estimation from two successive mechanical and thermal analyses and full-field measurements. *European Journal of Mechanics-A/Solids*, *38*, 1-11.

[24] Nowak, M., & Maj, M. (2018). Determination of coupled mechanical and thermal fields using 2D digital image correlation and infrared thermography: Numerical procedures and results. *Archives of Civil and Mechanical Engineering*, *18*(2), 630-644.

[25] Dæhli, L. E. B., Johnsen, J., Berstad, T., Børvik, T., & Hopperstad, O. S. (2023). An experimental–numerical study on the evolution of the Taylor–Quinney coefficient with plastic deformation in metals. *Mechanics of Materials*, *179*, 104605.

[26] Knysh, P., & Korkolis, Y. P. (2015). Determination of the fraction of plastic work converted into heat in metals. *Mechanics of materials*, *86*, 71-80.

[27] Vazquez-Fernandez, N. I., Soares, G. C., Smith, J. L., Seidt, J. D., Isakov, M., Gilat, A., ... & Hokka, M. (2019). Adiabatic heating of austenitic stainless steels at different strain rates. *Journal of Dynamic Behavior of Materials*, *5*(3), 221-229.

[28] Smith, J. L., Seidt, J. D., & Gilat, A. (2018, October). Full-Field Determination of the Taylor-Quinney coefficient in tension tests of Ti-6Al-4V at strain rates up to 7000s-1. In *Advancement of Optical Methods & Digital Image Correlation in Experimental Mechanics, Volume 3: Proceedings of the 2018 Annual Conference on Experimental and Applied Mechanics* (pp. 133-139). Cham: Springer International Publishing.

[29] Rittel, D., Ravichandran, G., & Venkert, A. (2006). The mechanical response of pure iron at high strain rates under dominant shear. *Materials Science and Engineering: A*, *432*(1-2), 191-201.

[30] Audoly, B., & Hutchinson, J. W. (2016). Analysis of necking based on a one-dimensional model. *Journal of the Mechanics and Physics of Solids*, *97*, 68-91.

[31] Audoly, B., & Hutchinson, J. W. (2019). One-dimensional modeling of necking in rate-dependent materials. *Journal of the Mechanics and Physics of Solids*, *123*, 149-171.

[32] Johnson, G. R. (1983). A constitutive model and data for metals subjected to large strains, high strain rates and high temperatures. In *Proceedings of the 7th International Symposium on Ballistics, Am. Def. Prep. Org.(ADPA), Netherlands, 1983* (pp. 541-547).

Chapter 7

Investigation into anisotropic materials

With the aim of investigating scenarios of increasing complexity, the present chapter shifts the focus from the isotropic materials considered in all previous chapters to anisotropic ones. Anisotropy may result not only from metal working operations executed on the components but also from the material itself, as for the case of hexagonal close-packed (HCP) structures (e.g., magnesium and titanium alloys). In any case, this makes the material response, both in terms of strength and deformation, dependent on the direction. Typically, anisotropic materials are studied by testing sheet specimens characterized by different orientations of material preferential directions with respect to the loading axis. However, testing cylindrical specimen may still be relevant for characterizing the hardening behavior of bulk components. The purpose of this chapter is to provide a strategy for investigating hardening of an anisotropic material even via tensile tests (virtually only one) performed on equally oriented cylindrical specimens. Key requirements of the proposed method were limited experimental and computational costs, along with the capability of extracting as much information as possible, consistently with the approaches adopted so far. To this end, managing post-necking data properly is of utmost importance. For anisotropic cylindrical specimens, this is significantly more challenging than for isotropic ones, since the cross-sections deviate progressively from circular shapes towards non-axisymmetric and generally unknown shapes. Given the complexity of dealing with anisotropic necking, the analysis is restricted here to strain-dependent hardening, under the assumption of negligible strain rate sensitivity and self-heating. Moreover, since only one orientation is assumed to be tested, the hypothesis of isotropic hardening is also adopted.

On one hand, it could be interesting to extend the database-driven approach to anisotropic materials, since it provided successful results in previous chapters. On the other hand, such approach relied on specific lines of reasoning, reported in Sections 2.1 and 2.2, based on the hypothesis of isotropic behavior. If analogous line of thinking is not developed for anisotropic materials, the size of the database would increase dramatically when 3D FE analyses would be added to account for anisotropic behaviors.

Thus, in this chapter a database-driven solution was not pursued, adopting instead a simplified inverse approach. This consists of applying an analytical correction to the post-necking area-based true curve and then verifying, and possibly refining, the identified strain-hardening law through a FE analysis. Since the cross-sectional shape is unknown, even the determination of the area-based true curve is not straightforward. 360° shape-monitoring techniques may in principle be used, however the proposed method hypothesizes elliptical cross-section so that a more versatile setup could be used.

To understand the literature background in which this approach is placed, Section 7.1 reviews the main works on post-necking characterization of anisotropic cylindrical specimens, as well as possible experimental setups and post-processing techniques for reconstructing the 3D shape. In Section 7.2 and 7.3 the proposed reconstruction technique and the identification strategy are presented respectively, while Section 7.4 reports an experimental application.

7.1 Literature background

In this section, a literature review on post-necking analysis of anisotropic cylindrical specimens is presented. Research contributions in this field have addressed both the identification strategy and the experimental setup. These two elements are tightly related: while the identification method depends on the information gathered from the experimental setup, the choice of the setup itself can be driven by the identification method for reasons of computational efficiency or accuracy. Hereinafter, the discussion focuses first on identification methods and subsequently on possible experimental configurations.

Early research on the topic was presented by Eisenberg and Yen [1, 2] in the eighties. They elaborated an analytical model to account for necking triaxiality in initially axisymmetric bars made of orthotropic materials, similarly to what Bridgman did for isotropic ones. Indeed, the method determines the average equivalent stress at the neck cross-section by correcting the average axial stress, i.e., the true stress σ_t. The proposed correction formula was the following:

$$\sigma_{eq,avg} = \sigma_t \Bigg/ \left[\frac{1}{2} + \frac{1}{4\left(1+\frac{\rho_a}{a}\right)\ln\left(1+\frac{a}{\rho_a}\right)} + \frac{1}{4\left(1+\frac{\rho_b}{b}\right)\ln\left(1+\frac{b}{\rho_b}\right)}\right], \tag{7.1}$$

being a and b the major and minor semi-axes of the ellipse representing the neck cross-section, and ρ_a and ρ_b the radii of curvature at the neck in the major and minor symmetry planes. This correction was recently employed by Arthington et al. [3] to evaluate the average equivalent stress at the neck just before failure of zirconium specimens.

A different correction formula to account for triaxiality during necking of cylindrical specimens made of anisotropic materials was used by Mirone and Corallo [4]. Specifically, it was the MLR correction developed for isotropic metals by Mirone [5]. The validity of the methodology on X100 steel was confirmed by the fact that the numerical predictions implementing the identified law matched well the experimental results, in terms of true curve and evolution of the ratio of the semi-axes at the neck. Mirone and Corallo [4] also demonstrated that, when employing a Hill yield criterion [6], the true curve from a single experiment is mostly independent of yielding parameters, which primarily influence the specimen's deformed geometry. This finding explains why both the MLR and Eisenberg's corrections allow the hardening behavior to be identified regardless of parameters that explicitly describe anisotropy.

Finally, another analytical method for dealing with investigated scenarios was introduced by Chandran and Verleysen [7]. It consists of imposing the plane-stress condition within Hill's normal yield criterion [6], thus obtaining the same correction formula for anisotropic sheet specimens. The only difference lies in the fact that the r-ratio represented the differential ratio between average strains along the major and minor axes of the neck cross-section. This approach differs from the previous ones for the need to assume a yield criterion and identify its parameters.

While above researchers were working on direct identification strategies, others preferred implementing hybrid experimental-numerical methods. For instance, Khadyko et al. [8] employed a FEMU technique with the experimental true curve as target function for optimizing the hardening parameters. The anisotropic yield function needed for the FE simulations was previously calibrated through crystal plasticity (CP) simulations based on material's crystallographic structure. Specifically, the 18-parameter empirical model by Barlat et al. [9] was chosen and calibrated. Comparison of simulated and experimental r-ratio suggested that further improvement was necessary. Thus, in a follow-up study, Khadyko et al. [10] used CP-FE models to simulate experiments directly. The unknown parameters of the models were optimized using as target function the equivalent stress-strain curve previously identified by the empirical FE model. Despite the significant improvement in predicting cross-section shapes, some discrepancies appeared in the force vs. diameter response. These differences were attributed to mesh simplification and assumptions in estimating the equivalent curve used as target of the optimization. Overall, as already stated for isotropic materials, the principal drawback of FEMU strategy is represented by the computational cost; this issue is further worsened when CP simulations are run. The proposal of this chapter is, thus, to correct the true curve with Eisenberg's formula and then run a FE analysis with the identified strain-hardening law to possibly refine it without significantly compromising efficiency.

All above methods rely on true stress evolution: in analytical methods, it represents the variable to which the correction is applied, whereas in hybrid experimental-numerical strategies it represents the target function of the optimization. True stress can be computed as the ratio between the current force and the current cross-section area at the neck (as for isotropic materials). However, while this areal measurement is straightforward for isotropic materials, it is much more challenging for anisotropic ones. As a matter of fact, recordings of a single fixed camera provide sufficient information for isotropic materials but not for anisotropic ones.

This issue has been addressed with different experimental configurations, also depending on additional deformation data needed by the selected identification method. Moreover, some shape-monitoring techniques have been proposed but have not yet been employed for hardening identification in this field. These include, for instance, Computed Tomography (CT), whose main advantage would be the possibility of gathering information about the inner material too. However, conducting *in situ* CT tests [11] for the considered application may not worth the cost of this facility. If only superficial data are needed, a 360° DIC system can be preferrable. This was proposed by Genovese et al. [12] and employs a single camera which grabs images while rotating about the specimen axis. Moreover, if only the outer shape, and not strain data, is of interest, an alternative strategy could be to post-process a 360°-scan by a single camera with the shape-from-silhouette technique pioneered by Baugmart [13] and Laurentini [14]. Nevertheless, 360°-access to the specimen is not always possible, since, for example, dynamic tests cannot be interrupted at predefined elongations for executing the scan over 360°.

This is why imaging setups based on two or more cameras, maintained in a fixed position, and possibly replaced by mirrors [15], were those practically adopted for material identification. For instance, Chandran and Verleysen [7] employed two cameras and reconstructed the specimen's outer shape, along with the strain field, by combining DIC stereovision with monocular cues. Other researchers chose silhouette-based approaches, instead of DIC-based techniques. For instance, Arthington et al. [15] proposed to reconstruct the 3D geometry of the sample by using the silhouettes seen from three distinct views and assuming an elliptical shape of the cross-sections at every time and axial position. Mirone and Corallo [4] also hypothesized elliptical cross-sections but focused the analysis only on the evolution of the neck. Moreover, differently from Arthington et al. [15], they employed only two views, and the information from the third view was replaced by the measurement of the major axis orientation on the failed specimen at the end of the test. This strategy implicitly assumed that the major axis orientation remained constant during testing. Finally, Khadyko et al. [8] simply monitored, through a custom laser-based measuring system, the dimensions of the neck along two directions representing the semi-axes of a hypothetical ellipse. This solution is, however, limited to situations in which the orientation of the main axes is known *a priori*. Given this context and the intended use of the proposed method, the approach described in the next sections adopts the two-cameras-solution for reconstructing the 3D geometry of the specimen and, thus, the area-based true curve.

7.2 Geometrical reconstruction of the necking shape

This section details how, under the hypothesis of elliptical cross-sections, the silhouettes seen from two different viewing angles can be combined with the orientation of the major axis to reconstruct the 3D geometry of the specimen.

It is crucial to note that when the cross-sections are no longer circular, the measurements derived directly from recorded images typically represent apparent quantities, namely, the projections of actual physical dimensions of the specimen onto the plane perpendicular to the optical axis of the camera. This aspect should be accounted for appropriately when dealing with anisotropic deformation of cylinders.

Consider an initially axisymmetric bar made of an anisotropic material, whose cross-sections become perfect ellipses during deformation; also hypothesize that the semi-axes of the different cross-sections remain aligned as deformation proceeds. At a given necking deformed configuration, a neighborhood of the neck would have the geometry displayed in Figure 7.1. Furthermore, consider a camera whose optical axis is perpendicular to the specimen's longitudinal axis and whose projection plane is oriented at an angle α relative to the ellipse's minor axis.

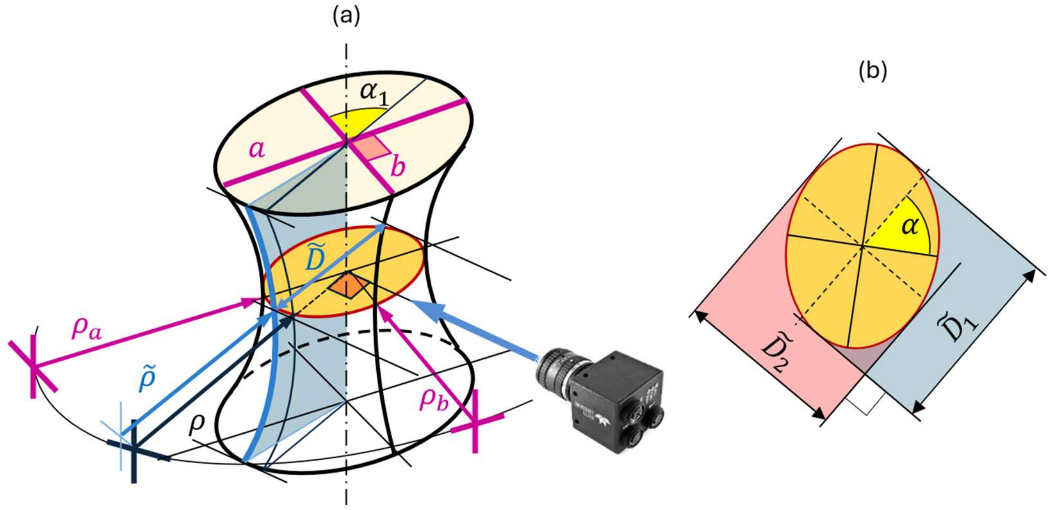

Figure 7.1 Scheme of a specimen with elliptical cross-sections: (a) zoom view of a small surrounding of the neck, with highlighted in blue the projection seen by a camera, (b) top view of the minimum cross-section, showing the apparent diameters that would be measured by two cameras.

At each longitudinal coordinate z, the silhouette seen by the camera is defined by the two points where the optical path is tangent to the ellipse of that specific cross-section. Physically, the segment connecting these two tangency points has a length D. However, in the 2D image acquired by the camera, only the projection of D onto the sensor plane is measurable; this quantity is indicated as $\widetilde{D}$. Consequently, the camera detects a projected diameter $\widetilde{D}$ that varies along the longitudinal axis z. Only if the optical axis of the camera is aligned with one of the ellipse's semi-axes, do the projected and physical dimensions coincide. In such cases, $D = \widetilde{D}$ corresponds to twice the other semi-axis. Otherwise, $\widetilde{D}$ can be analytically related to the ellipse semi-axes (a and b) and to the angle α between the minor axis and the projection plane. This means that, when two projected dimensions $\widetilde{D}_1$ and $\widetilde{D}_2$ are known, as well as the orientation of their projection axes relative to the minor axis (indicated as α_1 and α_2), the semi-axes can be determined. It can be proved that the expressions are the following:

$$a = \frac{1}{2}\sqrt{\frac{(\widetilde{D}_1 \sin\alpha_2)^2 - (\widetilde{D}_2 sin\alpha_1)^2}{(\cos\alpha_1)^2 - (cos\alpha_2)^2}}, \tag{7.2}$$

$$b = \frac{1}{2}\sqrt{\frac{(\widetilde{D}_2 cos\alpha_1)^2 - (\widetilde{D}_1 cos\alpha_2)^2}{(cos\alpha_1)^2 - (co\quad_2)^2}}. \tag{7.3}$$

These definitions need to be interchanged if that $\widetilde{D}_1 < \widetilde{D}_2$.

Applying Equations 7.2 and 7.3 at each longitudinal coordinate allows the 3D geometry of the specimen to be reconstructed as a series of elliptical slices. In the special case where the two cameras are oriented at 90° one to another, previous equations can be simplified into the following ones:

$$a = \frac{1}{2}\sqrt{\frac{\widetilde{D}_1^{\,2}\cos^2\alpha - \widetilde{D}_2^{\,2}\sin^2\alpha}{cos^2\alpha - sin^2\alpha}}, \tag{7.4}$$

$$b = \frac{1}{2}\sqrt{\frac{\widetilde{D}_2 cos^2\alpha - \widetilde{D}_1^{\,2} sin^2\alpha}{cos^2\alpha - sin^2\alpha}}, \tag{7.5}$$

with $\alpha = \alpha_1$. Practical aspects related to estimating the required variables, especially the major axis orientation relative to the cameras, are addressed in Section 7.4. Finally, it is worth noting that this 3D reconstruction technique is not strictly related to the identification strategy presented in the next section but could in principle be used with any identification strategy based on the specimen deformed shape.

7.3 Identification strategy

Coming to the identification methodology, it is worth recalling that the pre-necking regime of anisotropic materials is characterized by stress uniaxiality and uniform strain and stress fields, as in the case of isotropic materials. Thus, pre-necking strain-hardening law can be identified using the same Equations reported in Section 1.2.1. The traditional length-based approach is recalled hereinafter:

$$\varepsilon_{eq,p} = \varepsilon_{a,p} \simeq \ln(1+e), \tag{7.6}$$

$$\sigma_{eq} = \sigma_a = s(1+e). \tag{7.7}$$

Instead, during post-necking, strain localization and stress triaxiality need to be accounted for properly. As anticipated, the present proposal entails applying Eisenberg's theory, hence it is first necessary to estimate the true curve through the area-based approach applied at the neck section. The equations, despite being the same as Section 1.2.1, are rewritten here for the sake of readability:

$$\varepsilon_t = \varepsilon_{a,avg} = \ln(A_0/A), \tag{7.8}$$

$$\sigma_t = \sigma_{a,avg} = F/A. \tag{7.9}$$

To estimate the current area A of the minimum cross-section, it is suggested to apply the ellipse-based 3D reconstruction technique described in Section 7.2. By repeating this at different times, the time history of the area is found, and the true curve $\sigma_t(\varepsilon_t)$ is determined. Then, Eisenberg's analytical correction (Equation 7.1) is used to scale down the part of the true curve beyond the necking onset in order to obtain a first estimate of the hardening law $\sigma_{eq}^{(0)}(\varepsilon_{eq})$. Such correction requires the semi-axes at the neck and the curvature radii in the corresponding planes which can be derived from the 3D reconstruction.

Finally, an FE analysis is used to improve the estimate of the post-necking hardening law by comparing numerical results with experimental ones. Practically, the previously identified hardening law $\sigma_{eq}^{(0)}(\varepsilon_{eq})$ is input into a FE simulation modeling the experimental test. Then, the numerical prediction of the true curve $\sigma_{t,FE}(\varepsilon_t)$, determined by applying Equations 7.8 and 7.9 to the simulation outputs, is compared with the experimental one. The possibly difference between them is attributed to an incorrect hardening law since the true curves have been seen to be influenced mainly by the hardening law [4]. The hardening law is, thus, modified by following an approach originally proposed by Joun et al. [16] for isotropic materials. Specifically, $\sigma_{eq}^{(0)}(\varepsilon_{eq})$ is multiplied for a strain-dependent coefficient determined as:

$$k_{\sigma,E} = \frac{\sigma_t}{\sigma_{t,FE}}, \tag{7.10}$$

trying to improve the prediction of the experimental true curve and, hence, of the hardening law.

To minimize the computational effort of this last identification step, the assumption of elliptical cross-section can be exploited to model only one-eighth of the specimen, as displayed in Figure 7.2. A prescribed speed is applied to one end,

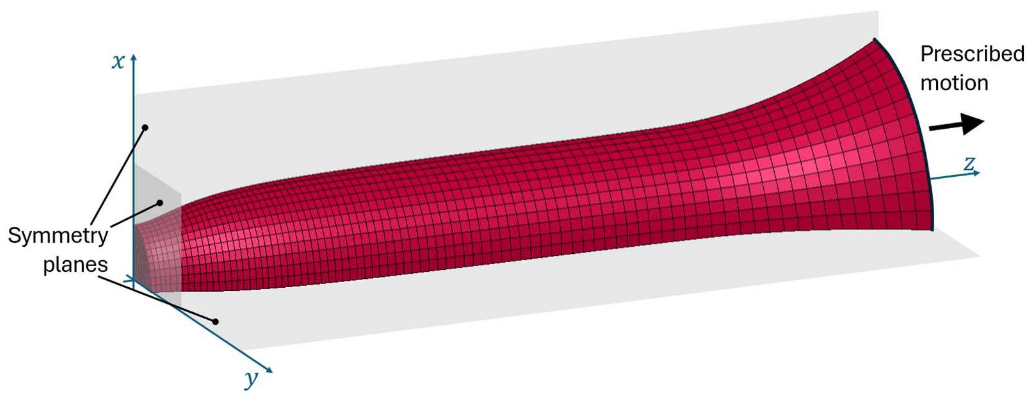

Figure 7.2 Example of a necking deformed configuration of the 3D FE model used for simulating tensile tests on anisotropic materials.

while symmetry constraints can be assigned to the opposite end and to the side surfaces aligned with the expected principal deformation planes. To further limit the computational effort, the geometry can be meshed using hexahedral elements with one integration point. Moreover, another advantageous strategy is to use smaller elements near the necking region.

For executing FE simulations, additional information on material behavior is required, among which the yield criterion is the most critical due to the hypothesized unavailability of specimens with different orientations. To address this issue a simplified approach based on Hill's 1948 yield criterion [6] is proposed in Section 7.3.1.

Furthermore, it should be noted that the entire procedure cannot be applied if the 3D shape reconstruction fails due to unfavorable configurations which cause Equations 7.4. and 7.5 to degenerate. This may happen when the material principal directions are unknown, so that this issue cannot be overcome by mounting the specimen with the desired orientation relative to the cameras. Section 7.3.2 investigates a possible approach for handling these cases.

7.3.1 Simplified modelling of anisotropic yielding

As anticipated, Hill's 1948 yield criterion is chosen for the FE-assisted stage of the proposed identification method. The present section motivates this choice and discusses its calibration with the limited available data.

Nowadays, when characterizing material anisotropy, Hill's yield criterion with associated flow rule is not commonly used. This is due to its acknowledged incapability to concurrently reflect both stress and strain anisotropy [17]. Indeed, when the model is calibrated through yield stresses obtained from tests in various directions, the corresponding deformations are often poorly predicted. *Viceversa*, a calibration based on directional deformations lead to imprecise predictions of the corresponding stresses. To address this limitation, non-quadratic orthotropic yield criteria can be used [18-21], sometimes combined with non-associated flow rules [22]. These advanced models would, however, need identification of several parameters, which is unfeasible for the cases under investigation here.

Nevertheless, for these scenarios, such complex models may not even be necessary. As a matter of fact, a test campaign in which cylindrical specimens are all characterized by the same material orientation does not aim to identify an anisotropic yielding model for predicting stress response in directions other than the one of the campaign itself. Instead, the intent is to identify a material model able to predict the strength and deformation that the material would exhibit when loaded primarily in the direction of the campaign itself. Considering that in a single tensile test the main evidence of anisotropy is given by deformation, using Hill's 1948 yield criterion, calibrated on strains (which is the only possible way), can still provide satisfactory results.

Moving on to the calibration, first consider that the chosen yield criterion can be written as:

$$\sigma_{eq} = \sqrt{F\left(\sigma_{yy}-\sigma_{zz}\right)^2 + G\left(\sigma_{zz}-\sigma_{xx}\right)^2 + H\left(\sigma_{xx}-\sigma_{yy}\right)^2 + 2L\sigma_{yz}^2 + 2M\sigma_{zx}^2 + 2N\sigma_{xy}^2}, \tag{7.11}$$

being x, y, z material directions, and F, G, H, L, M, N the yield parameters. Such parameters are unique up to a multiplicative constant, and the loading direction (represented by the z-axis in Figure 7.2) is selected as the reference direction; this implies $F + G = 1$.

Under the hypothesis of associated flow rule, strain-based calibration relies on the following expressions:

$$\frac{d\varepsilon_{xx,p}}{d\varepsilon_{yy,p}} = \frac{G}{F}; \quad \frac{d\varepsilon_{xx,p}}{d\varepsilon_{zz,p}} = -G; \quad \frac{d\varepsilon_{yy,p}}{d\varepsilon_{zz,p}} = -F; \tag{7.12}$$

which refer to the case of pure tension along the principal z-axis.

Hypothesizing that the anisotropy axes are initially aligned with the global reference frame, they remain aligned with it for elements located on the symmetry planes, as long as the specimen undergoes uniform deformation. During such phase, thus, the strains ε_{xx} and ε_{yy} can be calculated using polar positions a and b of the points on the symmetry planes as:

$$\varepsilon_{xx} = \ln\frac{a}{R_0}; \quad \varepsilon_{yy} = \ln\frac{b}{R_0}. \tag{7.13}$$

It can be concluded that, during pre-necking, an analytical estimate of the G/F ratio is possible (under the assumption of constant G/F) by knowing the semi-axes of the elliptical cross-section. Then, as G is the additive complement of F with respect to unity, both parameters can be identified.

In experimental campaigns on specimens characterized by the same material orientations, if material anisotropy can be considered constant among the loading conditions analyzed, it may be advantageous to conduct one test using a 360° shape-monitoring technique. Since this approach allows the actual 3D geometry to be determined, it would be more suitable for calibrating anisotropic yielding.

In any case, issues arise if uniform deformation is too short to appreciate the differential deformation of the semi-axes. During necking, extracting information analytically on anisotropy may be challenging and requires further investigation, not addressed in this thesis.

Finally, Equation 7.12 demonstrates that the yield parameter H does not influence the tensile response during uniform deformation and, as a result, cannot be identified. Nevertheless, Mirone and Corallo [4] showed that such parameter is negligible throughout the test in the loading conditions considered. Finally, the shear-related parameters L, M, and N could not be determined using the proposed methodology and are arbitrarily set.

7.3.2 Equivalent isotropic approach

As anticipated, the entire approach could not be applied if the ellipse-based 3D reconstruction fails due to particular orientations of the hypothetical semi-axes relative to the cameras' optical axes. Focusing on a setup with two orthogonally arranged cameras, this occurs when the semi-axes are found to lie between the two optical axes, i.e. $\alpha = 45° + k\pi/2$. When the material principal directions are unknown *a priori*, it cannot be guaranteed that such situations are always avoided. To address these problematic configurations, a further simplification is explored in this section. Specifically, each cross-section is assumed to be a circle with a diameter equal to the average of the apparent diameters evaluated from cameras' recordings. Since the resulting 3D geometry is axisymmetric, as if the material was isotropic, this strategy has been called "equivalent isotropic" approach.

Given the significant simplification that it represents, assessing the consequent error in area estimation is essential, as this in turn affects hardening identification. This evaluation was performed on an idealized necked specimen, as the one shown in Figure 7.1. For a generic elliptical cross-section with semi-axis b inclined at an angle α to the projection plane of camera 1, the two orthogonal cameras measure apparent diameters given by:

$$\widetilde{D}_1 = 2\sqrt{(asin\alpha)^2 + (bcos\alpha)^2}, \tag{7.14}$$

$$\widetilde{D}_2 = 2\sqrt{(acos\alpha)^2 + (bsin\alpha)^2}. \tag{7.15}$$

These quantities can be averaged either arithmetically (Equation 7.16) or geometrically (Equation 7.17) to estimate approximate cross-sectional areas with the following relationships:

$$\tilde{A}_a = \frac{\pi}{4}\left(\frac{\widetilde{D}_1+\widetilde{D}_2}{2}\right)^2, \tag{7.16}$$

$$\tilde{A}_g = \frac{\pi}{4}\left(\frac{\sqrt{\widetilde{D}_1\widetilde{D}_2}}{2}\right)^2. \tag{7.17}$$

These expressions can be reformulated as:

$$\tilde{A}_a = \frac{\pi}{4}(bcos\alpha)^2\left[\left(1+\left(\frac{a}{b}\right)^2\right)(1+tg^2\alpha) + 2\sqrt{\left(\frac{a}{b}\right)^2 + tg^2\alpha\left(1+\left(\frac{a}{b}\right)^4\right) + tg^4\alpha\left(\frac{a}{b}\right)^2}\right], \tag{7.18}$$

$$\tilde{A}_g = \frac{\pi}{4}(bcos\alpha)^2\sqrt{\left(1+\left(\frac{a}{b}\right)^2 tg^2\alpha\right)\left(\left(\frac{a}{b}\right)^2 + tg^2\alpha\right)} \tag{7.19}$$

By defining a percentage error as:

$$error\ (\%) = \frac{\tilde{A}-A}{A}\cdot 100, \tag{7.20}$$

where $A = \pi ab = \pi b^2(a/b)$ for an ellipse, it is evident that the parameters influencing it are the ratio between the semi-axes and the ellipse orientation relative to the cameras. These dependencies are illustrated through contour plots in Figure 7.3; dashed and solid lines refer to arithmetic and geometric average respectively.

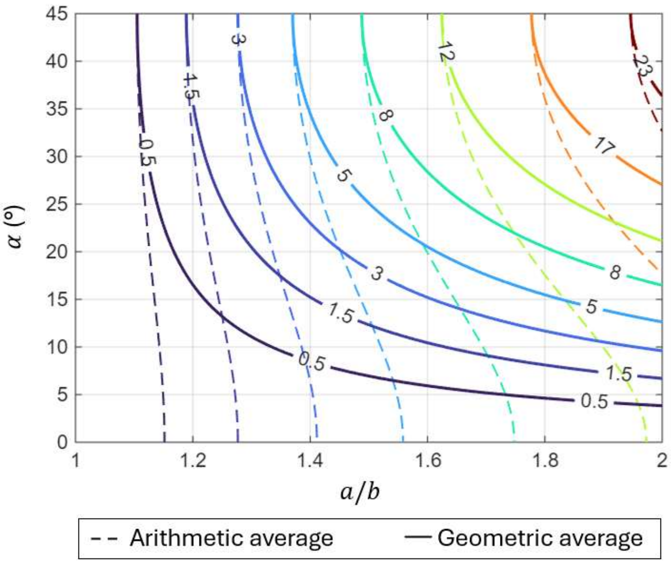

Figure 7.3 Contour plot of the percentage error made in the determination of the cross-section area when adopting the equivalent isotropic approach.

Regarding the aspect ratio, the error of both equivalent isotropic methods is zero when the cross-section is a circle ($a/b = 1$), as expected. Then, for higher a/b ratios, both strategies share a monotonically increasing trend of the error; this is valid at any given angle $\alpha \in (0°, 45°]$. For the orientation angle, investigating the 0°÷45° range was enough thanks to periodicity and symmetry properties of the problem. It is interesting to notice that $\alpha = 45°$ represents the worst configuration for both methods and for any a/b ratio, but with errors remaining smaller than 5% for $a/b < 1.4$. Moreover, arithmetically and geometrically equivalent isotropic approaches generate almost identical errors for angles close enough to 45° but progressively deviate for decreasing angles. The geometrically equivalent isotropic approach is exact for $\alpha = 45°$ since, being the cameras aligned with the semi-axes, they are directly measured and Equation 7.19 recovers the correct area of an ellipse. Conversely, the arithmetically equivalent isotropic approach introduces a non-negligible error, even if smaller than that of the 45°-configuration.

Overall, this analysis leads to the conclusion that, despite its simplicity, the equivalent isotropic approach (especially the one based on the geometrical mean) can yield acceptable results for limited a/b ratios. This is essential for unfavorable configurations (i.e, $\alpha \approx 45°$) but may also be useful in all other cases, if an extremely simple method for determining the area-based true curve is needed.

7.4 Experimental case study

This section evaluates the effectiveness of the proposed post-necking identification method for anisotropic materials through its application to experimental tests. Even though the method has been developed for critical scenarios with limited optical access to the specimen, in principle it could be applied even to less demanding conditions by intentionally considering only two viewpoints. Nevertheless, a true critical case study was chosen to highlight the practical relevance of the proposed method.

The material investigated was a precipitation hardened copper alloy, specifically Copper Chrome Zirconium (CuCrZr), which underwent annealing at 580 °C for two hours. Since the cylindrical specimens were machined along the transversal direction of a plate with 13 mm of thickness and 85 mm of width, the exhibited anisotropic behavior (immediately detectable from the fractured surface, as shown Figure 7.4) could be reasonably attributed to the plate manufacturing process.

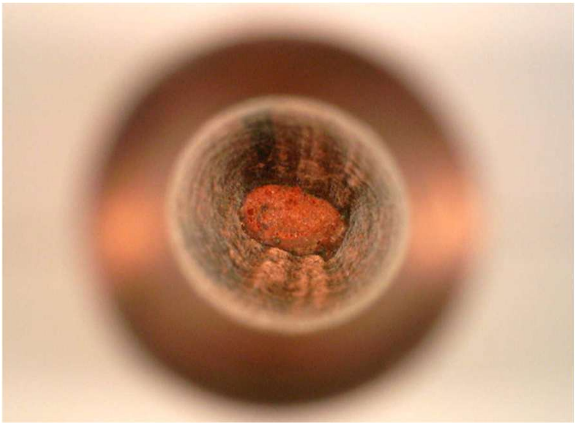

Figure 7.4 Fractured surface of an initially cylindrical CuCrZr specimen.

Moreover, as CuCrZr is of particular interest to the nuclear field [23] where components are subjected to extreme loading conditions, among which high temperatures, the present tests were performed across a temperature range reaching 580°C.

Details on the experimental setup are provided in Section 7.4.1, but it is worth anticipating that the limited optical access to the specimens was caused by the need to perform experiments within a closed chamber with inert atmosphere to avoid material oxidation. As anticipated in Section 7.2, the geometrical reconstruction from two camera views requires knowing how the hypothetical ellipses are oriented with respect to the cameras. This is addressed through post-mortem analyses, explained in Section 7.4.2. Then, Section 7.4.3 regards data analysis for identifying the strain-hardening laws, finally reported and discussed in Section 7.4.4.

7.4.1 Experimental setups

As already mentioned, given the high temperatures involved and the expected anisotropic deformation resulting from the plate manufacturing process, the experimental setup required careful attention. It must allow tests to be conducted under a non-oxidizing atmosphere, while preserving the possibility of monitoring specimen deformation.

For this purpose, a specialized chamber featuring water-cooled supports was used, as illustrated schematically in Figure 7.5. Before testing, a vacuum pump connected to the chamber removed air, while an argon reservoir supplied inert gas; then, a slight overpressure of inert gas was maintained during testing.

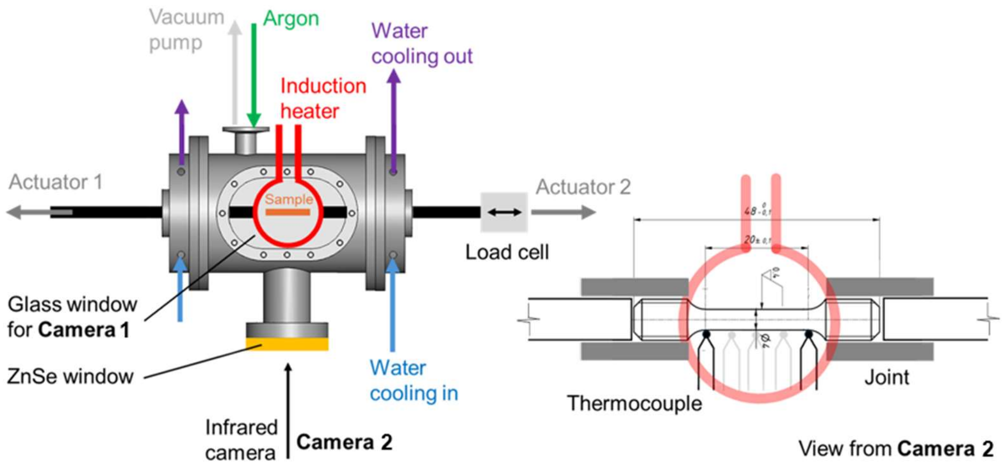

Figure 7.5 Detailed schematic representation of the experimental setup.

Optical access to the sample was enabled by two windows arranged perpendicularly one to the other and the illumination was placed inside the chamber. Tests were recorded using two high-resolution cameras Opto Engineering ITA32-GM-10C, fitted with Tokina AT-X Pro 100 mm f/2.8 lenses. This configuration allowed for resolutions of 9 μm/px and 12 μm/px. Image acquisition from the two cameras was carefully synchronized to ensure accurate reconstruction of the 3D specimen geometry.

The specimens were heated with an induction system employing an open solenoid coil to maintain optical access to the samples. Throughout the tests, two K-type thermocouples spot-welded onto the gauge length were used to monitor the temperature. Figure 7.6a shows a picture of the specimen as seen through one of the optical ports.

To verify temperature uniformity within the gauge length, a preliminary validation phase was conducted on a pure copper dummy sample. Five thermocouples were spot-welded along its gauge length, and a high-emissivity coating was applied on its surface. One of the two optical ports was equipped with a ZnSe window and an infrared camera viewed at a dummy sample through it. The dummy specimen was heated to each target temperature and, once steady-state conditions were attained, infrared imaging and thermocouple readings were used to assess the axial temperature profile. Figure 7.6b presents an example of this thermal uniformity assessment.

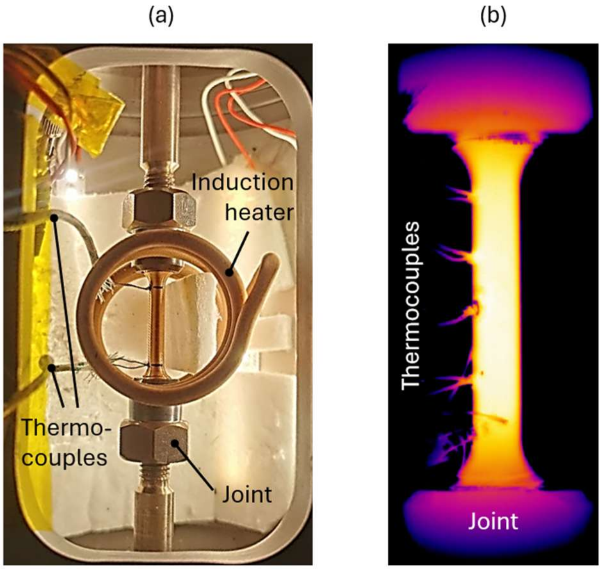

Figure 7.6 Specimen mounted inside the chamber (a) and preliminary evaluation of heating uniformity (b).

Two linear actuators, moving at identical speeds in opposite directions, were used to apply a uniaxial tensile load to the specimens, as depicted in Figure 7.5. This arrangement guaranteed that the specimen stayed centered relative to the induction coil during testing, thereby enabling consistent heating. The load exerted by the system was measured by a load cell. Regarding specimen geometry, it was characterized by a 4 mm gauge diameter, 20 mm gauge length, and threaded ends. The speed applied to its heads, resulted in a nominal strain rate of $2.5\ 10^{-4}\ s^{-1}$.

Finally, a post-mortem analysis of each fractured sample was performed; this aims at providing useful information for the 3D reconstruction of the specimen geometry during the test. This practically consisted of a 360°-scan realized by recording the failed specimen as it rotated around its axis. The Opto Engineering TCBENCH036 telecentric optical bench (11 μm/px of resolution) was used, and the acquisition of 600 frames during the specimen rotation was time-gated by an encoder.

In addition to above tests executed in the closed chamber, an auxiliary room-temperature test with full 360° shape-monitoring was executed. Since all specimens were obtained along the same plate direction, the purpose of this test was to better understand the evolution of the cross-sections and, thus, the anisotropic behavior. Practically, the setup of Figure 7.5 was modified by removing the chamber and adding the telecentric optical bench Opto Engineering TCBENCH036. While grabbing images, the system rotated around the specimen's axis; it was also fitted with an angular position sensor to correlate each image with the corresponding viewing angle.

7.4.2 Post-mortem analysis

Before explaining how images acquired during each post-mortem scan were post-processed, it is important to underline that these analyses aim at identifying how cameras were oriented with respect to the ellipse semi-axes during each test. Knowing *a priori* this orientation with sufficient accuracy may not be feasible. For instance, in the present campaign, specific information regarding the specimen orientation within the plate was missing. However, even if it was available, it would have been helpful to use the method proposed hereinafter to precisely determine the orientation. Basically, the post-mortem scan is used to reconstruct the 3D geometry of the failed specimen, whose principal directions can be identified. Then, comparison with test recordings allows cameras' viewing angles to be determined. The detailed explanation provided in the following paragraphs refers to a single test, but the procedure was actually applied to all those of interest.

The proposed post-mortem 3D reconstruction entailed applying the shape-from-silhouette technique to images acquired during the 360°-scan. Although this method cannot detect internal voids and special concave shapes, it is suitable for describing typical necking shapes of tensile specimens. More specifically, it required segmenting the images obtained from several viewpoints, and then projecting the silhouettes into the 3D space to form visual cones, one for each silhouette. The intersection of these cones provided the specimens' outer envelope, referred to as "visual hull". This technique was implemented in MATLAB, starting from an open-source script [24] and customizing it for the present experimental arrangement. A representative example of this result is depicted in Figure 7.7.

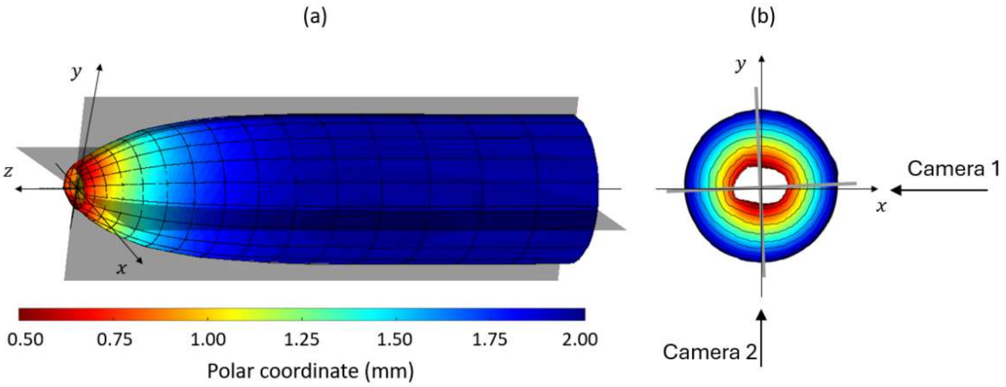

Figure 7.7 Post-mortem analysis of a specimen tested at 450°C: (a) 3D reconstruction together with identified symmetry planes; (b) view normal to the longitudinal axis, indicating the cameras' viewing angles.

Subsequently, the resulting geometry was post-processed through the Principal Component Analysis (PCA) so that the longitudinal axis was determined and the specimen could be aligned with the reference frame (as already done in Figure 7.7). By analyzing the cross-sections, it was possible to roughly verify the hypothesis of elliptical cross-section for a wide axial portion of the specimen. The principal axes of individual cross-sections were again determined by PCA. In this phase, the part of the specimen close to the fracture was excluded due to the likely presence of ductile damage. Likewise, the part far from the necking zone was ignored too in tests where necking occurred soon after yielding. As a matter of fact, in such situations the cross-sections far from the neck remained nearly circular throughout deformation, which means that the determination of principal axes would be badly conditioned.

The principal axes orientations derived from the analyzed cross-sections were averaged to establish a single, time-invariant orientation for the entire duration of the test. In the example of Figure 7.7, the planes perpendicular to the two principal directions of the cross-sections are shown in gray.

Finally, the viewing angles of the cameras during the test were identified by comparing the images at the end of the test with post-mortem scan images. In Figure 7.7b cameras' optical axes are indicated through arrows; in the chosen reference frame, Camera 1 was aligned with the x-axis and Camera 2 with the y-axis.

7.4.3 Data analysis

This section provides a description of the post-processing steps required for determining the hardening law, along with the presentation of intermediate results. Briefly, the 3D specimen geometries during the tests were reconstructed, thereby allowing the area-based true curves to be determined, and corrected with Eisenberg's theory; finally, the laws were refined through FE simulations.

As already mentioned, quasi-static tensile tests were carried out across a wide range of temperatures. The analysis presented here focuses on five temperatures, at intervals of about 150 °C, namely room temperature, 150 °C, 300 °C, 450 °C, and 580 °C. One test per condition was considered since repetitions for high temperature tests proved high repeatability.

The first step involved reconstructing the 3D specimen geometries by assuming elliptical cross-sections and then applying the method described in Section 7.2. Ellipses were determined by combining their orientation with respect to the cameras (see Section 7.4.2) with measurements of the cameras. The latter data was obtained by analyzing the specimen silhouettes extracted using image segmentation. Figure 7.8 shows some frames acquired synchronously by the two cameras, with the specimen contours highlighted in blue and red for Camera 1 and Camera 2 respectively. An experiment in which the cameras were nearly aligned with the main axes of the elliptical cross-sections was chosen to emphasize material anisotropy; this was the same one of the post-mortem analysis of Figure 7.7.

Then, the apparent diameters $\widetilde{D}_1$ and $\widetilde{D}_2$ along the specimen longitudinal axis z were calculated, for each camera and time, as the distance between edges on opposite sides of that axis. During necking development, the resulting datasets $(z_1, \widetilde{D}_1)$ and $(z_2, \widetilde{D}_2)$ were spatially referred to one another by considering the position of the neck. For subsequent analysis, only the portion of the datasets corresponding to the specimen side with the longest axial extension was considered.

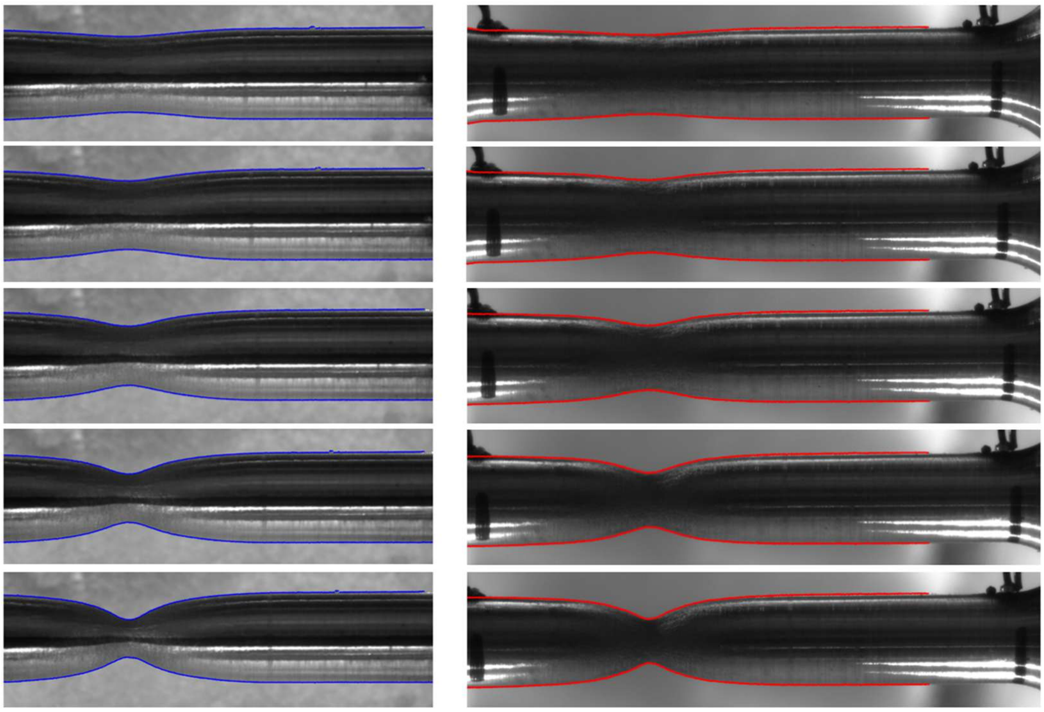

Figure 7.8 Sequence of acquired images for the same test of Figure 7.7 (Camera 1 on the left, Camera 2 on the right).

A fourth-order polynomial fit was applied to reduce experimental noise and Equations 7.4 and 7.5 were used to determine the specimen profiles on the planes of minor and major deformation, namely $a(z)$ and $b(z)$ respectively. These profiles were in turn fitted with a fourth-order polynomial to facilitate determination of curvature radii ρ_a and ρ_b at the neck. This analysis was repeated for each time and also for each analyzed test, since none of them was in an unfavorable condition for elliptical fitting. Figure 7.9a displays the results for the same test considered in previous figures. Figure 7.9b, instead, shows four contour plots representing the

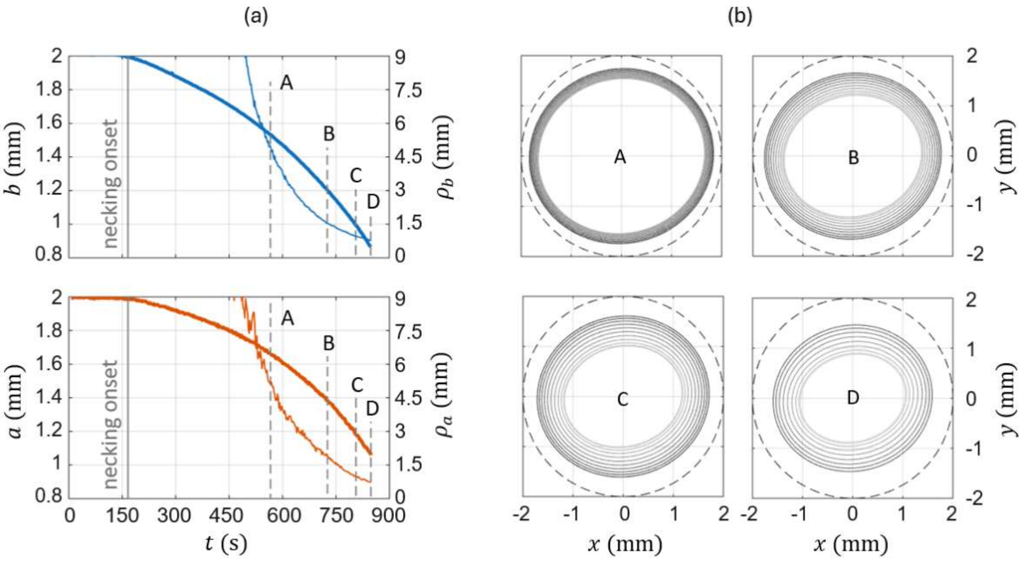

Figure 7.9 3D reconstruction for the same test of previous figures: (a) evolution of semi-axes (thick lines) and of corresponding curvature radii; dashed lines indicate configurations analyzed in (b) in terms of cross-sections at 10 constant axial offsets from the neck, with a spacing of 0.2 mm.

ellipse-based reconstructed geometry at various stages, those indicated by dashed lines in subplot (a). Each contour plot provides a top view of the specimen, depicting cross-sections at specific axial distances from the minimum area, with 0.2 mm intervals, until 2 mm. For reference, the initial circular cross-section is indicated by dashed lines. The fact that the last contour line, corresponding to the z-coordinate of 2 mm, progressively reduces its size is due to having considered a limited portion of the specimen with a Eulerian perspective.

Once the specimens' cross-sections, especially the one at the neck, had been reconstructed, true strain and stress were calculated using Equations 7.8 and 7.9. The resulting true curves are displayed in Figure 7.10a with each color representing a different testing temperature. Figure 7.10b, instead, focuses on a single test, the room-temperature one, to highlight the true curves that would be found with methods other than the ellipse-based one. The dotted lines refer to cases where single-camera measurements are considered as if they were diameters of a circular cross-section. Such an approach completely ignored material anisotropy, hence introducing a significant error. Instead, the equivalent isotropic approach (dashed line) of Section 7.3.2 provided results quite similar to the elliptical-based method (solid line). Although both curves are affected by experimental errors (apparent diameter measurements the first and also orientation angle the second), their similarity can still be partly attributed to an a/b ratio that remains enough close to 1. As a matter of fact, although post-mortem fracture surfaces might suggest higher ratios, tests where specimens were favorably oriented relative to the cameras (e.g., Figure 7.7) showed that the ratio reached a maximum of 1.25 at the last configuration. According to the analysis of Section 7.3.2, such ratio introduces an acceptable error in the true curve identified by the equivalent isotropic approach.

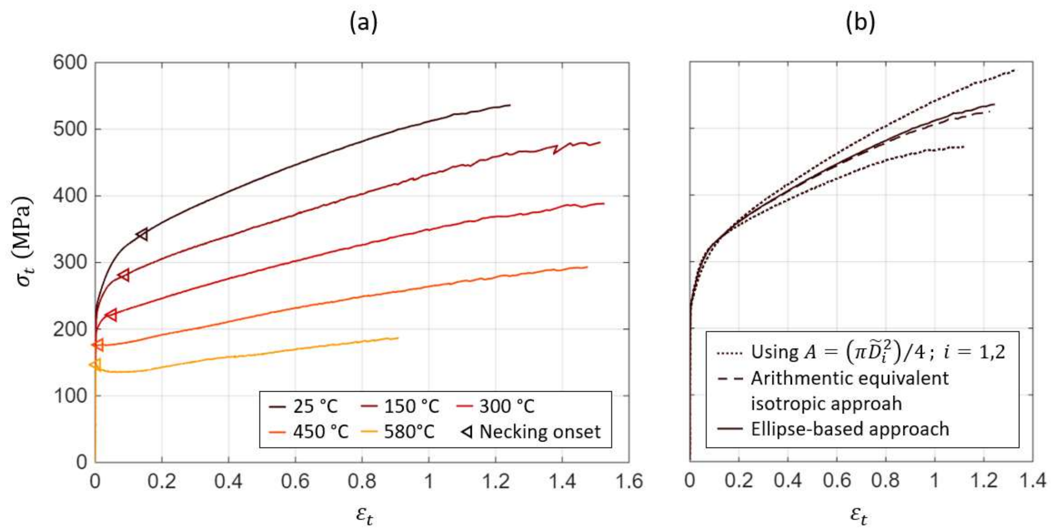

Figure 7.10 Result of the ellipse-based approach in terms of true curves (a); the approach is compared to simpler strategies for the test at room-temperature (b).

Finally, it is important to notice, from triangular markers of Figure 7.10a, that the onset of necking occurred at decreasingly lower strains as the test temperature rose. This highlights the importance of correcting the true stress for the necking triaxiality, especially for the high temperature tests, to determine the hardening behavior. For this purpose, Eisenberg's analytical correction (Equation 7.1) was applied first, using the semi-axes and curvature radii at the neck derived from the 3D reconstruction.

Subsequently, FE simulations were conducted with Ansys LS-DYNA to evaluate whether the identified laws were able to predict experimental results. The main features of the models have been described in Section 7.3. For what the mesh size is concerned, given that the specimen gauge length was 20 mm, the minimum element size in the axial direction in the undeformed configuration was set to 0.05 mm. This proved to be a good trade-off between computational cost and accuracy. Regarding material constants, density, Poisson's ratio, and Young's modulus were treated as isotropic and independent of temperature. These assumptions are justified by the negligible inertial effects in quasi-static tests and the negligible elastic strains during large plastic deformation. Plastic behavior was modelled through Hill's 1948 yield criterion [6] and a tabular definition of the stress-strain-temperature relationship (*MAT_HILL_3R_3D).

Since all tested specimens were obtained along the same plate direction, complete calibration of an anisotropic yield criterion, even as simple as the chosen one, was unfeasible. Thus, the simplified approach proposed in Section 7.3.1 was adopted for estimating at least F (and its complement G) from pre-necking data. To this end and to avoid uncertainties related to the elliptical approximation, the additional room-temperature test with 360° shape-monitoring technique was conducted. The scans were executed at given elongations and post-processed via the shape-from-silhouette technique, explained in Section 7.4.2. Once the major and minor axes of the cross-sections had been estimated for uniformly deformed configurations, the strains along such directions were determined via Equation 7.13. Assuming constant yield parameters, F and G were identified as 0.62 and 0.38, respectively. Then, H was set equal to G under the assumption of transverse isotropy, and shear parameters were set to 1.5 due to the lack of data. These parameters were supposed to be representative of all tests as the specimens came from the same plate.

The results from these FE simulations suggested that there was room for improvement and this was accomplished with the refinement strategy proposed in Section 7.3. This aimed at a more precise description of the material's true response by accounting for inaccuracies from experimental uncertainties and simplifying assumptions of Eisenberg's theory. Results are presented and analyzed in the following section.

7.4.4 Results and discussion

The resulting hardening laws identified from tests at different temperatures are compared in Figure 7.11. In spite of the copper-based matrix, the overall thermal softening behavior is not the typical one of FCC metals, instead, it is more similar to that of BCC ones. This can be attributed to the presence of precipitates which alter the behavior with respect to pure copper. Similar results were reported for the dispersion hardened copper alloy Glidcop Al-15 [25].

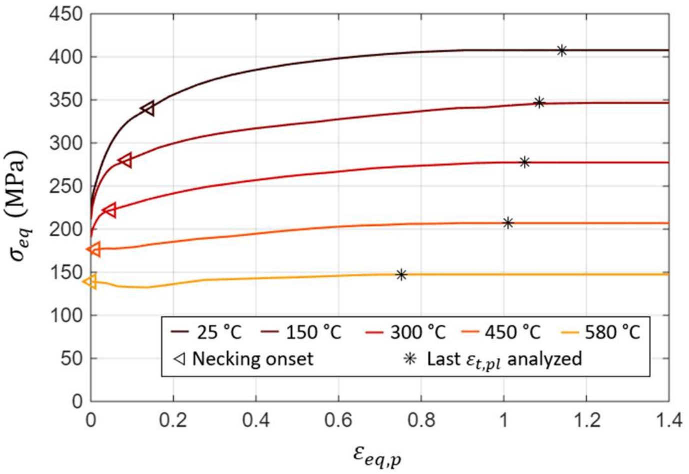

Figure 7.11 Identified hardening laws; the last configuration analyzed refers to those shown in Figure 7.12-7.16.

The capability of these laws to describe experimental results in terms of area-based true curves and silhouettes can be evaluated from Figures 7.12-7.16. The silhouettes were actual profiles recorded by the cameras at specific post-necking true strains $\varepsilon_t - \varepsilon_{t,n}$, starting from 0.25 and increasing by 0.25 increments. Within the stress-strain diagrams, the hardening laws are also included to emphasize how much true stress deviates from equivalent stress.

Regarding the true curves, good experimental-numerical agreement can be observed over a wide strain range. Deviations begin to appear at large strains, with a maximum relative error of about 4% for the test at 450 °C test, at 120% of plastic deformation. On one hand, it must be recalled that the experimental true curve was used as a sort of target function when correcting the first estimate of the hardening law. On the other hand, the fact that a single iteration was able to provide such good results was not guaranteed. This highlights the potential of well-guided FE-assisted iterative strategies (as those proposed in Section 6.3.2 too).

Coming to the comparison of projected silhouettes, the difference between experiments and FE models was evaluated using the following expression:

$$error = \sqrt{\frac{1}{N} \sum_{i=1}^{N} \left(\frac{\tilde{R}_{i,FE} - \tilde{R}_{i,exp}}{\tilde{R}_{i,exp}} \right)^2}, \tag{7.21}$$

where $\tilde{R}_{i,FE}$ and $\tilde{R}_{i,exp}$ are the numerical and experimental apparent radii of the i-th point of the projection. For the experiments performed at room temperature and at

150 °C, this discrepancy remains lower than 1.1% for both cameras and the different configurations analyzed. For the 300 °C test, it can be readily observed from Figure 7.14b that the model's predictions worsen towards more highly deformed configurations. Nevertheless, the error always remains lower than 2%. At 450 °C, the error increases further, reaching a peak of 3% in configuration D. On the contrary, at 580 °C, the largest discrepancy recorded is 1.2%.

It can be noted from subplots (b) of Figures 7.12-7.16 that, in some cases, the numerical and experimental profiles mainly differ in the portion where convexity changes. This may be caused by shear-related yield parameters as these portions are subjected to relatively high shear stress. In other cases, instead, the profiles differ also at the neck, thus suggesting potential inaccuracies in the yield parameter F. Furthermore, discrepancies could also be attributed to the influence of temperature on the yield parameters. Actually, understanding the physical cause of these differences, thereby knowing which specific aspect requires adjustment, is extremely challenging due to the complex interaction between hardening and anisotropy and the limited data availability.

Nevertheless, the results can be considered satisfactory, in view of the simplifications adopted to deal with the limited data available, especially regarding anisotropy. This underlines the effectiveness of the proposed approach in characterizing strain-hardening behavior for anisotropic cases where it is not possible to explore various loading conditions or directions.

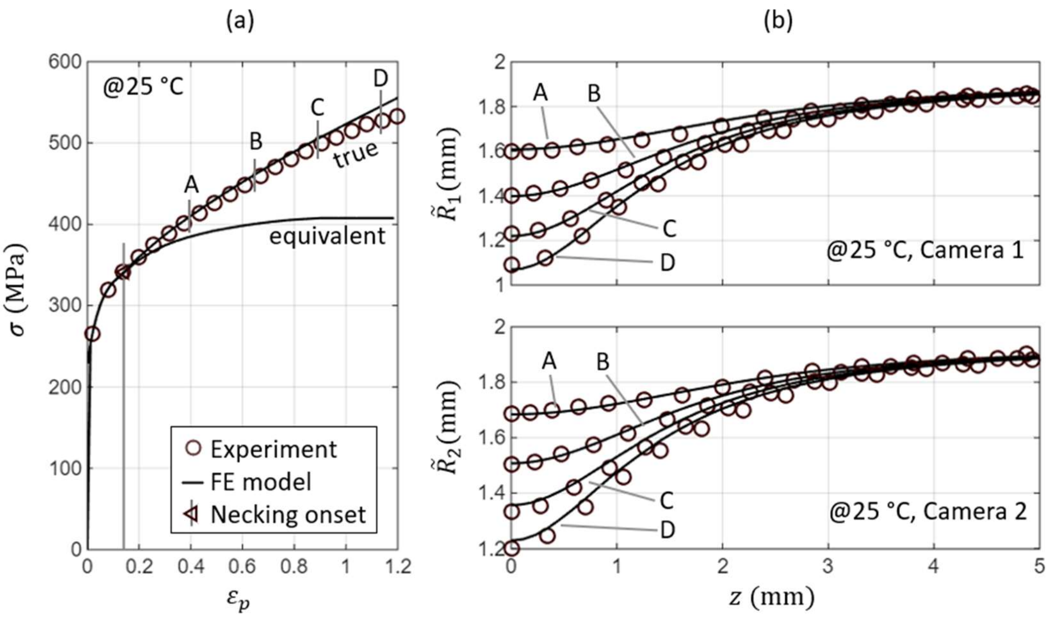

Figure 7.12 Experimental results at 25 °C compared with FE predictions in terms of true curve (a) and projected silhouettes seen by the two cameras (b), being $\tilde{R} = \tilde{D}/2$.

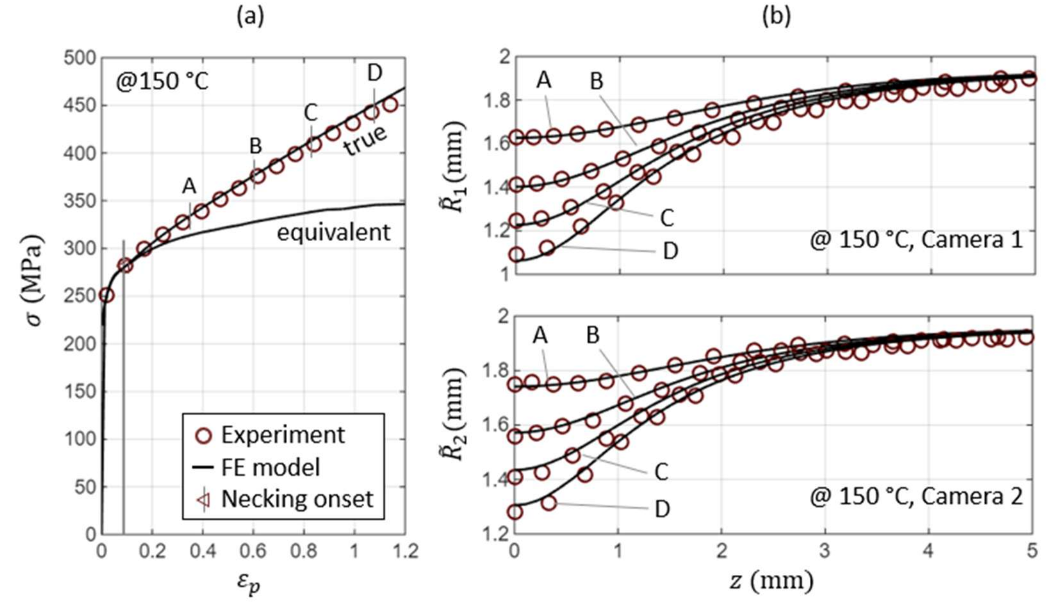

Figure 7.13 Experimental results at 150 °C compared with FE predictions in terms of true curve (a) and projected silhouettes seen by the two cameras (b), being $\tilde{R} = \tilde{D}/2$.

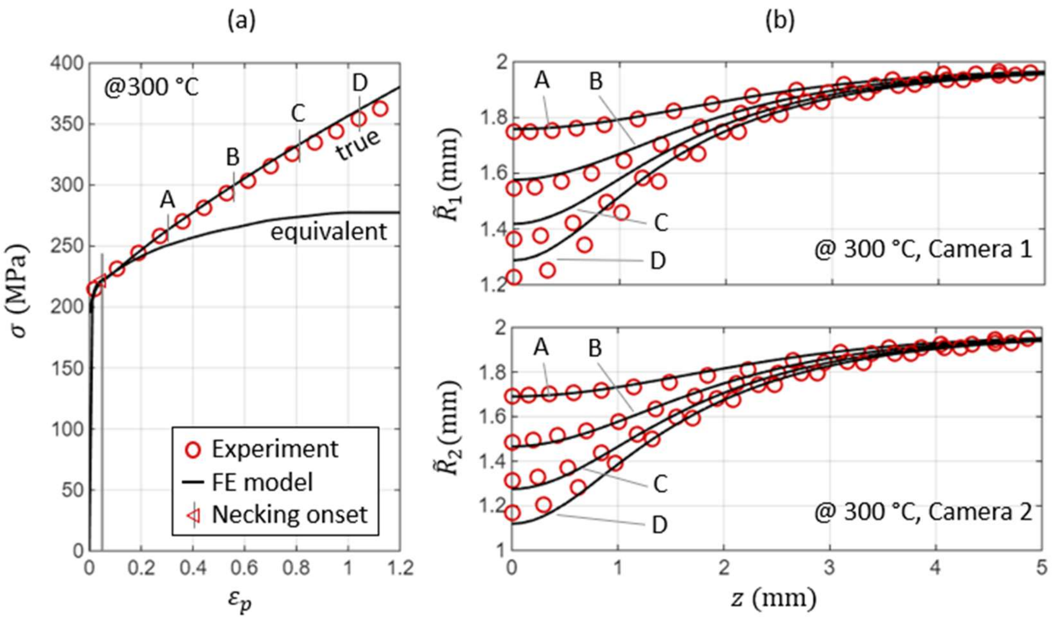

Figure 7.14 Experimental results at 300 °C compared with FE predictions in terms of true curve (a) and projected silhouettes seen by the two cameras (b), being $\tilde{R} = \tilde{D}/2$.

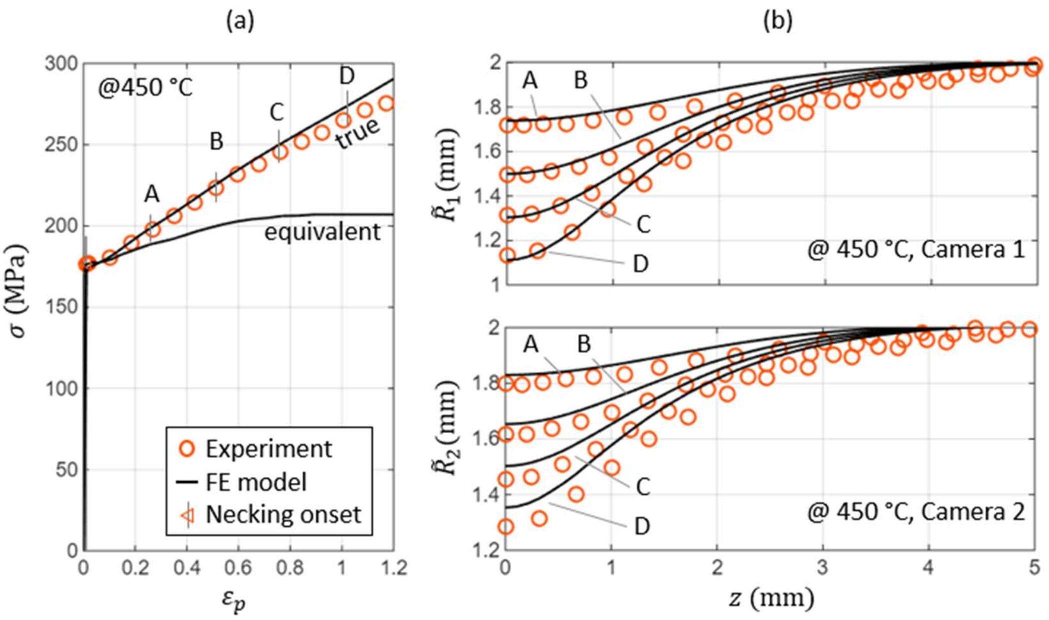

Figure 7.15 Experimental results at 450 °C compared with FE predictions in terms of true curve (a) and projected silhouettes seen by the two cameras (b), being $\tilde{R} = \tilde{D}/2$.

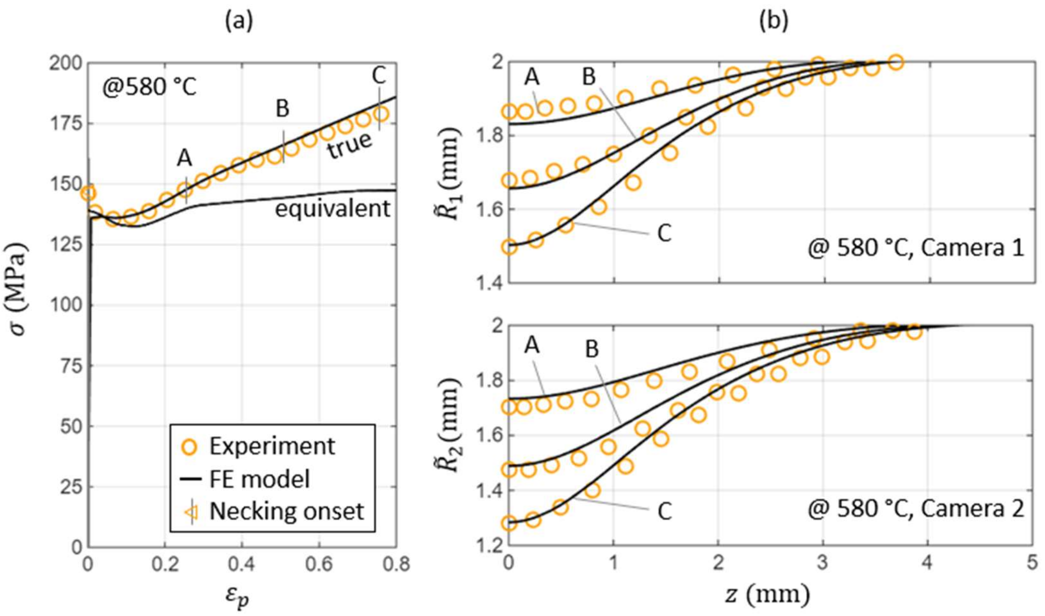

Figure 7.16 Experimental results at 580 °C compared with FE predictions in terms of true curve (a) and projected silhouettes seen by the two cameras (b), being $\tilde{R} = \tilde{D}/2$.

7.5 Concluding remarks

This chapter dealt with the identification of post-necking hardening from a tensile test during which a cylindrical specimen exhibits anisotropic deformation. This involved addressing two issues: one related to determining the non-axisymmetric geometry of the specimen precisely, and the other related to considering the complex strain and stress fields developed during necking appropriately. The former required balancing versatility and accuracy of the experimental setup, while the latter efficiency and reliability of the characterization strategy.

The proposed method accomplished the first requirements by adopting an ellipse-based reconstruction technique for the determination of the 3D shape of the specimen. Being based on test recordings from only two different viewpoints, this strategy is adequate even for demanding loading conditions with limited optical access to the specimen. Nevertheless, if more viewpoints are available, the method can be extended to account for all of them, thus resulting in improved accuracy. It was then proposed to use the acquired geometrical data for estimating the post-necking hardening law by combining Eisenberg's correction of the area-based true stress-strain curve with subsequent refinement through a FE simulation. This strategy enhances efficiency, while still capturing the main features of anisotropic necking. Since FE simulations require a yield criterion, the present chapter also tackled the yield criterion determination in critical scenarios where only a material orientation is available for testing.

The proposed framework provided acceptable results when applied to a case study characterized by all above-mentioned critical points, namely limited optical access and availability of specimens obtained along the same plate direction. Since only the true curve was used directly in the FE-assisted refinement phase, improvements could be possible by including also the deformed specimen geometry. Overall, in light of the simplifications applied, the results suggest the suitability of the approach for experiments under demanding testing conditions (such as high temperature or high strain rate) which aim at a first-order estimate of the material strain-hardening behavior. Finally, it is worth noting that validation was carried out on manufacturing-induced anisotropy; thus, future endeavors should be devoted to investigating cases where anisotropy arises from the crystallographic structure (e.g., HCP metals).

References

[1] Eisenberg, M. A., & Yen, C. F. (1983). An anisotropic generalization of the Bridgman analysis of tensile necking.

[2] Eisenberg, M. A. (1985). Anisotropic tensile necking. *International journal of plasticity*, *1*(1), 29-38.

[3] Arthington, M. R., Siviour, C. R., & Petrinic, N. (2012). Improved materials characterisation through the application of geometry reconstruction to quasi-static and high-strain-rate tension tests. *International Journal of Impact Engineering*, *46*, 86-96.

~~[4]~~[1] Mirone, G., & Corallo, D. (2013). Stress–strain and ductile fracture characterization of an X100 anisotropic steel: Experiments and modelling. *Engineering Fracture Mechanics*, *102*, 118-145.

~~[5]~~[2] Mirone, G. (2004). A new model for the elastoplastic characterization and the stress–strain determination on the necking section of a tensile specimen. *International Journal of Solids and Structures*, *41*(13), 3545-3564.

~~[6]~~[3] Hill, R. (1948). A theory of the yielding and plastic flow of anisotropic metals. *Proceedings of the Royal Society of London. Series A. Mathematical and Physical Sciences*, *193*(1033), 281-297.

~~[7]~~[4] Chandran, S., & Verleysen, P. (2024). A hybrid optical technique to evaluate the instantaneous specimen shape during static and dynamic material testing. *Optics and Lasers in Engineering*, *181*, 108417.

~~[8]~~[5] Khadyko, M., Dumoulin, S., Børvik, T., & Hopperstad, O. S. (2014). An experimental–numerical method to determine the work-hardening of anisotropic ductile materials at large strains. *International Journal of Mechanical Sciences*, *88*, 25-36.

~~[9]~~[6] Barlat, F., Aretz, H., Yoon, J. W., Karabin, M., Brem, J. C., & Dick, R. (2005). Linear transfomation-based anisotropic yield functions. *International journal of plasticity*, *21*(5), 1009-1039.

~~[10]~~[7] Khadyko, M., Dumoulin, S., Børvik, T., & Hopperstad, O. S. (2015). Simulation of large-strain behaviour of aluminium alloy under tensile loading using anisotropic plasticity models. *Computers & Structures*, *157*, 60-75.

~~[11]~~[8] Buffiere, J. Y., Maire, E., Adrien, J., Masse, J. P., & Boller, E. (2010). In situ experiments with X ray tomography: an attractive tool for experimental mechanics. *Experimental mechanics*, *50*(3), 289-305.

~~[12]~~[9] Genovese, K., Cortese, L., Rossi, M., & Amodio, D. (2016). A 360-deg digital image correlation system for materials testing. *Optics and Lasers in Engineering*, *82*, 127-134.

~~[13]~~[10] Baumgart, B. G. (1974). Geometric modeling jor computer vision. *Computer Science Dept. of Stanford Univ*, *1*.

~~[14]~~[11] Laurentini, A. (2002). The visual hull concept for silhouette-based image understanding. *IEEE Transactions on pattern analysis and machine intelligence*, *16*(2), 150-162.

~~[15]~~[12] Arthington, M. R., Siviour, C. R., Petrinic, N., & Elliott, B. C. F. (2009). Cross-section reconstruction during uniaxial loading. *Measurement Science and Technology*, *20*(7), 075701.

~~[16]~~[13] Joun, M., Eom, J. G., & Lee, M. C. (2008). A new method for acquiring true stress–strain curves over a large range of strains using a tensile test and finite element method. *Mechanics of Materials*, *40*(7), 586-593.

~~[17]~~[14] Lian, J., Shen, F., Jia, X., Ahn, D. C., Chae, D. C., Münstermann, S., & Bleck, W. (2018). An evolving non-associated Hill48 plasticity model accounting for anisotropic hardening and r-value evolution and its application to forming limit prediction. *International Journal of Solids and Structures*, *151*, 20-44.

~~[18]~~[15] Barlat, F., Lege, D. J., & Brem, J. C. (1991). A six-component yield function for anisotropic materials. *International journal of plasticity*, *7*(7), 693-712.

~~[19]~~[16] Karafillis, A. P., & Boyce, M. C. (1993). A general anisotropic yield criterion using bounds and a transformation weighting tensor. *Journal of the Mechanics and Physics of Solids*, *41*(12), 1859-1886.

~~[20]~~[17] Cazacu, O., & Barlat, F. (2001). Generalization of Drucker's yield criterion to orthotropy. *Mathematics and Mechanics of Solids*, *6*(6), 613-630.

~~[21]~~[18] Cazacu, O. (2018). New yield criteria for isotropic and textured metallic materials. *International Journal of Solids and Structures*, *139*, 200-210.

~~[22]~~[19] Stoughton, T. B. (2002). A non-associated flow rule for sheet metal forming. *International Journal of Plasticity*, *18*(5-6), 687-714.

~~[23]~~[20] Gorley, M., Diegele, E., Gaganidze, E., Gillemot, F., Pintsuk, G., Schoofs, F., & Szenthe, I. (2020). The EUROfusion materials property handbook for DEMO in-vessel components—Status and the challenge to improve confidence level for engineering data. *Fusion Engineering and Design*, *158*, 111668.

~~[24]~~[21] Maxim (2026). Visual Hull Matlab (https://it.mathworks.com/matlabcentral/fileexchange/45989-visual-hull-matlab), MATLAB Central File Exchange.

~~[25]~~[22] Scapin, M., Peroni, L., & Fichera, C. (2014). Mechanical behavior of glidcop Al-15 at high temperature and strain rate. *Journal of materials engineering and performance*, *23*(5), 1641-1650.

Chapter 8

8Conclusions

During the last decades, the use of FEA has become increasingly widespread in many engineering applications, thus highlighting the importance of reliable material models for describing accurately the material response under the conditions of interest. This in turn leads to the capability of calibrating appropriately those models. Focusing on plastic deformation in metals, a crucial aspect is represented by characterizing hardening behavior.

The main objective of this thesis was the development of efficient phenomenological methods for identifying hardening up to large strains. More specifically, for limiting experimental complexity, all identification methods were devised for relying on experimental data provided by uniaxial tensile tests on dog-bone cylindrical specimens. This choice also aimed to enhance versatility, since proper setups allow tensile tests to be conducted at different speeds and temperatures, hence enabling investigation into both strain rate and temperature sensitivity of the material.

As necking usually occurs during tensile tests on ductile materials, the primary issue to tackle was accounting for the resulting non-uniformities of strain and stress fields, as well as the loss of stress uniaxiality. It is well established that necking is an intrinsic feature of tensile tests that can still provide useful data when analyzed properly. Thus, the first part focused on post-necking identification strategies proposed in the literature, from the pioneering work by Bridgman (1952), who paved the way for analytical corrections, up to advanced numerical strategies based on FEA or VFM. Most of the methods proposed so far were found to have opposite advantages and drawbacks: direct methods are computational efficiency but lack accuracy and sometimes robustness, while advanced numerical strategies prioritized reliability over computational cost, resulting in time-consuming techniques. In light of these observations, the present thesis pursued alternative approaches that improve accuracy while maintaining a limited computational effort.

The core idea was to fulfill the first requirement by relying on FEA and the second by storing precomputed simulations in a database queried during the identification process. In developing this strategy, a key aspect was the choice of an adequate query variable, similar to the definition of the target function required in FEMU approaches. Specifically, the deformed shape of the specimen during necking was chosen. This mainly resulted from observing its central role in interpreting post-necking data in several proposed methods. Virtually all analytical corrections consider the time history of the geometry in a small neighborhood of the neck, while advanced numerical strategies extend the analysis to a wider specimen region, usually adopting DIC technique for full-field strain measurements. Comparison of these two ways for accounting specimen deformation highlighted that the first is less robust whereas the second is more challenging, especially considering the cylindrical geometry of the specimens used. Hence, the present work employed a trade-off solution: considering the specimen silhouette over a wide region surrounding the neck. This enhanced robustness without requiring complex experimental techniques, such as stereo-DIC: only segmentation and edge-detection algorithms are needed for silhouette determination. Since the quality of the results depends on the acquired images, special care was taken to employ appropriate imaging systems in terms of resolution, lighting, lens distortion, and acquisition rates in dynamic tests.

As profile-based identification methods are quite uncommon in literature, a detailed analysis to highlight the shape-law correlation for cylindrical bars of isotropic materials subjected to uniaxial monotonic tensile loading was conducted. The resulting outcomes supported the use of necking profile as query variable in the proposed database-driven approach, and more generally profile-based post-necking identification strategies.

Going into more details of the shape-law correlation, it was first demonstrated that there are cases in which a single highly deformed necking configuration is representative of the entire post-necking response in the $\sigma_{eq} - \varepsilon_{eq,p}$ plane. More specifically, this was shown to be valid in normalized terms and regardless of the uniform deformation phase. This category of behaviors includes materials and/or conditions where equivalent plastic strain is the only variable affecting plasticity. For these scenarios, one geometrical shape allows the normalized post-necking hardening law to be identified, whereas information on the force is needed for determining the absolute stress values. As anticipated, this was implemented with a database-driven approach. The identification procedure simply consisted of searching this database for the numerical shape which best matches the experimental one, regardless of the absolute size. This allows the normalized post-necking hardening to be determined and adjusted to reconstruct the actual post-necking hardening law of the material under investigation.

Regarding the precomputed library, the explicit solver of the commercial FE code Ansys LS-DYNA was used to run the simulations. Several tensile tests, conducted on cylindrical bars that differed one from another in terms of strain-hardening behavior, were modelled. It was verified, through numerical benchmarks, that a database of cylindrical bars enhances generality (from the geometric point of view) without introducing significant errors when used for experiments conducted on dog-bone specimens. Moreover, numerical benchmarks also validated the method against geometrical uncertainties in silhouette measurements. Finally, experiments conducted on pure copper, Al6082-T6, and 17-4PH were used as relevant case studies for the proposed method, due to their different behavior in terms of strength, ductility, and hardening rate. They demonstrated the practical applicability of the database-driven approach for strain-hardening identification, with a computational effort comparable to analytical strategies and an accuracy approaching that of FEMU techniques.

The range of applicability of the method, however, is not limited to cases where equivalent plastic strain is the only governing variable. It can be applied in principle to all cases in which other relevant variables remain constant during testing (e.g., isothermal tests at non-standard temperatures) or are univocally linked to the equivalent plastic strain (namely, temperature for strain rate insensitive materials). Issues would arise when there are variables affecting plastic behavior, which evolve within the single test in a way not univocally linked to the equivalent plastic strain.

This is the case of strain rate: if strain rate sensitivity is sufficiently high, it can affect the material response within a single test due to the strain rate heterogeneity typical of necking. As a matter of fact, in these cases, a single necking profile is not sufficient to identify the post-necking behavior. However, it was proved that, even in such critical scenarios, necking profiles contain information about superficial distributions of equivalent plastic strain, equivalent plastic strain rate, and equivalent stress. This was shown to be valid again in normalized terms, which implies that if the normalized necking profiles of two materials coincide, one material can be used to instantaneously approximate those distributions for the other one, once instantaneous force and speed are accounted for. More importantly, this correlation is valid even between a rate sensitive material and a rate insensitive one. This means that a rate sensitive material during a test can be approximated as a sequence of different rate insensitive materials, one per each time considered. Hence, the database-driven approach was readily extended for dealing with these situations, without the need to include rate sensitive materials in the database. The proposed procedure involves repeating the brute-force search at different times, thus obtaining $\sigma_{eq}(\varepsilon_{eq,p})$ curves that represent the states of superficial material points at these times. Then, the information of local equivalent plastic strain rate can be added thanks to the database itself and by accounting for the instantaneous speed of radial contraction. The output of the proposed method is finally represented by a point cloud in the space $\varepsilon_{eq,p} - \dot{\varepsilon}_{eq,p} - \sigma_{eq}$ that reflects the material's visco-plastic behavior during the single test, without any assumption about material behavior, apart from isotropic Von Mises plasticity. The potential of the approach was illustrated through the successful application to pure molybdenum, a material known to be highly sensitive to strain rate. Nevertheless, the method remains applicable to the special case of negligible strain rate sensitivity, as proved with an experimental case study on pure copper: despite slightly increasing the computational cost, it significantly improved stability and robustness.

Among the possible issues that may arise when focusing on a single tensile test, the one that still needed to be addressed was the strain rate-temperature interaction typical of self-heating conditions. For these cases, it was shown that determining the thermo-visco-plastic response in the $\varepsilon_{eq,p} - \dot{\varepsilon}_{eq,p} - T - \sigma_{eq}$ hyperspace did not represent a problem of higher complexity for the database-driven approach in the generalized form summarized above. This is thanks to its distinctive capability of providing a good approximation of the instantaneous equivalent stress distribution on the specimen surface, independently of the physical variables that generated it and even if some relevant variables are not explicitly included in the database. Nevertheless, this was possible as the database included also non-monotonically increasing $\sigma_{eq}(\varepsilon_{eq,p})$ laws to account for thermal softening behaviors. If the objective is to identify the plastic flow surface, equivalent stress distribution can be associated with the fields of physical variables affecting plastic response. Equivalent plastic strain and strain rate distributions can be estimated through the database, while temperature can be measured experimentally via infrared imaging. In practice, the database-driven approach is applied to several necking configurations and to each of them the superficial thermal field measured by an infrared camera is added. The resulting point cloud in the 4D space represents the states experienced by superficial material points during the test analyzed. The identification of material response as a point cloud represents a significant advantage of the proposed approach for thermo-visco-plastic characterization since it does not require assuming a model *a priori*. By simply applying the proposed method to tests conducted under different loading conditions the material response is reconstructed over broad ranges of strain, strain rate and temperature. This was practically demonstrated through some experimental tests conducted on 17-4 PH, at different loading rates. Material self-heating during non-isothermal tests was monitored with a high-speed high-resolution infrared camera and the measured thermal fields were used within the proposed framework of analysis. Then, for verifying the reliability of the identified model by implementing it in FE simulations of the tests, the identified point cloud was fitted with a tabularly defined material model for strain, strain rate and temperature dependencies. However, it was also necessary to define heat conversion in all non-isothermal tests: in a preliminary phase, a constant TQC was roughly estimated and no additional heat losses were considered. Thus, the resulting model was used for simulating only isothermal and adiabatic tests, which were both found to be in good agreement with experimental results (also in terms of superficial thermal fields for the adiabatic test).

With the aim of gaining further insights into intermediate strain rates condition, where thermal fields result from both self-heating and heat conduction, the focus shifted to investigating the work-to-heat conversion. Specifically, the possibility of further exploiting the database-driven approach for determining the TQC from the post-necking phase of tensile tests was explored. It was found that, under adiabatic conditions, the method allowed the work-to-heat conversion to be estimated with a direct approach based on the heat equation. Instead, for dealing with non-adiabatic conditions, an inverse approach based on thermal-structural FE simulations was developed, but the use of the database-driven approach for mechanical identification proved to be advantageous. This is because the database-driven strategy can identify the thermo-visco-plastic flow without knowing how the measured temperature has been affected by heat losses. Thus, the inverse approach only needs to focus on this second aspect, thereby limiting the computational time of FEMU strategies that, in the more general case, would require simultaneous identification of structural behavior and heat losses. The overall feasibility and accuracy of both methods was demonstrated first through ad-hoc numerical benchmarks and then through the 17-4PH experimental case study. In particular, it is worth underlining that the inverse procedure, despite employing an approximate modeling of heat losses and a tentative iterative procedure, provided very promising results in all conditions analyzed.

Extending the analysis to even more complex scenarios, the last part of the thesis took the first steps towards post-necking hardening identification for initially cylindrical specimens that exhibit anisotropic deformation. In this phase, the current form of the database-driven approach lost representativeness, as it relies on lines of reasoning formulated for isotropic materials. Nevertheless, the overarching objective of developing accurate and efficient methodologies was still considered when seeking an alternative strategy for anisotropic materials. FE simulations were again employed to ensure that the main features of plastic anisotropic deformation, especially during necking, were caught. Regarding the computational cost, this was limited by relying on an analytical estimate of the hardening law as a starting point for a single FE-assisted refinement step, properly targeted. From the experimental point of view, determination of the deformed shape was more challenging than for isotropic materials due to the loss of axialsymmetry. In agreement with the methodologies adopted throughout this thesis, a simple and versatile solution was chosen. Two cameras were used during the test for measuring the projected silhouettes of the specimen, whose 3D shape was reconstructed *a posteriori* by hypothesizing elliptical cross-sections orientated as found from a post-mortem 360°-scan. The applicability of the method was verified on quasi-static experimental tests on CuCrZr specimens obtained along the transversal direction of a plate. Given the limited information about anisotropy that could be gained from such tests, isotropic hardening was assumed and simplified yield modeling was adopted. Despite its simplicity, the proposed approach yielded encouraging results. This demonstrated that whenever the intent is determining the strain-hardening behavior under a given tensile loading condition, rather than a complete description of yield anisotropy, tensile tests on cylindrical samples can provide first-order results if anisotropic necking is addressed properly.

To conclude, necking deformed shapes were seen to provide insightful information about the plastic behavior of isotropic materials, which consequently led to considerable advantages in plastic flow identification. This suggests that future work on post-necking identification of initially cylindrical specimens made of anisotropic materials should focus on better exploiting their necking deformed shapes. Further investigation is required to assess whether an efficient database-driven approach, analogous to the one developed for isotropic materials, can be feasible.

For what isotropic materials are concerned, the database-driven approach can be seen, from a broader perspective, as a preliminary study towards silhouette-based ML algorithms. In its final form, the proposed method shows how effective datasets can be established for efficient and informed implementation of ML algorithms for thermo-visco-plastic characterization, using necking silhouettes as main input.

9Appendix A

Consider a cylindrical bar of radius R_0 and denote with coordinate X each cross-section in the undeformed configuration. During necking, the cross-sections become curved and cannot be identified by a unique axial position. The average coordinate is, thus, used and is denoted by $\Lambda(X)$. This is schematically depicted in Figure A.1.

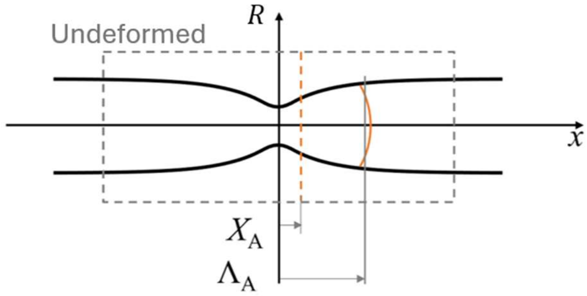

Figure A.1 Cylindrical bar in undeformed and necking deformed configuration (adapted from [1]).

Assuming material isotropy and incompressibility, Audoly and Hutchinson's 1D theory [2] predict that the deformed coordinates (x, r) of a point of initial coordinates (X, R) become:

$$x(X,R) = \Lambda(X) + \frac{1}{4\,\lambda(X)^3}\frac{d\lambda(X)}{dX}\left(R^2 - \frac{R_0^2}{2}\right), \tag{A.1a}$$

$$r(X,R) = \frac{R}{\sqrt{\lambda(X)}}, \tag{A.1b}$$

where $\lambda(X) \stackrel{\text{def}}{=} \frac{d\Lambda}{dX}$ represents the stretch and terms of higher order than $\frac{d\lambda}{dX}$ have been neglected.

Focusing on material points on the specimen surface, $R = R_0$ and previous Equations A.1 become:

$$x(X) = x(X,R_0) = \Lambda(X) + \frac{1}{4\,\lambda(X)^3}\frac{d\lambda(X)}{dX}\frac{R_0^2}{2}, \tag{A.2a}$$

$$r(X) = r(X,R_0) = \frac{R_0}{\sqrt{\lambda(X)}}. \tag{A.2b}$$

This last equation highlights that the stretch at a certain configuration is related to specimen normalized profile:

$$\lambda(X) = \left(\frac{R_0}{r(X)}\right)^2. \tag{A.3}$$

By introducing the radius R_n (the one at the necking onset configuration), it is possible to separate the "total" stretch into a contribution from uniform deformation and another one from necking deformation:

$$\lambda(X) = \left(\frac{R_0}{R_n}\frac{R_n}{r(X)}\right)^2 = \left(\frac{R_0}{R_n}\right)^2 \left(\frac{R_n}{r(X)}\right)^2. \quad (A.4)$$

The first multiplicative factor represents the stretch at the necking onset (as inferable from Equation 3):

$$\lambda_n = \left(\frac{R_0}{R_n}\right)^2. \quad (A.5)$$

The other multiplicative factor of Equation A.4, thus, represents the contribution of the post-necking deformation:

$$\lambda_p(X) = \left(\frac{R_n}{r(X)}\right)^2. \quad (A.6)$$

It results that Equation A.4 can be rewritten as:

$$\lambda(X) = \lambda_u \lambda_p(X). \quad (A.7)$$

At this point, consider two geometrically identical cylindrical bars made of two materials (1 and 2), that share the same normalized necking silhouette, namely the pairs $(x_1/R_{n1}, r_1/R_{n1})$ overlap with $(x_2/R_{n2}, r_2/R_{n2})$. By introducing the geometric scaling coefficient $k_g = R_{n1}/R_{n2}$, it results that the pairs (x_1, r_1) overlap with $(k_g x_2, k_g r_2)$. Nevertheless, it is challenging to understand which are the material points of material 2 equivalent to those of material 1. In other words, which *j*-th point of material 2 is equivalent to the *i*-th point of material 1, i.e., which are *i* and *j* satisfying the Equations A.8:

$$x_{1i} = k_g x_{2j}; \quad (A.8a)$$

$$r_{1i} = k_g r_{2j}. \quad (A.8b)$$

The solution to this problem was derived in [3] and is reported hereinafter.

As stated at the right beginning of this appendix, points are identified by their position in the undeformed configuration: (X_{1i}, R_{1i}) and (X_{2j}, R_{2j}). Considering that the analysis focuses on points on the outer surface and that the specimens share the same initial radius R_0, material points can be identified by their initial axial coordinates X_{1i} and X_{2j}. To find the relationship between these positions, Equation A.8a is enforced, expressing each term through Equation A.2a:

$$x_{1i} = \Lambda_{1i} + \frac{1}{4\,\lambda_{1i}^3}\frac{d\lambda_1}{dX_1}\bigg|_{X_{1i}} \frac{R_0^2}{2}; \quad (A.9a)$$

$$x_{2j} = \Lambda_{2j} + \frac{1}{4\,\lambda_{2j}^3}\frac{d\lambda_2}{dX_2}\bigg|_{X_{2j}} \frac{R_0^2}{2}. \quad (A.9b)$$

Regarding the first addendum, the following equations are obtained:

$$\Lambda_{1i} = \int_0^{X_{1i}} \lambda_1(X_1)\, dX_1 = \int_0^{X_{1i}} \lambda_{n1}\lambda_{p1}(X_1)\, dX_1 = \lambda_{n1}\int_0^{X_{1i}} \lambda_{p1}(X_1)\, dX_1 \quad (A.10a)$$

$$\Lambda_{2j} = \lambda_{n2}\int_0^{X_{2j}} \lambda_{p2}(X_2)\, dX_2. \quad (A.10b)$$

For further developing these expressions, consider that the post-necking stretch is the same (see Equations A.6 and A.8b):

$$\lambda_{p1}(X_{1i}) = \lambda_{p2}(X_{2j}), \qquad \text{(A.11)}$$

or more concisely $\lambda_{p1i} = \lambda_{p2j}$.

This result allows a change of variables to be applied in Equations A.10. Specifically, the following relationship between Λ_{1i} and Λ_{2j} can be found:

$$\Lambda_{1i} = \lambda_{n1} \int_0^{X_{2j}} \lambda_{p2}(X_2)\, dX_2 c = c\lambda_{n1} \frac{\Lambda_{2j}}{\lambda_{n2}} = \frac{c}{k_g^2} \Lambda_{2j}, \qquad \text{(A.12)}$$

by reasonably hypothesizing $\frac{dX_1}{dX_2} = c$ and considering that:

$$\frac{\lambda_{n1}}{\lambda_{n2}} = \frac{(R_0/R_{n1})^2}{(R_0/R_{n2})^2} = \left(\frac{R_{n2}}{R_{n1}}\right)^2 = \frac{1}{k_g^2}. \qquad \text{(A.13)}$$

Referring again to Equations A.9, attention shifts to the stretch derivatives. Using Equation A.7 first and Equation A.6 subsequently, the following expressions are obtained:

$$\left.\frac{d\lambda_1}{dX_1}\right|_{X_{1i}} = \lambda_{n1} \left.\frac{d\lambda_{p1}}{dX_1}\right|_{X_{1i}} = \lambda_{n1} \frac{d}{dX_1} \left(\frac{R_{n1}}{r_1(X_1)}\right)^2 = \lambda_{n1} {R_{n1}}^2 \left(-2 \frac{dr_1}{dX_1} \frac{1}{r_1^3(X_1)}\right) =$$
$$-\lambda_{n1} \frac{2{R_{n1}}^2}{r_1^3(X_1)} \frac{dr_1}{dX_1} \qquad \text{(A.14a)}$$

and similarly:

$$\left.\frac{d\lambda_2}{dX_2}\right|_{X_{2j}} = -\lambda_{n2} \frac{2{R_{n2}}^2}{r_2^3(X_2)} \frac{dr_2}{dX_2}. \qquad \text{(A.14b)}$$

By replacing $r_1(X_1)$ with $k_g r_2(X_2)$ in Equation A.14a, it results that:

$$\left.\frac{d\lambda_1}{dX_1}\right|_{X_{1i}} = -\frac{\lambda_{n2}}{k_g^2} \frac{2{R_{n1}}^2}{k_g^3 r_2^3(X_2)} k_g \frac{dr_2}{dX_2} \frac{dX_2}{dX_1} = -\frac{\lambda_{n2}}{k_g^2} \frac{2{R_{n1}}^2}{k_g^2 r_2^3(X_2)} \frac{dr_2}{dX_2} \frac{1}{c}. \qquad \text{(A.15)}$$

while Equation A.14b can be used for deriving the following relationship:

$$\lambda_{n2} \frac{2}{r_2^3(X_2)} \frac{dr_2}{dX_2} = -\frac{1}{{R_{n2}}^2} \left.\frac{d\lambda_2}{dX_2}\right|_{X_{2j}}. \qquad \text{(A.16)}$$

Hence, plugging it into Equation A.15, the latter becomes:

$$\left.\frac{d\lambda_1}{dX_1}\right|_{X_{1i}} = \frac{1}{k_g^4} \frac{{R_{n1}}^2}{{R_{n2}}^2} \frac{1}{c} \left.\frac{d\lambda_2}{dX_2}\right|_{X_{2j}} = \frac{1}{k_g^2 c} \left.\frac{d\lambda_2}{dX_2}\right|_{X_{2j}}. \qquad \text{(A.17)}$$

Finally, it is possible to plug Equations A.12 and A.17 into Equation A.9a, obtaining:

$$x_{1i} = \frac{c}{k_g^2} \Lambda_{2j} + \frac{k_g^6}{4\, \lambda_{2j}^3} \frac{1}{k_g^2 c} \left.\frac{d\lambda_2}{dX_2}\right|_{X_{2j}} \frac{R_0^2}{2}. \qquad \text{(A.18)}$$

Comparing this result with the condition imposed by Equation A.8a, it is evident that c must be equal to k^3. This leads to the conclusion that material points analogous for the post-necking phase are characterized by initial axial coordinates linked through the relationship: $X_{1i} = k^3 X_{2j}$.

References

[1] Beltramo, M., Scapin, M., & Peroni, L. (2023). An advanced post-necking analysis methodology for elasto-plastic material models identification. *Materials & Design*, *230*, 111937.

[2] Audoly, B., & Hutchinson, J. W. (2016). Analysis of necking based on a one-dimensional model. *Journal of the Mechanics and Physics of Solids*, *97*, 68-91.

[3] Beltramo, M., Scapin, M., & Peroni, L. (2025). Analysis of the work-to-heat conversion beyond the necking onset in non-isothermal tensile tests. *International Journal of Impact Engineering*, 105503.